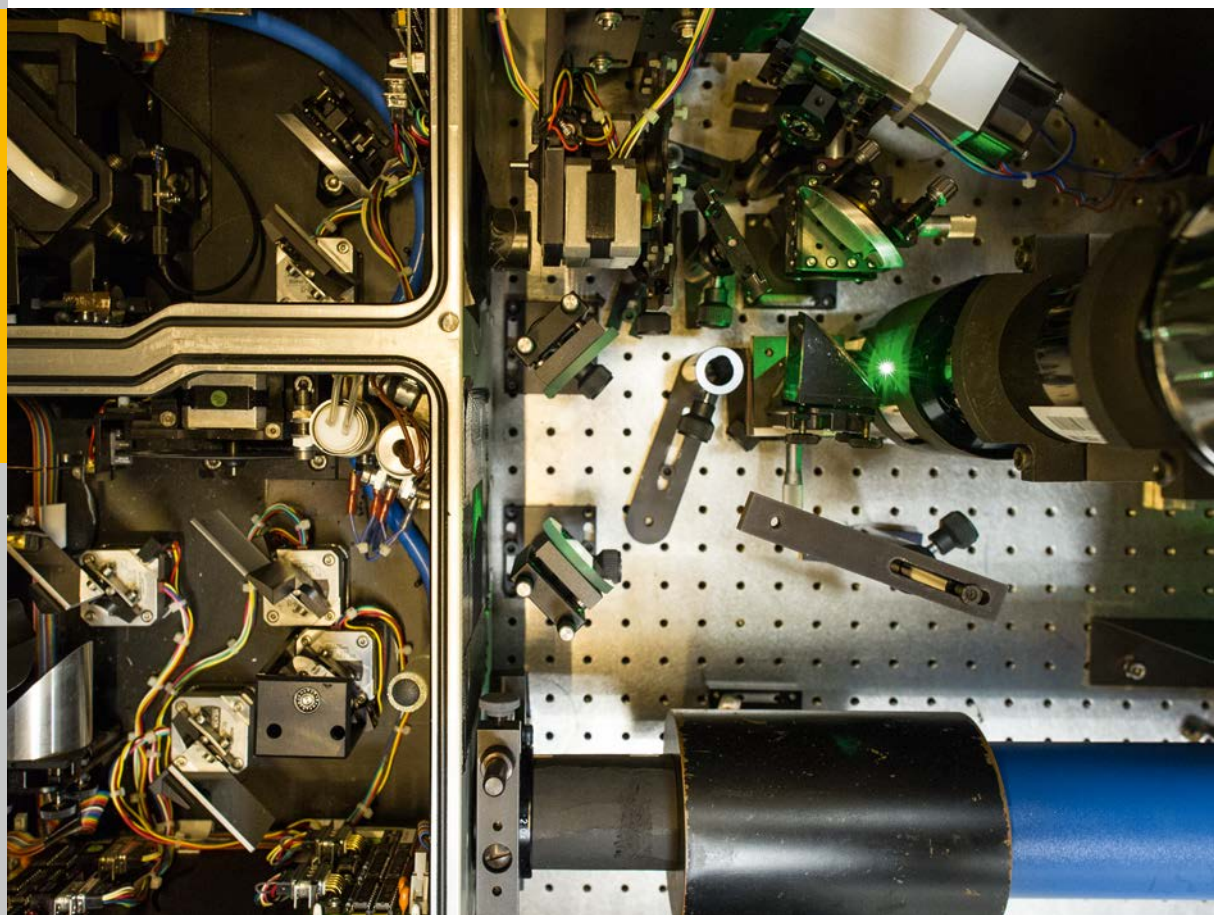


# Light Absorption and Radiative Recombination in Thin-Film Solar Cells

Thomas Christian Mathias Müller



Energie & Umwelt/  
Energy & Environment  
Band/ Volume 272  
ISBN 978-3-95806-068-5





Forschungszentrum Jülich GmbH  
Institute of Energy and Climate Research  
IEK-5 Photovoltaics

# **Light Absorption and Radiative Recombination in Thin-Film Solar Cells**

Thomas Christian Mathias Müller

Schriften des Forschungszentrums Jülich  
Reihe Energie & Umwelt / Energy & Environment

Band / Volume 272

---

ISSN 1866-1793

ISBN 978-3-95806-068-5

Bibliographic information published by the Deutsche Nationalbibliothek.  
The Deutsche Nationalbibliothek lists this publication in the Deutsche  
Nationalbibliografie; detailed bibliographic data are available in the  
Internet at <http://dnb.d-nb.de>.

Publisher and Distributor:	Forschungszentrum Jülich GmbH Zentralbibliothek 52425 Jülich Tel: +49 2461 61-5368 Fax: +49 2461 61-6103 Email: <a href="mailto:zb-publikation@fz-juelich.de">zb-publikation@fz-juelich.de</a> <a href="http://www.fz-juelich.de/zb">www.fz-juelich.de/zb</a>
Cover Design:	Grafische Medien, Forschungszentrum Jülich GmbH
Printer:	Grafische Medien, Forschungszentrum Jülich GmbH
Copyright:	Forschungszentrum Jülich 2015

Schriften des Forschungszentrums Jülich  
Reihe Energie & Umwelt / Energy & Environment, Band / Volume 272

D 82 (Diss. RWTH Aachen University, 2015)

ISSN 1866-1793  
ISBN 978-3-95806-068-5

The complete volume is freely available on the Internet on the Jülicher Open Access Server (JuSER)  
at [www.fz-juelich.de/zb/openaccess](http://www.fz-juelich.de/zb/openaccess).

Neither this book nor any part of it may be reproduced or transmitted in any form or by any  
means, electronic or mechanical, including photocopying, microfilming, and recording, or by any  
information storage and retrieval system, without permission in writing from the publisher.

# Contents

<b>Abstract</b>	<b>1</b>
<b>Zusammenfassung</b>	<b>3</b>
<b>1 Introduction</b>	<b>5</b>
<b>2 Fundamentals</b>	<b>9</b>
2.1 Solar Cells . . . . .	9
2.2 Electronic States in Semiconductors . . . . .	10
2.2.1 Extended Band States . . . . .	11
2.2.2 Localized Band-Tail States . . . . .	13
2.2.3 Mid-Gap Defect States . . . . .	17
2.3 Reciprocity Relation between Electroluminescence and External Quantum Efficiency . . . . .	21
2.4 Radiative Recombination . . . . .	23
2.4.1 Chalcopyrite $\text{Cu}(\text{In,Ga})\text{Se}_2$ . . . . .	24
2.4.2 Hydrogenated Microcrystalline Silicon $\mu\text{c-Si:H}$ . . . . .	25
2.4.3 Hydrogenated Amorphous Silicon $a\text{-Si:H}$ . . . . .	26
2.5 Light Absorption . . . . .	27
<b>3 Experimental Methods and Simulations</b>	<b>29</b>
3.1 Experiments . . . . .	29
3.1.1 Devices . . . . .	29
3.1.2 Electro- and Photoluminescence . . . . .	33
3.1.3 External Quantum Efficiency . . . . .	33
3.2 Simulations and Modeling . . . . .	35
3.2.1 Full Device Simulations – ASA . . . . .	35
3.2.2 Luminescence Simulations – LUME . . . . .	42
<b>4 Chalcopyrite <math>\text{Cu}(\text{In,Ga})\text{Se}_2</math> Based <math>np</math> Heterojunction Devices</b>	<b>45</b>
4.1 Experimental Results . . . . .	46
4.1.1 Accelerated Light Soaking . . . . .	46
4.1.2 Change of Luminescence Spectra . . . . .	48
4.1.3 Reciprocity Relation . . . . .	51

4.1.4	Radiative Ideality Factor . . . . .	53
4.2	Discussion . . . . .	57
4.2.1	Modeling of Luminescence Spectra and External Quantum Efficiency . . . . .	57
4.2.2	Radiative Ideality Factor and Shift of Luminescence . . . . .	59
4.2.3	Reciprocity Relation . . . . .	60
<b>5</b>	<b>Hydrogenated Microcrystalline Silicon Based <i>pin</i> Devices</b>	<b>63</b>
5.1	Experimental Results . . . . .	64
5.1.1	Temperature and Voltage Dependent Luminescence Spectra . . . . .	64
5.1.2	Reciprocity Relation . . . . .	66
5.1.3	Radiative Ideality Factor . . . . .	67
5.2	Discussion . . . . .	69
5.2.1	Device Modeling and Characterization . . . . .	69
5.2.2	Change of Luminescence Spectra . . . . .	74
5.2.3	Radiative Ideality Factor . . . . .	78
5.2.4	Reciprocity Relation . . . . .	84
<b>6</b>	<b>Hydrogenated Amorphous Silicon Based <i>pin</i> Devices</b>	<b>89</b>
6.1	Experimental Results . . . . .	90
6.1.1	Temperature and Voltage Dependent Luminescence Spectra . . . . .	93
6.1.2	Reciprocity Relation . . . . .	94
6.1.3	Radiative Ideality Factor . . . . .	96
6.2	Discussion . . . . .	99
6.2.1	Device Modeling and Characterization . . . . .	99
6.2.2	Change of Luminescence Spectra . . . . .	108
6.2.3	Radiative Ideality Factor . . . . .	110
6.2.4	Reciprocity Relation . . . . .	114
<b>7</b>	<b>Conclusions and Outlook</b>	<b>117</b>
	<b>Bibliography</b>	<b>121</b>
	<b>List of Symbols</b>	<b>139</b>
	<b>List of Publications</b>	<b>143</b>
	<b>Curriculum Vitae</b>	<b>145</b>
	<b>Acknowledgements</b>	<b>147</b>

# Abstract

*Solar cells* and light emitting diodes are generally the same kind of device. Whereas *solar cells* are optimized for *light absorption*, light emitting diodes are optimized for light emission, *i.e. radiative recombination*. Both processes are present in each of these devices. The electroluminescence depends on the transport of injected charge carriers and *radiative recombination*, whereas the external quantum efficiency originates from *light absorption* and the extraction of photo generated charge carriers.

According to Donolato and Rau, the external quantum efficiency and the luminescence are connected by the *reciprocity relation*. However, the *reciprocity relation* only holds under certain circumstances. Whereas these circumstances are given in defect-free *solar cells* made from crystalline silicon for instance, the situation can be different in *thin-film* devices. The physics in *thin-film* devices can be affected by localized inter-band defect states, which also affect the *reciprocity relation*. These states are found in *thin-film* chalcopyrite  $\text{Cu(In,Ga)Se}_2$  *np* heterojunction, hydrogenated microcrystalline silicon *pin*, and hydrogenated amorphous silicon *pin* devices as investigated in this thesis. This thesis is structured within this sequence, studying systems with increasing concentrations of defect states in their band gap to investigate these circumstances, where the *reciprocity relation* still holds.

The requirements of the *reciprocity relation* are investigated with temperature and charge carrier injection dependent experiments as well as comprehensive simulations. Since the electroluminescence is affected by series resistance, in most cases it is complemented with photoluminescence, where charge carrier transport is negligible. An expanded *Fourier transform infrared spectroscopy* setup is used to perform the luminescence experiments, and the external quantum efficiency is measured with a *constant photocurrent method* setup. The simulations use a commercial one dimensional numerical device simulator, which solves the optics and the semiconductor equations. A self-developed program, which uses full band diagrams of the one dimensional device simulator as input parameters, yields the luminescence and external quantum efficiency calculations.

The luminescence in  $\text{Cu(In,Ga)Se}_2$  originates from transitions between the bands and localized band-tail states. Since the band-tail densities of states are rather steep, the almost unshifted luminescence spectra are compatible to the external quantum efficiency in terms of the *reciprocity relation*. Around room temperature, the radiative ideality factor, which is determined from luminescence/voltage characteristics by fitting a common diode law, is found to be close to unity. However, temperature dependent experiments and simulations show that the *reciprocity relation* only holds if the thermal energy is higher than the characteristic energy of the band-tail densities



of states.

Transitions between band-tail states yield the luminescence in hydrogenated microcrystalline silicon. However, the *reciprocity relation* between the luminescence and the external quantum efficiency only holds in a small spectral range, since the band-tails are broad, *i.e.* their characteristic energies are higher than the thermal energy, even at room temperature. This yields blue shifted luminescence spectra with increasing charge carrier injection and a temperature dependent radiative ideality factor, which exceeds unity and increases with decreasing temperature. However, detailed simulations show that the *reciprocity relation* holds if the device under luminescence conditions is close to thermal equilibrium. These conditions yield very low luminescence intensities, which are not accessible within experiments.

The luminescence in hydrogenated amorphous silicon originates from transitions between localized band-tails, which are even broader than in hydrogenated microcrystalline silicon. Additionally, around room temperature and/or at low injection, transitions between band and neutral amphoteric mid-gap defect states contribute to the luminescence beside the tail-to-tail luminescence. The band-to-defect luminescence spectra do not shift under different charge carrier injection levels, since the occupation of mid-gap defect states is almost constant, even if the charge carrier injection is moderate. This yields a radiative ideality factor of around two. However, the presence of additionally Stokes-shifted tail-to-tail luminescence, where the luminescence loses photon energy to the lattice, completely hampers the validity of the *reciprocity relation* within experiments. Only simulations can show that the *reciprocity relation* holds if the device is almost in thermal equilibrium at extreme low charge carrier injection.

# Zusammenfassung

*Solarzellen* und Leuchtdioden sind generell die gleichen Bauelemente. Während *Solarzellen* für die *Lichtabsorption* optimiert sind, sind Leuchtdioden für die Lichtemission, d.h. *strahlende Rekombination* optimiert. Beide Prozesse sind in jedem dieser Bauelemente vorhanden. Die Elektrolumineszenz hängt von dem Transport injizierter Ladungsträger und der *strahlenden Rekombination* ab, wohingegen die externe Quanteneffizienz durch *Lichtabsorption* und Extraktion von photogenerierten Ladungsträgern entsteht.

Gemäß Donolato und Rau stehen die externe Quanteneffizienz und die Lumineszenz in einem *reziproken Verhältnis*. Allerdings gilt dieses *reziproke Verhältnis* nur unter bestimmten Bedingungen. Wohingegen solche Umstände in defektfreien *Solarzellen*, z. B. aus kristallinem Silizium, gegeben sind, kann dies in *Dünnschicht*-Bauelementen anders sein. Die Physik in *Dünnschicht*-Bauelementen kann durch lokale Interband-Defektzustände beeinflusst werden, die wiederum das *reziproke Verhältnis* beeinflussen. Solche Zustände sind in *Dünnschicht* chalkopyriten  $\text{Cu(In,Ga)Se}_2$  *np* Heteroübergängen, hydrierten mikrokristallinen Silizium *pin*, und hydrierten amorphen Silizium *pin* Bauelementen, wie sie in dieser Arbeit untersucht werden, zu finden. Diese Arbeit ist gemäß dieser Reihenfolge mit ansteigender Defektkonzentration in der Bandlücke strukturiert, um solche Bedingungen zu untersuchen, in denen das *reziproke Verhältnis* weiterhin gilt.

Die Anforderungen des *reziproken Verhältnisses* werden mit temperatur- und ladungsträgerinjektionsabhängigen Experimenten sowie umfassenden Simulationen untersucht. Da die Elektrolumineszenz durch Serienwiderstände beeinflusst wird, wird sie in den meisten Fällen durch Photolumineszenz, bei der Ladungsträgertransport vernachlässigbar ist, ergänzt. Ein erweiterter *Fourier-Transform-Infrarotspektroskopie*-Aufbau wird genutzt, um die Lumineszenz Experimente durchzuführen, und die externe Quanteneffizienz wird mit einem *Konstantphotostrom*-Aufbau gemessen. Die Simulationen nutzen einen kommerziellen eindimensionalen numerischen Bauteile-Simulator, der die Optik und Halbleitergleichungen löst. Ein selbst entwickeltes Programm, das die vollständigen Banddiagramme des eindimensionalen Bauteile-Simulators als Eingangsparameter nutzt, errechnet die Lumineszenz und externe Quanteneffizienz.

Die Lumineszenz in  $\text{Cu(In,Ga)Se}_2$  entsteht durch Übergänge zwischen den Bändern und lokalisierten Zuständen in den Bandausläufern. Da die Zustandsdichten der Bandausläufer ziemlich steil sind, stehen die fast unverschobenen Lumineszenzspektren im *reziproken Verhältnis* zur externen Quanteneffizienz. Bei etwa Raumtemperatur ist der strahlende Idealitätsfaktor, der durch das Anpassen einer gewöhnlichen Diodenkennlinie an Lumineszenz/Spannung Charakteristika bestimmt wird, nahe eins. Allerdings zeigen temperaturabhängige Experimente und Simula-

tionen, dass das *reziproke Verhältnis* nur besteht, falls die thermische Energie größer ist als die charakteristische Energie der Zustandsdichten der Bandausläufer.

Übergänge zwischen Zuständen der Bandausläufer ergeben die Lumineszenz in hydriertem mikrokristallinem Silizium. Allerdings besteht das *reziproke Verhältnis* zwischen der Lumineszenz und der externen Quanteneffizienz nur in einem kleinen Spektralbereich, da die Bandausläufer breit sind, d. h. ihre charakteristischen Energien sind sogar bei Raumtemperatur größer als die thermische Energie. Dies führt zu blau-verschobenen Lumineszenzspektren mit ansteigender Ladungsträgerinjektion und einem temperaturabhängigen strahlenden Idealitätsfaktor, der über eins hinaus reicht und mit fallender Temperatur weiter ansteigt. Detaillierte Simulationen zeigen allerdings, dass das *reziproke Verhältnis* Bestand hat, falls das Bauelement unter Lumineszenz-Bedingungen nah am thermischen Gleichgewicht ist. Unter solchen Bedingungen sind die Intensitäten der Lumineszenz sehr niedrig und deshalb nicht messbar.

Die Lumineszenz in hydriertem amorphem Silizium entsteht durch Übergänge zwischen lokalisierten Bandausläufern, die noch breiter sind als in hydriertem mikrokristallinem Silizium. Zusätzlich tragen etwa bei Raumtemperatur und/oder geringer Ladungsträgerinjektion, Übergänge zwischen Band- und neutralen amphoteren Defektzuständen in der Bandlückenmitte zur Lumineszenz bei. Diese Band-zu-Defekt Lumineszenzspektren verschieben sich nicht unter verschiedenen Ladungsträgerinjektionsraten, da die Besetzung der Defektzustände in der Bandlückenmitte sogar unter moderater Ladungsträgerinjektion fast konstant ist. Dies ergibt einen strahlenden Idealitätsfaktor, der etwa zwei ist. Allerdings verhindert eine zusätzliche Stokes-Verschiebung der Lumineszenzspektren der lokalisierten Bandausläufer, bei der die Photonen dieser Spektren Energie an das Gitter verlieren, die Gültigkeit des *reziproken Verhältnisses* im Experiment. Nur mit Hilfe von Simulationen kann gezeigt werden, dass das *reziproke Verhältnis* gilt, falls das Bauelement bei extrem niedrigerer Ladungsträgerinjektion nahe des thermischen Gleichgewichts ist.

# Chapter 1

## Introduction

About 90 % of the consumed energy comes from fossil fuels [1]. The burning of fossil fuels leads to man-made global warming [2]. The temperature of the earth raised more than 0.74 K in the last hundred years, and due to increased energy consumption from fossil fuels the heating also increased [3]. The world energy consumption in 2010 was  $3.63 \times 10^{20}$  J per year [1]. However, the amount of energy, which is delivered to earth every year in the form of solar irradiation is  $3.15 \times 10^{24}$  J [4]. Although the energy production from sunlight is still more expensive than from other renewable energies [5], the demand for *solar cells* increases. Whereas the world *solar cell* market in 1980 was a few Mega Watt peak per year, the market grew to  $27.4 \times 10^9$  W<sub>p</sub> in 2011.

The first *solar cell* was presented in 1954, which resulted from investigations on silicon *pn* junctions [6]. Since the presentation of the first *solar cell*, completely different approaches for photovoltaic devices have been developed [7, 8], *i.e.* the use of organic semiconductors [9–14], semiconductor nano-particles [15–18], or dye sensitized *solar cells* [19] for example. However, the basic physics of *light absorption*, charge carrier separation, and therefore energy generation remain the same.

A light emitting diode (LED) utilizes the opposite process (*radiative recombination*) as used in *solar cells* (*light absorption*). For this reason a *solar cell* cannot only convert light to electric energy, it can also convert electric energy to light, although *solar cells* are optimized for absorbing a broad spectrum of light rather than for emitting light. The emission of light (luminescence) by a *solar cell* can be driven electrically (electroluminescence) or optically (photoluminescence). The *reciprocity relations* as formulated by Donolato [20] and Rau [21, 22] connect the *solar cell* quantum efficiency of absorbed light to the LED quantum efficiency of emitted light. As a consequence of the principle of detailed balance, Donolato connected the minority carrier concentration in a *solar cell* under forward voltage in the dark with the local collection probability of photo generated charge carriers within the same device [20]. Rau expanded this *reciprocity relation* by Donolato by the junction of the device and formulated the final *reciprocity relation* between the quantum efficiency and the luminescence [21, 22]. Using this *reciprocity relation* by Rau, one can thus characterize certain aspects of solar cells in luminescence experiments.

In recent years many characterization methods based on the *reciprocity relation* have been

developed. The photo- and electroluminescence are commonly used characterization methods to study recombination processes in semiconductor devices to evaluate the optical band gap [23], defect-states [24–28], or the quasi-Fermi level separation [29, 30]. Interpretation of photo- or electroluminescence imaging in *thin-film solar cells* is mainly based on the analysis of spatial variations of the local quasi-Fermi level separation. Generally, light induced degradation [31,32], shunts [33,34], series resistance [35–37], or charge carrier diffusion lengths [38–41] can be investigated fast and spatially resolved, amongst others. Additionally, performance mapping of multijunction *solar cells*/modules is feasible [28,42]. This technique is successfully used as inline characterization tool [43] for *e.g.* mono-crystalline silicon.

However, the *reciprocity relation* by Donolato and Rau makes simplifications that do not hold equally well for all technologies. The *reciprocity relation* between the external quantum efficiency and the electroluminescence implicitly requires the luminescence spectrum to be independent of the applied voltage, a luminescence intensity/voltage characteristic with a radiative ideality factor of one, and electro- and photoluminescence to superimpose linearly under a simultaneous electrical and optical excitation. The radiative ideality factor is obtained from the luminescence intensity/voltage characteristic by fitting a common diode law.

Within experiments it was shown that the *reciprocity relation* holds for band-to-band transitions in  $\text{Cu(In,Ga)Se}_2$  [44]. However, it is also shown that *radiative recombination* from additional localized band-tail states in the gap leads to an radiative ideality factor unequal to one [45], *i.e.* radiative transitions involving states in the gap violate the *reciprocity relation*. These radiative transitions lead to spectral changes in various disordered materials. Pieters *et al.* derived a simple *local recombination model* for photoluminescence of hydrogenated microcrystalline silicon solar cells, which can explain the radiative ideality factor, and therefore the voltage dependency of the *radiative recombination* [45]. This work demonstrates how luminescence may be used for the characterization of the (local) quasi-Fermi level separation in *thin-film* silicon based *solar cells*, despite that the *reciprocity relations* do not hold for these devices. However, the model in Ref. [45] also has shortcomings, most notably the model does not include electronic transport, limiting the accuracy of the model, and making the model unsuitable for electroluminescence.

This thesis studies how *reciprocity relation* holds and fails for various *thin-film solar cell* technologies with the aim to extend the list of useful applications of photo- and electroluminescence. High absorption and/or low charge carrier transport mobilities led to *thin-film solar cells* like chalcopyrite  $\text{Cu(In,Ga)Se}_2$  *np* heterojunctions [46, 47], hydrogenated microcrystalline silicon ( $\mu\text{-Si:H}$ ) *pin* [48–51], and hydrogenated amorphous silicon (*a-Si:H*) *pin* [52] devices. This thesis is structured within this sequence, studying systems with increasing concentrations of defect states in their band gap to investigate these circumstances, where the *reciprocity relation* still holds.

The *reciprocity relation* in  $\text{Cu(In,Ga)Se}_2$  holds if band-to-band transitions [44, 53–56] like in mono-crystalline silicon [57] yield the luminescence. Since the charge carrier transport mobilities in  $\text{Cu(In,Ga)Se}_2$  are rather high, the modeling of photo- and electroluminescence, and external quantum efficiency in  $\text{Cu(In,Ga)Se}_2$  *np* heterojunctions is relatively simple. Therefore,

the experiments are discussed with a self-developed *local recombination model*.

However, the situation is different in  $\mu\text{c-Si:H}$  and  $a\text{-Si:H}$ . Similar to  $a\text{-Si:H}$  [58], the luminescence in  $\mu\text{c-Si:H}$  originates from direct tail-to-tail transitions from localized band-tail states [59]. Additionally to this tail-to-tail transition, the luminescence in  $a\text{-Si:H}$  shows a second transition from band to neutral mid-gap defect states [60]. Localized states in the gap and low charge carrier transport mobilities require a more complex, one dimensional approach for the  $\mu\text{c-Si:H}$  and  $a\text{-Si:H}$  *pin* devices. For this reason, the self-developed *local recombination model*, which was introduced by Pieters *et al.* for  $\mu\text{c-Si:H}$  [45] is combined with full one dimensional device simulations using the commercial device simulator *Advanced Semiconductor Analysis* [61]. This approach allows to consistently model photoluminescence, electroluminescence, current/voltage characteristics, and external quantum efficiency to the *solar cells*.

First, in **Chapter 2**, the fundamentals of the relevant electronic states in  $\text{Cu(In,Ga)Se}_2$ ,  $\mu\text{c-Si:H}$ , and  $a\text{-Si:H}$  are given. The electronic states yield the luminescence and the external quantum efficiency, which are connected by the concept of *reciprocity relation*. Since this thesis investigates the photo- and electroluminescence, and the external quantum efficiency with the comparison of experimental results and simulations, the concept of the simulations and the experimental setup are introduced in **Chapter 3** beside the sample preparation.

The following main part of this thesis includes the investigations of the already mentioned three types of *solar cells*, namely  $\text{Cu(In,Ga)Se}_2$  *np* heterojunctions,  $\mu\text{c-Si:H}$  *pin*, and  $a\text{-Si:H}$  *pin* devices, where the density of localized inter-band states increases within this sequence.

**Chapter 4** presents the temperature and charge carrier injection dependent experimental results from  $\text{Cu(In,Ga)Se}_2$ , which account for the metastabilities, and the *reciprocity relation*, which still holds in  $\text{Cu(In,Ga)Se}_2$  for steep band-to-tail luminescence. The temperature dependent photo- and electroluminescence, and dark and illuminated current/voltage characteristics of a  $\mu\text{c-Si:H}$  *pin* device can be consistently modeled with *Advanced Semiconductor Analysis* in **Chapter 5**. These fitted simulations can explain the observed temperature dependent radiative ideality factor from tail-to-tail transitions, which is useful for determining junction voltages from electroluminescence imaging. This chapter concludes with a detailed analysis of the improvement of the *reciprocity relation* in  $\mu\text{c-Si:H}$ , which is based on the fitted simulations. Band-to-defect transitions, which are observed from the photo- and electroluminescence in  $a\text{-Si:H}$  [60] beside the already mentioned tail-to-tail transitions, affect the *reciprocity relation* discussed with experiments and simulations in **Chapter 6**. This chapter concludes by summarizing the luminescence intensities and the corresponding radiative ideality factors from band-to-tail, tail-to-tail, and band-to-defect transitions as observed in this thesis.



## Chapter 2

# Fundamentals

The interaction between light and semiconductors depends on the available electronic states and their occupation. This chapter introduces in the physics of *light absorption* and its opposite process, the *radiative recombination*, i.e. the light emission. Both processes are strictly connected to each other in terms of the *reciprocity relation* [20–22].

This chapter begins with a basic description of *solar cells*, and introduces to *light absorption* and *radiative recombination* in Section 2.1. Furthermore, a detailed description of the relevant density of electronic states within *solar cells*, especially in chalcopyrite  $\text{Cu}(\text{In,Ga})\text{Se}_2$  *np* heterojunction, hydrogenated microcrystalline silicon ( $\mu\text{c-Si:H}$ ), and hydrogenated amorphous silicon (*a-Si:H*) *pin* type devices, which are investigated in this thesis is given in Section 2.2. Subsequently, in Section 2.3 the interaction between the electronic states and light is described for the *radiative recombination*, and the *light absorption*. A detailed analysis of the *radiative recombination* is given in Section 2.4, and of the *light absorption* in Section 2.5.

### 2.1 Solar Cells

The Figure 2.1(a) shows a circuit diagram of a *solar cell*. A *solar cell* basically consists of a diode, which is connected to the recombination, and a (photo) current source, which is connected to the light absorption. The recombination is either radiative or non-radiative. In case of *radiative recombination*, the recombination in turn is connected to the light absorption, and vice versa. Both processes are connected with the *reciprocity relation*, which is the main topic of this thesis. The light absorption yields the photo current, which flows through the diode in dependence of the bias voltage. And the diode itself then yields the bias voltage dependent recombination current.

Additional components are a parallel and a series resistance. The parallel resistance originates from shunts, which partly short circuits the contacts of the diode. Since the series resistance hampers the charge carrier transport, the photovoltaic conversion efficiency is affected by this series resistance.

The Figure 2.1(b) shows a common current/voltage characteristic of a diode, which is plotted as black dotted lines. The (*radiative*) *recombination* current increases with increasing bias voltage. In case of *light absorption*, the diode is further known as solar cell and the dark cur-



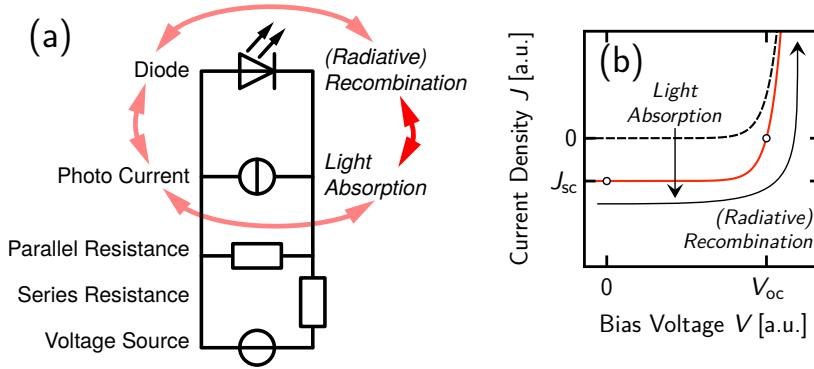


**Figure 2.1:** Solar cell concept accentuated to *light absorption* and *radiative recombination*. (a) Circuit diagram of a *solar cell*, where the diode itself is connected to the *(radiative) recombination*, and the photo current is connected to the *light absorption*. (b) Common dark (black dashed line) and illuminated (red solid line) current/voltage characteristics of a *solar cell*. The *light absorption* yields the short circuit current density ( $J_{sc}$ ) and the open circuit voltage ( $V_{oc}$ ).

rent/voltage characteristic is shifted. The illuminated current/voltage characteristic is plotted as red solid line. The *light absorption* yields a photo current ( $J_{ph}$ ), as already mentioned. However, due to the charge carrier transport, the determinable short circuit current is generally smaller than the photo current, *i.e.*  $J_{sc} < J_{ph}$ . Not every photo generated electron/hole pair is collected by the contacts, since the charge carrier transport is limited.

The increase of the bias voltage at the contacts of the illuminated solar cell also increases the *(radiative) recombination*. In the case, where no net current flows at  $V_{oc}$ , *i.e.* with the solar cell contacts opened, the photo generated electron/hole pairs fully recombine.

## 2.2 Electronic States in Semiconductors

The electronic states in  $\text{Cu(In,Ga)Se}_2$ ,  $\mu\text{c-Si:H}$ , and  $a\text{-Si:H}$  are the extended states in the conduction and valence band, and the localized states, energetically located between the band states, which are introduced in detail in the following sections. These localized states are band-tail states connected to the band edges, and amphoteric states deep in the band gap in  $\mu\text{c-Si:H}$  and  $a\text{-Si:H}$ . Additional states in the band gap in  $\text{Cu(In,Ga)Se}_2$  are induced through doping atoms. These states are energetically close to the band edges.

The derivations for occupation statistics, which are shown here, are in some parts related to the derivations given in [62, 63].

### Semiconductor Equations for Charge Carrier Transport

Charge carrier transport in semiconductor devices in one dimension ( $z$ ) is described with the Poisson equation (Eq. (2.1)) in connection with the continuity equations for electrons and holes (Eq. (2.2a) and Eq. (2.2b), respectively):

$$\frac{d^2 \Psi}{dz^2} = -\frac{dE}{dz} = -\frac{\rho}{\varepsilon_0 \varepsilon_r}, \quad (2.1)$$

where  $\Psi$  is the vacuum level related electrostatic potential induced by the space charge density ( $\rho$ ), which is normalized to the dielectric constant of vacuum ( $\varepsilon_0$ ) and a relative dielectric constant ( $\varepsilon_r$ ), which depends on the semiconductor. The connected electrical field is denoted as  $E$ . The continuity equations are

$$\frac{dn}{dt} = \frac{1}{q} \frac{dJ_n}{dz} + G - R \quad (2.2a)$$

$$\frac{dp}{dt} = -\frac{1}{q} \frac{dJ_p}{dz} + G - R, \quad (2.2b)$$

where  $n$  and  $p$  are the charge carrier concentrations for electrons and holes, respectively,  $G$  is the generation rate through photon absorption,  $R$  the recombination rate,  $t$  the time, and  $q$  the elementary charge. The electron and hole current densities, respectively, can be written as

$$J_n = \mu_n n \frac{dE_{fn}}{dz} \quad (2.3a)$$

$$J_p = \mu_p p \frac{dE_{fp}}{dz}, \quad (2.3b)$$

where  $\mu_n$  and  $\mu_p$  are the band drift mobilities for electrons and holes.

#### 2.2.1 Extended Band States

The extended electronic states in semiconductors are in the conduction and valence band, respectively. Electron wave functions can propagate through the interaction of these states. Due to this, these states are mostly relevant for charge carrier transport. However, in disordered semiconductors the electrons are losing coherence due to scattering. Therefore they are different from those in  $c$ -Si for instance.

Though, thin-film devices are investigated in this thesis, quantum confinement can be neglected. The density of conduction ( $N_{cb}$ ) and valence band ( $N_{vb}$ ) states can be described with square root like functions

$$N_{cb} = N_c \sqrt{E - E_c} \quad (2.4a)$$

$$N_{vb} = N_v \sqrt{E_v - E}, \quad (2.4b)$$

where  $N_c$  and  $N_v$  are the effective density of states at the mobility band edge energies,  $E_c$  and  $E_v$ , respectively (Figure 2.2) [64, 65].

The gap between the mobility band edges is defined as band gap  $E_\mu = E_c - E_v$ . As long as

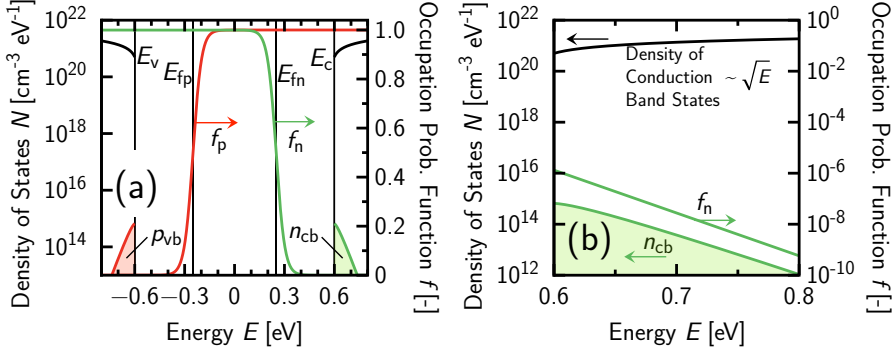


**Figure 2.2:** Density of extended states in the conduction and valence band, and corresponding occupation probability for electrons ( $f_n$ ) and holes ( $f_p$ ). (a) Mobility gap between the conduction ( $E_c$ ) and valence ( $E_v$ ) band edge. Occupation of the extended states is described by the Fermi-Dirac function (Eq. (2.6)) for conduction ( $f_n$ ) and valence band ( $f_p$ ) states at the Fermi level for electrons ( $E_{fn}$ ) and holes ( $E_{fp}$ ), respectively. Temperature is  $T = 300$  K. (b) Extended states are described by square root like density functions (Eq. (2.4)). The occupied band states yield the electron ( $n_{cb}$ ) and hole ( $p_{vb}$ ) density, respectively.

the energy separation between extended and localized states is rather sharp, most of the charge carrier transport takes place just below  $E_v$  for holes, and just above  $E_c$  for electrons, respectively [66, 67]. Therefore in  $\mu c$ -Si:H and  $a$ -Si:H,  $E_\mu$  is defined as the distance between the energies of the mobile states. Consequently, this leads the band gap to be called mobility gap. Typical values for  $\mu c$ -Si:H are  $E_\mu = 1.18$  eV [61, 63], and for  $a$ -Si:H  $E_\mu = 1.75$  eV [62, 68].

The temperature dependency of the band gap of  $c$ -Si was investigated by Varshni [69]. The temperature dependent band gap writes as

$$E_\mu(T, T_0) = E_\mu(T_0) - \frac{\alpha_\mu T^2}{T + \beta_\mu} + \frac{\alpha_\mu T_0^2}{T_0 + \beta_\mu} \quad (2.5)$$

with  $\alpha_\mu = 7.02 \times 10^{-4}$  eV K $^{-1}$  and  $\beta_\mu = 1108$  K for  $c$ -Si. Measurements of the temperature-dependence of the optical band gap from optical absorption spectroscopy [70], and electro-absorption measurements [71, 72] in  $a$ -Si:H yielded a  $\alpha_\mu = 4.7 \times 10^{-4}$  eV K $^{-1}$ . Another  $\alpha_\mu = 4.3 \times 10^{-4}$  eV K $^{-1}$  is found by Tsang *et al.* [73]. However, the investigations in  $a$ -Si:H show linear behavior at temperatures  $T > 100$  K, *i.e.*  $\beta_\mu \rightarrow 0$  K. The reference temperature for this thesis is  $T_0 = 300$  K.

Due to high thermalization rates in the extended states, quasi thermal equilibrium can be as-

summed and therefore, the occupation probability functions for electrons ( $f_n$ ) and holes ( $f_p$ ) are described by

$$f_n = \frac{1}{\exp\left(\frac{E-E_{fn}}{kT}\right) + 1} \quad (2.6a)$$

$$f_p = 1 - \frac{1}{\exp\left(\frac{E-E_{fp}}{kT}\right) + 1}, \quad (2.6b)$$

where  $E_{fn}$  and  $E_{fp}$  denote the corresponding quasi-Fermi levels. The thermal energy is given by  $kT$ , where  $k$  is the Boltzmann factor and  $T$  the temperature.

The integration over the occupied band density of states yields the electron (Eq. (2.7a)) and hole (Eq. (2.7b)) concentration, respectively. The integration can be simplified with the Maxwell-Boltzmann approximation and written as

$$n = \int_{E_c}^{\infty} N_{cb} f_n \, dE \approx N_c \exp\left(\frac{E_{fn} - E_c}{kT}\right) \quad (2.7a)$$

$$p = \int_{-\infty}^{E_v} N_{vb} f_p \, dE \approx N_v \exp\left(\frac{E_v - E_{fp}}{kT}\right). \quad (2.7b)$$

In general it is accepted [74] that the  $N_c$  and  $N_v$  increase with increasing temperature. From the Eq. (2.7) follows:

$$N_{c,v}(T, T_0) = N_{c,v}(T_0) \left(\frac{T}{T_0}\right)^{3/2}. \quad (2.8)$$

### 2.2.2 Localized Band-Tail States

This section describes the localized single electron trapping states in the mobility gap at the band edges. The huge amount of trapping states blurs out the energy levels, which enables to describe these states with one continuous distribution. It is commonly accepted that in  $\mu c$ -Si:H or  $\alpha$ -Si:H these densities of trapping states decay exponentially into the mobility gap [75–77]. In Cu(In,Ga)Se<sub>2</sub> it is unclear for now if single electron states are either similarly or Gaussian-like distributed [78–82]. This depends on the doping of the chalcopyrite, but luminescence spectra for instance can give indicators.

#### Tail States

In disordered semiconductors like  $\mu c$ -Si:H or  $\alpha$ -Si:H, localized band-tail states exist, which behave like acceptor states at the conduction band and like donor states at the valence band edge. These localized states are single electron states and can be either occupied by an electron or empty. Therefore, an occupied acceptor-like state is negatively charged, and neutral if it is empty. A donor-like state behaves the other way round. This state is neutral if occupied, and

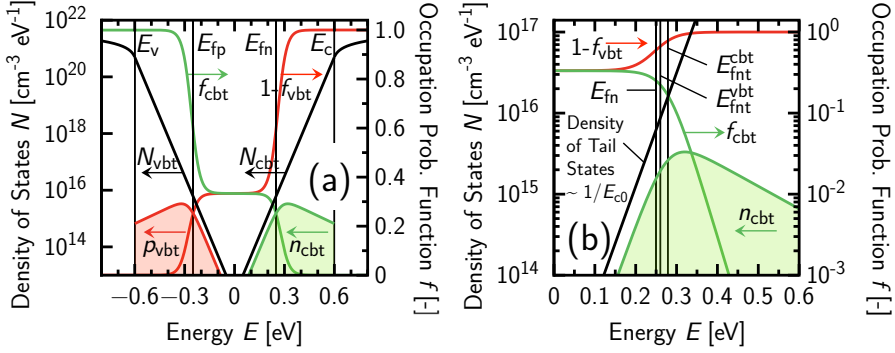


**Figure 2.3:** Density of localized band-tail states at the conduction ( $N_{cvt}$ ) and valence band ( $N_{vbt}$ ) edge, and corresponding occupation probability for electrons and holes. (a) Mobility gap between the conduction ( $E_c$ ) and valence ( $E_v$ ) band edge. Occupation is described by a two-step Fermi-Dirac distribution (Eq. (2.15)) for conduction ( $f_{cvt}$ ) and valence band ( $1-f_{vbt}$ ) band-tail states. Temperature is  $T = 300$  K. (b) Occupation probabilities, and conduction band-tail states between mid-gap and conduction band edge ( $E_c$ ). The electron quasi-Fermi level for valence ( $E_{fnt}^{vbt}$ ) and conduction ( $E_{fnt}^{cvt}$ ) band-tail state occupation is at higher energies than the quasi-Fermi level for band state occupation ( $E_{fn}$ ). The occupied band-tail states yield the electron ( $n_{cvt}$ ) and hole ( $p_{vbt}$ ) concentration density, respectively.

positively charged if it is empty. The double occupation of band-tail states is neglected for the simulations in this thesis.

The densities of the localized band-tail states can be described by  $N_{cvt}$  (Eq. (2.9a)) for the conduction, and  $N_{vbt}$  (Eq. (2.9b)) for the valence band-tail distribution [77]:

$$N_{cvt} = N_{c0} \exp\left(\frac{E - E_c}{E_{c0}}\right) \quad (2.9a)$$

$$N_{vbt} = N_{v0} \exp\left(\frac{E_v - E}{E_{v0}}\right), \quad (2.9b)$$

where  $N_{c0}$  and  $N_{v0}$  are the density of states at the conduction ( $E_c$ ) and valence ( $E_v$ ) band edge, respectively (see Figure 2.3). The characteristic band-tail slope energies are denoted as  $E_{c0}$  and  $E_{v0}$ . Typical values in  $\mu\text{-Si:H}$  are temperature independent and symmetrical  $E_{c0} = E_{v0} = 31$  meV [61]. The characteristic band-tail slopes in  $a\text{-Si:H}$  are temperature dependent and generally not the same. After Stutzmann [83] the temperature dependence of the characteristic energy of the valence band-tail can be written as

$$E_{v0}(T, T_0) = \sqrt{E_{v0}^2 - (1.1 kT_0)^2 + (1.1 kT)^2}. \quad (2.10)$$

According to Aljishi *et al.* [84] the characteristic energy of the conduction band-tail is also temperature dependent. This temperature dependence  $E_{c0}(T, T_0)$  is assumed to be the same as for the valence band-tail. Typical values in  $a\text{-Si:H}$  are  $E_{c0} = 31$  meV and  $E_{v0} = 45$  meV at temperature  $T_0 = 300$  K [85].

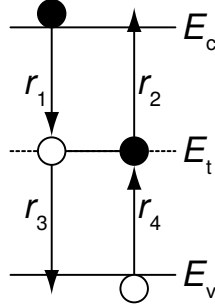


**Figure 2.4:** Capture and emission process on a single electron trap state. Band edge energies are  $E_c$  for conduction and  $E_v$  for valence band. The trap state energy is denoted as  $E_t$ . The capture and emission rates ( $r_i$ ) are given in Table 2.1.

**Table 2.1:** Capture and emission rates of single electron trap states.

PROCESS		RATE
electron capture	$r_1$	$n v_{th} \sigma_n N_t (1 - f_{FD})$
electron emission	$r_2$	$e_n N_t f_{FD}$
hole capture	$r_3$	$p v_{th} \sigma_p N_t f_{FD}$
hole emission	$r_4$	$e_p N_t (1 - f_{FD})$

### Shockley-Read-Hall Recombination

The theory of recombination via above mentioned single electron trap states  $N_t = N_{cvt}$  and  $N_t = N_{vbt}$  (Eq. (2.9)) is known as Shockley-Read-Hall (SRH) recombination [86, 87]. This process considers two capture and two emission processes as shown in Figure 2.4. Recombination takes place if an empty state captures an electron from the conduction band and a hole from the valence band. These capture and emission rates ( $r_i$ ) are given in Table 2.1. Electrons can be captured by positively charged states at the valence band ( $\sigma_n = \sigma_n^+$ ) and neutral states at the conduction band edge ( $\sigma_n = \sigma_n^0$ ), where  $\sigma_n$  is the electron capture cross-section. The hole capture cross-section  $\sigma_p$  identifies with  $\sigma_p^0$  for neutral states at the valence band and  $\sigma_p^-$  at the conduction band edge. The capture rates are also determined by the thermal velocity

$$v_{th} \propto \sqrt{kT}. \quad (2.11)$$

We assume  $v_{th} = 10^7 \text{ cm s}^{-1}$  at temperature  $T = 300 \text{ K}$ .

In thermal equilibrium the electron occupation of a localized state is given by the Fermi-Dirac distribution  $f_{FD} = [1 + \exp(\frac{E - E_{fn}}{kT})]^{-1}$  at the quasi-Fermi level  $E_{fn}$ . Thermal equilibrium also

yields to the principle of *detailed balance*, where is no net recombination. This means  $r_1 = r_2$  and  $r_3 = r_4$ . Together with Eq. (2.7), this yields the emission coefficients

$$\begin{aligned} e_n &= \sigma_n v_{th} n (1 - f_{FD}) / f_{FD} \\ &= \sigma_n v_{th} N_c \exp\left(\frac{E_{fn} - E_c}{kT}\right) \exp\left(\frac{E - E_{fn}}{kT}\right) \\ &= \sigma_n v_{th} N_c \exp\left(\frac{E - E_c}{kT}\right) \end{aligned} \quad (2.12a)$$

$$e_p = \sigma_p v_{th} N_v \exp\left(\frac{E_v - E}{kT}\right). \quad (2.12b)$$

In non-equilibrium steady-state conditions, electrons from the conduction band recombine with holes from the valence band. This yields the recombination rate

$$\begin{aligned} R &= \frac{dn}{dt} = -\frac{dp}{dt} \\ \rightarrow R &= r_1 - r_2 = r_3 - r_4. \end{aligned} \quad (2.13)$$

From the rates in Table 2.1 and Eq. (2.13) the occupation probability function can be determined as

$$f_t = \frac{nv_{th}\sigma_n + e_p}{nv_{th}\sigma_n + pv_{th}\sigma_p + e_n + e_p}. \quad (2.14)$$

This Eq. (2.14) is used for device simulations.

A more readable occupation probability function ( $f_{TS}$ ) was given by Taylor and Simmons [88, 89]. The Taylor and Simmons approximation yields a two-step Fermi-Dirac distribution

$$f_{TS} = \frac{\sigma_p p}{\sigma_n n + \sigma_p p} \frac{1}{1 + \exp\left(\frac{E - E_{fpt}}{kT}\right)} + \frac{\sigma_n n}{\sigma_n n + \sigma_p p} \frac{1}{1 + \exp\left(\frac{E - E_{fnt}}{kT}\right)} \quad (2.15)$$

as illustrated in Figure 2.3(a), where  $E_{fpt}$  and  $E_{fnt}$  are the quasi-Fermi levels for trapped charge. Generally, the occupation probabilities for both kinds of trap states are different due to different capture cross-sections ( $\sigma_p \neq \sigma_n$ ). Therefore, the occupation probabilities are denoted as  $f_{vbt}$  for states at the valence band, and  $f_{cbt}$  at the conduction band edge. The plateau between both quasi-Fermi levels for trapped holes ( $E_{fpt}$ ) and electrons ( $E_{fnt}$ ) scales with the ratio between the capture cross-sections and the charge carrier densities (see Figure 2.3, and Figure 2.5). It is often assumed that charged states have a larger capture cross-section than neutral states due to the coulombic interaction between charged states and charge carriers with opposite charge [90].

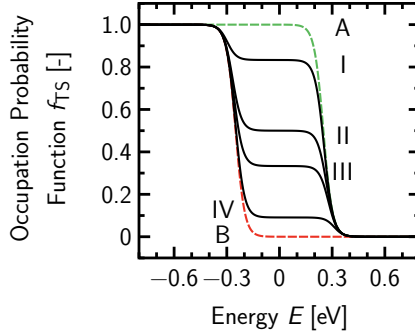


**Figure 2.5:** Occupation probability function of trap states ( $f_{TS}$ ) from Taylor and Simmons approximation (see Eq. (2.15)) in dependence of capture cross-sections for electrons ( $\sigma_n$ ) and holes ( $\sigma_p$ ). The hole capture cross-section  $\sigma_h = 10^{-16} \text{ cm}^2$  is kept constant. The electron capture cross-section is varied: I  $\sigma_p/\sigma_n = 0.2$ , II  $\sigma_p/\sigma_n = 1$ , III  $\sigma_p/\sigma_n = 5$ , IV  $\sigma_p/\sigma_n = 10$ . The cases A and B show the corresponding Fermi-Dirac distributions. In case A,  $\sigma_p$  is negligible compared to  $\sigma_n$ , and vice versa in case B.

This means  $\sigma_p > \sigma_n$  for trap states at the valence band, and  $\sigma_p < \sigma_n$  for trap states at the conduction band edge. The position of

$$E_{\text{fnt}} = E_c + kT \ln \left( \frac{\sigma_n n + \sigma_p p}{N_c \sigma_n} \right) \quad (2.16a)$$

$$E_{\text{fpt}} = E_v - kT \ln \left( \frac{\sigma_n n + \sigma_p p}{N_v \sigma_p} \right) \quad (2.16b)$$

also depends on the capture cross-sections (Figure 2.3(b)).

### 2.2.3 Mid-Gap Defect States

Additional to the earlier described band-tail states, defect states in the middle of the gap are relevant to describe the physics in  $\mu\text{c-Si:H}$  and  $a\text{-Si:H}$  devices. In these materials the atomic arrangement has some degree of disorder, which induces these defect states. These defect states are usually ascribed to *dangling bonds*.

#### Dangling Bonds

In comparison to  $c\text{-Si}$ , which exhibits a strict periodic repetition of a unit cell, a variation in atomic bond lengths and angles leads to a lack in long range order. Due to this lack, it happens that neighbored atoms are only weakly bonded. Weak bonds like these fracture and therefore lead to additional dangling bonds [91]. To reduce mid-gap defect states, the dangling bonds are passivated with hydrogen. This passivation can reduce the dangling bond concentration from  $10^{19} - 10^{20}$  to  $10^{15} - 10^{16} \text{ cm}^{-3}$  [62, 92, 93].

Every defect is described by one localized electronic state. The huge amount of localized states



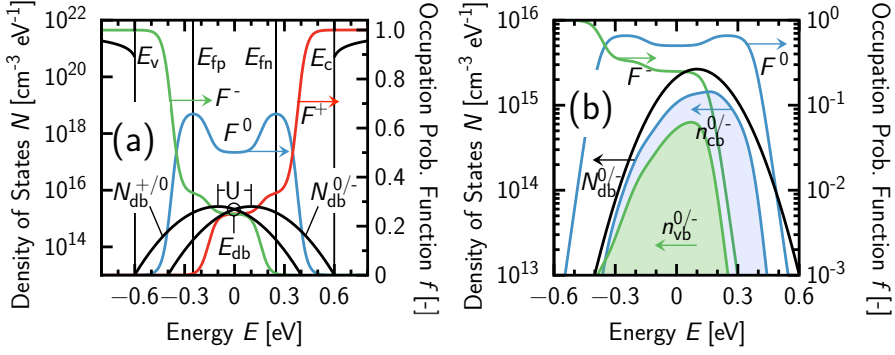


**Figure 2.6:** Density of amphoteric defect states ( $N_{db}^{+/0}$ ,  $N_{db}^{0/-}$ ) in the mobility gap, and corresponding occupation probability distributions ( $F^-$ ,  $F^0$ ,  $F^+$ ). (a) Mobility gap between the conduction ( $E_c$ ) and valence ( $E_v$ ) band edge. Defect states are either unoccupied, or occupied by one or two electron(s). Correlation energy between both transition states is denoted as  $U$ . Quasi-Fermi levels for electrons ( $E_{fn}$ ) and holes ( $E_{fp}$ ), respectively, cross the defect states. Temperature is  $T = 300$  K. (b) Detailed sketch of amphoteric defect states for transitions from single to double electron occupation ( $N_{db}^{0/-}$ ). Single ( $n_{cb}^{0/-}$ ) and double electron occupied states ( $n_{vb}^{0/-}$ ) are coloured.

blurs out the energy levels, which enables to describe the localized defect states with one distribution [66].

The defect states are amphoteric. The amphoteric defect state distribution  $N_{db}^{+/0}$  describes the transition from a positively charged and therefore unoccupied to a neutral and therefore single electron occupied defect state. The amphoteric defect state distribution  $N_{db}^{0/-}$  describes the transition from a neutral and therefore single electron occupied to a negatively charged and therefore double electron occupied defect state. Both energy levels  $E_{db}^{+/0}$  and  $E_{db}^{0/-}$ , which correspond to  $N_{db}^{+/0}$  and  $N_{db}^{0/-}$ , respectively, are coupled, *i.e.* the occupation of a defect state at  $E_{db}^{0/-}$  is only possible if this defect state is occupied at  $E_{db}^{+/0}$ .

The distribution of dangling bond states in the mobility gap is mostly described with the standard and the defect-pool model. The defect pool model describes the chemical equilibrium between weak Si-Si bonds and two dangling bonds [91, 94–100]. However, this work uses the simple approach of the standard model to describe the dangling bond distribution. This standard model assumes the dangling bonds to be Gaussian distributed as

$$N_{db}^{+/0} = N_{db} \frac{1}{\sigma_{db} \sqrt{2\pi}} \exp \left( -\frac{(E - E_{db} + U/2)^2}{2\sigma_{db}^2} \right) \quad (2.17a)$$

$$N_{db}^{0/-} = N_{db} \frac{1}{\sigma_{db} \sqrt{2\pi}} \exp \left( -\frac{(E - E_{db} - U/2)^2}{2\sigma_{db}^2} \right), \quad (2.17b)$$

where  $N_{db}$  is the dangling bond concentration, and  $\sigma_{db}$  the standard deviation of the Gaussian distributions. Not much is known about the position of the dangling bonds, therefore the

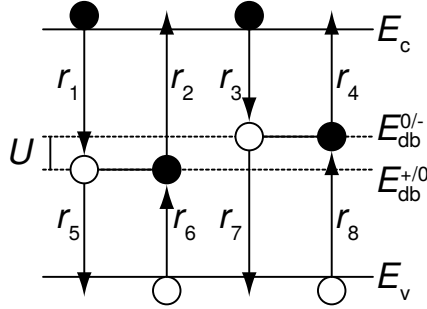


**Figure 2.7:** Capture and emission process on an amphoteric trap state. Mobility edge energies are  $E_c$  for conduction and  $E_v$  for valence band. The defect state energy levels are denoted as  $E_{db}^{+/0}$  for transition from positively charged to neutral, and  $E_{db}^{0/-}$  for transition from neutral to negatively charged. The capture and emission rates ( $r_i$ ) are explained in Table 2.2.

**Table 2.2:** Capture and emission rates of amphoteric states.

PROCESS		RATE
electron capture	$r_1$	$n v_{th} \sigma_n^+ N_{db} F^+$
electron emission	$r_2$	$e_n^0 N_{db} F^0$
electron capture	$r_3$	$n v_{th} \sigma_n^0 N_{db} F^0$
electron emission	$r_4$	$e_n^- N_{db} F^-$
hole capture	$r_5$	$p v_{th} \sigma_p^0 N_{db} F^0$
hole emission	$r_6$	$e_p^+ N_{db} F^+$
hole capture	$r_7$	$p v_{th} \sigma_p^- N_{db} F^-$
hole emission	$r_8$	$e_p^0 N_{db} F^0$

dangling bonds are often assumed to be in the middle of the gap, *i.e.*  $E_{db} = 0.0$  eV. This is shown in Figure 2.6(a). The energy distance between the defect states is the correlation energy ( $U$ ). In  $\mu c$ -Si:H and  $a$ -Si:H, it is generally accepted that  $U > 0$ , and therefore  $N_{db}^{+/0}$  is closer to the valence band mobility edge than  $N_{db}^{0/-}$ . The charge carrier occupation functions for neutral, positively, and negatively charged mid-gap defect states are given by  $F^0$ ,  $F^+$ , and  $F^-$ . A detailed sketch of the occupied  $E_{db}^{0/-}$  energy levels is shown in Figure 2.6(b).

### Recombination Statistics for Amphoteric States

The model for recombination and trapping statistics on amphoteric defect states like dangling bonds was developed by Sah and Shockley [101]. Emission and capture of electrons and holes at three different occupation states yield eight rates ( $r_i$ ) as shown in Figure 2.7. The rate equations equivalent to Table 2.1 are given in Table 2.2. The occupation probability functions here are denoted as  $F^+$ ,  $F^0$ , and  $F^-$ . The probability a state is empty is given by  $F^+$ . Single and double occupied states are denoted as  $F^0$  and  $F^-$ , respectively.

As shown in Section 2.2.2, the emission coefficients can be determined with the principle of detailed balance, *i.e.*  $r_1 = r_2$ ,  $r_3 = r_4$ ,  $r_5 = r_6$ , and  $r_7 = r_8$ . With the thermal equilibrium electron ( $n_{\text{eq}}$ ) and hole ( $p_{\text{eq}}$ ) concentration from Eq. (2.7), and the thermal equilibrium occupation probabilities [102, 103]

$$F_{\text{eq}}^+ = \frac{1}{1 + 2 \exp\left(\frac{E_{\text{f}} - E^{+/0}}{kT}\right) + \exp\left(\frac{2E_{\text{f}} - E^{+/0} - E^{0/-}}{kT}\right)} \quad (2.18a)$$

$$F_{\text{eq}}^0 = \frac{2 \exp\left(\frac{E_{\text{f}} - E^{+/0}}{kT}\right)}{1 + 2 \exp\left(\frac{E_{\text{f}} - E^{+/0}}{kT}\right) + \exp\left(\frac{2E_{\text{f}} - E^{+/0} - E^{0/-}}{kT}\right)} \quad (2.18b)$$

$$F_{\text{eq}}^- = \frac{\exp\left(\frac{2E_{\text{f}} - E^{+/0} - E^{0/-}}{kT}\right)}{1 + 2 \exp\left(\frac{E_{\text{f}} - E^{+/0}}{kT}\right) + \exp\left(\frac{2E_{\text{f}} - E^{+/0} - E^{0/-}}{kT}\right)}, \quad (2.18c)$$

the emission coefficients can be found as

$$e_{\text{n}}^0 = v_{\text{th}} \sigma_{\text{n}}^+ n_{\text{eq}} \frac{F_{\text{eq}}^+}{F_{\text{eq}}^0} = \frac{1}{2} v_{\text{th}} \sigma_{\text{n}}^+ N_{\text{c}} \exp\left(\frac{E^{+/0} - E_{\text{c}}}{kT}\right) \quad (2.19a)$$

$$e_{\text{n}}^- = v_{\text{th}} \sigma_{\text{n}}^0 n_{\text{eq}} \frac{F_{\text{eq}}^0}{F_{\text{eq}}^-} = 2 v_{\text{th}} \sigma_{\text{n}}^0 N_{\text{c}} \exp\left(\frac{E^{0/-} - E_{\text{c}}}{kT}\right) \quad (2.19b)$$

$$e_{\text{p}}^+ = v_{\text{th}} \sigma_{\text{p}}^0 p_{\text{eq}} \frac{F_{\text{eq}}^0}{F_{\text{eq}}^+} = 2 v_{\text{th}} \sigma_{\text{p}}^0 N_{\text{v}} \exp\left(\frac{E_{\text{v}} - E^{+/0}}{kT}\right) \quad (2.19c)$$

$$e_{\text{p}}^0 = v_{\text{th}} \sigma_{\text{p}}^- p_{\text{eq}} \frac{F_{\text{eq}}^-}{F_{\text{eq}}^0} = \frac{1}{2} v_{\text{th}} \sigma_{\text{p}}^- N_{\text{v}} \exp\left(\frac{E_{\text{v}} - E^{0/-}}{kT}\right). \quad (2.19d)$$

And again, in non-equilibrium steady state conditions there is net recombination or generation, *i.e.*  $F \neq F_{\text{eq}}$ . The statistics can be obtained by the rate equations of the occupation functions

$$\begin{aligned} \frac{dF^+}{dt} &= -r_1 + r_2 + r_5 - r_6 \\ &= -n v_{\text{th}} \sigma_{\text{n}}^+ F^+ - e_{\text{n}}^0 F^0 + p v_{\text{th}} \sigma_{\text{p}}^0 F^0 - e_{\text{p}}^+ F^+ \end{aligned} \quad (2.20a)$$

$$\begin{aligned} \frac{dF^-}{dt} &= r_3 - r_4 - r_7 + r_8 \\ &= n v_{\text{th}} \sigma_{\text{n}}^0 F^0 - e_{\text{n}}^- F^- - p v_{\text{th}} \sigma_{\text{p}}^- F^- + e_{\text{p}}^0 F^0. \end{aligned} \quad (2.20b)$$

Taking into account that  $F^+ + F^0 + F^- \stackrel{!}{=} 1$ , the non-equilibrium occupation functions are obtained as

$$F^+ = \frac{P^0 P^-}{N^+ P^- + P^0 P^- + N^+ N^0} \quad (2.21a)$$

$$F^0 = \frac{N^+ P^-}{N^+ P^- + P^0 P^- + N^+ N^0} \quad (2.21b)$$

$$F^- = \frac{N^0 N^+}{N^+ P^- + P^0 P^- + N^+ N^0}, \quad (2.21c)$$

where

$$N^+ = nv_{\text{th}}\sigma_n^+ + e_p^+ \quad (2.22a)$$

$$N^0 = nv_{\text{th}}\sigma_n^0 + e_p^0 \quad (2.22b)$$

$$P^- = pv_{\text{th}}\sigma_p^- + e_n^- \quad (2.22c)$$

$$P^0 = pv_{\text{th}}\sigma_p^0 + e_n^0 \quad (2.22d)$$

are introduced for readability.

## 2.3 Reciprocity Relation between Electroluminescence and External Quantum Efficiency

As indicated earlier, the *light absorption* and the *radiative recombination* are complementary physical processes, which can be transformed from one to the other. Explicitly, this means that the electroluminescent emission ( $\varphi_{\text{EL}}$ ), and the photovoltaic external quantum efficiency ( $Q_e$ ) of *solar cells* and light emitting diodes are connected, which is known as *reciprocity relation* [21, 29, 104–107]. This *reciprocity relation* again is based on the validity of the *reciprocity relation* derived by Donolato [20]. It connects the charge carrier concentration in the dark under electrical bias with the collection efficiency of photo generated charge carriers under optical bias.

Moreover this *reciprocity relation* between  $\varphi_{\text{EL}}$  and  $Q_e$  is extended from electroluminescence (EL) to luminescence in general [22]. This implies the combination of photo- (PL) and electroluminescence, which represents experimental conditions in most cases, *i.e.* PL under electrical bias or EL under optical bias.

For basic understanding, an optoelectronic device can be separated into optical and electrical terminals connected to the *solar cell* or light emitting diode [21] (see Figure 2.8(b)). Therefore, PL conditions are given with the electrical terminals short-circuited, which yields a spectrally distributed luminescence ( $\varphi_{\text{PL}}^{\text{sc}}(E_\gamma)$ ). Under these conditions, most of the optically injected charge carriers are extracted through the electrical terminals. Due to low luminescent quantum yield, this conditions are hard to detect within experiments. Under EL conditions the electrical terminals of the device are connected to a electrical source, which yields the junction voltage ( $V$ ). Charge carriers are electrically injected to the device and recombine radiatively. More generally spoken, in EL conditions the ambience of the device works as an optical drain. Since  $Q_e(E_\gamma)$

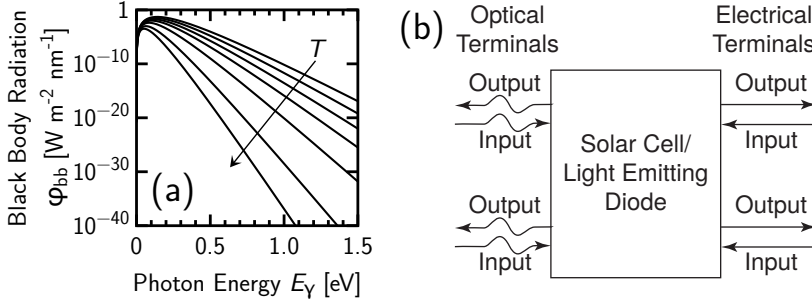


**Figure 2.8:** (a) Black body radiation at different temperatures  $T = 330, 300, 270, 240, 200, 150$ , and  $120$  K (arrow) as used within external quantum efficiency measurements in this thesis. (b) Optoelectronic device like *solar cell* or *light emitting diode* reduced to its input and output terminals after Rau [21].

implies  $\alpha(E_\gamma)$ , *i.e.* all possible transitions for electrons to get excited, the spectrally distributed electroluminescence ( $\varphi_{EL}(E_\gamma)$ ) scales with  $Q_e$ . However, not every possible electron transition due to absorption is equally probable for luminescence. Therefore,  $\varphi_{EL}(E_\gamma) \propto \varphi_{bb}(E_\gamma, T)$ , where

$$\varphi_{bb}(E_\gamma, T) = \frac{2\pi E_\gamma^5}{h^4 c^3} \frac{1}{\exp\left(\frac{E_\gamma}{kT}\right) - 1} [\text{W m}^{-2} \text{nm}^{-1}] \quad (2.23)$$

denotes the spectral photon flux density of a black body, which radiates into a hemisphere. The constants are the velocity of light ( $c$ ) and the Planck constant ( $h$ ), respectively. In summary, the luminescence can be written as

$$\begin{aligned} \varphi(E_\gamma, T) &= \varphi_{PL}^{sc}(E_\gamma) + \varphi_{EL}(E_\gamma) \\ &= \varphi_{PL}^{sc}(E_\gamma) + Q_e(E_\gamma) \varphi_{bb}(E_\gamma, T) \left[ \exp\left(\frac{qV}{kT}\right) - 1 \right], \end{aligned} \quad (2.24)$$

where  $kT/q$  is the thermal voltage. In the end, the *reciprocity relation* holds if [22]

- the EL spectrum ( $\varphi_{EL}(E_\gamma)$ ) is compatible to the external quantum efficiency ( $Q_e(E_\gamma)$ ),
- the spectral shape of  $\varphi_{EL}(E_\gamma)$  does not change at different (electrical or optical) bias conditions,
- the integrated luminescence ( $\phi_{EL}(V) = \int \varphi_{EL} dE_\gamma$ ) follows a diode law with the ideality factor of one,
- and the voltage-driven  $\varphi_{EL}$  and the illumination-driven  $\varphi_{PL}^{sc}$  superimpose linearly.

The first two criteria are already verified for a series of *solar cells* [44,56,108]. The latter criteria are not verified so far. The first three criteria strictly belong to the *reciprocity relation* and are equivalent for this reason. The superposition of the photo- and electroluminescence is optional.

This gives the motivation for the given structure of this thesis. The thesis is structured from a material system, where the *reciprocity relation* can make good predictions, *i.e.* Cu(In,Ga)Se<sub>2</sub>, over  $\mu\text{c-Si:H}$ , which follows partly the rules of the *reciprocity relation*, to *a-Si:H*, where the *reciprocity relation* does not hold. As shown in Figure 2.9, Cu(In,Ga)Se<sub>2</sub> should follow the rules of the *reciprocity relation* due to few localized states, which are involved in the device physics. And moreover, around room temperature the localized band-tail density of states decay steeper into the band gap than the occupation probability function decays. This is different in  $\mu\text{c-Si:H}$ , where the localized band-tail densities of states are higher. The band-tail densities of states decay shallower into the mobility gap than in Cu(In,Ga)Se<sub>2</sub>. In *a-Si:H* the localized band-tail densities of states are reported to be even shallower than in  $\mu\text{c-Si:H}$ , and therefore far from the slope of the thermal occupation probability around room temperature and below. Additionally, in *a-Si:H* mid-gap defect states play an important role for *radiative recombination*. As long as only discrete material systems are available from experiments, well modeled devices, and additional device simulations with parameters varied, are necessary to find that conditions, which change well behaving to non working devices in terms of the *reciprocity relation*.

## 2.4 Radiative Recombination

Beside the thermalization, the relaxation process of an excited electron/hole pair in a semiconductor is known as recombination. This is the opposite process of the generation of an electron/hole pair by the absorption of a photon. Both process rates are equal in quasi thermal equilibrium. Whilst recombination, the excited electron loses its energy. This energy generates either a photon or phonons. The generation of phonons raises the temperature of the semiconductor. If the recombination process releases a photon, this is called *radiative recombination* or luminescence.

Semiconductors can be classified by the band gap, which is either direct or indirect. The recombination in semiconductors with a direct band gap needs only one particle. In contrast, the recombination of an electron/hole pair in an indirect semiconductor with minimal distance between the ground and the excited state releases a phonon with energy  $\hbar\Omega$ , additional to the photon with energy  $E_\gamma$ . The right momentum  $\hbar k$  of the phonon is needed for this. Due to the need of two particles for this recombination in an indirect semiconductor, *radiative recombination* is less probable than in semiconductors with a direct band gap.

Chalcopyrite Cu(In,Ga)Se<sub>2</sub> is a direct semiconductor. Silicon in its crystalline structure has an indirect band gap. However, due to the lattice disorder in  $\mu\text{c-Si:H}$  and *a-Si:H* the bands blur out and broaden. Therefore, the higher the lattice disorder the more the semiconductor becomes quasi-direct.

The luminescence from *radiative recombination* is spectrally distributed and gives advice to the electronic states of the recombining charge carriers. Generally, the luminescence density distribution, or shortly luminescence spectrum, is given by

$$\varphi_i^f(E_\gamma) \propto \int p_f(E) n_i(E + E_\gamma) dE, \quad (2.25)$$

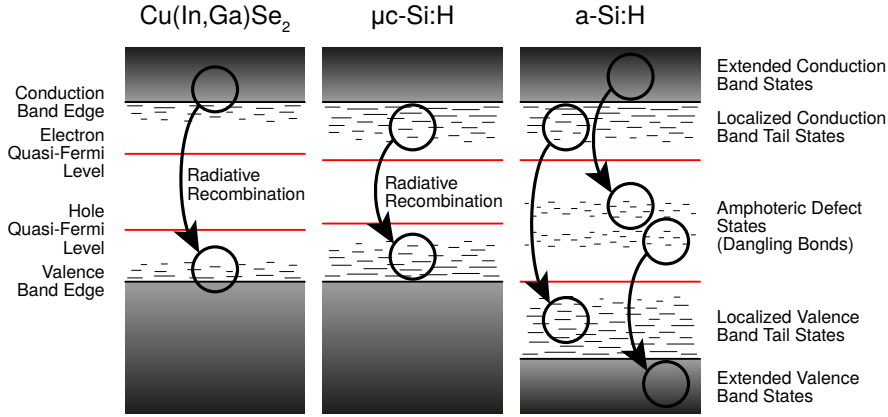


**Figure 2.9:** Dominant *radiative recombination* processes in chalcopyrite ( $\text{Cu(In,Ga)Se}_2$ ) *np* heterojunction, hydrogenated microcrystalline silicon ( $\mu\text{c-Si:H}$ ) *pin*, and hydrogenated amorphous silicon ( $\text{a-Si:H}$ ) *pin* devices.

where  $E_\gamma$  is the photon energy. Due to relaxation, the excited electrons with initial distribution  $n_i$  recombine with the holes with the final distribution  $p_f$ . Based on the generalized Planck's law [29, 104], the quasi-Fermi level separation ( $\Delta E_f$ ) can be extracted from the luminescence. As it is known from *c-Si*, where most of the luminescence comes from band-to-band transitions [57, 109], there is a relation between the integrated luminescence ( $\phi = \int \varphi_1^f dE_\gamma$ ) and the quasi-Fermi level separation,  $\phi \propto \exp(\Delta E_f/kT)$ , which is used to derive the local  $\Delta E_f$  from wafers, or the contact voltage from devices for instance [21, 106, 107].

Generally, the  $n_i$  and  $p_f$  can be identified with all occupied electron and hole states, respectively, given in Section 2.2. However, only a few transitions are relevant for *radiative recombination*, and the determination of the local quasi-Fermi level separation depends on the kind of transition. This in turn depends on the material as shown in detail in the following (see Figure 2.9).

### 2.4.1 Chalcopyrite $\text{Cu(In,Ga)Se}_2$

In chalcopyrite  $\text{Cu(In,Ga)Se}_2$  it was shown that the luminescence yields from recombination between extended band and localized acceptor, and donor states, also known as impurities [110–112]. However, as long as the doping concentration in  $\text{Cu(In,Ga)Se}_2$  affects the localized states at the band edges, also luminescence from band-to-tail recombination is feasible. This localized states in  $\text{Cu(In,Ga)Se}_2$  are very close to the band edges and decay very steep into the mobility gap. Since the occupation in  $\text{Cu(In,Ga)Se}_2$  is primarily in the band states, the luminescence from tail-to-tail transitions like in  $\mu\text{c-Si:H}$  or  $\text{a-Si:H}$  for instance, is hampered (see Figure 2.9).

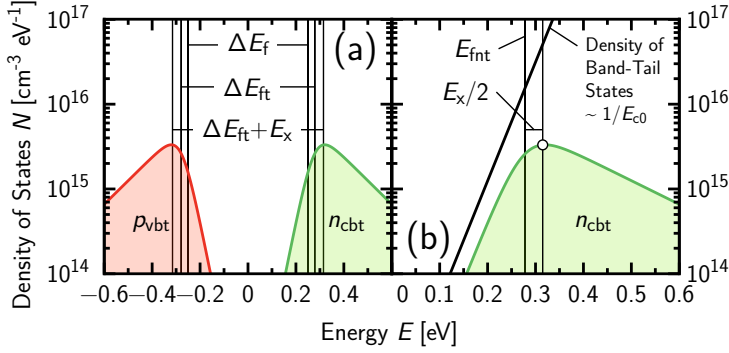


**Figure 2.10:** (a) Density of occupied localized band-tail states at the valence ( $p_{vbt}$ ) and the conduction ( $n_{cbt}$ ) band edge, and the corresponding quasi-Fermi level separation for band states ( $\Delta E_f$ ), for trapped charge ( $\Delta E_{ft}$ ), and the difference between the peak energies of  $p_{vbt}$  and  $n_{cbt}$  as  $\Delta E_{ft} + E_x$ . (b) Detail of density of occupied localized conduction band-tail states.

If band-to-tail recombination is assumed, the luminescence then writes with Eqs. (2.4), (2.6), (2.9) and (2.14) as

$$\varphi_{cb}^{vbt}(E_\gamma) \propto \int N_{cbt}(E) [1 - f_{vbt}(E, E_{fp})] N_{cb}(E + E_\gamma) f_n(E + E_\gamma, E_{fn}) dE \quad (2.26a)$$

$$\varphi_{cbt}^{vb}(E_\gamma) \propto \int N_{vb}(E) f_p(E, E_{fp}) N_{cbt}(E + E_\gamma) f_{cbt}(E + E_\gamma, E_{fn}) dE. \quad (2.26b)$$

Beside the band-to-tail recombination, which mainly yields the luminescence found in this thesis, also band-to-impurity [82], donor-to-acceptor [56, 82, 113, 114], and band-to-band [56, 115, 116] transitions are observed from the luminescence in  $\text{Cu}(\text{In,Ga})\text{Se}_2$  *np* heterojunction devices.

### 2.4.2 Hydrogenated Microcrystalline Silicon $\mu\text{c-Si:H}$

The luminescence in  $\mu\text{c-Si:H}$  behaves similar to the luminescence in *a-Si:H* [45, 59, 117]. Since *a-Si:H* was investigated earlier in time than  $\mu\text{c-Si:H}$ , the references for the luminescence in *a-Si:H* can be found in the corresponding Section 2.4.3. Therefore, following *a-Si:H*, it is accepted that the main part in luminescence comes from tail-to-tail transitions. This yields the luminescence in  $\mu\text{c-Si:H}$ , which is calculated with Eqs. (2.9) and (2.14) as

$$\varphi_{cbt}^{vbt}(E_\gamma) \propto \int N_{vbt}(E) [1 - f_{vbt}(E, E_{fp})] N_{cbt}(E + E_\gamma) f_{cbt}(E + E_\gamma, E_{fn}) dE. \quad (2.27)$$

From Figure 2.9 it can be seen that the quasi-Fermi level separation is slightly less than in  $\text{Cu}(\text{In,Ga})\text{Se}_2$ . The density of trapping states in  $\mu\text{c-Si:H}$  is much higher than in  $\text{Cu}(\text{In,Ga})\text{Se}_2$ . Therefore, the luminescence from trapping states in  $\mu\text{c-Si:H}$  is predominant compared to chalcopyrite  $\text{Cu}(\text{In,Ga})\text{Se}_2$ . And the luminescence from band states is negligible in  $\mu\text{c-Si:H}$ .



The luminescence from tail-to-tail transitions, of course contains information about the band-tail density of states. A relation between the quasi-Fermi level separation and the luminescence from tail-to-tail transitions is derived by Pieters *et al.* [45] for  $\mu\text{c-Si:H}$ . The general approach for tail-to-tail luminescence from Eq. (2.27) is solved for the peak photon energy ( $\hat{E}_\gamma$ ). Therefore, the density of trapped electrons in the conduction ( $n_{\text{cvt}}$ ) and holes in the valence ( $p_{\text{vbt}}$ ) band-tail can be simplified with

$$n_{\text{cvt}} = N_{\text{cvt}}(E)f_{\text{cvt}} \propto \exp\left(\frac{E}{E_{\text{c0}}}\right) \left[1 + \exp\left(\frac{E - E_{\text{fnt}}}{kT}\right)\right]^{-1} \quad (2.28a)$$

$$p_{\text{vbt}} = N_{\text{vbt}}(E)(1 - f_{\text{vbt}}) \propto \exp\left(-\frac{E}{E_{\text{c0}}}\right) \left[1 + \exp\left(\frac{E_{\text{fpt}} - E}{kT}\right)\right]^{-1}. \quad (2.28b)$$

Substituting the Eq. (2.28) and assuming  $E_{\text{c0}} = E_{\text{v0}} = E_0$  in Eq. (2.27) yields

$$\varphi(E_\gamma) \propto \frac{(E_\gamma + E_{\text{fpt}} - E_{\text{fnt}}) \exp(E_\gamma/E_0)}{\exp((E_\gamma + E_{\text{fpt}} - E_{\text{fnt}})/kT) - 1} = \frac{(E_\gamma - \Delta E_{\text{ft}}) \exp(E_\gamma/E_0)}{\exp((E_\gamma - E_{\text{ft}})/kT) - 1}, \quad (2.29)$$

where  $\Delta E_{\text{ft}}$  is the quasi-Fermi level separation between trapped holes in the valence and electrons in the conduction band-tail. From Figure 2.10 (compare Figure 2.3) it can be seen that the distance between the peaks of  $p_{\text{vbt}}$  and  $n_{\text{cvt}}$  is higher than  $\Delta E_{\text{ft}}$ . The peak of luminescence can be written as  $\hat{E}_\gamma = \Delta E_{\text{ft}} + E_x$ , where  $E_x$  is a constant offset, which depends on  $E_0$  and  $T$ . The lower  $T$  or  $E_0$  the smaller is  $E_x$ . Substitution of the photon energy  $E_\gamma = \hat{E}_\gamma = \Delta E_{\text{ft}} + E_x$  in Eq. (2.29) yields

$$\varphi(\Delta E_{\text{ft}} \propto \hat{E}_\gamma) \propto \exp\left(\frac{\Delta E_{\text{ft}}}{E_0}\right). \quad (2.30)$$

As long as the quasi-Fermi level separation is given by  $\Delta E_{\text{f}} = \Delta E_{\text{ft}} - 2kT \ln(1 + \sigma_r)$ ,  $E_0$  can be derived from  $\mu\text{c-Si:H-pin}$  devices, where  $\sigma_r = \sigma_n/\sigma_p$  for valence and  $\sigma_r = \sigma_p/\sigma_n$  for conduction band-tails.

Note that Eq. (2.30) evaluates the convolution integral from Eq. (2.27) only for the highest luminescence signal. The luminescence spectrum can be significantly broaden due to high temperatures,  $\sigma_r \rightarrow 1$ , and/or due to charge carrier transport effects. Such transport effects yield unequal quasi-Fermi level separation and therefore broaden the recombination profile through the device. A previously presented comparison between experiment and simulation from  $\mu\text{c-Si:H-pin}$  devices validated this relation from Eq. (2.30) [118].

### 2.4.3 Hydrogenated Amorphous Silicon $a\text{-Si:H}$

It is generally accepted that the main part of the luminescence of  $a\text{-Si:H}$  originates from tail-to-tail transitions [58, 73, 119–123]. The luminescence is also calculated from Eq. (2.27) as it is for  $\mu\text{c-Si:H}$ . As it can be seen from Figure 2.9, due to shallow decaying localized states, the quasi-Fermi levels are very close to this states. This means that compared to  $\text{Cu(In,Ga)Se}_2$  many of the trapping states are occupied. However, in  $a\text{-Si:H}$  it is often observed that luminescence photons lose extra energy to the lattice, which is known as Stokes-shift. This Stokes-shift is

often cited in the range 0.2 – 0.3 eV [119, 121–126].

The luminescence processes in  $a$ -Si:H are more complex than in Cu(In,Ga)Se<sub>2</sub> or  $\mu$ c-Si:H. A second kind of recombination in  $a$ -Si:H is also illustrated in Figure 2.9. Mid-gap defect states play an import role for device physics. It can be easily seen that the occupation of the mid-gap defect density of states at reasonable quasi-Fermi level separation is quantitatively in the range of the occupation of the band-tail density of states. For this reason, these states are also important for luminescence. It was found that around room temperature the band-to-defect luminescence is almost as intense as the tail-to-tail luminescence or even more intense if the  $a$ -Si:H material is slightly doped (concentration above  $10^{17} \text{ cm}^{-3}$ ) [60, 123, 127, 128]. This doping induces defect states to the material. The Eqs. (2.4), (2.6), (2.17) and (2.21) yield the luminescence

$$\varphi_{\text{cb}}^{0/-}(E_\gamma) \propto \int N_{\text{db}}^{0/-}(E) F^0(E, E_{\text{fp}}, E_{\text{fn}}) N_{\text{cb}}(E + E_\gamma) f_{\text{n}}(E + E_\gamma, E_{\text{fn}}) \text{d} E \quad (2.31\text{a})$$

$$\varphi_{\text{vb}}^{+/0}(E_\gamma) \propto \int N_{\text{vb}}(E) f_{\text{p}}(E, E_{\text{fp}}) N_{\text{db}}^{+/0}(E + E_\gamma) F^0(E + E_\gamma, E_{\text{fp}}, E_{\text{fn}}) \text{d} E \quad (2.31\text{b})$$

from conduction band edge to neutral dangling bonds at around  $\hat{E}_\gamma = 0.8 \text{ eV}$  peak energy for  $n$ -type material, and  $\hat{E}_\gamma = 0.9 \text{ eV}$  for valence band edge to neutral dangling bond transitions in  $p$ -type material [60]. A Stokes-shift seems to be negligible for band-to-defect transitions.

## 2.5 Light Absorption

*Light absorption* yields the generation of electron/hole pairs. The complementary process to the *light absorption* is the *radiative recombination*. Therefore, the energy relation between electron, photon, and phonon, which is given in Section 2.4 also holds up for the *light absorption*. Whilst a high absorption, and therefore a high external quantum efficiency in *solar cells* is essential to yield a high photovoltaic conversion efficiency, the recombination in contrast reduces this efficiency. However, both processes are based on the same electronic states (see Section 2.2). *Light absorption* is the excitation of electrons from occupied ground states to unoccupied excited states. Therefore, in general the absorption is the convolution of all initially occupied ( $n_i$ ) with all unoccupied (finally occupied) states ( $n_f$ ) [129] and can be written as

$$\alpha(E_\gamma) = \frac{C}{E_\gamma} \int n_i(E) n_f(E + E_\gamma) \text{d} E, \quad (2.32)$$

where  $C$  depends on the refractive index and the momentum matrix elements. In the one electron approximation,  $C$  is assumed to be constant for all optical transitions [129–131]. Due to this relation between absorption and densities of states, the densities of states are often determined from deconvoluted absorption measurements done with the *constant photocurrent method* [129, 132–136], which is, in addition, affected by the charge carrier transport. The deconvolution of  $\alpha$  for possible transitions between electronic states, which are given in Section 2.2, shows Figure 2.11.

The external quantum efficiency ( $Q_e$ ), which can be easily determined from devices, relies on  $\alpha$ . In contrast to  $\alpha$ , the collection efficiency ( $f_c$ ), *i.e.* the charge carrier transport affects the  $Q_e$ . If

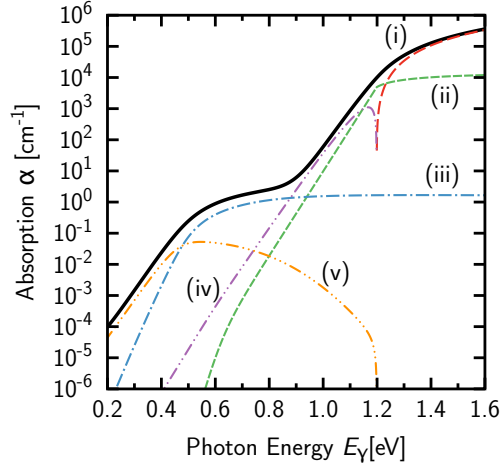


**Figure 2.11:** Calculated absorption ( $\alpha$ ) from convolution of different electronic states. Transitions are (i) valence band  $\rightarrow$  conduction band, (ii) valence band  $\rightarrow$  conduction band-tail and valence band-tail  $\rightarrow$  conduction band, (iii) valence band  $\rightarrow$  danling bonds and dangling bonds  $\rightarrow$  conduction band, (iv) valence band-tail  $\rightarrow$  conduction band-tail, and (v) valence band-tail  $\rightarrow$  dangling bonds and dangling bonds  $\rightarrow$  conduction band-tail.

$f_c \approx 1$  and the light transmission at the mirrored rear side of the device is assumed to be  $T = 0$ , the  $Q_e$  writes as

$$Q_e(E_\gamma) = f_c(E_\gamma) A(E_\gamma) \approx (1 - R) [1 - \exp(-\alpha d)], \quad (2.33)$$

where the absorbance ( $A$ ) is approximated with Lambert-Beer's law. The  $R$  is the front side reflectance of the device and  $d$  the thickness of the absorber layer.

## Chapter 3

# Experimental Methods and Simulations

This chapter gives a short overview for the used *radiative recombination* (luminescence) and *light absorption* experiments (see Section 3.1), and how this is simulated (see Section 3.2) in this thesis.

The chalcopyrite  $\text{Cu(In,Ga)Se}_2$  *np* heterojunction, the hydrogenated microcrystalline silicon ( $\mu\text{c-Si:H}$ ) *pin*, and the hydrogenated amorphous silicon (*a-Si:H*) *pin* devices as used for the experiments are described in Section 3.1.1. Furthermore, the photo- (PL) and electroluminescence measurements (see Section 3.1.2), and the external quantum efficiency measurements are presented (see Section 3.1.3).

The full one dimensional numerical device simulations, and the connected luminescence and external quantum efficiency calculations are presented in Section 3.2.1 and Section 3.2.2, respectively.

### 3.1 Experiments

There are three types of devices investigated, namely chalcopyrite  $\text{Cu(In,Ga)Se}_2$  *np* heterojunction, hydrogenated microcrystalline silicon  $\mu\text{c-Si:H}$  *pin*, and hydrogenated amorphous silicon *a-Si:H* *pin*. The investigations are mainly based on photo- (PL) and electroluminescence (EL), and, in terms of *reciprocity relation* (Section 2.3), its physical counterpart, the external quantum efficiency ( $Q_e$ ). The device temperature and the charge carrier injection rate, *i.e.* charge carrier generation rate under optical bias, and injection current under electrical bias, are the varied external parameters.

#### 3.1.1 Devices

The investigated  $\text{Cu(In,Ga)Se}_2$ ,  $\mu\text{c-Si:H}$ , and *a-Si:H* devices and its layer structure are shown in Figure 3.1.

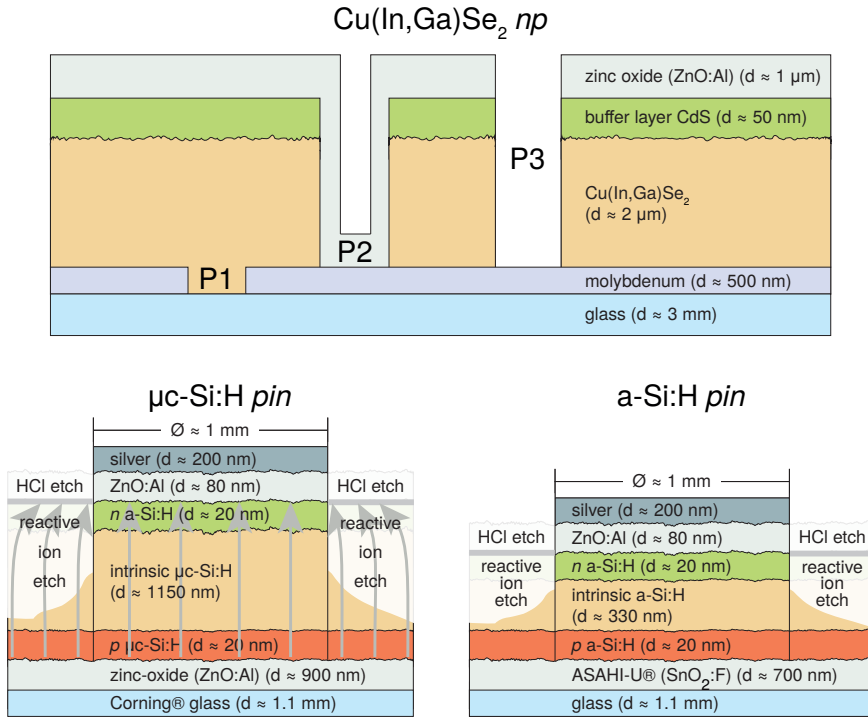


**Figure 3.1:** Layer structure of photovoltaic devices used in this work. The chalcopyrite  $\text{Cu(In,Ga)Se}_2$  np heterojunction devices are structured as modules. Module stripes are connected in series. The hydrogenated microcrystalline  $\mu\text{c-Si:H}$  pin and hydrogenated amorphous  $a\text{-Si:H}$  pin devices are single layer stacks. To reduce lateral current collection from areas, which are not covered with a silver back contact, the pin devices are etched back outside this back contact. The etch process is done with reactive ions.

### Chalcopyrite Cu(In,Ga)Se<sub>2</sub> *np* Heterojunction

Chalcopyrite Cu(In,Ga)Se<sub>2</sub> belongs to the group of I-III-VI semiconductors. Materials of this group crystallize in the chalcopyrite lattice structure similar to the structure of diamond. Many chalcopyrite materials have a high *light absorption* and are semiconductors. One of the main characteristics of I-III-VI semiconductors is its miscibility. Due to this, the elements of the I. (copper, silver), III. (indium, iron, aluminum, gallium), and VI. (sulfur, selenium, tellurium) group can be exchanged, leading to different element concentrations. Thereby, the lattice spacing and the band gap can be tuned. For photovoltaic applications, CuInS<sub>2</sub> and Cu(In,Ga)Se<sub>2</sub> are mostly used and therefore also investigated.

The Cu(In,Ga)Se<sub>2</sub> *np* heterojunction device used in this thesis is industrially produced by the Manz AG, formerly Würth Solar GmbH & Co. KG as a whole module, *i.e.* several single devices are monolithically connected in series. As can be seen from Figure 3.1, the *solar cells* are deposited on mechanically stable glass with a thickness of  $d \approx 3$  mm, but without optical requirements. The back contact, made of molybdenum, is DC sputtered on top of the glass substrate with a thickness of  $d \approx 500$  nm. After this, the molybdenum layer is mechanically structured (see P1 in Figure 3.1) to isolate the contact of adjacent cells. On top of this layer, the *p*-doped absorber layer made of Cu(In,Ga)Se<sub>2</sub> is coevaporated. Not much is known about this modules, which are used in this thesis, however, the Manz standard process leads to a graded band gap absorber associated to a varying Ga content [137]. After coevaporation, typical layers have a root mean square roughness  $RMS \approx 230$  nm, which enhances light scattering into the absorber [138]. The roughness seems to depend on the copper concentration [139]. Due to the high absorption, the thickness of the layer can be less than  $d = 2$   $\mu$ m. The absorber layer thickness does not matter in terms of collection efficiency due to the high charge carrier mobilities. As a next step, a thin ( $d \approx 50$  nm) *n*-doped CdS buffer layer is radio frequency sputtered. After the deposition of the absorber and the CdS layers, a second line is structured (see P2 in Figure 3.1), which serves to contact the front and rear contacts of two adjacent cells. The last layer is a DC sputtered aluminum doped zinc oxide with a thickness of  $d = 1$   $\mu$ m. This front contact has to be highly conductive and transparent for the solar spectrum at the same time. A last mechanically structured line (see P3 in Figure 3.1) isolates the ZnO contact of two adjacent cells.

To characterize one single device, the module is cut into small pieces. The device used in this thesis has an active area of 4.5 mm  $\times$  9.7 mm. The electrical contact then is applied to the front contact of two adjacent stripes. This may lead to partial shading.

### Hydrogenated Microcrystalline Silicon $\mu$ c-Si:H *pin*

The  $\mu$ c-Si:H *pin solar cell*, which is used in this thesis, is deposited with *Plasma Enhanced Chemical Vapor Deposition* (PECVD) from silane and hydrogen at a substrate temperature of 160 °C [49, 51, 140]. The layer structure is shown in Figure 3.1. The substrate is a 1.1 mm thick XG-type glass from Corning®. A transparency in the region of the solar spectrum is required. The device consists of a *pin*-layer stack with a 20 nm thick *p*-doped, a 1150 nm intrinsic absorber, and a 20 nm *n*-doped layer. Whereas the *p*-doped and the intrinsic layer consist of  $\mu$ c-Si:H, the *n*-doped layer consists of *a*-Si:H. The *a*-Si:H layer yields a band offset, which ensures a barrier for holes at the *n*-contact.

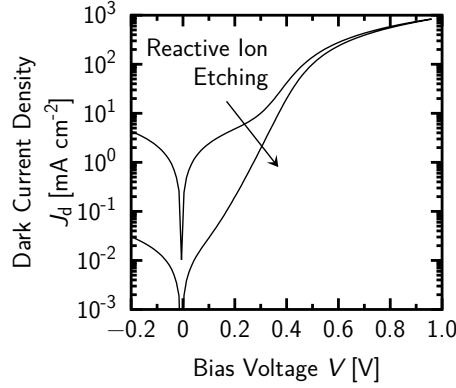


**Figure 3.2:** Effect of reactive ion etching process on dark current/voltage characteristic at a  $\mu\text{c-Si:H}$  *pin* device.

The front contact consists of texture etched sputtered aluminum doped zinc oxide ( $\text{ZnO:Al}$ ). The texture of the front contact determines the roughness of the other almost coplanar grown interfaces and ensures effective light scattering into the cell [141]. Its root mean square roughness is  $RMS \approx 100$  nm. For the back reflector and contact we use a layer stack of  $\text{ZnO:Al}$  and a 200 nm thick silver layer. A reactive ion-etch is used to remove the *n*-doped layer beyond the back-contact (see Figure 3.1). This removal of material around the contact serves to have a well defined cell area. Without this etch step, lateral current affect the measured current/voltage characteristics, in particular at low currents [62]. The Figure 3.2 shows the influence to a  $\mu\text{c-Si:H}$  *pin* device. Since the silver back contact is corroded by the reactive ion-etch, it is protected with paint during the process. This paint is removed with acetone after the etch step.

The cell, which is used in this thesis is circular with a diameter of 1 mm. The *solar cell* parameters of this device under *AM1.5G* conditions [142] are a power conversion efficiency  $\eta = 8.15\%$ , an open circuit voltage  $V_{oc} = 499$  mV, and a short circuit current density  $J_{sc} = 23.2$  mA cm<sup>-2</sup>.

### Hydrogenated Amorphous Silicon *a-Si:H pin*

The *a-Si:H pin* device, which is used in this thesis, is also deposited with PECVD from silane and hydrogen [143], similar to the first *a-Si:H solar cells* [52]. The substrate temperature is 180 °C. The PECVD is used with high gas flow at high pressure. The layer structure shows Figure 3.1. The substrate is an *U*-type glass from ASAHI®. It is 1.1 mm thick, and an already textured fluorine doped tin oxide ( $\text{SnO}_2\text{:F}$ ) is deposited on top of it. The roughness of the front contact determines the roughness of the other almost coplanar grown interfaces and ensures effective light scattering into the cell.

The device also consists of a *pin*-layer stack with a 20 nm thick *p*-doped, a 330 nm intrinsic absorber, and a 20 nm *n*-doped layer. Due to a higher absorption than in *c-Si* or  $\mu\text{c-Si:H}$ , the intrinsic absorber layer can be thin. However, if a good photovoltaic conversion efficiency should be achieved, the thickness is limited to a few hundred nanometers, since the charge carrier mo-

bility is low.

The back reflector again is of the same type as in  $\mu\text{c-Si:H}$  *pin* devices. Therefore, the *a-Si:H* devices are also etched back with reactive ions to reduce lateral extra current flow (see Figure 3.1 and Figure 3.2).

The cell, which is used in this thesis is circular with a diameter of 1 mm. The *solar cell* parameters of this device under *AM1.5G* conditions [142] are a power conversion efficiency  $\eta = 9.27\%$ , an open circuit voltage  $V_{oc} = 939\text{ mV}$ , and a short circuit current density  $J_{sc} = 14.5\text{ mA cm}^{-2}$ .

### 3.1.2 Electro- and Photoluminescence

This section gives a brief overview of the photo- (PL) and electroluminescence (EL) measurement setup in Figure 3.3, which is used to characterize *radiative recombination*. Generally, the PL and EL is measured with a liquid nitrogen cooled germanium avalanche detector with a spectral sensitivity between about 0.7 and 1.7 eV (see Figure 3.4). The spectrally resolved measurements are made using a *Fourier transform infrared spectroscopy* setup. All spectra are corrected with a reference measurement of a calibration lamp, which spectrum is known. Solid state lasers with wavelengths of  $\lambda = 473, 532$ , and  $671\text{ nm}$  are used for the PL measurements. Whereas the short wavelength laser light is absorbed within  $d_{\alpha} = 200\text{ nm}$  in  $\mu\text{c-Si:H}$ , the long wavelength laser ensures homogeneous photo-generation of charge carriers through the device ( $d_{\alpha} = 2.5\text{ }\mu\text{m}$ ). A dichroic filter ensures reduction of near infrared bias laser light to the detector. For the modulation of the light intensity within one order of magnitude, the lasers are voltage controlled. A wheel with neutral density filters modulates the light intensity over two orders of magnitude. The light intensity is measured with a calibrated reference diode.

The luminescent light coming from the device in the cryostat is collected and focused to an aperture wheel at the optical input of the *Fourier transform infrared spectrometer* with two off-axis gold mirrors.

To measure low intensity luminescence signals, the device is in both cases electrically modulated with a frequency of  $f = 68\text{ Hz}$ , which allows the use of lock-in technique and suppressing signal noise. For PL measurements the lock-in technique also ensures that the signal only originates from the *pin*-device itself and not either from any other layer, which is not part of the active device or from the optics in the setup. In this case, the device is switched between zero volt, where the generated charge carriers are extracted, resulting in a short circuit current ( $J_{sc}$ ), and the open circuit voltage ( $V_{oc}$ ), where the net current is zero and all generated charge carriers recombine within the device. In case of EL the device is switched between zero volt and the injection current density ( $J_d$ ) corresponding to  $J_{sc}$  under illuminated conditions within PL measurements, i.e.  $J_d = -J_{sc}$ .

A *Source Measure Unit* (SMU) applies and measures the electrical currents and voltages at the device. For the frequency modulated luminescence measurement, this SMU only helps to set a frequency generator, which is connected to the device.

### 3.1.3 External Quantum Efficiency

The *light absorption* measurements in terms of external quantum efficiency are made with a *constant photocurrent method* (CPM) setup shown in Figure 3.5. The device under test is placed in a cryostat to vary the temperature. The photocurrent through the device is measured under





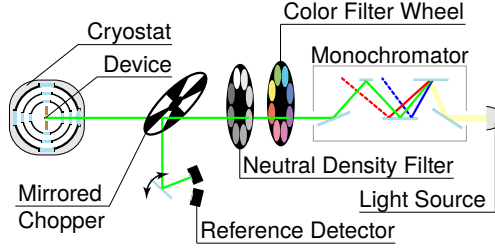


**Figure 3.5:** Experimental *constant photocurrent method* setup to measure temperature dependent external quantum efficiency under constant photocurrent conditions. Monochromatic light is altered in its intensity to hold the device photocurrent constant. The reference light is measured with different detectors, which depends on the wavelength. The usage of lock-in technique needs a mirrored chopper wheel to yield highest light signal at the device and the reference.

monochromatic light conditions. The light is reduced in its intensity to hold the device photocurrent constant. The reference light intensity is measured with different detectors, which depends on the wavelength. For the use of lock-in technique and to yield highest signal at both, the device and the reference, the chopper wheel is mirrored. With this setup, the lock-in frequency is  $f = 8 \text{ Hz}$ .

## 3.2 Simulations and Modeling

This section introduces the numerical device simulations, which are used within this thesis to model local recombination in  $\text{Cu(In,Ga)Se}_2$  *np* heterojunction devices, and  $\mu\text{c-Si:H}$  and *a-Si:H* *pin* devices in one dimension.

Generally, the simulations use two programs. The commercial full one dimensional numerical device simulator *Advanced Semiconductor Analysis (ASA)* from the Technical University of Delft is used for optoelectronic simulations [144], and in addition to that, an Octave script called *LUME* is used for the photo- and electroluminescence, and the external quantum efficiency calculations. The interaction of both programs is shown in Figure 3.6. The details are presented in the following.

### 3.2.1 Full Device Simulations – ASA

The optoelectronic simulations are separated into two parts, *i.e.* the optical and the electrical simulations. These are both part of *ASA*, which calculates a generation profile ( $G(z, \lambda)$ ) and solves the semiconductor equations (see Eqs. (2.1) and (2.2)) in one dimension, *i.e.* for planar devices in  $z$ -direction from the front to the back contact. The optoelectronic interaction within *ASA* is shown in Figure 3.7.

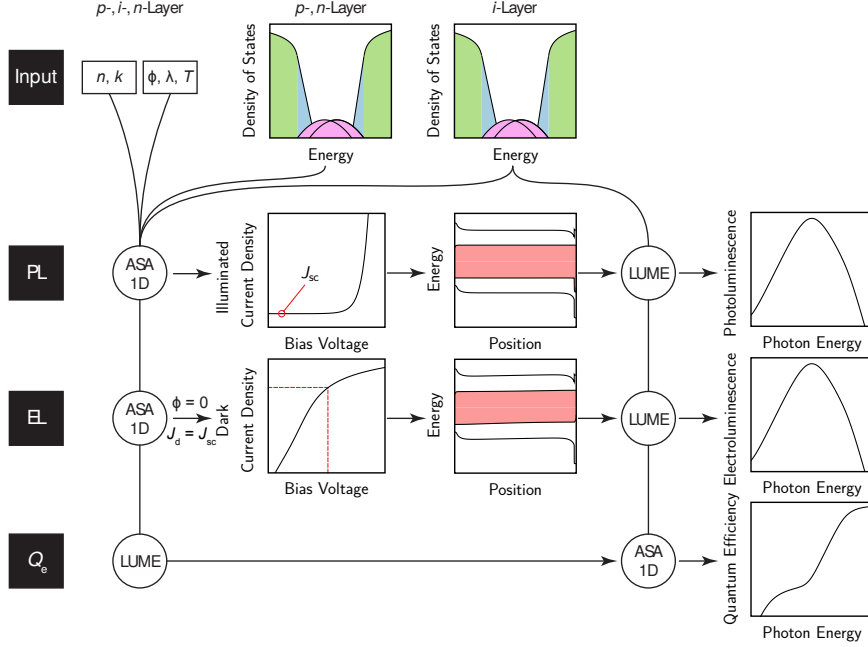


**Figure 3.6:** Flow process chart for use of the optoelectronic solver *Advanced Semiconductor Analysis* (ASA) in connection with luminescence and external quantum efficiency calculations in the Octave script *LUME*. The densities of electronic states and the optical layer properties are the input parameters for ASA and *LUME*. The photo- (PL) and electroluminescence (EL), and the external quantum efficiency ( $Q_e$ ) is calculated with *LUME* from full band diagrams, which are calculated by ASA.

## Optical Simulations

For the optics, the Snellius refraction law

$$\frac{n_1}{n_2} = \frac{\sin \theta_1}{\sin \theta_2} \quad (3.1)$$

at the interface between two optical layers with complex refraction index ( $n_1, n_2$ ), and the angle of incidence ( $\theta_1$ ) and diffraction ( $\theta_2$ ) is solved with *GenPro3* [145, 146], which is part of ASA, together with the Fresnel equations

$$r = \frac{n_1 - n_2}{n_1 + n_2} \quad (3.2a)$$

$$t = \frac{2n_1}{n_1 + n_2}, \quad (3.2b)$$

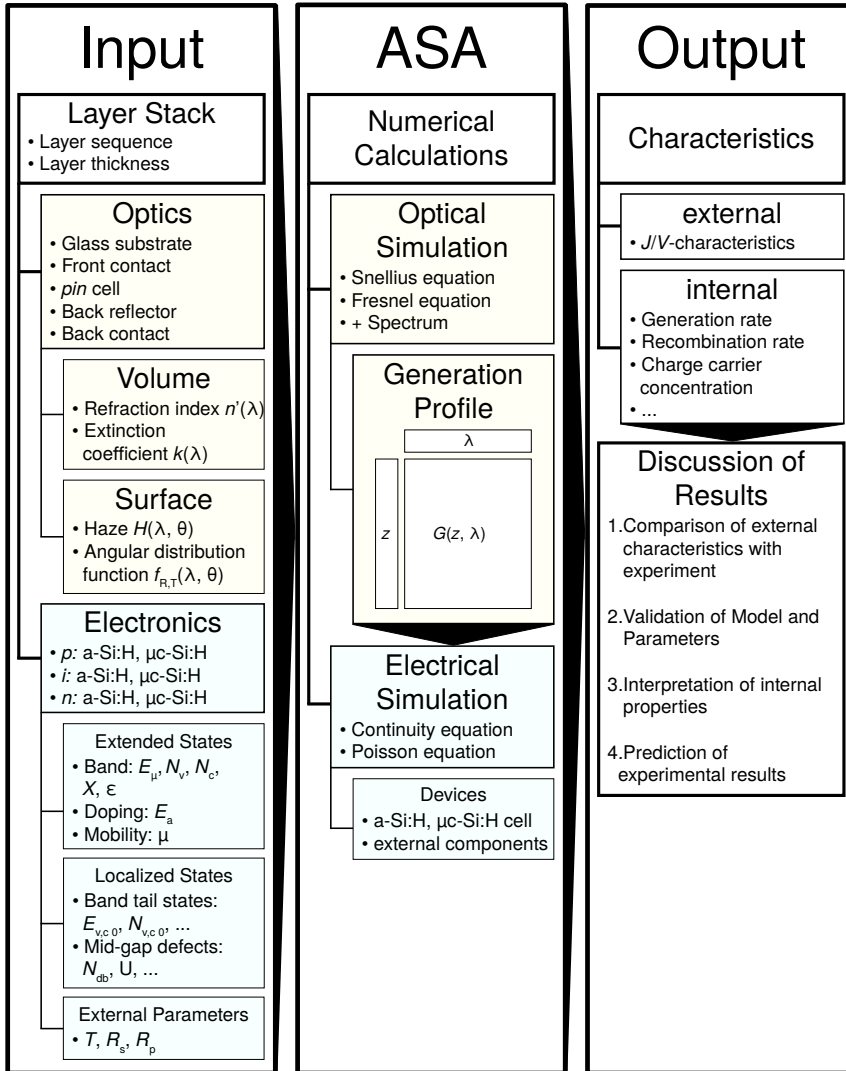


**Figure 3.7:** Flow process chart for the usage of *Advanced Semiconductor Analysis (ASA)* program.

where the reflectance  $R = |n_2/n_1||r|^2$  and the transmittance identifies with  $T = |t|^2$  [147]. The description of the whole layer stack and the electronic characteristics of each layer are the input parameters for ASA. The wavelength dependent refraction index ( $n'$ ) and extinction coefficient ( $\kappa$ ) are the optical input parameters. *Solar cells*, which should yield a high photovoltaic conversion efficiency need to absorb as much light as possible. To enhance the *light absorption*, the interfaces between the optical layers scatter the light into the *solar cell* due to a textured substrate, which yields rough interfaces. To model *solar cells* with rough interfaces, the light scattering properties at each interface has to be taken into account. In this thesis, the multi rough-interface model is used [145, 146, 148, 149], which assumes the same amount of light to be reflected at a rough interface as at a flat interface. At a rough interface, a certain amount of the reflected/transmitted light is scattered. The ratio between the scattered and the entire light is the haze. The haze for the reflected light can be described by [150]

$$H_R = 1 - \exp \left[ - \left( \frac{4\pi \delta_{\text{rms}} n_1}{\lambda} \right)^2 \right], \quad (3.3)$$

where  $n_1$  is the refractive index of the medium of incidence, and  $\delta_{\text{rms}}$  the root-mean-square roughness of the interface. The haze for the transmitted light can be described by [149]

$$H_T = 1 - \exp \left[ - \left( \frac{4\pi \delta_{\text{rms}} C |n_1 - n_2|}{\lambda} \right)^3 \right], \quad (3.4)$$

where  $C$ , which depends on the media  $n_1$  and  $n_2$  is assumed to be unity. The scattered reflectance

$$R_{\text{sct}} = H_R f_R^{\text{in}}(\theta^{\text{in}}) f_R^{\text{out}}(\theta^{\text{out}}) R \quad (3.5)$$

and transmittance

$$T_{\text{sct}} = H_T f_T^{\text{in}}(\theta^{\text{in}}) f_T^{\text{out}}(\theta^{\text{out}}) T \quad (3.6)$$

depend on the angle of incident light, which is described by an angular distribution function  $f_{R,T}^{\text{in}}(\theta^{\text{in}})$  for the scattering in dependence of the angle of incident light ( $\theta^{\text{in}}$ ) for reflectance and transmittance, and  $f_{R,T}^{\text{out}}(\theta^{\text{out}})$  for the scattering in dependence of the angle of the outbound reflected or transmitted light ( $\theta^{\text{out}}$ ), respectively. The  $R$  and  $T$  are the total reflectance and transmittance, respectively, which originate from the Fresnel equations (see Eq. (3.2)). In summary, the interfaces between two layers are described with the root-mean-square roughness dependent haze, and the scattering angle dependent angular distribution functions.

These optical calculations yield a wavelength and depth dependent optical generation profile ( $G(z, \lambda)$ ).

## Electrical Simulations

For the electrical simulations, which are connected to the optical generation profile in case of illumination bias, the electronic layer properties need to be specified by its parameters, which are

introduced in Section 2.2. The band, band-tail, and mid-gap defect states have to be parameterized for each electronic layer in the device. Additional to this, a series and a shunt resistance with ohmic behavior, which yield as external components have to be specified. And last but not least the device temperature ( $T$ ) has to be given.

For the modeling of (full) devices, several parameters can be tuned, and most of them are not known explicitly. Therefore, the input parameters are either taken from literature, through physical arguments, determined with measurements, and/or deduced by fitting the simulations to the measurements. Since the simulations use the effective medium approach, the modeled parameters are also effective quantities.

**Ohmic Contact Series Resistance** In order to reduce *free* parameters for the modeling of the devices with ASA, the external ohmic contact series resistance is determined with a method first introduced by Wolf and Rauschenbach [151], which compares the dark voltage ( $V_d$ ) at a given injection current with the open circuit voltage ( $V_{oc}$ ) under illumination, and the same injection current, namely the short circuit current ( $J_{sc}$ ). At high bias voltage, the dark injection current is limited by the ohmic contact, and therefore this yields the external ohmic contact series resistance  $R_s^e$ . The determination of the voltage dependent series resistance is written as

$$R_s(V) = \frac{V_d - V_{oc}}{J_{sc}}. \quad (3.7)$$

Specially for low mobility materials like  $\mu c$ -Si:H or  $a$ -Si:H used in *pin* cell structures with highly conductive contacts, where highest  $J_{sc}$  does not limit the dark injection current density, the experimentally determined series resistance from Eq. (3.7) can be fitted with [152]

$$R_s(V, T) = R_s^e + d \rho_{s,0}^i(T) \exp\left(-\frac{qV}{2kT}\right), \quad (3.8)$$

where  $kT/q$  is the thermal voltage,  $d$  the thickness of the intrinsic absorber/recombination layer, and  $\rho_{s,0}^i(T)$  its temperature dependent specific resistance.

**Activation Energy and Mobility Gap** And again, in order to reduce *free* modeling parameters of  $\mu c$ -Si:H and  $a$ -Si:H *pin*-devices, the mobility band gap of the intrinsic absorber/recombination layer ( $E_\mu$ ) is determined via activation energy measurements ( $E_a(V)$ ). The activation energy can be determined from dark current/voltage characteristics as

$$E_a(V) = -\frac{d \ln J_d(V, \frac{1}{kT})}{d \frac{1}{kT}}, \quad (3.9)$$

where  $J_d$  is the dark current density and  $kT$  the thermal energy. Due to approximately equal charge carrier concentration of electrons ( $n$ ) and holes ( $p$ ), *i.e.*  $n \approx p$ , and therefore symmetric

quasi-Fermi level separation at the position, where the contribution to the charge carrier recombination rate is highest, the  $E_a \propto -V/2$ . The mobility band gap then can be written as [61, 63]

$$E_\mu = 2E_a(0\text{ V}) - 6kT. \quad (3.10)$$

In *a*-Si:H Zhu *et al.* reported  $E_\mu = 1.74\text{ eV}$  from optical absorption measurements, and assumed the mobility gap to be identical [68]. A somewhat larger value was reported by Chen and Wronski, which bases on internal photoemission measurements [153].

In  $\mu\text{c}$ -Si:H, Pieters *et al.* determined  $E_\mu = 1.19\text{ eV}$  with activation energy measurements as used in this thesis [61, 63].

The following set of parameters for  $\mu\text{c}$ -Si:H or *a*-Si:H is partly based on the references [61, 63, 72, 154]. However, the parameters, which are fitted in this thesis can be found in the modeling Section 4.2.1 for Cu(In,Ga)Se<sub>2</sub>, Section 5.2.1 for  $\mu\text{c}$ -Si:H, and Section 6.2.1 for *a*-Si:H.

**Effective Density of States** In *a*-Si:H the effective density of valence band states  $N_v = 4.0 \times 10^{20}\text{ cm}^{-3}$  was estimated from temperature-dependent open circuit voltage measurements [68]. Sellmer found a smaller  $N_v = 0.5 - 1.1 \times 10^{19}\text{ cm}^{-3}$  [155] with thermoelectric power and Hall effect measurements in *p*-doped *a*-Si:H and  $\mu\text{c}$ -Si:H with the crystallinity increased from  $X_c = 1 - 57\%$ , which is determined with Raman scattering. The effective density of conduction band states is often arbitrary set  $N_c = N_v$  [72, 154].

According to Pieters *et al.* [61], in  $\mu\text{c}$ -Si:H the  $N_v = 5.2 \times 10^{18}\text{ cm}^{-3}$  and  $N_c = 1.4 \times 10^{19}\text{ cm}^{-3}$  should be similar to *c*-Si ( $N_v = 1.0 \times 10^{19}\text{ cm}^{-3}$ ,  $N_c = 2.8 \times 10^{19}\text{ cm}^{-3}$  at  $T = 300\text{ K}$ ). The electronic transport in non crystalline semiconductors like  $\mu\text{c}$ -Si:H or *a*-Si:H is based on the percolation theory [156–158]. The percolation path in  $\mu\text{c}$ -Si:H is mainly determined by the crystallite clusters [159–161], which are embedded in an *a*-Si:H matrix. Therefore, it is commonly accepted that the electronic transport properties in  $\mu\text{c}$ -Si:H are mainly determined by the properties of these crystallites [155, 162]. In accordance to this, the current flows only through a small fraction of the material, namely through these crystallites, which make a long range connection. Due to this, the  $N_c$  and  $N_v$  are determined by the number and the size of those crystallite clusters. Since, the  $E_\mu$  of  $\mu\text{c}$ -Si:H and the band gap of *c*-Si are similar, the band structure of  $\mu\text{c}$ -Si:H is also assumed to be similar.

In summary, the  $N_c = N_v$ , which are assumed to be symmetric for the sake of convenience, are mainly fitted with the help of current/voltage characteristics within small variations around the here given  $N_c$  and  $N_v$ .

**Electron Affinity** The electron affinity ( $\chi$ ) of  $\mu\text{c}$ -Si:H is deduced from the band offset ( $\Delta\chi$ ) at a *c*-Si/*a*-Si:H heterojunction. The  $\Delta\chi = 0.15\text{ eV}$  of the conduction band is determined from capacitance/voltage and current/voltage characteristics [163]. The  $\chi = 3.98\text{ eV}$  of *a*-Si:H was determined with  $\chi = 4.13\text{ eV}$  of *c*-Si to be assumed. Similar to this, investigations at a  $\mu\text{c}$ -Si:H/*a*-Si:H heterojunction found  $\Delta\chi = 0.14\text{ eV}$  [164].

As long as the band structure from  $\mu\text{c}$ -Si:H can be assumed to be similar to *c*-Si due to its crystalline clusters, the  $\chi$  of both materials are also assumed to be similar.

**Band Mobility** Schiff estimated the band mobilities for holes in the valence band  $\mu_p = 1 \text{ cm}^2 \text{ V}^{-1} \text{ s}^{-1}$  in *a*-Si:H from hole time-of-flight measurements with the *exponential band-tail trapping model* [85]. High temperature measurements for electrons in the conduction band suggest a larger  $\mu_n = 7 \text{ cm}^2 \text{ V}^{-1} \text{ s}^{-1}$  [85].

The  $\mu_n = 50 \text{ cm}^2 \text{ V}^{-1} \text{ s}^{-1}$  and  $\mu_p = 15 \text{ cm}^2 \text{ V}^{-1} \text{ s}^{-1}$  in  $\mu\text{c}$ -Si:H are determined from thin-film transistors [165]. The  $\mu_p$  was not directly measured, but it is often assumed to be 3 times lower than  $\mu_n$ . Pieters *et al.* used these values [61].

**Defect States** Two different dangling bond distributions exist in  $\mu\text{c}$ -Si:H, since  $\mu\text{c}$ -Si:H consists of crystallites, which are embedded in an *a*-Si:H matrix. The dangling bond distributions in  $\mu\text{c}$ -Si:H are investigated with electron spin resonance [166]. Each distribution can be assigned to either the *a*-Si:H matrix or the embedded crystallites separately. For this reason, both distributions are also spatially separated [167]. As long as the total defect density is determined to be  $N_{\text{db}} = 5 \times 10^{15} - 1 \times 10^{16} \text{ cm}^{-3}$ , however, the main charge carrier transport is assumed to flow through the crystallites, thus not all defects may be equally relevant to device operation.

The width of the gaussian distributed defects ( $\sigma_{\text{db}}$ ) is found to be broad [166, 167].

Lee and Schiff used for the correlation energy  $U = 0.30 \text{ eV}$  between the  $E_{\text{db}}^{+/0}$  and  $E_{\text{db}}^{0/-}$  transition levels [168].

In  $\mu\text{c}$ -Si:H Pieters *et al.* fitted  $N_{\text{db}} = 6.0 \times 10^{15} \text{ cm}^{-3}$ ,  $\sigma_{\text{db}} = 150 \text{ meV}$ , and  $U = 0.20 \text{ eV}$  [61].

**Band-Tails** The characteristic energy of the valence band-tail in *a*-Si:H is estimated around  $E_{v0} \approx 45 \text{ meV}$  [85, 169, 170]. Although values for the characteristic energy of the conduction band-tail ( $E_{c0}$ ) in *a*-Si:H are often cited in a broad range  $18 - 41 \text{ meV}$  [77, 85, 171, 172], Wang *et al.* [173], and Winer *et al.* [174] reported  $E_{c0} \approx 27 - 32 \text{ meV}$ , which is similar to  $\mu\text{c}$ -Si:H. However, the  $E_{v0}$  and  $E_{c0}$  are temperature dependent above its freeze-in temperature [83, 84]. Therefore, in this thesis the  $E_{v0}(T, T_0)$  and  $E_{c0}(T, T_0)$  of *a*-Si:H are scaled with temperature like shown in Eq. (2.10).

Following *a*-Si:H, localized band-tail states are also assumed in  $\mu\text{c}$ -Si:H [45, 58, 59, 61, 63, 117]. Merdzhanova *et al.* fitted symmetric band-tails  $E_0 = E_{c0} = E_{v0} = 31 \text{ meV}$  to PL spectra [59]. Pieters *et al.* used the same value for the fitting of dark and illuminated J/V characteristics [61, 63]. Pieters *et al.* also fitted PL spectra with quite the same value [45]. All these results assume that the band-tails do not change with temperature. The results of transient photocurrent measurements could be well explained with a constant valence band-tail  $E_{v0} = 31 \text{ meV}$  at temperatures up to  $T = 300 \text{ K}$  [167, 175]. Additionally, Reynolds *et al.* characterized the conduction band-tail  $E_{c0} = 33 \text{ meV}$  also with transient photocurrent measurements in the temperature range  $T = 150 - 250 \text{ K}$  [176]. Therefore, in this thesis, the characteristic energy of the band-tail densities of states of  $\mu\text{c}$ -Si:H are assumed to be constant and symmetric.

The  $E_{v0}$  and  $E_{c0}$  are mostly fitted with PL and EL spectra, and with external quantum efficiency measurements. Additionally, the luminescence/voltage characteristics from integrally measured PL are a good indicator.



**Capture Cross-sections** The capture cross-sections for electrons onto positively charged defect states ( $\sigma_n^+ = 4.0 \times 10^{-15} \text{ cm}^2$ ) is estimated from the lifetime-mobility product of deep trapped electrons in slightly boron doped *a*-Si:H samples [177]. The same kind of measurements of holes in intrinsic *a*-Si:H samples yields  $\sigma_p^0 = 7.5 \times 10^{-16} \text{ cm}^2$ , and in slightly phosphorous doped *a*-Si:H samples yields  $\sigma_p^- = 3.0 \times 10^{-15} \text{ cm}^2$  [177]. Antoniadis and Schiff also applied this deep-trapping measurements to undoped *a*-Si:H samples and found  $\sigma_n^0 = 1.8 \times 10^{-16} \text{ cm}^2$  [178].

The capture cross-sections of neutral conduction ( $\sigma_n^0$ ) and valence ( $\sigma_p^0$ ) band-tail states are estimated with electron and hole drift-mobility measurements from *a*-Si:H samples fitted to the band-tail trapping model. The fitting yields an attempt-to-escape frequency ( $\nu$ ), which describes the emission from the band-tail traps. The ( $\sigma_n^0$ ) and ( $\sigma_p^0$ ) follow from the *detailed balance* relation  $\nu = N_c \sigma_n^0 v_{th}$  and  $\nu = N_v \sigma_p^0 v_{th}$ , respectively, where  $v_{th} = 10^7 \text{ cm s}^{-1}$  is the thermal velocity. The  $\nu = 5 \times 10^{11} \text{ s}^{-1}$  is found for the conduction band-tail by Wang *et al.* [173], which yields  $\sigma_n^0 = 1.3 \times 10^{-16} \text{ cm}^2$ . Dinca *et al.* [170], and Zhu *et al.* [68] found  $\nu = 10^{12} \text{ s}^{-1}$ , which yields  $\sigma_p^0 \approx \sigma_n^0$  for the valence band-tail.

Juska *et al.* [179] reported  $\sigma_p^- \approx 10^{-16} \text{ cm}^2$  in the valence band-tails in *a*-Si:H samples, which is much smaller than expected from a fundamental argument due to *Langevin* recombination [180]. However, absolute values of the capture cross-sections are not known very well. Generally, the capture cross-sections of the neutral mid-gap defect and band-tail states are expected to be smaller than these of the charged states due to the coulomb interaction [90]. The ratio of 10 between charged and neutral states is often used for and fitted with simulations of *a*-Si:H and  $\mu\text{c-Si:H}$  devices [61, 181–183].

The capture cross-sections are arbitrary and for this reason, the quantities are fitted with the help of  $J/V$  characteristics. The ratio between both kinds of capture cross-sections in band-tail states can be easily fitted with the width of the PL and EL spectra, which is done in this thesis.

After solving the virtual device, the output yields the current/voltage characteristics of the device in the dark or under illumination. For the PL and EL simulations, the recombination profile with its corresponding band diagram is calculated. This band diagram and all density of states of the recombination layer are then passed to the Octave script *LUME* (see Figure 3.6).

### 3.2.2 Luminescence Simulations – LUME

Additional to *ASA*, the simulations use an Octave script called *LUME*. *ASA* can calculate common current/voltage characteristics beside others, however, the luminescence and external quantum efficiency calculations have to be done externally. This *LUME* script uses either a full band diagram calculated by *ASA* or a local (zero-dimensional) quasi-Fermi level separation as input parameters. In all these calculations, *LUME* manages the density and occupation probability of band, band-tail, and mid-gap defect states (see Chapter 2). In addition to this, the temperature dependent mobility gap (Eq. (2.5)), effective densities of states at the band edges (Eq. (2.8)), the characteristic energies of the band-tail densities of states (Eq. (2.10)), and the thermal velocity (Eq. (2.11)) are calculated by *LUME*.

### Local Recombination Model

The  $\text{Cu(In,Ga)Se}_2$  *np* heterojunction device simulations use a *local recombination model*, which neglects the charge carrier transport. Beside the electrical layer properties, the quasi-Fermi level separation and the corresponding band edge energies are passed through *LUME* for the photo-, electroluminescence, and external quantum efficiency calculations.

However, in contrast to the one-dimensional simulations in *ASA*, this *local recombination model* accounts for the band gap fluctuations, which are reported in  $\text{Cu(In,Ga)Se}_2$  [23, 115, 116].

### One Dimensional Luminescence

The one dimensional luminescence simulations are applied to the  $\mu\text{c-Si:H}$  and *a-Si:H pin* devices, which are connected to the *ASA* simulations. Instead of a local quasi-Fermi level separation and the corresponding band edge energies, a full band diagram is passed through *LUME*, which is calculated by *ASA*. This is beneficial, since common current/voltage characteristics in the dark and under illumination can be consistently modeled in connection to the photo-, electroluminescence, and external quantum efficiency experiments.



## Chapter 4

# Chalcopyrite Cu(In,Ga)Se<sub>2</sub> Based *np* Heterojunction Devices

This chapter shows (see Section 4.1) and discusses (see Section 4.2) measurements of chalcopyrite Cu(In,Ga)Se<sub>2</sub> based *np* heterojunction devices as presented in Section 3.1.1. It is intended to show the validity of the *reciprocity relation* (*RR*) (see Section 2.3) and its limitations. For this reason, photo- (PL) and electroluminescence (EL) spectra are measured in a wide temperature range with changed charge carrier injection rate within two orders of magnitude (see Section 4.1.2). As it is known from Cu(In,Ga)Se<sub>2</sub>, (metastable) defect states, which can be thermally annealed (permanently) [184] and temporarily charged with light soaking [185, 186], play an important role in the device physics [184, 187–192]. For the reason of defect reduction, the device is accelerated light soaked at  $T = 400$  K (see Section 4.1.1). The effect of accelerated light soaking on PL and EL is presented with a comparison between the relaxed device as fabricated and the treated device within various kinds of measurements. These experiments partly reproduce already shown results [44, 56, 108], which are required by the *RR* between the EL emission ( $\varphi_{\text{EL}}$ ) and the external quantum efficiency ( $Q_{\text{e}}$ ) in Section 4.1.3, as well as an unaltered spectral shape of  $\varphi_{\text{EL}}$  under different bias voltage conditions. In addition to that, new results in terms of the *RR*, which are not shown before, are presented in Section 4.1.4. The radiative ideality factor, which is required to be  $n_{\text{r}} = 1$ , is determined by fitting a common diode law to the luminescence/voltage characteristics.

At the end of this chapter in Section 4.2, the measured PL, EL, and  $Q_{\text{e}}$  are modeled with the *local recombination model* (see Section 3.2) for discussion of the experiments. This implies the modeling of the radiative ideality factor in Section 4.2.1 and the shift of the luminescence spectra in Section 4.2.2 as well as the *RR* between the electroluminescence and the external quantum efficiency in Section 4.2.3.

The modeled experimental results yield the band gap and its fluctuations as well as the characteristic energy of the band-tail density of states, since the PL and EL originate from band-to-tail transitions.

## 4.1 Experimental Results

As already explained in the introduction, the experiments focus on the *RR* with respect to (meta-stable) defect states at the heterojunction CdS/Cu(In,Ga)Se<sub>2</sub> interface and/or in the bulk. It is not clearly known, where the metastability originates from, either interface or bulk properties. However, these defects can be permanently annealed at elevated temperatures, which reduces defects due to lattice relaxation [184]. Due to light soaking, holes are stored in deep defect levels in the CdS layer near to the Cu(In,Ga)Se<sub>2</sub> interface [185, 193], which temporarily saturates/occupies these defects. The recombination through this states is then hampered due to this occupation. This photo-doping mechanism is one that can only occur in heterojunctions [185].

### 4.1.1 Accelerated Light Soaking

To reduce the influence of defect states, the device in this thesis is light soaked for 3 hours under illumination of three lasers with wavelengths  $\lambda = 473, 532$ , and  $671$  nm simultaneously. Three lasers are used simultaneously to achieve highest accessible photon flux. Additionally to this, the device is annealed at temperature  $T = 400$  K at the same time. As can be seen from Figure 4.1(a) the open circuit voltage increases almost  $\Delta V_{oc} = 28$  mV at an open circuit voltage  $V_{oc} = 471$  mV, which is comparable to the results found in [185, 186]. The reason for the drop in  $\Delta V_{oc}$  after  $10^4$  s light soaking is unknown.

However, before this accelerated light soaking, the same procedure at room temperature yields only  $\Delta V_{oc} = 9$  mV. This indicates that most of the defects are thermally annealed rather than temporarily photo-doped by light soaking. Therefore, it is expected that most of the defect reduction lasts permanently [184].

The Figure 4.1(b) shows the dark current/voltage characteristics of the relaxed and dark stored device as fabricated, and the treated device after the accelerated light soaking at room temperature and at annealing temperature  $T = 400$  K. The relaxed device as fabricated shows dominant recombination through mid-gap defect states in the voltage range  $V = 0 - 350$  mV, which can be observed from a common diode law ideality factor around 2. Beyond  $V \geq 350$  mV most of the recombination comes from band edge states. Around  $V \geq 650$  mV the current/voltage characteristic saturates due to series resistance effects. With a method first introduced by Wolf and Rauschenbach [151], the external ohmic contact series resistance is determined  $R_s^e = 16 \Omega \text{ cm}^2$  (see Section 3.2.1). After the accelerated light soaking the external ohmic contact series resistance is increased to  $R_s^e = 22 \Omega \text{ cm}^2$ . It is known that tempered zinc oxide, which yields the front contact, is less conductive. However, essentially, the accelerated light soaking strongly reduces defect recombination at low bias voltage as expected.

The accelerated light soaking also affects the PL and EL as can be seen from Figure 4.1(c) and (d). The PL and EL under constant charge carrier injection conditions is reduced at the light soaking temperature due to smaller quasi-Fermi level separation. However, after the accelerated light soaking, the PL is 1.7 times and the EL is 2.0 times more intense than before. This also indicates reduced defect states, which yield as additional recombination centers.

For the following measurements, it is expected that the cell mainly keeps its defect states as it is shortly after the accelerated light soaking, due to the lowered temperature compared to the accelerated light soaking temperature.

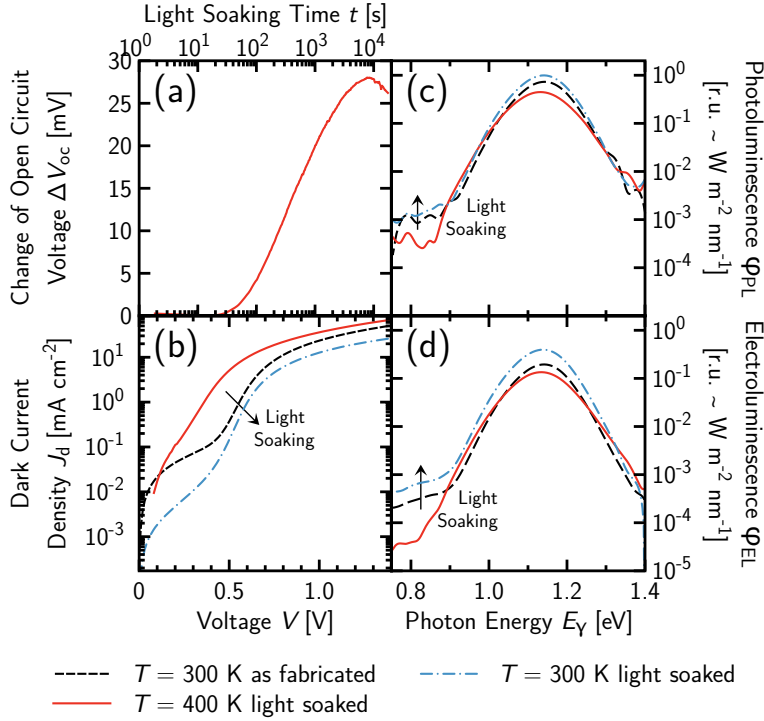


**Figure 4.1:** Accelerated light soaking of Cu(In,Ga)Se<sub>2</sub> np heterojunction device at temperature  $T = 400$  K. Accelerated light soaking is applied for 3 hours. Measurements before accelerated light soaking at temperature  $T = 300$  K are plotted as black dashed lines, and afterwards at  $T = 400$  K as red solid lines and at  $T = 300$  K as blue dashed/pointed lines. (a) The change of the open circuit voltage ( $V_{oc}$ ) versus the time ( $t$ ) during accelerated light soaking at temperature  $T = 400$  K. (b) Dark current/voltage characteristics of the device before and after accelerated light soaking. (c) Measured spectra from photoluminescence (PL) normalized to the highest signal from PL after accelerated light soaking. (d) Measured spectra from electroluminescence normalized to the highest signal from PL after accelerated light soaking. The current density before accelerated light soaking is  $J = 41$  mA cm<sup>-2</sup> and  $J = 33$  mA cm<sup>-2</sup> afterwards. Photoluminescence is excited at the wavelengths  $\lambda = 473$ , 532, and 671 nm simultaneously to achieve highest accessible photon flux.

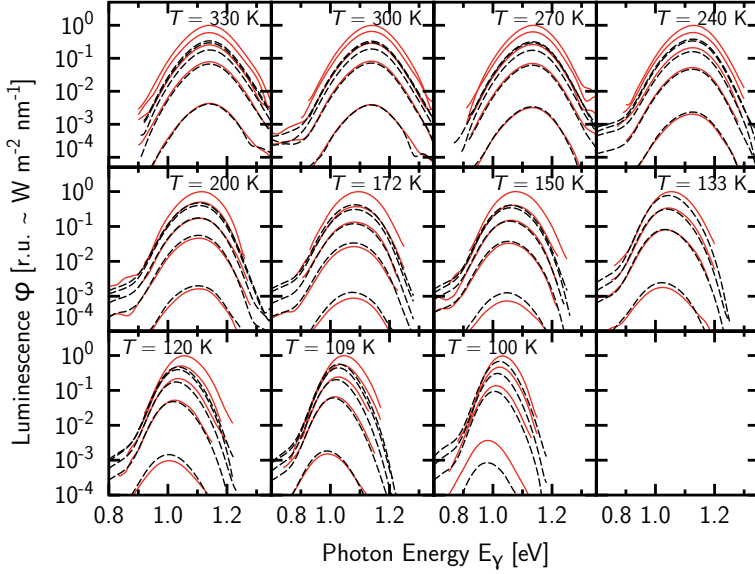


**Figure 4.2:** Measured spectra from photo- and electroluminescence of Cu(In,Ga)Se<sub>2</sub> *np* heterojunction device after 3 hours of accelerated light soaking at temperature  $T = 400$  K. Electroluminescence is plotted as black dashed lines, and photoluminescence as red solid lines. All spectra are normalized to the highest signal for each temperature. Spectra are measured at the temperatures  $T = 330, 300, 270, 240, 200, 172, 150, 133, 120$ , and  $100$  K. Photoluminescence is excited with photon fluxes  $\phi = 2.7 \times 10^{21}, 2.3 \times 10^{21}, 1.3 \times 10^{21}, 5.2 \times 10^{20}$ , and  $5.7 \times 10^{19} \text{ m}^{-2} \text{ s}^{-1}$  at the wavelengths  $\lambda = 473, 532$ , and  $671$  nm simultaneously. This yields current densities  $J = 33, 28, 16, 6.3$ , and  $0.69 \text{ mA cm}^{-2}$ .

#### 4.1.2 Change of Luminescence Spectra

The *RR* requires unaltered luminescence spectra under different bias conditions. To test if this requirement holds, the PL and EL spectra after the accelerated light soaking are measured at a sequence of temperatures  $T = 330 - 100$  K (see Figure 4.2). At each temperature the PL is excited with photon fluxes  $\phi = 2.7 \times 10^{21}, 2.3 \times 10^{21}, 1.3 \times 10^{21}, 5.2 \times 10^{20}$ , and  $5.7 \times 10^{19} \text{ m}^{-2} \text{ s}^{-1}$  at the wavelengths  $\lambda = 473, 532$ , and  $671$  nm simultaneously to achieve highest accessible photon flux. This yields short circuit current densities  $J_{sc} = 33, 28, 16, 6.3$ , and  $0.69 \text{ mA cm}^{-2}$ . The dark injection current density ( $J_d$ ) in case of EL is the same as in case of PL, *i.e.*  $J_d = -J_{sc}$ .

#### Temperature Dependent Spectral Shape

As expected from the thermal behavior of the occupation probability, PL and EL spectra broaden with increasing temperature. The photon energy peak position around room temperature is constant  $\hat{E}_\gamma \approx 1.13 \text{ eV}$  under different bias conditions. Below  $T = 270$  K, the  $\hat{E}_\gamma$  shows a blue shift under different bias conditions. This shift increases with decreasing temperature. Note the

shoulder at low photon energies, which seems to be constantly  $10^3$  times less intense than the main luminescence.

Different kinds of luminescence transitions are reported. Kirchartz *et al.* reported band-to-band transitions with peak energies  $\hat{E}_\gamma = 1.17$  eV around room temperature with a shift to donor-to-acceptor transitions at peak energies  $\hat{E}_\gamma = 1.08$  eV from selenium and copper vacancies at low temperatures below  $T = 180$  K [56]. According to Cheng *et al.*, the main transition around room temperature should originate from band-to-impurity transitions, *i.e.* transitions from band to the already mentioned vacancies at  $\hat{E}_\gamma = 1.10$  eV [112]. A clear shift from one transition to another with decreasing temperature cannot be observed in these measurements in this thesis. Band-to-band transitions cannot be neglected. In crystalline semiconductors these transitions are expected to be rather sharp. However, band-to-band transitions in  $\text{Cu}(\text{In,Ga})\text{Se}_2$  are expected to be broadened due to band gap fluctuations [23, 115, 116]. Furthermore, donor-to-acceptor transitions are broadened due to potential fluctuations [82, 113, 114, 194]. Therefore, the origin of the main luminescence in this thesis is unclear for now. However, it can be solved with well fitted simulations in the following, since each kind of transition shows distinctive PL and EL spectra, and external quantum efficiency. The radiative ideality factor from luminescence/voltage characteristics completes this analysis. It is found that the main luminescence originates from band-to-tail transitions.

Furthermore, the PL spectra in Figure 4.2 diverge from the EL spectra, although the charge carrier injection is the same, *i.e.*  $J_d = -J_{sc}$ . The PL intensity increases faster with the charge carrier injection than the EL. Both kinds of spectra converge in case of low injection. This convergence can be explained with the superposition of a common diode law with the photocurrent. With decreasing illumination, the conditions of a device under illumination converge to the conditions of a device in the dark. Since PL and EL are measured under electro-modulation, this convergence indicates the linear superposition of the EL with the PL as required by the *RR* (see Eq. (2.24)).

### Voltage Dependent Spectral Emission

A detailed view on the shift of the PL and EL photon peak energy ( $\hat{E}_\gamma$ ) in Figure 4.3 indicates the transitions from band to band-tail states. The  $\hat{E}_\gamma$  from PL spectra shows Figure 4.3(a), and from EL spectra Figure 4.3(b) in the same temperature range  $T = 330 - 100$  K. Since the forward bias voltage under EL conditions is strongly influenced by series resistance effects, and presumably by temperature dependent contact barriers, the  $V_{oc}$  under PL conditions is also allocated to the photon peak energy under EL conditions. This gives a better estimate for the quasi-Fermi level separation in the recombination region under EL conditions, since the PL and EL injection are the same, *i.e.*  $J_d = -J_{sc}$ . The Figures 4.3(a) and (b) show  $\hat{E}_\gamma$  of the device as fabricated (closed symbols), and of the treated device (open symbols), which is determined from the spectra shown in Figure 4.2.

The  $\hat{E}_\gamma$  decreases with decreasing temperature. Whereas the  $\hat{E}_\gamma$  around room temperature and above does not shift under different injection current conditions, below room temperature, the  $\hat{E}_\gamma$  starts to shift slightly. This shift increases with decreasing temperature down to lowest temperature, where at  $T = 100$  K the  $V_{oc} = 918 - 949$  mV from the treated device (accelerated light soaked) almost saturates. The accelerated light soaking affects the  $V_{oc}$  and  $\hat{E}_\gamma$  remarkably



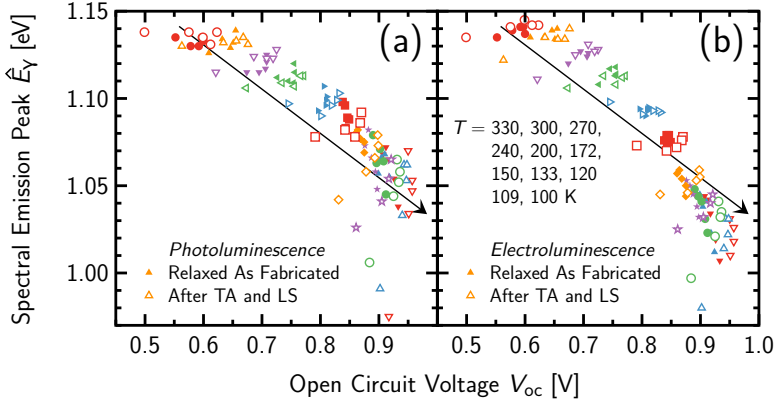


**Figure 4.3:** Temperature dependent spectral emission peak energy ( $\hat{E}_\gamma$ ) as a function of open circuit voltage ( $V_{oc}$ ) derived from measured electro- (EL) and photoluminescence (PL) spectra, respectively, of Cu(In,Ga)Se<sub>2</sub> *np* heterojunction device shown in Figure 4.2. Temperatures are  $T = 330, 300, 270, 240, 200, 172, 150, 133, 120, 109$ , and  $100$  K (arrows). The photon flux is varied in the range  $\phi = 2.7 \times 10^{21}, 2.2 \times 10^{21}, 1.1 \times 10^{21}$ , and  $4.6 \times 10^{20} \text{ m}^{-2} \text{ s}^{-1}$  for the device as fabricated, and  $\phi = 2.7 \times 10^{21}, 2.3 \times 10^{21}, 1.3 \times 10^{21}, 5.2 \times 10^{20}$ , and  $5.7 \times 10^{19} \text{ m}^{-2} \text{ s}^{-1}$  after accelerated light soaking at  $T = 400$  K. The PL is excited at the wavelengths  $\lambda = 473, 532$ , and  $671$  nm simultaneously. The  $V_{oc}$  at PL conditions is also allocated to the EL with corresponding injection current densities. The values derived from PL and EL before the accelerated light soaking are plotted as closed symbols, and after light soaking are plotted as open symbols. (a) Emission peak energy ( $\hat{E}_\gamma$ ) from PL. (b) Emission peak energy ( $\hat{E}_\gamma$ ) from EL.

at low temperatures. The device as fabricated shows a distinctive bending, *i.e.* a decreasing  $V_{oc}$  with increasing  $\hat{E}_\gamma$  compared to the treated (accelerated light soaked) device. However, the difference between  $\hat{E}_\gamma$  under PL and EL conditions increases with decreasing temperature. At lowest temperature  $T = 100$  K the difference in peak energy is  $\Delta \hat{E}_\gamma \approx 40 \text{ meV}$ . The  $\hat{E}_\gamma/V_{oc}$  characteristics in Figure 4.3 does not indicate a shift from band related to donor-to-acceptor transitions as it is definitely observable from Ref. [56]. And luminescence from pure band-to-band transitions can be also neglected, since these transitions do not change under different bias conditions. In case of band-to-band transitions, the quasi-Fermi levels are far from the band states and the Fermi-Dirac occupation probability becomes a simple exponential function, *i.e.* the shape of the occupied densities of band states does not change. However, here in case of band-to-tail transitions, the quasi-Fermi levels are close to the band-tail densities of states, *i.e.* the shape of the occupied densities of band-tail states changes and the distance between the maximum occupied density of band-tail states and the band edges increases, which therefore shifts the  $\hat{E}_\gamma$  under different bias conditions, predominantly at low temperatures. Band gap fluctuations, which are known from Cu(In,Ga)Se<sub>2</sub> [23, 115, 116], explain the broadening of the observed spectra.

A detailed view to the change of the spectral shape of PL (red dashed lines) and EL (black solid lines) under different bias conditions is given in Figure 4.4. As long as the PL, which

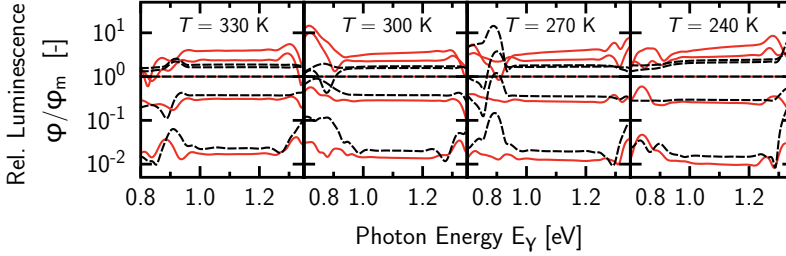


**Figure 4.4:** Measured spectra ( $\varphi$ ) from electro- and photoluminescence of Cu(In,Ga)Se<sub>2</sub> np heterojunction device as shown in Figure 4.2 related to the medium signal ( $\varphi_m$ ) each.

originates from an electro-modulated device under different bias voltage conditions, *i.e.* different  $V_{oc}$  originate from different excitation photon fluxes, the  $RR$  also applies to this PL. To evaluate whether the spectral shape changes, the Figure 4.4 shows the luminescence spectra divided by the mean luminescence spectrum ( $\varphi/\varphi_m$ ) at moderate temperatures  $T = 330 - 240$  K. Outside the photon energy range  $E_\gamma = 0.93 - 1.28$  eV the spectra are fairly noisy, which leads to artifacts in Figure 4.4.

Unchanged spectra under different bias conditions are given at temperature  $T = 330$  K. Whilst the spectra of EL at lower temperatures seem to be unchanged in shape, the spectra of PL show a clear blue shift with increasing injection. Whereas most of the EL originates from charge carrier recombination in the space charge region between the CdS buffer layer and the Cu(In,Ga)Se<sub>2</sub> absorber layer, the PL can, in addition, originate from the CdS buffer layer. The CdS buffer layer is a wide band gap  $E_\mu \approx 2.40$  eV material [195], and the PL is also excited with photon energies higher than this band gap. The increased quasi-Fermi level separation at lower temperatures may yield an extra contribution to the PL, which originates from the CdS buffer layer. It is not completely clear. However, the recombination region under PL conditions is different under EL conditions. And this difference increases with decreasing temperature, since the EL is strongly influenced by temperature dependent charge carrier transport phenomena.

Interestingly, at  $T = 240$  K, where the low energy shoulder in EL spectra is present, it can be seen that also this shoulder follows the  $RR$  in terms of the shape of the spectrum.

### 4.1.3 Reciprocity Relation

The main aspect of the  $RR$  between the EL spectrum ( $\varphi_{EL}(E_\gamma)$ ) and the external quantum efficiency ( $Q_e(E_\gamma)$ ) (see Eq. (2.24)), which are required to be compatible to each other, is plotted in Figure 4.5. In Figure 4.5(a) the measured EL spectra are compared to the EL spectra calculated from the measured external quantum efficiency ( $\varphi'_{EL} \propto Q_e \times \varphi_{bb}$ ), and vice versa ( $Q'_e \propto \varphi_{EL}/\varphi_{bb}$ ) in Figure 4.5(b), where  $\varphi_{bb}$  is the hemispheric black body radiation. The supporting temperatures are limited to  $T = 300, 240, 200$ , and  $150$  K for the reasons of clarity. Generally, the  $RR$  decreases with decreasing temperatures. Since the exponentially decaying slopes of the EL spectra in the high energy range beyond the peak are determined by temperature, the  $\varphi'_{EL}$  fits well to the  $\varphi_{EL}$ . However, the  $\varphi_{EL}$  deviates from  $\varphi'_{EL}$  for highest photon

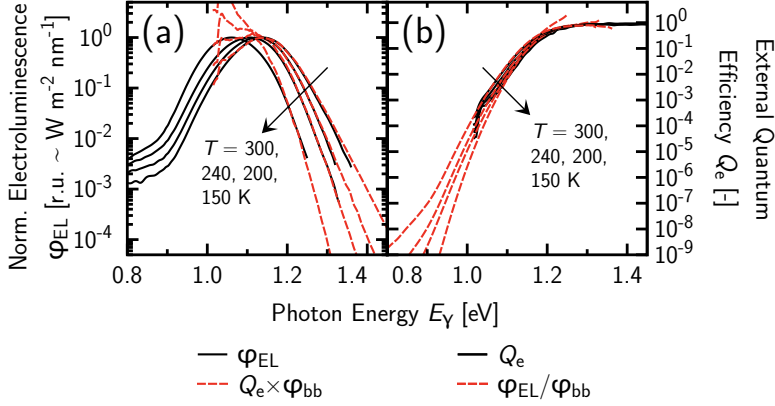


**Figure 4.5:** Measured electroluminescence spectra ( $\varphi_{\text{EL}}$ ) with injection current density  $J_d = 33 \text{ mA cm}^{-2}$  compared to external quantum efficiency ( $Q_e$ ) of Cu(In,Ga)Se<sub>2</sub> *np* heterojunction device. Temperature varies in the range  $T = 300, 240, 200$ , and  $150 \text{ K}$  (arrows). (a) Normalized  $\varphi_{\text{EL}}$  is plotted as black solid lines, and  $\varphi'_{\text{EL}} \propto Q_e \times \varphi_{\text{bb}}$ , where  $\varphi_{\text{bb}}$  is the hemispheric black-body radiation is plotted as red dashed lines. (b) The  $Q_e$  is plotted as black solid lines, and  $Q'_e \propto \varphi_{\text{EL}} / \varphi_{\text{bb}}$  is plotted as red dashed lines.

energies at  $T = 300 \text{ K}$ . Due to the slight blue shift in the PL spectra (see Figure 4.4), it is observed that the PL fits better to the  $\varphi'_{\text{EL}}$  than the EL at highest injection current.

In the low energy range the agreement between  $\varphi_{\text{EL}}$  and  $\varphi'_{\text{EL}}$  is reduced with decreasing temperature (see Figure 4.5(a)). Only at room temperature, the peak in  $\varphi_{\text{EL}}$  can be reproduced with  $\varphi'_{\text{EL}}$ . This means that below room temperature an additional contribution to  $Q_e$  can be observed in comparison to  $\varphi_{\text{EL}}$ , since the  $\varphi'_{\text{EL}}$  below the peak is more intense than  $\varphi_{\text{EL}}$ . There are two possible reasons for this. One reason could be the divergence between the charge carrier recombination and the absorption region, *i.e.* the recombination region gets narrower and/or shifts to the interface between the CdS buffer and the Cu(In,Ga)Se<sub>2</sub> absorber layer with decreasing temperatures. The other more plausible reason arises from the characteristic energy of the band-tail densities of states. The blurring of the density of occupied band-tail states increases with increasing temperature, *i.e.* at high temperatures, the exponential decay of the band-tail densities of states (the characteristic energy) is negligible compared to the exponential decay of the occupation probability function (Fermi-Dirac). In contrast, low temperatures mean a higher occupation of the band-tail states due to a higher quasi-Fermi level separation, *i.e.* the shape of the density of band-tail states gets more distinctive in comparison to the temperature dependent occupation probability function. In conclusion, the  $\varphi_{\text{EL}}$  and  $Q_e$  are compatible in terms of the *RR* if either the slopes of the band-tail densities of states are rather steep or the quasi-Fermi level separation is small.

Note that the measurements at lowest photon energies  $E_\gamma \approx 1.03 \text{ eV}$ , which show a small bump, are not reliable due to a change of the edge filters in the used measurement setup (RG780, see

Figure 3.5 in Section 3.1.3).

#### 4.1.4 Radiative Ideality Factor

The *RR* postulates a common diode law behavior of the luminescence/voltage characteristics with the *radiative* ideality factor  $n_r = 1$ . A constant  $n_r = 1$  originates from band-to-band transitions. The luminescence can be approximated with Eq. (2.25) as

$$\phi \propto \exp\left(\frac{qV}{2kT}\right) \exp\left(\frac{qV}{2kT}\right) \quad (4.1)$$

if the quasi-Fermi level separation  $\Delta E_f = V$  in the recombination region. From the denominators of the exponential functions then, directly follows

$$n_r = 1. \quad (4.2)$$

However, this requirement for the radiative ideality factor was never verified within measurements before. For this reason, the integrated luminescence  $\phi = \int \varphi(E_\gamma) dE_\gamma$  is measured. To determine the  $n_r$ , the temperature and the  $\Delta E_f$  in the recombination region, where the luminescence originates, has to be known. The temperature is set with a steady state tempered continuous nitrogen gas flow round the device in the cryostat, *i.e.* the temperature is well defined. However, the quasi-Fermi level separation in the recombination region, where the luminescence originates, is derived from the contacts of the device, *i.e.* this quasi-Fermi level separation is influenced by these contacts. Since in case of EL, the contact voltage is strongly influenced due to transport phenomena, the luminescence measurements to determine  $n_r$  are conducted under PL conditions. This means that the voltage allocated to  $n_r$  is the  $V_{oc}$ , which yields PL spectra  $\varphi(E_\gamma) = \varphi_{PL}(E_\gamma)$ .

Another critical point is the number of measurement sampling points to precisely determine  $n_r$ . There are two methods to measure integrated PL. First, the PL can be measured spectrally resolved, and the integration over the spectrum can be done numerically afterwards. Second, the PL can be directly measured without spectral resolution. This yields two benefits, namely faster and more sensitive measurements, down to injection current densities  $J < 0.3 \text{ mA cm}^{-2}$ . The determination of relative quantities like  $n_r$  are without difficulty, as long as the spectral shape of the PL does not change under different bias conditions (see Figure 4.4) and/or the measurement detector is equally sensitive in the whole relevant spectral range (see Figure 3.4). However, both conditions are not fulfilled.

Note that the EL, which is allocated to  $V_{oc}$  under PL conditions yields similar results for  $n_r$ , as long as the shift in PL spectra is small compared to the change of  $V_{oc}$ .

The Figure 4.6(a) shows integrated PL ( $\phi_{PL}(V_{oc})$ ) versus  $V_{oc}$ , and Figure 4.6(b) shows  $\phi(J)$  versus the injection current density, either  $J_d$  in case of EL or  $J_{sc}$  in case of PL, where again  $J = J_d = -J_{sc}$ . Figure 4.6(a) differentiates between the measurements from the device as fabricated and the treated device. Figure 4.6(b) only shows the results from the treated device after the accelerated light soaking. To check if the the integrally measured PL and EL fits the numerically integrated PL and EL spectra (see Figure 4.2), these numerically integrated PL and

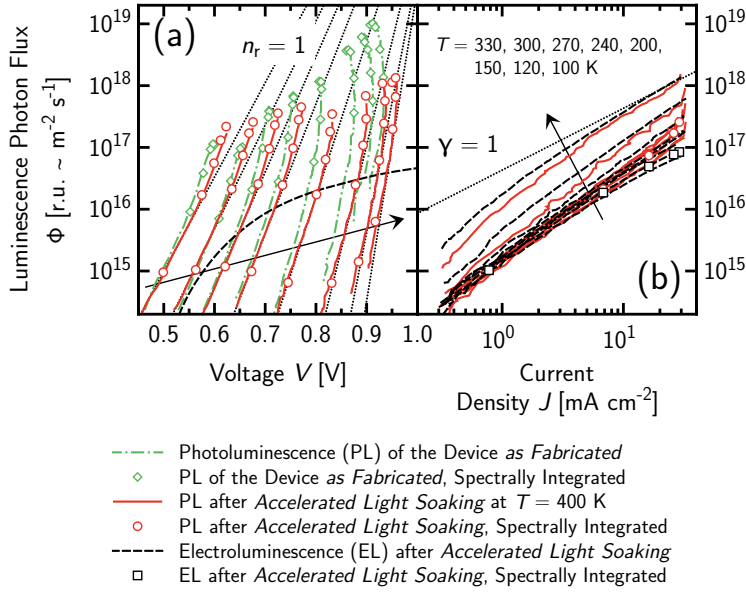


**Figure 4.6:** Integrally measured photo- (PL) and electroluminescence (EL) of Cu(In,Ga)Se<sub>2</sub> *np* heterojunction device at temperatures  $T = 330, 300, 270, 240, 200, 150, 120$ , and  $100$  K (arrows). The PL of the device as fabricated is plotted as green dot-dashed lines. Corresponding integrated signals from PL spectra are plotted as green open rhombi. The EL of the accelerated light soaked device is plotted as black dashed lines, and the PL is represented as red solid lines. Integrated signals from EL spectra are shown as black open squares, and from PL as red open circles. The PL is excited at the wavelengths  $\lambda = 473, 532$ , and  $671$  nm simultaneously to achieve highest accessible photon flux. (a) The PL as a function of the open circuit voltage. The PL/voltage characteristics, which follow a common diode law with the ideality factor  $n_r = 1$  are plotted as black dotted lines for different temperatures. (b) The PL and EL as a function of injection current density  $J = J_d = -J_{sc}$ , where  $J_d$  is the dark injection current density under EL conditions, and  $J_{sc}$  the short circuit current density under illumination, *i.e.* PL conditions. The luminescence, which scales linearly with  $J$  is plotted as black dotted line.

EL spectra are additionally plotted as points. The  $\phi_{\text{PL}}$  before the accelerated light soaking is plotted as green open rhombi, and afterwards as red open circles. The corresponding  $\phi_{\text{EL}}$  is plotted as black open squares. Black dotted lines are plotted as a guide for the eye. In Figure 4.6(a) this black dotted line marks a diode with  $n_{\text{r}} = 1$  each, and in Figure 4.6(b) this marks a linear behavior between  $J$  and  $\phi$ .

Generally Figure 4.6(a) shows that the integrally measured PL fits the numerically integrated PL very well. This guarantees only little influence through spectral shifts in the integrally measured PL. The PL intensity of the device as fabricated increases faster with decreasing temperature as the device after treatment. It can be seen that the accelerated light soaking helps to reduce the upward bending of the  $\phi_{\text{PL}}/V_{\text{oc}}$  characteristics, where a strong deviation from  $n_{\text{r}} \approx 1$  can be observed. In connection to this, the  $\phi_{\text{PL}}/V_{\text{oc}}$  characteristics of the accelerated light soaked device fit very well to a diode law with  $n_{\text{r}} = 1$  in the temperature range  $T = 300 - 200$  K, whereas the device as fabricated shows steeper  $\phi_{\text{PL}}/V_{\text{oc}}$  characteristics, which correspond to  $n_{\text{r}} < 1$ . Below  $T = 200$  K both kinds of  $\phi_{\text{PL}}/V_{\text{oc}}$  characteristics tend to show  $n_{\text{r}} > 1$ . However, these characteristics show also a more distinctive upward bending.

If the quasi-Fermi level separation in the recombination region directly corresponds to the contact voltage  $V_{\text{oc}}$ , this could yield a  $V_{\text{oc}}/\phi_{\text{PL}}$  characteristic with  $n_{\text{r}} = 1$ . However, the quasi Fermi-level separation in the recombination region is higher than the  $V_{\text{oc}}$  at the contacts. The  $V_{\text{oc}}$  is affected by parasitic recombination, which originates from defect states at the CdS/Cu(In,Ga)Se<sub>2</sub> interface, which are (partly) thermally annealed and saturated with light soaking [185, 186]. Therefore, the  $V_{\text{oc}}/\phi_{\text{PL}}$  characteristics from the device after the accelerated light soaking fit better to  $n_{\text{r}} = 1$  and show less upward bending than the device as fabricated.

As long as  $n_{\text{r}}$  from EL is of interest, actually, Figure 4.6(b) helps to compare PL and EL. This comparison, in addition, also indicates the linear superposition of the PL and EL, since both kinds of luminescence are measured under electro-modulation. The PL is plotted as red solid lines, and EL as black dashed lines. At temperatures above  $T = 150$  K both PL and EL yield approximately the same intensities, which increase only a little with decreasing temperature. At injection current densities higher than  $J \approx 8 \text{ mA cm}^{-2}$ , the PL yields higher intensities than the EL, whereas the slope of the  $\phi_{\text{EL}}/J_{\text{d}}$  characteristics decreases with increasing  $J_{\text{d}}$ . Below  $T = 150$  K the PL and EL increase abruptly. The luminescence intensities at  $T = 100$  K are almost 10 times higher than at  $T = 150$  K.

The Figure 4.7 summarizes the  $\phi_{\text{PL}}/V_{\text{oc}}$ ,  $\phi_{\text{PL}}/J_{\text{sc}}$ , and  $\phi_{\text{EL}}/J_{\text{d}}$  results from Figure 4.6. The shown values are derived in the injection range  $J = 0.5 - 7 \text{ mA cm}^{-2}$ . As already discussed, the Figure 4.7(a) shows increasing  $n_{\text{r}}$  with decreasing temperature plotted as red circles connected to solid lines. The  $n_{\text{r}}$  determined from the device as fabricated (open circles) yields a lower  $n_{\text{r}}$  in the whole temperature range than the  $n_{\text{r}}$  from the device after the accelerated light soaking (closed circles). Obviously, no constant  $n_{\text{r}} = 1$  can be observed from any of both devices. However, in the temperature range  $T = 330 - 240$  K, the  $n_{\text{r}} \approx 0.93 - 0.98$  from the accelerated light soaked device is almost constant. And the device as fabricated shows also an almost constant  $n_{\text{r}} \approx 0.88 - 0.89$  in the same temperature range, however, this  $n_{\text{r}}$  strongly deviates from  $n_{\text{r}} = 1$ . Below  $T = 172$  K the  $n_{\text{r}}$  increases in both cases. Note that the upward bending in the  $\phi_{\text{PL}}/V_{\text{oc}}$  characteristics predominantly at low temperatures yields high fitting errors for  $n_{\text{r}}$ .

The fitting of an exponential behavior  $\phi = \phi_0 J^\gamma$  to the  $\phi_{\text{PL}}/J_{\text{sc}}$  and  $\phi_{\text{EL}}/J_{\text{d}}$  characteristics

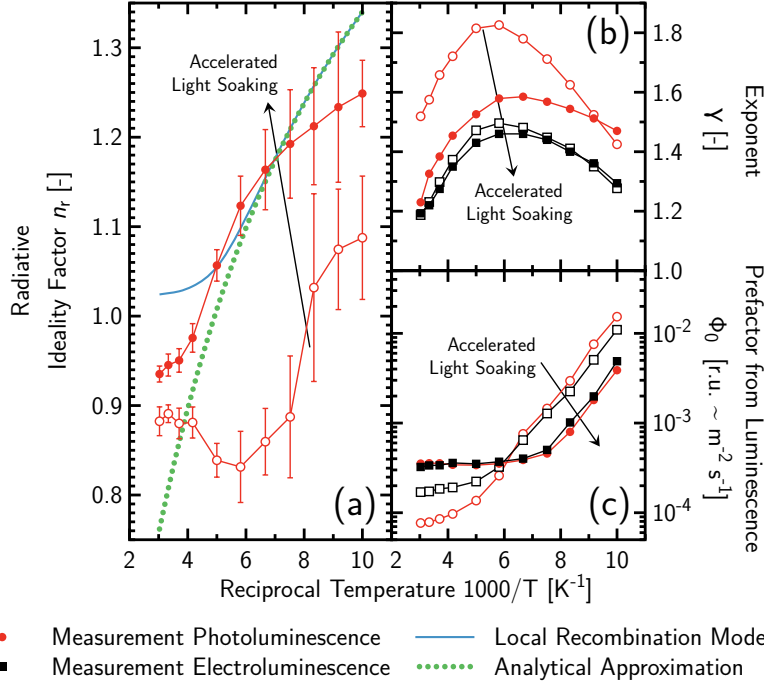


**Figure 4.7:** Temperature dependent evaluation of integrally measured photo- (PL) and electroluminescence (EL) of Cu(In,Ga)Se<sub>2</sub> *np* heterojunction device as shown in Figure 4.6. Temperatures are  $T = 330, 300, 270, 240, 200, 172, 150, 133, 120$ , and  $100$  K. The values derived from PL are plotted as red circles (open and closed) connected with lines. The values derived from EL are plotted as black squares. All values from the luminescence from the device as fabricated are plotted as open symbols. The values after accelerated light soaking are plotted as closed symbols. The values are derived in the injection current density range  $J = 0.5 - 7 \text{ mA cm}^{-2}$ . (a) The radiative ideality factor ( $n_r$ ) derived from Figure 4.6(a) by fitting a common diode law to the PL/voltage characteristics. Due to the upward bending in the PL/voltage characteristics at high injection, the error in the determination of  $n_r$  increases with decreasing temperature. Additionally, the solid blue line shows the  $n_r$  determined with the *local recombination model*, and the green dotted line shows the  $n_r$  determined with Eq. (4.4) and the characteristic energy of the band-tail densities of states  $E_0 = 17.5 \text{ meV}$ . (b)+(c) The fitting of an exponential behavior  $\phi = \phi_0 J^\gamma$  to the PL and EL/current characteristics in Figure 4.6(b) yields the exponent  $\gamma$  and the prefactor  $\phi_0$  as a function of the temperature.

from Figure 4.6(b) yields the exponent ( $\gamma$ ) in Figure 4.7(b) and the prefactor ( $\phi_0$ ) in Figure 4.7(c). The PL and EL generally behave super-linearly ( $\gamma > 1$ ). From above room temperature to around  $T = 172$  K the super-linear behavior increases, and then decreases below  $T = 172$  K. Whereas the PL from the device as fabricated (red open circles) increases faster with increasing injection current than the corresponding EL (black open squares), the  $\gamma$  of the PL (red closed circles) and EL (black closed squares) from the treated device are quite close. And moreover, whereas the accelerated light soaking leads the PL to a reduced  $\gamma$ , the EL is nearly not influenced by this treatment. The presence of a maximum in  $\gamma$  may indicate two competitive luminescence processes. Kirchartz *et al.* reported a shift from band-to-band to donor-to-acceptor transitions at  $T = 180$  K [56]. For this reason, the maximum in  $\gamma$  could indicate the reported increasing donor-to-acceptor transition with decreasing temperature, while this transition to donor-to-acceptor luminescence cannot be observed from the measured spectra in Figure 4.2.

The Figure 4.7(c) shows the effect from the accelerated light soaking to the PL and EL intensity. Whereas the PL and EL intensity from the device as fabricated increases around two orders of magnitude within the temperature range  $T = 330 - 100$  K, the observed increase from the treated device is around one order of magnitude. This device shows almost constant PL and EL intensities above  $T = 150$  K as mentioned before (see Figure 4.6). The device as fabricated, in contrast, shows a reasonable increase of the PL and EL intensities, already below room temperature. Below  $T = 172$  K the PL and EL intensities from this device are higher than from the treated device. And again this treatment let the PL and EL behave similar to each other.

In summary, the temperature dependent radiative ideality factor ( $n_r$ ),  $\gamma$ , and  $\phi_0$  point out the already discussed influence of the defects at the CdS/Cu(In,Ga)Se<sub>2</sub> interface. And additionally, the  $\gamma$  tends to point out the shift from band-to-tail to donor-to-acceptor transitions for PL and EL, although the measured spectra (see Figure 4.2) do not clearly show such a shift in shape. For the determination of  $n_r$  from PL, the accelerated light soaking of the device makes the PL comparable to the EL at least above  $T \approx 172$  K. Therefore, the determined  $n_r$  can be also allocated to the EL. And the PL linearly superimposes the EL, predominantly at low injection and higher temperatures, *i.e.* under small quasi-Fermi level separation. However, around room temperature, where most of the requirements for the *RR* hold, the measured  $n_r$  is a bit smaller than expected from the *RR* ( $n_r = 1$ ). A  $n_r < 1$  may yield from parasitic recombination, which decreases the  $V_{oc}$  at the contacts compared to the quasi-Fermi level separation in the recombination region.

## 4.2 Discussion

This section discusses the results from the shown measurements in summary. The comparison between measurements and the *local recombination model* clearly indicates the dominant luminescence from band-to-tail transitions. And furthermore, from the fitted simulations an outlook is given to the luminescence and external quantum efficiency in hydrogenated microcrystalline silicon ( $\mu\text{c-Si:H}$ ) *pin* devices.

### 4.2.1 Modeling of Luminescence Spectra and External Quantum Efficiency

The measurements after the accelerated light soaking show good results to hold up with the *RR*. However, measurements do not clearly show, which transition yields the here observed lumin-



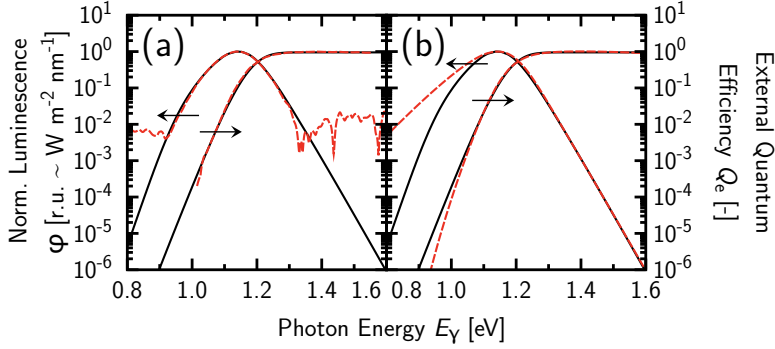


**Figure 4.8:** (a) Comparison between simulated (black solid lines) and measured (red dashed lines) luminescence ( $\phi$ ), and external quantum efficiency ( $Q_e$ ) at room temperature and open circuit voltage  $V_{oc} = 676$  mV under PL conditions of Cu(In,Ga)Se<sub>2</sub> *np* heterojunction device. (b) Test of *reciprocity relation* between  $\phi$  and  $Q_e$  (black solid lines) via hemispheric black-body radiation  $\phi_{bb}$ , *i.e.*  $\phi' \propto Q_e \times \phi_{bb}$  and  $Q'_e \propto \phi/\phi_{bb}$ , from numerical simulations of Cu(In,Ga)Se<sub>2</sub> *np* heterojunction device. For experimental conditions, see earlier in Figure 4.2.

escence. As already mentioned, band-to-band and donor-to-accept transitions [56], or band-to-impurity transitions, *i.e.* transitions from the band to the donor and/or acceptor states [112] are mostly cited. However, these transitions can be neglected by modeling the luminescence and the external quantum efficiency with the *local recombination model*.

Due to composition variations across the cell in stoichiometric compound semiconductors like Cu(In,Ga)Se<sub>2</sub>, band gap fluctuations arise [23, 115, 116]. The band gap is assumed to be blurred gaussian-like with a distribution width  $\sigma_{E_\mu}$ . This disorder at grain boundaries, in addition, causes band-tail states, beside other localized inter band states [54, 55, 196, 197]. According to Siebentritt *et al.* [82], band-to-tail transitions are used for the *local recombination model*, and additionally band gap fluctuations are assumed to fit the spectral broadening [23, 115, 116]. The well fitted results are shown in Figure 4.8(a). It is observed that the exponentially decaying high photon energy edge of the experimentally measured  $\phi_{PL}$  compared to  $\phi_{EL}$  fits slightly better to the  $\phi'_{EL} \propto Q_e \times \phi_{bb}$  at the given device temperature. Therefore, the device parameters are fitted with the measured (red dashed line)  $\phi_{PL}$  at  $V_{oc} = 676$  mV and room temperature. Additionally to this, the parameters are consistently fitted to the measured  $Q_e$ . Whereas the modeled (black solid line)  $Q_e$  fits the measurements very well, some discrepancies can be observed from the  $\phi_{PL}$ , predominantly in the low photon energy range. For the band gap fluctuations, which broaden  $\phi_{PL}$ , the quasi-Fermi level separation is assumed to be constant, *i.e.* the charge carrier densities are highest in regions, where the band gap is small. Note that this assumption implies diffusion lengths  $L_D = \sqrt{kT/q\mu\tau}$ , which are derived from the charge carrier mobilities ( $\mu$ ) and the life time ( $\tau$ ), to be larger than the distance between adjacent areas across the device with unequal band gaps.

The external quantum efficiency ( $Q_e$ ) and the luminescence spectrum ( $\varphi_{PL}$ ) in Figure 4.8 is each fitted with a gaussian distributed band gap with a mean value of  $E_\mu = 1.18$  eV and a width of  $\sigma_{E_\mu} = 38$  meV. The width can be mainly estimated from the width of the measured  $\varphi_{PL}$ . The effective density of states at the band edges are assumed to be symmetric and 15 times higher than band-tail densities of states:  $N_c/N_{c0} = N_v/N_{v0} = 15$  (compare Figure 2.3 and Eqs. (2.4) and (2.9)). The characteristic energy of the band-tail density of states  $E_0 = 17.5$  meV can be well fitted with the low energy slope in  $Q_e$  and also with the width of  $\varphi_{PL}$ . For the sake of completeness, the capture cross-sections of charged band-tail states are assumed to be 10 times higher than of neutral band-tail states:  $\sigma_p/\sigma_n = 10$ . However, as long as the band-tail states are rather steep, this ratio influences the spectral shape only little.

As long as the  $RR$  holds for the measurements (see Figure 4.5), this should also work for the simulations in the same way. The transition from  $\varphi$  (black solid lines) to  $Q'_e \propto \varphi/\varphi_{bb}$  (red dashed line) shows Figure 4.8(b) as well as the transition in the opposite direction, *i.e.* from  $Q_e$  (black solid line) to  $\varphi' \propto Q_e \times \varphi_{bb}$  (red dashed line). Whereas this transition fits well above the photon peak energy of  $\varphi$ , in the low photon energy range a deviation between  $\varphi$  and  $Q'_e$ , and  $Q_e$  and  $\varphi'$ , respectively, occurs. This deviation arises from the localized band-tail densities of states in the band gap at a rather high quasi-Fermi level separation. Although the corresponding measurements in the low photon energy region are affected by artifacts of the experimental setup (see Figure 4.5), the simulations show qualitatively the same deviation. Note that this comparison between the measurements and the simulations also indicates that the already mentioned bump around  $E_\gamma \approx 1.03$  eV in the measurements (see Figure 4.5) can be neglected.

#### 4.2.2 Radiative Ideality Factor and Shift of Luminescence

From the fitted luminescence spectra, either PL or EL, since transport is not considered in the *local recombination model*, the radiative ideality factor ( $n_r$ ) is determined in Figure 4.7(a), which is plotted as blue solid line. This  $n_r$  from simulations does not fit the measurements quantitatively, which cannot be expected as long as charge carrier transport is neglected in the simulations. Charge carrier transport can influence the  $n_r$  pretty much, since this value is derived from the contact voltage of the device. However, measurements and simulations are nearly similar in terms of shape. Both curves increase monotonically to low temperatures. In the temperature range  $T = 330 - 240$  K the  $n_r$  from both curves is almost constant in comparison to the increase at  $T = 200 - 100$  K. Both curves, predominantly the measurements show a concave shape in this temperature range. This concave shape can be understood with symmetric quasi-Fermi level separation and density of states. The integrated luminescence then, can be approximated with the Eq. (2.26) as

$$\phi \propto \exp\left(\frac{qV}{2E_0}\right) \exp\left(\frac{qV}{2kT}\right). \quad (4.3)$$

From the denominators of the exponential functions follows

$$n_r = \frac{2E_0}{kT + E_0}. \quad (4.4)$$

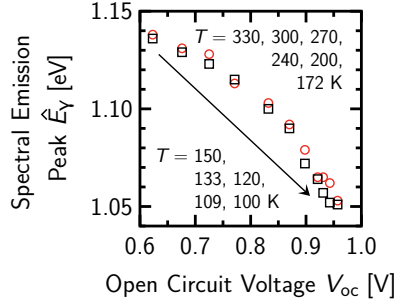


**Figure 4.9:** Comparison between the simulated (black open squares) and the measured (red open circles) temperature dependent (see arrow) spectral emission peak energy ( $\hat{E}_\gamma$ ) as a function of the open circuit voltage ( $V_{oc}$ ) derived from the photoluminescence spectra of the treated Cu(In,Ga)Se<sub>2</sub> *np* heterojunction device. For the experimental conditions, see earlier in Figure 4.2.

This function is plotted as green dotted line in Figure 4.7(a) with the  $E_0 = 17.5$  meV, which is fitted in Figure 4.8. As long as spectra around room temperature are significantly broadened, it is expected that this approximation for peak luminescence strongly holds at low temperatures, where spectra are reasonably sharp, *i.e.*  $kT < E_0$  [198]. However, within the approximation from Eq. (4.4) an  $E_0 = 19.5$  meV would fit better to the measurements in Figure 4.7(a) at  $T = 240 - 172$  K.

However, a higher  $E_0$  would shift the spectral peak position ( $\hat{E}_\gamma$ ) in Figure 4.8 to lower energies. The simulated  $\hat{E}_\gamma$  are compared to the measurements in Figure 4.9. As already shown (see Figure 4.3) the  $\hat{E}_\gamma$  shifts continuously to lower energies with decreasing temperature. As long as the simulated  $\hat{E}_\gamma$  fit very well to the measurements, this comparison also supports the assumption of luminescent band-to-tail transitions, even at low temperatures.

### 4.2.3 Reciprocity Relation

At this point, the influence of the characteristic energy of the band-tail densities of states ( $E_0$ ) to the *RR* between  $Q_e$  and  $\varphi$  can be investigated. The Figure 4.10 shows simulated  $\varphi$  and  $Q_e$  at temperature  $T = 300$  K and reasonable quasi-Fermi level separation  $\Delta E_f = 676$  mV, *i.e.* open circuit voltage under PL conditions with the parameters as fitted from Figure 4.8, which are plotted as black solid lines. The symmetric characteristic energies of the conduction and valence band-tail density of states are set to  $E_{c0} = E_{v0} = E_0 = 5, 15, 25.9$ , and 35 meV each. The  $\varphi' \propto Q_e \times \varphi_{bb}$  or  $Q'_e \propto \varphi / \varphi_{bb}$  are plotted as red dashed lines. The primarily simulated  $\varphi$  and the transformed  $\varphi'$ , or  $Q_e$  and  $Q'_e$ , respectively, continuously deviate from each other below  $\hat{E}_\gamma$  with increasing  $E_0$ . The  $E_0 = 25.9$  meV plays an important role, as long as this  $E_0 \approx kT$  is close to the thermal energy at  $T = 300$  K, which determines the charge carrier occupation probability function. In this case, the  $Q'_e$  in Figure 4.10 shows no distinctive maximum. Therefore, the  $Q_e$  and  $Q'_e$ , and the  $\varphi$  and  $\varphi'$  are compatible in terms of the *RR* if the  $E_0 < kT$ . Note that a high quasi-Fermi level separation in Figure 4.10 also yields discrepancies between  $\varphi$  and  $\varphi'$ , or

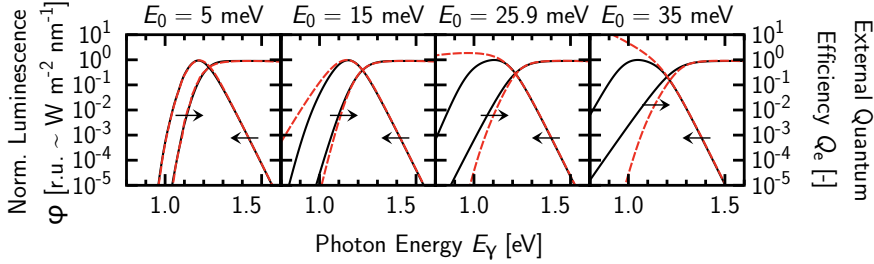


**Figure 4.10:** Influence of characteristic energy ( $E_0$ ) of localized band-tail states to *reciprocity relation* between the luminescence ( $\varphi$ ) and the external quantum efficiency ( $Q_e$ ) of a Cu(In,Ga)Se<sub>2</sub> np heterojunction device at temperature  $T = 300$  K and reasonable quasi-Fermi level separation  $\Delta E_f = 676$  mV. The  $E_0$  of the valence- and conduction band-tails are assumed to be equal:  $E_0 = E_{v0} = E_{c0}$ . The black solid lines show the results from the *local recombination model*. The red dashed lines show the correspondence in terms of the RR each, i.e.  $\varphi' \propto Q_e \times \varphi_{bb}$  and  $Q'_e \propto \varphi/\varphi_{bb}$ , where  $\varphi_{bb}$  is the hemispheric black body radiation.

$Q_e$  and  $Q'_e$  even with very steep band-tail slopes.

In case of tail-to-tail transitions, this boundary condition ( $E_0 < kT$ ) to hold the requirements of the RR has to be proven. Since the luminescence from hydrogenated microcrystalline ( $\mu$ c-Si:H) originates from tail-to-tail transitions, this can be tested with  $\mu$ c-Si:H *pin* devices. This is discussed in the following Chapter 5.



## Chapter 5

# Hydrogenated Microcrystalline Silicon Based *pin* Devices

This chapter shows measurements of hydrogenated microcrystalline silicon ( $\mu\text{c-Si:H}$ ) thin-film based *pin* devices (see Section 3.1.1) in Section 5.1, and discusses the results with the help of full one dimensional numerical device simulations (see Section 3.2) in Section 5.2.

Due to the requirements of the *reciprocity relation* (*RR*), this chapter is similarly structured as the previous Chapter 4. It begins with measurements of photo- (PL) and electroluminescence (EL) spectra in a wide temperature range with altered injection rates within one order of magnitude. In terms of the *RR* the change of the spectral shape of PL and EL under different injection conditions are derived from measurements (see Section 5.1.1). The main requirement to hold up with the *RR* is the comparison between the EL emission ( $\varphi_{\text{EL}}$ ) and the external quantum efficiency ( $Q_{\text{e}}$ ) in Section 5.1.2. The experimental results from the radiative ideality factor ( $n_{\text{r}}$ ), which is derived from luminescence/voltage characteristics by fitting a common diode law are presented in Section 5.1.3. The  $n_{\text{r}}$ , which is deduced from PL, indicates the characteristic energy of the band-tail density of states ( $E_0$ ). However, in terms of the *RR*, the PL and the EL should superimpose linearly. Therefore, and since the EL from  $\mu\text{c-Si:H}$  can be used as a fast material characterization tool for devices, which is already used for module imaging [31–42], or as inline characterization tool [43] of/for crystalline semiconductors, the reliability of EL/voltage characteristics to deduce the  $E_0$  is discussed in detail in Section 5.2.3.

In comparison to  $\text{Cu(In,Ga)Se}_2$ , which is discussed in Chapter 4,  $\mu\text{c-Si:H}$  is a material with considerably more localized states within the mobility gap. It is expected that the *RR* is less applicable to  $\mu\text{c-Si:H}$ , compared to  $\text{Cu(In,Ga)Se}_2$ .

An extensive analysis of the measurements is presented, featuring well fitted full one dimensional numerical device simulations using *ASA* in connection with *LUME* (see Section 3.2). Based on the model calibration in Section 5.2.1, the temperature and voltage dependent spectral shift is discussed in Section 5.2.2. In addition to that, predictions of luminescence/voltage characteristics of  $\mu\text{c-Si:H}$  *pin* devices with altered band-tail slopes and mid-gap defect states are made to elaborate the deduction of the characteristic energy of the band-tail density of states (see Section 5.2.3). The influence of band-tail slopes, mid-gap defect states, and quasi-Fermi level separation to the *RR* between the  $Q_{\text{e}}$  and  $\varphi_{\text{EL}}$  is additionally discussed in Section 5.2.4. These predictions focus on standard operation conditions of *solar cells*, namely room temperature and

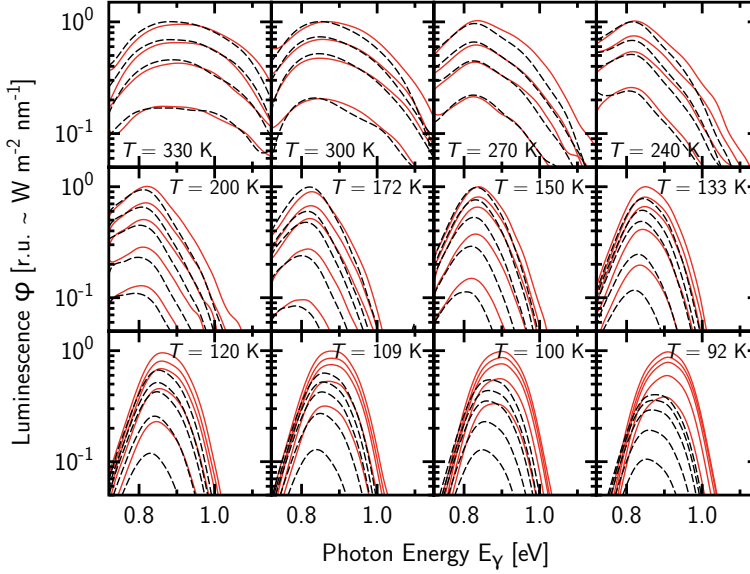


**Figure 5.1:** Measured spectra from photo- (PL) and electroluminescence (EL) of  $\mu\text{c-Si:H}$  *pin* device. The EL is plotted as black dashed lines, and the PL as red solid lines. All spectra are normalized to the highest signal at each temperature. Spectra are measured at the temperatures  $T = 330, 300, 270, 240, 200, 172, 150, 133, 120, 109, 100$ , and  $92$  K. The PL is excited with photon fluxes  $\phi = 2.1 \times 10^{22}, 1.5 \times 10^{22}, 1.2 \times 10^{22}, 6.3 \times 10^{21}$ , and for temperatures below  $240$  K, additionally  $2.5 \times 10^{21} \text{ m}^{-2} \text{ s}^{-1}$  at the wavelength  $\lambda = 532$  nm. This yields current densities  $J = 254, 184, 143$ , and  $74.5 \text{ mA cm}^{-2}$  at temperature  $T = 240$  K.

current injection rates, which correspond to the *AM1.5* sun spectrum. Former results from within this topic are previously published in [118].

## 5.1 Experimental Results

### 5.1.1 Temperature and Voltage Dependent Luminescence Spectra

The Figure 5.1 shows the measured PL and EL spectra. All spectra are normalized to the highest signal at each temperature. The temperature is varied in the range  $T = 330 - 92$  K. For PL, the excitation wavelength is  $\lambda = 532$  nm, with photon fluxes  $\phi = 2.1 \times 10^{22}, 1.5 \times 10^{22}, 1.2 \times 10^{22}, 6.3 \times 10^{21}$ , and for temperatures below  $240$  K, additionally  $2.5 \times 10^{21} \text{ m}^{-2} \text{ s}^{-1}$ . Lower excitation photon fluxes result in poor signal-to-noise ratio. And higher excitation photon fluxes change or even destroy the device.

Generally, the width of the spectra decreases with decreasing temperature. Around room temperature and above, an exponential decay of the spectra for higher photon energies cannot be

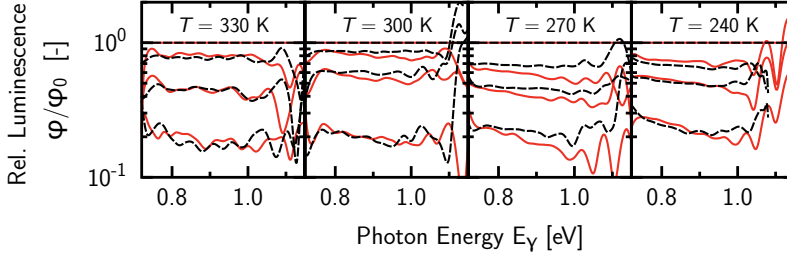


**Figure 5.2:** Measured spectra ( $\varphi$ ) from electro- (black dashed lines) and photoluminescence (red solid lines) of a  $\mu\text{c-Si:H}$  *pin* device as shown in Figure 5.1 related to the highest signal ( $\varphi_0$ ) each.

observed neither from PL nor from EL. However, below room temperature on both sides of the peak energy in the low and in the high photon energy range, PL and EL spectra show exponential behavior. The low energy slope results from a mixed density of valence and conduction band-tail states. The high energy slope should be determined from the band-tail states charge carrier occupation probability, and therefore from the device temperature.

At the temperatures  $T = 330$ , and  $300$  K the PL spectra coincide with the EL spectra within the measurement errors. Below room temperature the PL and EL start to diverge from each other. Whereas the PL and EL intensities in the low energy range are still at the same level, the EL intensities are reduced at medium and high photon energies, compared to the PL intensities. This effect increases with decreasing temperature. At lowest  $T = 92$  K the highest PL spectrum is 2.5 times more intense than the corresponding EL spectrum.

Since the photon peak energy ( $\hat{E}_\gamma$ ) is positively correlated with the injection current and the PL intensity dominates the EL (see Figure 5.2), the EL spectra are red shifted compared to the PL spectra. This general blue shift under different bias conditions is not compatible with the requirements of the *RR*. These bias conditions are either optical bias under PL conditions, which again yields the open circuit contact voltage, or electrical bias under EL conditions.

The Figure 5.2 shows the PL ( $\varphi_{\text{PL}}$ , red solid lines) and EL ( $\varphi_{\text{EL}}$ , black dashed lines) spectra from Figure 5.1 related to its most intense spectrum ( $\varphi_0$ ) each, *i.e.*  $\varphi_{\text{PL}}/\varphi_0$  and  $\varphi_{\text{EL}}/\varphi_0$  around room temperature  $T = 330 - 240$  K. The PL and EL show blue shifted spectra with increasing injection current under all circumstances. And the blue shift increases with decreasing temperature. Whereas only a slight blue shift can be observed from EL, the PL shows a distinctive blue shift. Below  $T = 270$  K the blue shift from EL spectra is almost the same as from PL.

A general blue shift can be understood with the density of band-tail states and the corresponding charge carrier occupation, which originates the PL and EL from tail-to-tail transitions [45, 58, 59]. In this case and with reasonable quasi-Fermi level separation, these quasi-Fermi levels lie within the distributions of the localized band-tail states. With a 0 K occupation function, the quasi-Fermi level separation is the same as  $\hat{E}_\gamma$ . This would definitely yield a blue shift in spectral shape. However, at finite temperatures this correlation is blurred and spectra are broadened. Therefore, this blue shift is less prominent the higher the temperature. However, as a matter of principle, unshifted spectra as can be observed from band-to-band transitions like



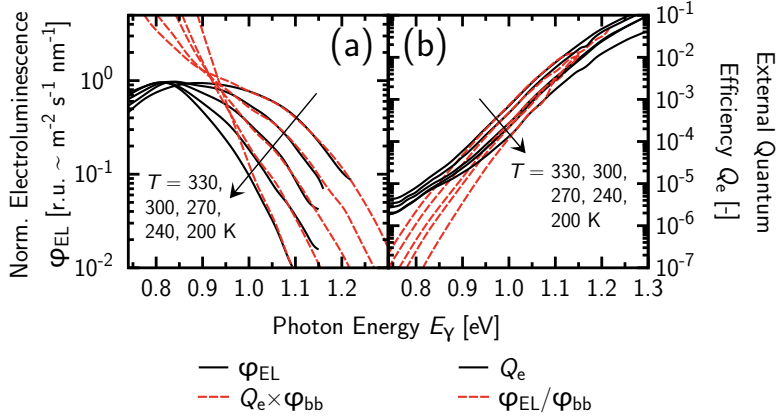


**Figure 5.3:** Measured electroluminescence (EL) spectra compared to external quantum efficiency ( $Q_e$ ) of  $\mu c$ -Si:H *pin* device. Temperature varies in the range  $T = 330, 300, 270, 240$ , and  $200$  K (arrows). (a) Normalized EL is plotted as black solid lines, and  $\phi'_{EL} \propto Q_e \times \phi_{bb}$ , which is scaled with hemispheric black-body radiation ( $\phi_{bb}$ ) is plotted as red dashed lines. (b) The  $Q_e$  is plotted as black solid lines, and the normalized EL ( $Q'_e \propto \phi_{EL}/\phi_{bb}$ ) is plotted as red dashed lines.

in *c*-Si or Cu(In,Ga)Se<sub>2</sub> [56] for instance, can be neglected for tail-to-tail transitions. However, unequal quasi-Fermi level separation over the depth of the recombination region yields extra blurring of the spectra, and therefore may reduce blue shifts.

### 5.1.2 Reciprocity Relation

The *RR* test between  $Q_e$  and  $\phi_{EL}$  for a  $\mu c$ -Si:H *pin* device shows Figure 5.3 for different temperatures  $T = 330 - 200$  K. The Figure 5.3(a) shows that the *RR* does not hold. For a decreasing temperature the mismatch between  $\phi_{EL}$  and  $\phi'_{EL} \propto Q_e/\phi_{bb}$  increases. Obviously, the  $\phi_{EL}$  in the low energy region energetically below the  $\hat{E}_\gamma$  of  $\phi_{EL}$  cannot be reproduced with the transformed  $\phi'_{EL}$ . However, in contrast, both curves match fairly well in the higher photon energy region above  $\hat{E}_\gamma$ , even at high temperatures, where the  $\phi_{EL}$  shows significant curvature instead of an exponential decay, which would indicate strictly temperature determined behavior.

The reason for this curvature of the  $\phi_{EL}$  in the higher photon energy region can be seen from Figure 5.3(b), where the  $Q_e$  and the transformed  $Q'_e \propto \phi_{EL}/\phi_{bb}$  are plotted. The  $Q_e$  at the highest measured photon energies is not fully saturated, which normally indicates full absorption within the charge carrier excitation from valence to conduction band. Therefore, the  $Q_e$  here, is determined by band-to-tail, tail-to-tail, and band-to-defect excitation from high to low photon energies (compare Figure 2.11). Whereas the  $\phi_{EL}$ , following *a*-Si:H, originates from tail-to-tail transitions [45, 58, 59], the primary measured  $Q_e$  and the transformed  $Q'_e$  deviate in the low energy range, where band-to-defect absorption is predominant.

From Cu(In,Ga)Se<sub>2</sub> *np* heterojunction devices in Chapter 4 the valid *RR* between the  $\phi_{EL}$  and the  $Q_e$  can be observed. This *RR* holds for band-to-tail transitions with the characteristic energy

of the band-tail densities of states  $E_0 < kT$ , where  $kT$  is the thermal energy. In case of tail-to-tail transitions in  $\mu\text{c-Si:H}$  the situation is different. The  $E_0 \approx 31 - 33 \text{ meV} > kT$  at room temperature, which is determined from time of flight measurements [167, 175], from transient photocurrent measurements [176], and with simulations of PL spectra [45, 59].

In summary, the prerequisite  $E_0 < kT$  for the  $RR$  between  $Q_e$  and  $\varphi_{\text{EL}}$  holds. This  $RR$  holds the better the higher the temperature, *i.e.* when  $kT$  is approximately equal or higher than  $E_0$ .

### 5.1.3 Radiative Ideality Factor

Up to this point, the requirements to hold up with the  $RR$  are only partly fulfilled. At highest temperature  $T = 330 \text{ K}$  the spectra are almost constant and the  $RR$  holds at high photon energies. However, they do not fit as well as the results from  $\text{Cu(In,Ga)Se}_2$   $np$  heterojunction devices. Since the transition, which yields the luminescence in  $\mu\text{c-Si:H}$ , is slightly different to the transition in  $\text{Cu(In,Ga)Se}_2$ , a different behavior from the luminescence/voltage characteristics is expected as well. The radiative ideality factor ( $n_r$ ) of  $\mu\text{c-Si:H}$ , which is determined from the luminescence/voltage characteristics by fitting a common diode law to the PL or EL intensity is strongly influenced by the broad band-tail state distribution. As long as the contact voltage under EL conditions is influenced by the contact series resistance and the charge carrier mobilities, PL conditions are necessary to deduce  $n_r$ . As at the open circuit voltage ( $V_{\text{oc}}$ ), all charge carriers recombine within the device and no net current flows, the potential at the contacts is not influenced by series resistance and therefore approximately equal to the quasi-Fermi level separation ( $\Delta E_f$ ) in the recombination region, where the main part of the luminescence originates from.

The Figure 5.4(a) shows the PL/voltage characteristics in the temperature range  $T = 330 - 86 \text{ K}$ . The integrally measured PL ( $\phi_{\text{PL}}$ ) is plotted as red solid lines, and the measured and integrated PL spectra ( $\phi'_{\text{PL}} = \int \varphi_{\text{PL}} [\text{W m}^{-2} \text{ nm}^{-1}] E_{\gamma}^{-1} d\lambda \propto \int \varphi_{\text{PL}} E_{\gamma}^{-3} dE_{\gamma}$ ) are plotted as red open circles. Since the spectral sensitivity of the used germanium detector is not constant (see Figure 3.4) and the PL spectra shift with varying bias conditions, the comparison between  $\phi_{\text{PL}}$  and  $\phi'_{\text{PL}}$  is necessary to guarantee that the deduced  $n_r$  is not too much influenced by these spectral effects. However, the influences are small and  $\phi_{\text{PL}}$  yields reasonable signal-to-noise ratio. Therefore, the  $n_r$  can be accurately determined from the  $\phi_{\text{PL}}/V_{\text{oc}}$  characteristics. Around room temperature, the PL efficiency is poor due to lower quasi-Fermi level separation compared to low temperatures. And due to the detector sensitivity, measurements around room temperature are not possible below injection current densities  $J \approx 5 \text{ mA cm}^{-2}$ . In contrast, a fairly good signal can be measured with approximately one order of magnitude less injection current  $J \approx 0.5 \text{ mA cm}^{-2}$  at the lowest temperature  $T = 86 \text{ K}$ .

The  $\phi_{\text{PL}}/V_{\text{oc}}$  characteristic in Figure 5.4(a) at  $T = 330 \text{ K}$  shows exponential behavior, where a diode law with  $n_r = 0.97$  is fitted. At highest  $\phi_{\text{PL}}$  a slight upward bending to lower  $V_{\text{oc}}$  can be observed, which may originate from a higher quasi-Fermi level separation in the recombination region, and therefore a higher  $\phi_{\text{PL}}$  than could be measured from the contacts. As long as the luminescence originates from tail-to-tail transitions, the  $n_r = E_{\text{r0}}/kT$  is interpreted

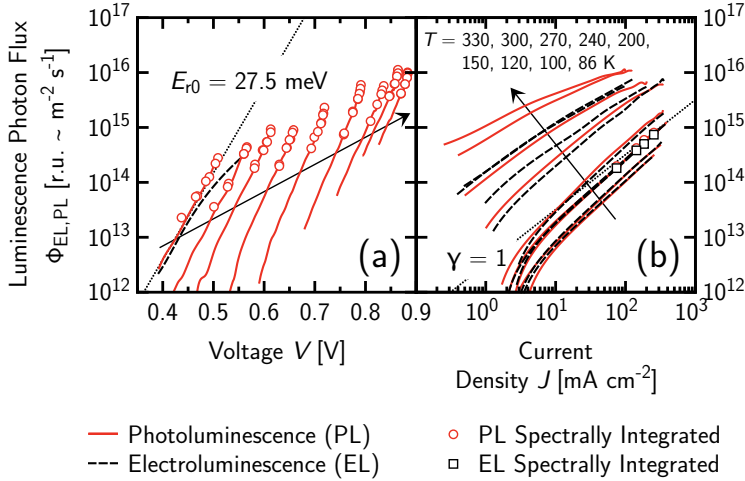


**Figure 5.4:** Integrated measured photo- (PL) and electroluminescence (EL) of  $\mu\text{c-Si:H}$  *pin* device at temperatures  $T = 330, 300, 270, 240, 200, 150, 120, 100$ , and  $86$  K (arrows). The EL is plotted as black dashed lines, and the PL as red solid lines. Integrated signals from EL spectra are plotted as black open squares, and from PL as red open circles. The PL is excited at the wavelength  $\lambda = 532$  nm. (a) The PL as a function of the open circuit voltage ( $V_{oc}$ ). The  $\phi_{PL}/V_{oc}$  characteristics following a common diode law with ideality factor times thermal energy  $n_r kT = 27.5$  meV are plotted as black dotted lines for different temperatures. (b) The EL and PL as a function of injection current density  $J = J_d = -J_{sc}$ , where  $J_{sc}$  is the short circuit current density under illumination, *i.e.* PL conditions, and  $J_d$  in case of EL. The luminescence, which scales linear with  $J$ , is plotted as black dotted line.

as the convoluted characteristic energy of the band-tail density of states of the conduction and valence band-tail  $E_{r0} = 27.5$  meV [45] (see Section 2.4.2). Furthermore, it can be seen that the integrally measured EL ( $\phi_{EL}$ ) shows the same exponential decaying slope as  $\phi_{PL}$ , however, only at lowest injection. Since the PL and EL are measured with electro-modulation technique, this converge at low injection indicates the linear superposition of the EL and PL as required by the *RR* (see Eq. (2.24)).

The  $\phi_{PL}/V_{oc}$  characteristics at temperatures below  $T = 330$  K also show exponential behavior at medium injection current, and an increasing  $\phi_{PL}$  with decreasing temperature as expected. However, the deduced  $E_{r0}$  decreases significantly with decreasing temperature to  $E_{r0} = 18.5$  meV at  $T = 150$  K.

An  $E_{r0}$ , which is very similar to the already deduced band-tail slopes  $E_0 = 31 - 33$  meV [45, 58, 59], can be deduced from  $\phi_{PL}/V_{oc}$  characteristics here. However, in terms of the *RR*, the PL is a auxiliary quantity, instead of the EL, actually.

As long as the contact voltage under EL conditions is influenced by the series resistance, even at moderate injection current, the  $\phi_{PL}$  and  $\phi_{EL}$  can be compared from the  $\phi_{PL}/J_{sc}$  and  $\phi_{EL}/J_d$  characteristics more easily. This may give additional indicators if EL behaves similar to the PL,

and therefore the PL superimposes linearly with the EL. Furthermore, this comparison indicates if  $E_0$  could be deduced from EL at low injection, where the sensitivity of the setup, which is used here, is not sufficient. The Figure 5.4(b) shows this comparison. As already mentioned, the luminescence intensity increases with decreasing temperature. And, in addition to this, the  $\phi/J$  characteristics show a shift from super-linear to sub-linear behavior with decreasing temperature. In the temperature region  $T = 330 - 240$  K,  $\phi_{PL}$ , and  $\phi_{EL}$  are very similar to each other. Below  $T = 240$  K the intensity of  $\phi_{PL}$  begins to increase faster with decreasing temperature than the  $\phi_{EL}$  does.

In summary, it seems that the  $E_0$  can be deduced from the  $\phi_{EL}/V$  characteristics of a  $\mu c$ -Si:H *pin* device in the same manner as it is done for the  $\phi_{PL}/V_{oc}$  characteristics here, and the superposition of the PL and EL holds as required by the *RR* (see Eq. (2.24)).

## 5.2 Discussion

After the presentation of the experimentally tested requirements for the *RR*, these results are discussed in depth. For this reason, the measured  $\mu c$ -Si:H *pin* device is modeled with the full one dimensional numerical device simulator ASA, which is presented in Section 3.2. After the modeling and a detailed discussion of the  $\mu c$ -Si:H *pin* device, the importance of these simulation results regarding the *reciprocity relation* are illustrated.

### 5.2.1 Device Modeling and Characterization

The first part of the modeling focusses on the calibration of the device parameters, which are fitted with common current/voltage characteristics ( $J/V$ ) of the device in the dark and under illumination. As expected from the models of PL and EL in Section 2.4.2, the PL and EL measurements are found to be very sensitive to the characteristic energy of the conduction ( $E_{c0}$ ) and valence ( $E_{v0}$ ) band-tail density of states, respectively. For this reason, the  $E_0 = E_{c0} = E_{v0}$ , which are assumed to be symmetric, are calibrated with PL and EL spectra. The external quantum efficiency ( $Q_e$ ), in addition, also indicates to  $E_0$ , and helps to fit the density of states, amongst others. In the second part of the modeling, the parameter fitting is tested with integrally measured PL and EL, and additionally with its temperature dependence in a wide temperature range  $T = 330 - 86$  K.

The fitting of the parameters is related to the parameters given in Section 3.2.1. As stated there, the Ohmic external contact series resistance ( $R_s^e$ ) and the mobility gap ( $E_\mu$ ) are determined from additional measurements.

### Contacts

The Figure 5.5(a) shows the results of the determination of  $R_s^e$ . The effective series resistance ( $R_s$ ) is deduced from a dark  $J/V$  characteristic at  $T = 330$  K and the difference to a  $J_{sc}/V_{oc}$  characteristic determined from the device under different illumination conditions (see Section 3.2.1). The  $R_s$  decays exponentially with increasing bias voltage and saturates at highest voltage. The higher the contact voltage, the more mobile charge carriers are in the extended band

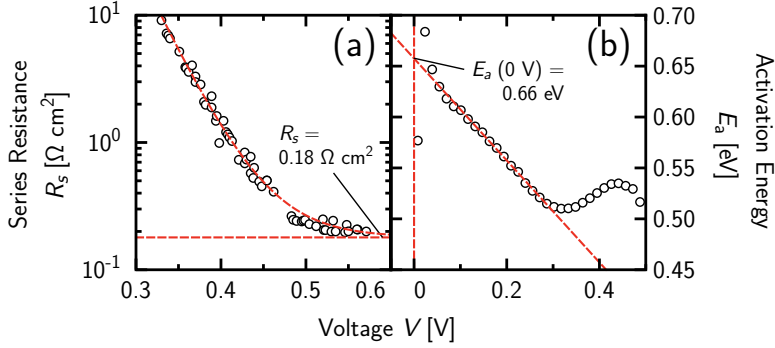


**Figure 5.5:** (a) Series resistance ( $R_s$ ) and (b) activation energy ( $E_a$ ) measured from  $\mu c$ -Si:H *pin* device. Measurements are plotted as black open circles. (a) Contact series resistance  $R_s = 0.18 \Omega \text{ cm}^2$  at temperature  $T = 330 \text{ K}$  is determined by fitting an offset value to an exponential behavior. This fit is plotted as red dashed lines. (b) Measured Activation Energy ( $E_a$ ) is determined from dark current/voltage characteristics at temperatures  $T = 290, 298, 309$ , and  $323 \text{ K}$ . Extrapolated linear fit shows  $E_a = 0.65 \text{ eV}$  at zero voltage. This fit is plotted as red dashed line.

states, and therefore the lower the  $R_s$ . This effect is limited by the external Ohmic contact series resistance  $R_s^e$ .

The red dashed curve line shows a fit from Eq. (3.8). From this fit, the external Ohmic contact series resistance is found to be  $R_s^e = 0.18 \Omega \text{ cm}^{-2}$ .

At the interface between the zinc oxide and either *p*- or *n*-layer, the surface recombination velocity is assumed to be equal to the thermal charge carrier velocity  $v_{th} \propto \sqrt{T}$ , with  $v_{th} = 10^7 \text{ cm s}^{-1}$  at  $T = 300 \text{ K}$ .

### Mobility Gap

The other explicitly measured parameter is the mobility gap ( $E_\mu$ ), which is determined from the dark current activation energy ( $E_a$ ) at the temperatures  $T = 290, 298, 309$ , and  $323 \text{ K}$  as presented in Section 3.2.1. The measurements are plotted in Figure 5.5(b).

The  $E_\mu \approx 1.16 \text{ eV}$  at  $T \approx 300 \text{ K}$  is determined with Eq. (3.10) and  $E_a = 0.66 \text{ eV}$  at  $0 \text{ V}$ , which is deduced from a linear extrapolation in the voltage range  $V \approx 50 - 250 \text{ mV}$ , where the  $E_a \propto -V/2$ . This fit is plotted as red dashed line. Pieters *et al.* found a similar value  $E_\mu = 1.19 \text{ eV}$  for a very similar  $\mu c$ -Si:H *pin* device [61].

Above  $V = 300 \text{ mV}$  the  $E_a$  shows a bump. This bump originates from a Schottky barrier at the contacts. However, this barrier is not taken into account anymore.

The  $E_\mu$  slightly increases with decreasing temperature, which is also taken into account here. The mobility gap shift in *c*-Si, which is investigated by Varshni [69], is calculated with Eq. (2.5) and  $\alpha_\mu = 7.02 \times 10^{-4} \text{ eV K}^{-1}$ . Cody *et al.* [70] and Liang *et al.* [71, 72] reported a  $\alpha_\mu = 4.7 \times 10^{-4} \text{ eV K}^{-1}$  in *a*-Si:H. And Tsang *et al.* found a similar value  $\alpha_\mu = 4.3 \times 10^{-4} \text{ eV K}^{-1}$  in *a*-Si:H [73]. Since  $\mu c$ -Si:H is a mixed phase material from *a*-Si:H and *c*-Si,

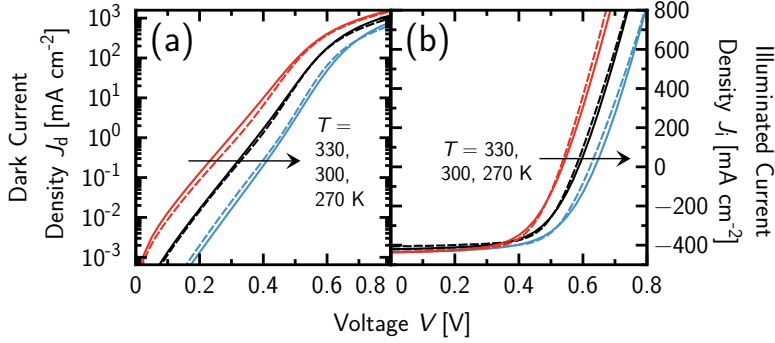


**Figure 5.6:** Temperature dependent current/voltage characteristics of  $\mu\text{c-Si:H}$  *pin* device (a) in the dark and (b) under illumination. Temperatures are  $T = 330, 300,$  and  $270$  K (arrows). Measurements are plotted as dashed lines, and simulations are plotted as solid lines. (b) Charge carrier generation is excited with a photon flux  $\phi = 3.5 \times 10^{22} \text{ m}^{-2} \text{ s}^{-1}$  at the wavelength  $\lambda = 532 \text{ nm}$ .

$\alpha_\mu = 4.7 \times 10^{-4} \text{ eV K}^{-1}$  is assumed. However,  $\beta_\mu$  is neglected, *i.e.*  $\beta_\mu = 0 \text{ K}$ .

A detailed description of the parameter fitting to  $J/V$  characteristics is given in the following through Figure 5.6. The Figure 5.6(a) shows a semilogarithmic  $J/V$  characteristic of the  $\mu\text{c-Si:H}$  *pin* device in the dark at  $T = 330, 300$  and  $270 \text{ K}$ . The corresponding linear  $J/V$  characteristics of the device under bias conditions of a photon flux  $\phi = 3.5 \times 10^{22} \text{ m}^{-2} \text{ s}^{-1}$  at the wavelength  $\lambda = 532 \text{ nm}$  shows Figure 5.6(b). The simulated  $J/V$  characteristics, which are plotted as solid lines, fit well with the measurements, which are plotted as dashed lines.

The effective densities of band states ( $N_c = N_v$ ) are mainly adjusted by the dark current density in the higher voltage region, right below the saturation of the  $J/V$  characteristics. And the corresponding  $E_\mu$  is characterized beforehand. The here fitted  $N_c = N_v = 1.0 \times 10^{19} \text{ cm}^{-3}$  shows very good agreement with the effective densities of band states determined from thermoelectric power and Hall effect measurements by Sellmer [155] at very similar devices.

In the saturation region of the dark  $J/V$  characteristics, the charge carrier band mobilities for electrons ( $\mu_n$ ) and holes ( $\mu_p$ ), respectively, can be fitted, altogether with  $R_{\text{sc}}^e$ , which is characterized beforehand. However, the  $\mu_n$  and  $\mu_p$  also influence the fill factor ( $FF$ ) in the illuminated  $J/V$  characteristics, *i.e.* the curvature at the point of maximum power, around  $V = 450 - 520 \text{ mV}$ . Furthermore, this  $FF$  is strongly influenced by the mid-gap defect states, *i.e.* the density of dangling bond states ( $N_{\text{db}}$ ) and its capture cross-sections can be modeled with the curvature of the illuminated  $J/V$  characteristics. The same holds for the dark  $J/V$  characteristics. Below  $V = 350 - 480 \text{ mV}$  the slopes of the curves get shallower compared to the higher voltage range, which shows dominant recombination through mid-gap defect states. Therefore, the density of these states and its capture cross-sections can be adjusted by fitting the dark  $J/V$  characteristic in this low voltage region.

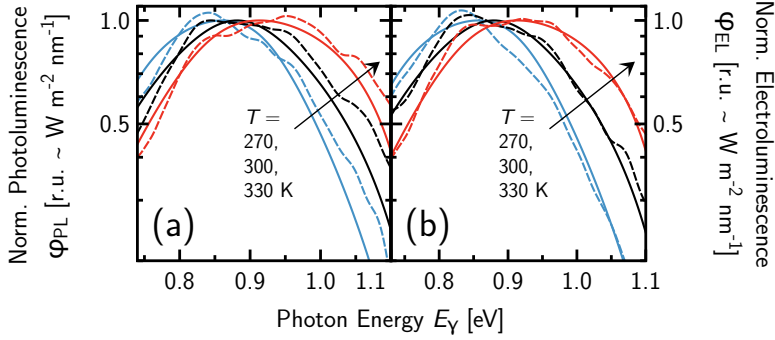


**Figure 5.7:** Temperature dependent (a) photo- (PL) and (b) electroluminescence (EL) spectra of  $\mu\text{c-Si:H}$  *pin* device. Temperatures are  $T = 330, 300$ , and  $270$  K (arrows). Measurements are plotted as dashed lines, and simulations are plotted as solid lines. All spectra are normalized to unity. (a) Charge carrier generation is excited with a photon flux  $\phi = 2.1 \times 10^{22} \text{ m}^{-2} \text{ s}^{-1}$  at the wavelength  $\lambda = 532 \text{ nm}$ . (b) Injection current density is  $J_d = -J_{sc} = 254 \text{ mA cm}^{-2}$  in case of EL, where  $J_{sc}$  is the short circuit current density of the device under illumination, e.g. PL conditions.

As stated before, the band-tail densities of states can be modeled more easily with PL and EL spectra, since this luminescence is dominated by tail-to-tail recombination. The Figure 5.7(a) shows the measured PL as dashed, and the fitted PL as solid lines. The same applies to Figure 5.7(b), which shows the EL. The PL and EL spectra are derived under the same conditions as the corresponding  $J/V$  characteristics, *i.e.* the same temperature range and the same bias illumination. Since the  $J/V$  characteristics and predominantly the  $V_{oc}$  are fitted well, the  $E_{c0} = E_{v0} = 31 \text{ meV}$  and the ratio of the capture cross-sections of band-tail states  $\sigma_r = \sigma_n/\sigma_p \approx 6.0$  of the conduction band for instance, are consistently modeled from PL and EL spectra. Here, the  $\sigma_r$  is smaller than fitted by Pieters *et al.*, who yield the best fitting results with  $\sigma_r = 7$  for the same measurement configuration, however, with spectrally uncorrected spectra [45]. Spectrally uncorrected spectra are narrower than the primordial, *i.e.* the corrected ones, since the spectral sensitivity of the used germanium detector decreases with increasing photon energy above the peak luminescence. Note that a lower  $\sigma_r$  yields a broader spectrum due to a higher contribution from the band-tail densities of states closer to the mid-gap. And fluctuations of the mobility gap, as stated for  $\text{Cu(In,Ga)Se}_2$  in Chapter 4 also broaden the luminescence spectra, however, these fluctuations are not taken into account here.

The comparison between measurements and simulations of the external quantum efficiency ( $Q_e$ ) indicates that the  $E_{c0}$  and  $E_{v0}$  in the photon energy range  $E_\gamma = 0.90 - 1.10 \text{ eV}$  is well modeled (see Figure 5.8). Additionally, the density of the band, band-tail, and mid-gap defect states can be adjusted with this. The high energy range  $E_\gamma > 1.20 \text{ eV}$  is dominated by transitions involving band states. And the curvature in the low energy range  $E_\gamma < 0.85 \text{ eV}$  in the  $Q_e$  originates from the interaction between band and mid-gap defect states.

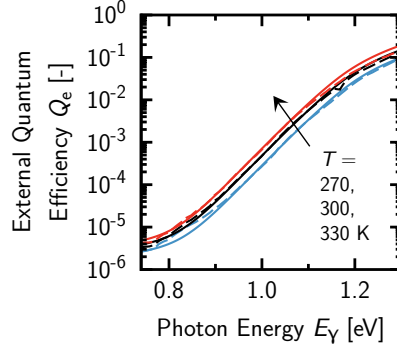


**Figure 5.8:** Measured external quantum efficiency ( $Q_e$ ) of  $\mu\text{c-Si:H}$  *pin* device compared to simulation. Temperature varies in the range  $T = 330, 300$ , and  $270$  K (arrow). Measurements are plotted as dashed lines, and simulations are plotted as solid lines.

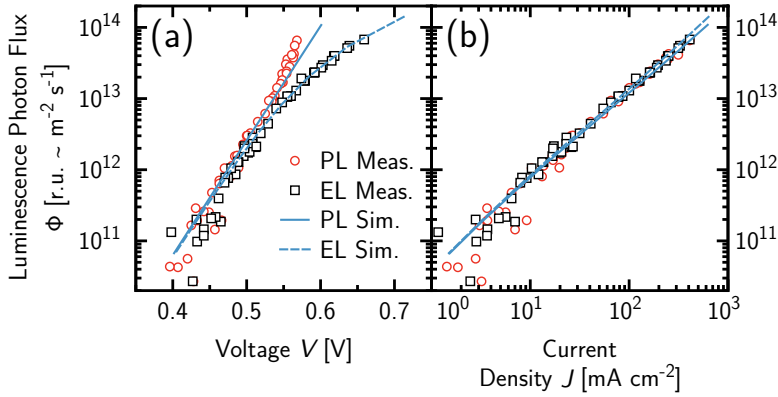


**Figure 5.9:** Comparison between measurement and simulation of integrated luminescence of  $\mu\text{c-Si:H}$  *pin* device at temperature  $T = 300$  K. Measured photoluminescence (PL) is plotted as red open circles, and electroluminescence (EL) is plotted as black open squares. Simulated PL is plotted as solid line, and EL is plotted as dashed line. Charge carrier generation is excited with photon fluxes  $\phi = 1.1 \times 10^{20} - 2.1 \times 10^{22} \text{ m}^{-2} \text{ s}^{-1}$  at the wavelength  $\lambda = 532 \text{ nm}$ . Injection current density  $J_d = -J_{sc}$  in case of EL, where  $J_{sc}$  is the short circuit current density of the device under illumination, *i.e.* PL conditions. (a) Luminescence/voltage characteristic. (b) Luminescence/current characteristic.



The simulated, and measured PL and EL intensities are compared in Figure 5.9. The measured  $\phi_{\text{PL}}$  at medium temperature  $T = 300$  K is plotted as red open circles, and  $\phi_{\text{EL}}$  as black open squares. The corresponding simulated PL is plotted as blue solid line, and the EL as blue dashed line. Note that the Figure 5.9 serves to verify the simulation models, and was not included in the fitting procedure.

The measured PL and EL in Figure 5.9(a) corresponds well to the simulations. However, in the high injection region above  $V = 520$  mV, the measured PL shows an already mentioned strong upward bending, which cannot imitated by simulations. This effect is often ascribed to space charge limited current [199–201], which is strongly related to the charge carrier mobilities [52, 202]. However, the EL in contrast fits very well in this region.

In the low injection region the simulations show higher luminescence intensities than the measurements. However, at these injection levels the measurements are not very reliable due to the low intensities.

Altogether, the relevant  $E_{\text{r0}}$ , which are derived from simulated ( $E_{\text{r0}} = n_{\text{r}}kT \approx 27$  meV) and measured ( $E_{\text{r0}} \approx 25$  meV)  $\phi_{\text{PL}}/V_{\text{oc}}$  characteristics correspond very well.

In the low injection region, where the  $R_{\text{s}}^{\text{e}}$  does not influence the  $\phi_{\text{EL}}/V$  characteristics, it can be seen from Figure 5.9(a) that the PL and EL are quite the same, and therefore superimpose as required by the  $RR$  in Eq. (2.24). The Figure 5.9(b) shows that this similarity also holds for the high injection region. Although, measured PL and EL are very similar, the simulated EL is a little higher than the PL. However, this similarity indicates that the  $E_{\text{r0}}$  derived from PL also holds under EL conditions, and therefore, also could be derived from EL with a more sensitive setup than used within this thesis. Moreover, the temperature dependence of the  $\phi/J$  characteristics either from PL or EL, in addition, indicates tail-to-tail luminescence, since band-to-defect recombination for instance, behaves linearly, which does not hold for the tail-to-tail luminescence. Fitting a  $\phi = \phi_0 J^\gamma$  to Figure 5.9(b) yields a super-linear behavior with  $\gamma \approx 1.25$ .

In summary, a parameter set is obtained, which accurately reproduces the observed characteristics of the  $\mu\text{c-Si:H}$  *pin* device over a wide range of experiments and conditions. The full parameter set can be found in Table 5.1. With this parameter set fitted, the results from PL and EL spectra under different bias conditions, the  $RR$  between EL and  $Q_{\text{e}}$ , and predominantly the  $n_{\text{r}}$  can be discussed in detail in the following.

### 5.2.2 Change of Luminescence Spectra

The PL and EL spectra from tail-to-tail recombination show a blue shift with increasing charge carrier injection, *i.e.* either excitation power under PL conditions or injection current under EL conditions. To illustrate this blue shift at various temperatures  $T = 330 - 86$  K, the Figure 5.10 shows the photon peak energy ( $\hat{E}_\gamma$ ) as a function of  $V_{\text{oc}}$ . For the reason of comparability, the  $V_{\text{oc}}$  from PL is allocated to the corresponding EL, *i.e.* the EL, where  $J = J_{\text{d}} = -J_{\text{sc}}$ . The measured  $\hat{E}_\gamma$  are derived from the spectra in Figure 5.1 (see for experimental details). The measured PL is plotted as colored open, and the EL as colored closed symbols. The corresponding simulations are plotted as colored solid lines for PL, and as colored dashed lines for EL conditions.

The  $V_{\text{oc}}$  increases with decreasing temperature and constant charge carrier concentration due to steeper occupation functions at lower temperatures.

**Table 5.1:** Simulation parameters of modeled  $\mu\text{c-Si:H}$  *pin* device.

	<i>p</i> -Layer	<i>i</i> -Layer	<i>n</i> -Layer	Unit
STRUCTURE				
<i>d</i>	20	1150	20	nm
TRANSPORT, DOPING, AND EXTENDED STATES				
$E_\mu$	1.16	1.16	1.70	eV
$\varepsilon_r$	11.9	11.9	11.9	—
$\chi$	4.05	4.05	3.90	eV
$\alpha_\mu$	0.47	0.47	0.47	meV K <sup>-1</sup>
$N_v$	$1.0 \times 10^{19}$	$1.0 \times 10^{19}$	$4.0 \times 10^{20}$	cm <sup>-3</sup>
$N_c$	$1.0 \times 10^{19}$	$1.0 \times 10^{19}$	$4.0 \times 10^{20}$	cm <sup>-3</sup>
$\mu_n$	45	45	15	cm <sup>2</sup> V <sup>-1</sup> s <sup>-1</sup>
$\mu_p$	15	15	5	cm <sup>2</sup> V <sup>-1</sup> s <sup>-1</sup>
$E_a$	0.15	0.00	0.30	eV
VALENCE BAND-TAIL STATES				
$E_{v,0}$	31	31	45	meV
$N_{v,0}$	$2.3 \times 10^{20}$	$2.3 \times 10^{20}$	$7.0 \times 10^{21}$	eV <sup>-1</sup> cm <sup>-3</sup>
$\sigma_p^0$	$6.7 \times 10^{-17}$	$6.7 \times 10^{-17}$	$7.0 \times 10^{-17}$	cm <sup>2</sup>
$\sigma_n^+$	$4.0 \times 10^{-16}$	$4.0 \times 10^{-16}$	$7.0 \times 10^{-16}$	cm <sup>2</sup>
CONDUCTION BAND-TAIL STATES				
$E_{c,0}$	31	31	31	meV
$N_{c,0}$	$2.3 \times 10^{20}$	$2.3 \times 10^{20}$	$7.0 \times 10^{21}$	eV <sup>-1</sup> cm <sup>-3</sup>
$\sigma_n^0$	$6.7 \times 10^{-17}$	$6.7 \times 10^{-17}$	$7.0 \times 10^{-17}$	cm <sup>2</sup>
$\sigma_p^-$	$4.0 \times 10^{-16}$	$4.0 \times 10^{-16}$	$7.0 \times 10^{-16}$	cm <sup>2</sup>
DANGLING BOND STATES				
$N_{db}$	$1.0 \times 10^{18}$	$3.0 \times 10^{15}$	$1.0 \times 10^{18}$	cm <sup>-3</sup>
$\sigma_{db}$	0.30	0.30	0.30	eV
$E_{db}$	0.00	0.00	0.00	eV
$U$	0.20	0.20	0.20	eV
$\sigma_p^0$	$5.0 \times 10^{-16}$	$5.0 \times 10^{-16}$	$7.0 \times 10^{-17}$	cm <sup>2</sup>
$\sigma_n^0$	$5.0 \times 10^{-16}$	$5.0 \times 10^{-16}$	$7.0 \times 10^{-17}$	cm <sup>2</sup>
$\sigma_p^-$	$5.0 \times 10^{-15}$	$5.0 \times 10^{-15}$	$7.0 \times 10^{-16}$	cm <sup>2</sup>
$\sigma_n^+$	$5.0 \times 10^{-15}$	$5.0 \times 10^{-15}$	$7.0 \times 10^{-16}$	cm <sup>2</sup>
ELECTRICAL CONTACT				
$R_s^{\text{ext}}$		0.18		$\Omega \text{ cm}^2$

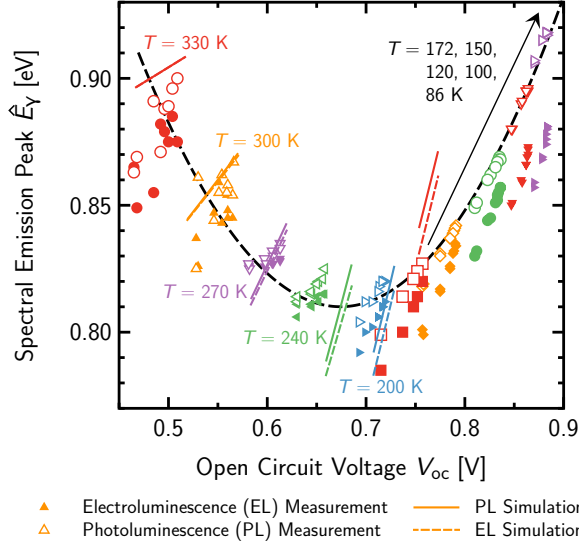


**Figure 5.10:** Temperature dependent (also see arrow) spectral emission peak energy ( $\hat{E}_\gamma$ ) as a function of open circuit voltage ( $V_{oc}$ ) derived from measured photo- (PL) and electroluminescence (EL) spectra of  $\mu\text{c-Si:H}$  *pin* device as shown in Figure 5.1 (see for experimental details). The values derived from EL are plotted as colored closed, and from PL as colored open symbols. The simulated EL is plotted as colored dashed, and the PL as colored solid lines, however, limited to  $T \geq 172$  K. The  $V_{oc}$  at PL conditions is also allocated to EL with the corresponding injection current density, i.e.  $J = J_d = -J_{sc}$ . The black dashed line is a guide to the eye.

The difference between PL and EL increases with decreasing temperature. The quasi-Fermi level separation ( $\Delta E_f$ ) in the recombination region, which is principally in the middle of the device, is smaller under EL than under PL conditions due to charge carrier transport phenomena. This yields the difference between the  $\hat{E}_\gamma$  from PL and EL at lower temperatures.

The simulations in Figure 5.10 slightly deviate from the measurements. Whereas the change of the open circuit voltage ( $\Delta V_{oc}$ ) seems to be right at all temperatures, the change of  $\hat{E}_\gamma$  in the simulations at high temperatures  $T = 330 - 300$  K is less, and at lower temperatures more than in the measurements. The reason for this is unknown.

However, a positive correlation between  $\hat{E}_\gamma$  and  $V_{oc}$  can be observed from all simulated and measured spectra at each temperature. This positive correlation is expected from the *local recombination model*. In the *local recombination model* the  $\hat{E}_\gamma = qV_{oc} + E_x$ , i.e.  $\Delta E_f$  is identified with  $V_{oc}$  at the contacts, and the charge carrier transport is neglected (see Section 2.4.2). The  $E_x$  represents a constant offset, which depends on  $E_{c0}$ ,  $E_{v0}$ , and the temperature (see Eq. (2.30)) [45]. This  $E_x$  yields the temperature dependent behavior in Figure 5.10 (see black dashed line). In the temperature range  $T = 330 - 200$  K the  $\hat{E}_\gamma$  from measurements decreases about  $\Delta \hat{E}_\gamma = 0.08$  eV at highest injection under PL conditions. And below  $T = 200$  K, the  $\hat{E}_\gamma$  in-

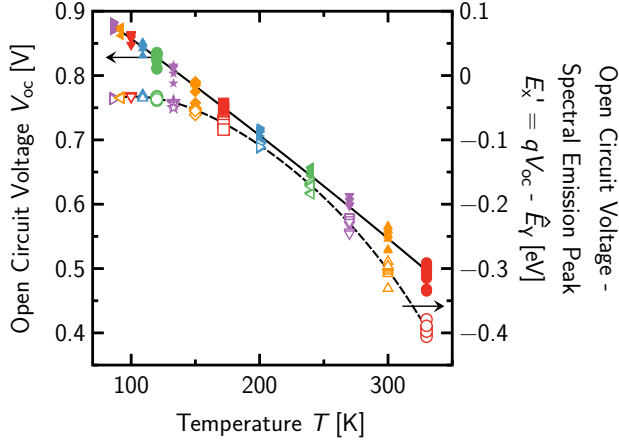


**Figure 5.11:** Temperature dependent difference between spectral emission peak energy ( $\hat{E}_\gamma$ ) and open circuit voltage ( $V_{oc}$ ) derived from measured photoluminescence (PL) spectra of  $\mu c$ -Si:H *pin* device shown in Figure 5.1 (compare Figure 5.10). The  $V_{oc}$  are plotted as colored closed, and the  $E'_x = qV_{oc} - \hat{E}_\gamma$  are plotted as colored open symbols.

creases about  $\Delta\hat{E}_\gamma = 0.10$  eV. The simulations show qualitatively the same behavior. And note that the band-tail slopes  $E_{c0} = E_{v0}$  in the simulations are assumed to be constant. Therefore, this observed behavior cannot originate from a temperature dependent  $E_{c0}$  or  $E_{v0}$ . In fact, above  $T = 200$  K, the  $E_x$  decreases faster with decreasing temperature than the  $V_{oc}$  increases, with  $E_{c0} = E_{v0} = 31$  meV, *i.e.*  $\Delta E_x / \Delta T > -\Delta V_{oc} / \Delta T$  (see Figure 5.11). Additionally, simulations show that this threshold temperature, here at  $T \approx 200$  K, decreases with decreasing  $E_{c0}$  and  $E_{v0}$ . Therefore, this threshold temperature also strongly indicates to the  $E_{c0}$  and  $E_{v0}$ . For comparison, lower characteristic energies of the band-tail densities of states like in  $\text{Cu(In,Ga)Se}_2$  in Chapter 4 (see Figure 4.9) show an only decreasing  $\hat{E}_\gamma$  in the same temperature range.

The temperature dependent measured  $E'_x = qV_{oc} - \hat{E}_\gamma$  from PL is plotted in Figure 5.11 as colored open symbols. The simulations coincide and are not plotted for this reason. The  $E'_x$  decreases with increasing temperature, since the charge carrier occupation functions blur at higher temperatures. However, in contrast, the temperature dependent  $V_{oc}$  decreases constantly, whereas the decrease of  $E'_x$  shows concave behavior. This difference between concave and linear behavior additionally illustrates the reason for the temperature dependent curvature in Figure 5.10.

In summary, the change of PL and EL spectra under different bias conditions can be well understood with tail-to-tail recombination. The broader the band-tail density of states, *i.e.* the higher the characteristic energies  $E_{c0}$  and/or  $E_{v0}$  of the band-tail densities of states, the more the  $V_{oc}$  shifts with increasing charge carrier injection, and therefore, the higher the shift of  $\hat{E}_\gamma$ .

The characteristic energies of the band-tail densities of states are indicated by the temperature dependent behavior of  $\bar{E}_\gamma$ .

### 5.2.3 Radiative Ideality Factor

The mixed characteristic energy of the band-tail densities of states, as a combination of  $E_{c0}$  and  $E_{v0}$  could be accessible from the radiative ideality factor ( $n_r$ ) by fitting a common diode law to the  $\phi_{PL}/V_{oc}$  characteristics from tail-to-tail recombination (see Figure 5.4). As already mentioned, this would be a fast material characterization tool for devices. For this reason, the significance of this method is checked by the comparison between the well fitted simulations and the measurements. And additionally, a detailed analysis via simulations explains the limits of this method. In the following, the simulated spectra, which yield the integrated luminescence ( $\phi$ ) are corrected for the spectral sensitivity of the measurement setup.

The Figure 5.12 shows the temperature dependency of the deduced quantities of measured and simulated  $\phi_{PL}/V_{oc}$ ,  $\phi_{PL}/J_{sc}$ , and  $\phi_{EL}/J_d$  characteristics. Measurements from PL are plotted as red closed circles, and from EL as black closed squares. The simulated PL is plotted as blue solid, and the EL as blue dashed line.

The Figure 5.12(a) shows the deduced  $n_r$  from the  $\phi_{PL}/V_{oc}$  characteristics under PL conditions. The  $n_r$  increases monotonically with decreasing temperature. At lowest temperatures the  $n_r$  may saturate. The simulations show a similar behavior at  $T = 330 - 150$  K. Below this temperature, the simulations increase faster compared to the measurements.

Since the luminescent recombination is dominated by tail-to-tail transitions, the luminescence intensity is

$$\phi \propto \exp\left(\frac{qV}{2E_{c0}}\right) \exp\left(\frac{qV}{2E_{v0}}\right) \quad (5.1)$$

if  $\Delta E_f = V$ . From the denominators of the exponential functions follows

$$n_r = \frac{E_0}{kT} \quad (5.2)$$

if  $E_{c0} = E_{v0} = E_0$ . The Figure 5.12(b) follows from Figure 5.12(a), where  $E_{r0}$  identifies with  $E_0$  in Eq. (5.2). Note that  $E_{r0}$  is deduced from  $n_r$ , and  $E_0$  is the characteristic energy. In a zero dimensional approach, where charge carrier transport is neglected, the  $E_{r0}$  is expected to be constant and equal to  $E_0$ . However, as long as the junction contact voltage, even in the situation, where no net current flows ( $V = V_{oc}$ ), is not the same as the  $\Delta E_f$  in the recombination region, the  $E_{r0} \neq E_0$  in general. The deduced  $E_{r0}$  from measurements monotonically decreases from above room temperature ( $E_{r0} = 27.2$  meV) to  $T = 150$  K ( $E_{r0} = 18.5$  meV) almost in the same way, as the simulation does. Note that  $E_0 = 31$  meV is assumed in the simulations. Below this temperature, the  $E_{r0}$  shows a concave curvature, which is much more distinctive from simulations than from measurements. The lower the temperature, the higher the difference between the  $\Delta E_f$  in the recombination region and the junction contact voltage ( $V_{oc}$ ). At room temperature and with moderate photon fluxes  $\phi < 10^{22} \text{ m}^{-2} \text{ s}^{-1}$ , the difference is a few percent. Even the excitation laser wavelength ( $\lambda$ ) may influence this method, due to inhomogeneous charge carrier generation. Former results are excited with  $\lambda = 671$  nm, and show an  $E_{r0}$ , which is closer to the

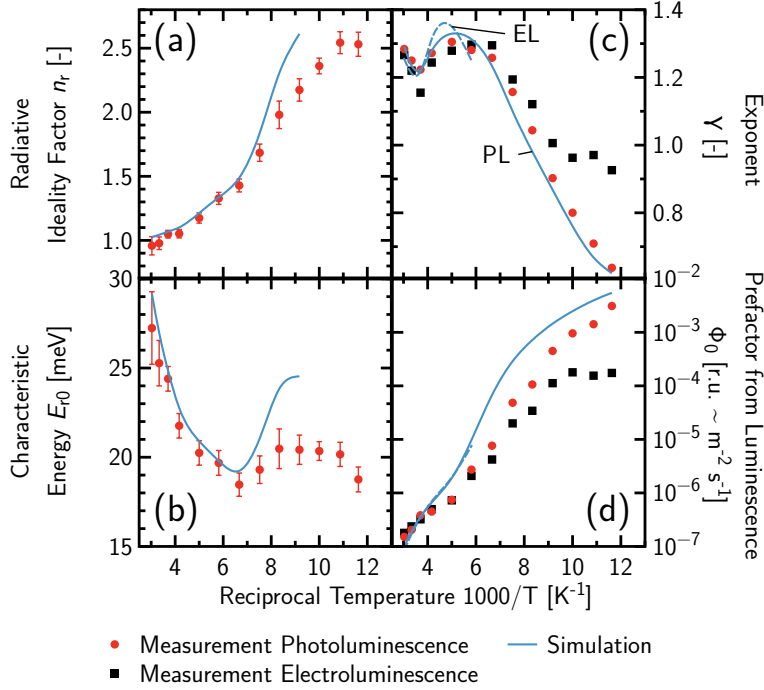


**Figure 5.12:** Temperature dependent evaluation of integrally measured electro- (EL) and photoluminescence (PL) of  $\mu\text{c-Si:H}$  pin device as shown in Figure 5.4. Temperatures are  $T = 330, 300, 270, 240, 200, 172, 150, 133, 120, 109, 100, 92$ , and  $86$  K. The values derived from PL are plotted as red circles, and values derived from EL are plotted as black squares. (a) The radiative ideality factor ( $n_r$ ) derived from Figure 5.4(a) by fitting a common diode law to the PL/voltage characteristics. (b) The radiative characteristic energy ( $E_{r0} = n_r kT$ ) derived from  $n_r$  in Figure 5.12(a), where  $kT$  is the thermal energy. (c)+(d) Fitting an exponential behavior  $\phi = \phi_0 J^\gamma$  to the PL and EL/current characteristics in Figure 5.4(b) yields the exponent ( $\gamma$ ) and the prefactor ( $\phi_0$ ) as a function of the temperature.

$E_0$ , which is determined from modeling [118], than can be observed here, where  $\lambda = 532$  nm. Since the determination of  $E_{r0}$  from measured  $\phi_{EL}/V$  characteristics under EL conditions is not possible due to the sensitivity of the setup, which is used here, the possibility to deduce  $E_{r0}$  from  $\phi_{EL}/V$  characteristics under low charge carrier injection conditions is experimentally deviated from  $\phi/J$  characteristics. For this reason the  $\phi_{PL}/J_{sc}$  characteristics from PL are compared to the  $\phi_{EL}/J_d$  characteristics from EL. These characteristics are fitted to  $\phi = \phi_0 J^\gamma$ . The Figure 5.12(c) shows the derived  $\gamma$ . The  $\gamma \approx 1.25 > 1$  shows almost constant super-linear behavior in the temperature range  $T = 330 - 150$  K and decreases to sub-linear behavior ( $\gamma < 1$ ) at lowest temperatures. The results from PL and EL are very similar. Below  $T = 133$  K both curves deviate from each other. Since the  $\gamma$  is derived from  $\phi/J$  characteristics, this deviation indicates to the charge carrier transport phenomena across the device, which hardly influence the EL. The simulations of PL reproduce the measurements very well in the whole temperature range. Due to limitations of numerical convergence, the EL is simulated at  $T = 330 - 172$  K and does not fit as well as the simulations of the PL. The kink at  $T = 300 - 240$  K originates from the non-uniform spectral sensitivity of the detector.

The Figure 5.12(d) illustrates the prefactor  $\phi_0$ . The evidence is very similar to  $\gamma$ . The PL and the EL are quite the same at  $T = 330 - 133$  K. Below this temperature, the influence of transport phenomena under EL conditions can be observed. The luminescence intensities from either PL or EL increase with decreasing temperature. The increase in case of PL is more than 4 orders of magnitude. The EL saturates below  $T = 120$  K. The simulations show this increase in the same manner. However, this is remarkably, since the simulations do not consider phonon interaction. Therefore, the increase of PL and EL intensity with decreasing temperature mostly originates from a higher quasi-Fermi level separation at lower temperatures.

Furthermore, the coincidence of the PL and EL in  $\mu c$ -Si:H again indicates the linear superposition of both kinds of luminescence, which holds in a wide temperature range  $T = 330 - 133$  K. This coincidence confirms the *reciprocity relation* in Eq. (2.24) even in low mobility materials like  $\mu c$ -Si:H.

The Figure 5.12(c) and (d) indicate that  $E_{r0}$ , which is deduced from  $\phi_{EL}/V$  characteristics, would yield the  $E_{c0} = E_{v0} = E_0$  in a similar way as the PL does if the EL is not influenced by series resistance. However, this resistance can never be evanescent. Though, this resistance strongly influences the contact voltage in the range, where the sensitivity of the used setup is reliable. However, also the  $E_{r0}$  deduced from PL does not match the evaluated  $E_0 = 31$  meV from extensive modeling. Figure 5.13(a) shows a simulated  $\phi_{PL}/V_{oc}$  characteristic plotted as blue solid line, and a  $\phi_{EL}/V$  characteristic plotted as blue dashed line at room temperature  $T = 300$  K. In this case, the spectral sensitivity of the used setup and the influence of an Ohmic contact series resistance are not included. Due to charge carrier transport phenomena arising from low mobilities, the  $\phi_{EL}/V$  characteristic still saturates at high injection. And the  $\phi_{PL}/V_{oc}$  characteristic shows slight upward bending due to a higher contribution of surface recombination at high injection levels. The corresponding  $E_{r0}$  are plotted in Figure 5.13(b). Following the modeling of the measurements,  $E_{c0} = E_{v0} = E_0 = 31$  meV is used for the simulations. The  $E_{r0}$  from PL and EL are quite the same up to  $V \approx 400$  mV, however, the difference to the true/simulated  $E_0$  is approximately 1.5 meV, *i.e.*  $\pm 5\%$ . At higher voltages  $V \geq 400$  meV the PL and the EL diverge, as already mentioned. The PL shows a distinctive  $E_{r0} \leq E_0$  and the EL

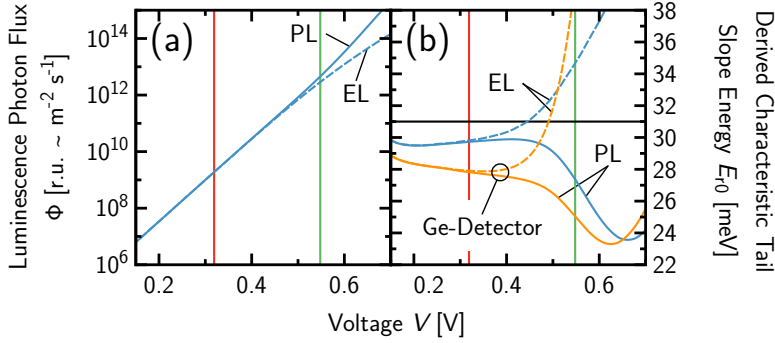


**Figure 5.13:** Simulated photo- (PL) and electroluminescence (EL) of  $\mu\text{c-Si:H}$  *pin* device at temperature  $T = 300\text{ K}$ . The EL is plotted as blue dashed line, and PL as blue solid line. The characteristic energy of the band-tail densities of states is  $E_0 = 31\text{ meV}$ . The red and green line at junction voltage  $V = 317$  and  $547\text{ mV}$  correspond to Figure 5.14. (a) Intensity of EL and PL ( $\phi \propto \exp(qV/E_{r0})$ ) as a function of junction voltage, where  $E_{r0}$  is allocated to  $E_0$ , and  $q$  the elementary charge. (b) Corresponding slope of luminescence/voltage characteristics interpreted as  $E_{r0} \propto (\partial\phi/\partial V)^{-1}$  (see Eq. (5.2)) plotted as blue lines, and the influence of the spectral sensitivity of the used setup and of an ohmic contact series resistance  $R_s^e = 0.18\ \Omega\text{ cm}^2$  is plotted as orange lines.

an  $E_{r0} \geq E_0$ .

The orange colored curves in Figure 5.13(b) show the influence of the spectral sensitivity of the used germanium detector and of an ohmic contact series resistance ( $R_s^e = 0.18\ \Omega\text{ cm}^2$ ). This increases the difference between  $E_{r0}$  and  $E_0$  in the low voltage range up to  $V \approx 400\text{ mV}$  to approximately  $3.0\text{ meV}$ , due to distinctive spectral shifts at different injection levels. This more realistic approach increases the error between the true/simulated  $E_0$  and the derived  $E_{r0}$  to approximately 10%. Since the EL is affected by the series contact resistance, the derived  $E_{r0}$  in the higher voltage range above  $V \approx 500\text{ mV}$  is very steep and cannot be allocated to  $E_0$ .

An analysis of  $E_0$  from  $E_{r0}$  may only be valid if  $V \leq V_{oc} \approx 500\text{ mV}$ . The reason for this can be understood with band diagrams across the device in Figure 5.14(a) under PL and in (b) under EL conditions. The quasi-Fermi levels in case of  $V = V_{oc} = 317\text{ mV}$  at low injection are plotted as red short dashed, and in case of  $V = V_{oc} = 547\text{ mV}$  at high injection are plotted as green dashed lines. Under EL conditions the contact is assumed to be influenced by an Ohmic series resistance. Therefore, the  $\Delta E_f$  under EL conditions at high injection is slightly smaller than for PL.

The quasi-Fermi level separation normalized to the junction contact voltage  $V_{oc}$  and  $V$ , respectively, is plotted in Figure 5.14(c) and (d). Additional to that, the normalized recombination profile  $R' = np/(n+p)^2$  [45] is plotted for high (green cross hatched area) and low injection (red patterned area). Although, the quasi-Fermi level separation looks quite uniform in Figure 5.14(a) and (b), the Figure 5.14(c) under PL and (d) under EL conditions show that it is not for high injection. The  $\Delta E_f \neq V_{oc} \neq V$  in general. In fact,  $\Delta E_f(z)$  across the device changes within the region of several percent of  $V_{oc}$  and  $V$ , respectively. At low injection, where  $E_{r0}$  is



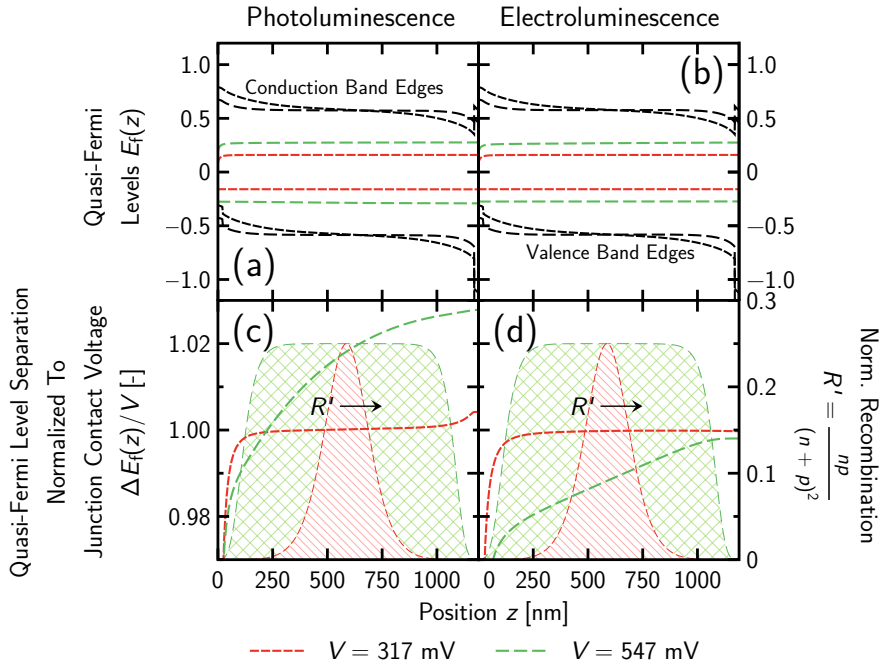


**Figure 5.14:** Simulated band diagrams of  $\mu c$ -Si:H *pin* device under (a) photo- (PL) and (b) electro-luminescence (EL) conditions at two different junction voltages ( $V = 317$  mV,  $V = 547$  mV) and temperature  $T = 300$  K as labeled in Figure 5.13. Quasi-Fermi level separation ( $\Delta E_f$ ) across the device under (c) PL and (d) EL conditions normalized to  $V_{oc}$  and  $V$ , respectively. Additionally, the normalized recombination profile  $R' = np/(n + p)^2$  [45] for high injection at  $V = 547$  mV is plotted as green cross hatched area, and for low injection at  $V = 317$  mV is plotted as red patterned area each.

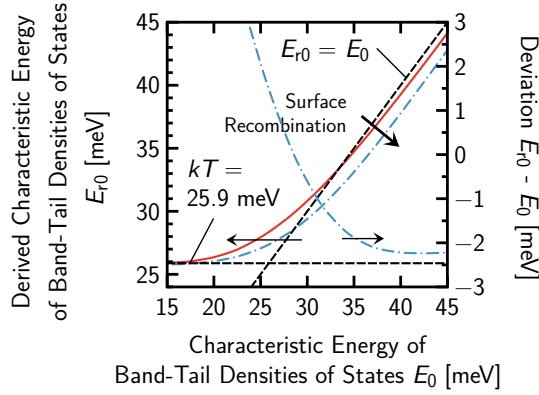


**Figure 5.15:** Influence of characteristic energy of localized band-tail densities of states ( $E_0$ ) to the deduced band-tail slope from luminescence ( $E_{r0}$ ) of a  $\mu\text{c-Si:H}$  *pin* device at temperature  $T = 300$  K and low injection  $J_d = 0.22 - 2.2 \text{ mA cm}^{-2}$ , *i.e.* conditions comparable to 1 – 10 % intensity of *AM1.5* standard *solar cell* conditions. The  $E_0$  of valence- and conduction band-tails are assumed to be equal, *i.e.*  $E_0 = E_{v0} = E_{c0}$ . The surface recombination and mid-gap defect states are neglected, *i.e.* band-tail recombination is dominant. The deduced  $E_{r0}$  is plotted as red line. Additionally, the influence of the surface recombination to  $E_{r0}$  is plotted as blue dot-dashed line. The influence of mid-gap defect states is rather small.

a good measure for  $E_0$ , the  $\Delta E_f \approx V_{oc} \approx V$  predominantly in the middle of the device, where most of the charge carriers recombine (see recombination profile  $R'$ ). However, mid-gap defect states in the doped layers and predominantly surface recombination at the contacts hamper the deduction of  $E_0$  under high injection levels, when the recombination profile ( $R'$ ) is rather broad.

The Figure 5.15 shows the deduced  $E_{r0}$  from  $\phi_{PL}/V_{oc}$  characteristics with  $E_0$  varied within simulations at  $T = 300$  K. The  $E_{r0}$  is deduced from low injection conditions, which yield short circuit current densities  $J_{sc} = 0.22 - 2.2 \text{ mA cm}^{-2}$  and  $V_{oc} = 390 - 450 \text{ mV}$  with  $E_0 = 31 \text{ meV}$ .

In the simulations of PL and EL the surface recombination and/or recombination through mid-gap defect states can be turned on or off. To better understand the influence of the various recombination processes, the surface recombination and the recombination through mid-gap defect states are neglected. The red solid line shows the deduced  $E_{r0}$ , where only band-tail state recombination is taken into account. The blue dot-dashed line in Figure 5.15 shows the influence of the surface and mid-gap defect state recombination. Simulations show that the influence of mid-gap defect states to  $E_{r0}$  is small. The surface recombination in contrast, lowers the deduced  $E_{r0}$  in comparison to  $E_0$ .

At low  $E_0$  the  $E_{r0}$  converges to the thermal energy  $kT \approx 25.9 \text{ meV}$  at  $T = 300$  K. The thermal energy limits the minimal  $E_{r0}$ , which can be deduced. Either the slope of the temperature determined charge carrier occupation probability edge, or the slope of the band-tail density of states dominates the  $E_{r0}$ . The shallowest of both slopes dominates the  $E_{r0}$ . The  $E_0 = 15 - 35 \text{ meV}$

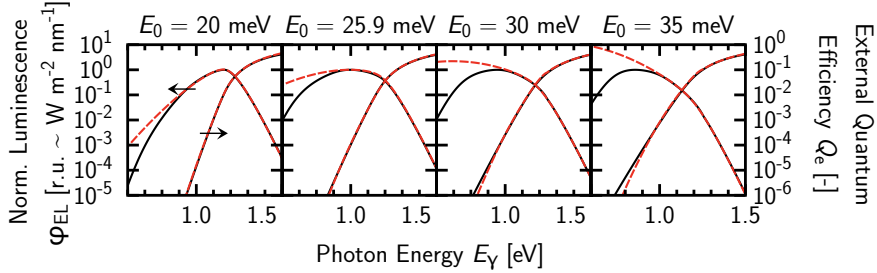


**Figure 5.16:** Influence of characteristic energy ( $E_0$ ) of localized band-tail density of states to reciprocity relation between electroluminescence ( $\varphi_{\text{EL}}$ ) and external quantum efficiency ( $Q_e$ ) of  $\mu\text{c-Si:H}$  *pin* device at temperature  $T = 300$  K and injection current density  $J_d = 21.0 \text{ mA cm}^{-2}$ . The  $E_0$  of valence- and conduction band-tails are assumed to be equal:  $E_0 = E_{v0} = E_{c0}$ . Black solid lines show full one dimensional numerical device simulations of  $\varphi_{\text{EL}}$  and  $Q_e$ . The red dashed lines show the correspondence each, i.e.  $\varphi'_{\text{EL}} \propto Q_e \times \varphi_{\text{bb}}$  and  $Q'_e \propto \varphi_{\text{EL}} / \varphi_{\text{bb}}$ , where  $\varphi_{\text{bb}}$  is the hemispheric black body radiation.

is a transition region, which gets sharper if the temperature is lowered. However, in reality (see blue dot-dashed line)  $E_{r0}$  can be allocated to  $E_0 = 27 - 32 \text{ meV}$  within the measurement error if the spectral sensitivity of the setup is uniform. Outside the transition region, a constant offset, which is approximately 2 meV, can be added to the deduced  $E_{r0}$ .

The simulations show that the  $E_0$  has only small influence on the photovoltaic conversion efficiency. In fact, the recombination in the doped layers limits the cell efficiency.

## 5.2.4 Reciprocity Relation

The *RR* between electroluminescence spectra ( $\varphi_{\text{EL}}$ ) and the external quantum efficiency ( $Q_e$ ) is influenced by the characteristic energy of the band-tail density of states, i.e.  $E_0$  and the injection. The influence of  $E_0$  was stated earlier for band-to-tail transitions in Section 4.2.3. The transition from  $E_0 = 20 \text{ meV} < kT \approx 25.9 \text{ meV}$  to  $E_0 = 30 - 35 \text{ meV} > kT$ , which is relevant for band-tail states in  $\mu\text{c-Si:H}$ , shows Figure 5.16 at  $T = 300$  K. The injection current density  $J_d = 21.0 \text{ mA cm}^{-2}$  is chosen to be equivalent to the  $J_{\text{sc}}$  under *AM1.5* standard solar cell conditions. The directly simulated  $\varphi_{\text{EL}}$  and  $Q_e$  are plotted with black solid lines. The indirectly deduced  $\varphi'_{\text{EL}} \propto Q_e \times \varphi_{\text{bb}}$  and  $Q'_e \propto \varphi_{\text{EL}} / \varphi_{\text{bb}}$  are plotted with red dashed lines, where  $\varphi_{\text{bb}}$  is the hemispheric black body radiation.

Note that beside the tail-to-tail recombination, which dominates the luminescence, the simulated  $\varphi_{\text{EL}}$  are additionally composed from band-to-tail and band-to-band transitions in the high photon energy region.

The difference between  $\varphi_{\text{EL}}$  and  $\varphi'_{\text{EL}}$  increases with increasing  $E_0$ . The peak photon energy can be reproduced with  $E_0 = 20 \text{ meV} < kT$ . And at  $E_0 = kT$  the peak is very broad. However, at  $E_0 \geq 30 \text{ meV} > kT$  the  $\varphi'_{\text{EL}}$  gets very broad and the peak photon energy cannot be reproduced. In contrast, the deviations between  $Q_e$  and  $Q'_e$  are very small for all cases in Figure 5.16.

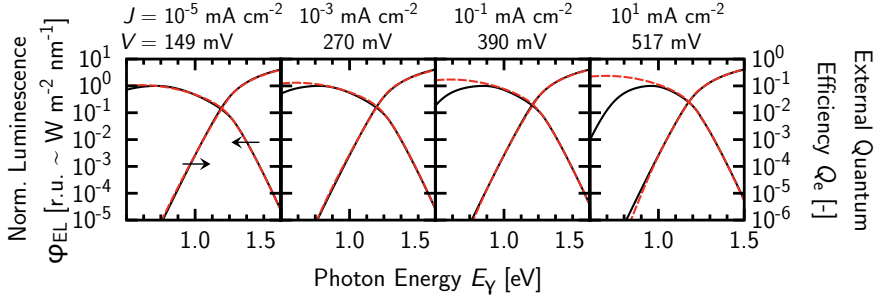


**Figure 5.17:** Influence of injection current density ( $J$ ) to reciprocity relation between electroluminescence ( $\varphi_{\text{EL}}$ ) and external quantum efficiency ( $Q_e$ ) of  $\mu\text{c-Si:H}$  pin device at temperature  $T = 300$  K and injection current densities  $J_d = 10^{-5}$ ,  $10^{-3}$ ,  $10^{-1}$ , and  $10^1$   $\text{mA cm}^{-2}$ . The  $E_0$  of valence- and conduction band-tails are assumed to be equal, i.e.  $E_0 = E_{v0} = E_{c0} = 30$  meV. Black solid lines show full one dimensional numerical device simulations of  $\varphi_{\text{EL}}$  and  $Q_e$ . The red dashed lines show the correspondence each, i.e.  $\varphi'_{\text{EL}} \propto Q_e \times \varphi_{\text{bb}}$  and  $Q'_e \propto \varphi_{\text{EL}} / \varphi_{\text{bb}}$ , where  $\varphi_{\text{bb}}$  is the hemispheric black body radiation.

Whereas, the sensitivity of the used measurement setup is limited to the lower end, simulations can work out  $\varphi_{\text{EL}}$  from low injection. The *RR* between  $Q_e$  and  $\varphi_{\text{EL}}$  versus the injection current density  $J_d = 10^{-5} - 10^1$   $\text{mA cm}^{-2}$  is shown in Figure 5.17. The simulations neglect mid-gap defect states, since luminescence from these states is not observed in the measurements. Simulations show that transitions from band to mid-gap defect states dominate the luminescence at room temperature if the injection is low, i.e. the quasi-Fermi level separation is small. This means that either the spectral sensitivity of the measurement setup or the high injection hampers the detection of the luminescence from mid-gap defect states in  $\mu\text{c-Si:H}$ .

The injection, and therefore the curvature of  $Q_e$  is constant in Figure 5.17. Under the conditions of  $Q_e$  the photon flux is small, i.e. the quasi-Fermi level separation is also small, and the contacts are short circuited. The deviation between  $\varphi_{\text{EL}}$  and  $\varphi'_{\text{EL}}$  increases with increasing injection, since low injection for  $\varphi_{\text{EL}}$  is close to the conditions of  $Q_e$ . Again, the deviations between  $Q_e$  and  $Q'_e$  are very small.

The deviations between  $\varphi_{\text{EL}}$  and  $\varphi'_{\text{EL}}$ , and  $Q_e$  and  $Q'_e$ , which are related through  $\varphi_{\text{bb}}$ , can be understood with the charge carrier occupation probability functions and the exponential decaying band-tail density of states. The difference between  $Q_e$  and  $\varphi_{\text{EL}}$  conditions in terms of the charge carrier occupation probability and the localized band-tail density of occupied states shows Figure 5.18 in case of high ( $J_d = 10$   $\text{mA cm}^{-2}$ ) and low ( $J_d = 10^{-5}$   $\text{mA cm}^{-2}$ ) injection with  $E_0 = 20$  meV  $< kT$  and  $E_0 = 35$  meV  $> kT$ . The reciprocity relation between  $Q_e$  and  $\varphi_{\text{EL}}$  decreases from left to right. The band-tail densities of occupied states under  $\varphi_{\text{EL}}$  conditions are plotted in the upper, and the corresponding occupation probability functions are plotted in the lower row as red dashed lines each. The same holds for the  $Q_e$  conditions, which are plotted as black solid lines. The transparent lines show the band-tail densities of empty states each. In the case of  $E_0 < kT$  the band-tail densities of states are steeper than the occupation probability functions, and therefore the band-tail densities of occupied states under  $\varphi_{\text{EL}}$  conditions

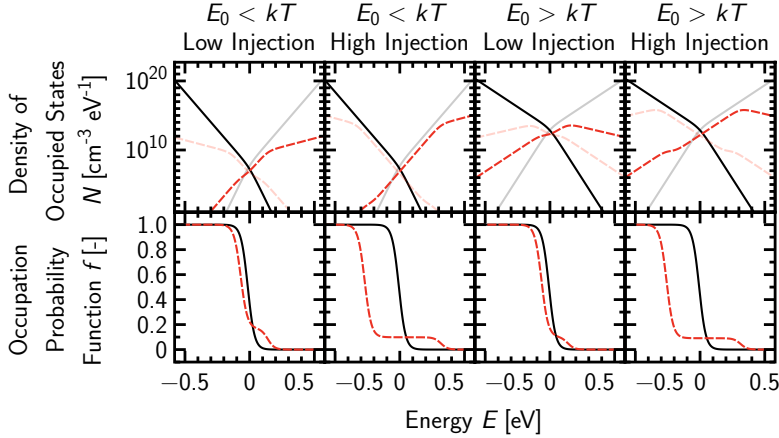


**Figure 5.18:** Comparison between *radiative recombination* and *light absorption* in terms of the band-tail densities of occupied states ( $N$ ) and the corresponding occupation probability functions ( $f$ ) of  $\mu\text{c-Si:H}$  *pin* device at temperature  $T = 300\text{ K}$ . The quasi-Fermi level separation is small for *light absorption*, which is plotted as black solid lines. In case of *radiative recombination* the quasi-Fermi level separation is large, which is plotted as red dashed lines. The transparent lines show the empty states in case of *light absorption* and *radiative recombination*, respectively. The characteristic energies of the band-tail densities of states ( $E_0 = E_{v0} = E_{c0}$ ) and the quasi-Fermi level separation are assumed to be symmetric. The  $E_0 = 20\text{ meV} < kT$  and  $E_0 = 35\text{ meV} > kT$ . The high and low injection current densities are  $J_d = 10\text{ mA cm}^{-2}$  and  $J_d = 10^{-5}\text{ mA cm}^{-2}$ , respectively.

show the same direction of the slope as under  $Q_e$  conditions. This is the reason, why the peak photon energy positions ( $\hat{E}_\gamma$ ) from  $\varphi_{\text{EL}}$  and  $\varphi'_{\text{EL}}$  are compatible, while the  $\varphi_{\text{EL}} < \varphi'_{\text{EL}}$  in the low energy region at  $E_\gamma < \hat{E}_\gamma$ .

In contrast, this is different in case of  $E_0 > kT$ , where the occupation probability function is more abrupt than the band-tail density of states. The two kinks at the quasi-Fermi levels for trapped charge in the band-tail density of occupied states originates from the two-step Fermi-Dirac occupation probability function in case of Shockley-Read-Hall recombination. The low energy kink is not as distinctive as the one in the high energy region, since the occupation probability function between both quasi-Fermi levels for trapped charge is almost a constant plateau (compare Figure 2.3).

In case of low injection, which is close to the thermal equilibrium, the quasi-Fermi level separation is small, and therefore the two kinks are close to each other. The two kinks merge at thermal equilibrium, which is then similar to the  $Q_e$  conditions.

Up to this point, the observed deviation between  $\varphi_{\text{EL}}$  and  $\varphi'_{\text{EL}}$ , or  $Q_e$  and  $Q'_e$  (from measurements) can be explained with a characteristic energy of the band-tail densities of states  $E_0 = 31\text{ meV} > kT$ . Additionally, the deviation originates from the difference between high injection under  $\varphi_{\text{EL}}$  conditions and low injection close to the thermal equilibrium under  $Q_e$  con-

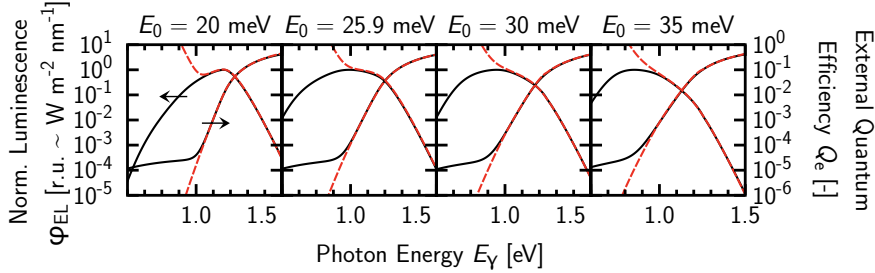


**Figure 5.19:** Influence of characteristic energy ( $E_0$ ) of localized band-tail density of states and mid-gap defect density of states to *reciprocity relation* between electroluminescence ( $\varphi_{\text{EL}}$ ) and external quantum efficiency ( $Q_e$ ) of  $\mu\text{c-Si:H}$  *pin* device. The mid-gap defect state concentration is  $N_{\text{db}} = 2 \times 10^{15} \text{ cm}^{-3}$ . For detailed description, see Figure 5.16.

ditions. However, the influence of mid-gap defect states is neglected so far. From the modeling of the measured  $\mu\text{c-Si:H}$  *pin* device, the concentration of the Gaussian-distributed amphoteric mid-gap defect states is determined to be  $N_{\text{db}} \approx 10^{15} \text{ cm}^{-3}$ . However, these mid-gap defect states contribute to  $Q_e$  as plotted earlier in Figure 5.3. This extra contribution decreases the *RR* between  $Q_e$  and  $\varphi_{\text{EL}}$  in the low energy range  $E_\gamma < \hat{E}_\gamma$ , since the contribution from mid-gap defect states to the  $\varphi_{\text{EL}}$  is only dominant at low injection. The influence of these mid-gap defect states to  $Q_e$  and  $\varphi_{\text{EL}}$  is plotted as black solid lines in Figure 5.19. The deduced  $Q'_e$  and  $\varphi'_{\text{EL}}$  are plotted as red dashed lines. The  $N_{\text{db}} = 2 \times 10^{15} \text{ cm}^{-3}$  is kept constant, while  $E_0 = 20\text{--}35 \text{ meV}$  is varied.

The value of  $\hat{E}_\gamma$  in  $\varphi_{\text{EL}}$  can be reproduced from  $\varphi'_{\text{EL}}$  within  $E_0 = 20 \text{ meV}$ . However, the *RR* does not hold if  $E_0$  is increased. And if  $N_{\text{db}}$  is very high,  $\hat{E}_\gamma$  cannot be reproduced from  $\varphi'_{\text{EL}}$  even at  $E_0 < kT$ .

Note that the case of  $E_0 = 30 \text{ meV}$  is very similar to the measurements in Figure 5.3.

In summary, the requirements to hold up with the *reciprocity relation* (*RR*) are not fulfilled very well if the luminescence originates from localized states, which are close to the quasi-Fermi levels. The investigations from tail-to-tail transitions in  $\mu\text{c-Si:H}$  support the already stated results from band-to-tail transitions, which are found from  $\text{Cu(In,Ga)Se}_2$  in Chapter 4.

As expected, the  $\varphi_{\text{EL}}$  from  $\mu\text{c-Si:H}$  shows a stronger blue shift than from  $\text{Cu(In,Ga)Se}_2$ , since the band-tail density of states in  $\mu\text{c-Si:H}$  are broader than in  $\text{Cu(In,Ga)Se}_2$ , and tail-to-tail transitions yield the luminescence in  $\mu\text{c-Si:H}$  instead of band-to-tail transitions like in  $\text{Cu(In,Ga)Se}_2$ . A blue shift exists in general if band-tail states are involved in luminescence processes.

Previous work suggested that  $n_r kT = E_{\text{r}0} = E_0$  [45]. Therefore, the radiative ideality factor  $n_r = 1$  in general, as postulated from the *RR*, is negated if band-tail states are involved in the luminescence. The  $n_r = 1$  from tail-to-tail transitions if  $E_0 = kT$ . While  $E_0 = 31 \text{ meV}$ , the  $n_r \approx 1$  is found around room temperature within measurements. Due to blue shifted PL and EL spectra, an unequal quasi-Fermi level separation across the device at high injection, and a non-uniform spectral sensitivity of the measurement setup, which is used here, it is hard to allocate  $n_r$  to  $E_0$  quantitatively. However, the investigations in this thesis show that  $E_{\text{r}0} = E_0$  from the

$n_r$  in  $\mu c\text{-Si:H}$  holds within 10% for moderate injection ( $J_d \approx 1 \text{ mA cm}^{-2}$ ) and  $E_0 > kT$  at room temperature if the measurement setup shows approximately uniform spectral sensitivity in the photon energy range of peak luminescence.

Since the characteristic energy of the band-tail densities of states in  $\text{Cu(In,Ga)Se}_2$  is found to be  $E_0 = 17.5 \text{ meV} < kT$ , the *RR* between the external quantum efficiency ( $Q_e$ ) and the electroluminescence spectra ( $\varphi_{\text{EL}}$ ) is fulfilled, even under high injection conditions. This requirement is only partly fulfilled in  $\mu c\text{-Si:H}$ , where  $E_0 = 31 \text{ meV}$ . The  $E_0 > kT$ , and due to this, the  $\varphi_{\text{EL}}$  is very sensitive to high injection, as long as  $Q_e$  is determined under very low injection close to the thermal equilibrium. Additional mid-gap defect states, which seem not to contribute to the  $\varphi_{\text{EL}}$ , yield extra contribution to the  $Q_e$ , and therefore break the *RR*.

The mid-gap defect states in hydrogenated microcrystalline silicon ( $\mu c\text{-Si:H}$ ) are moderate in quantity compared to hydrogenated amorphous silicon ( $a\text{-Si:H}$ ). Furthermore, *radiative recombination* from mid-gap defect states also contributes to the luminescence of  $a\text{-Si:H}$ , in addition to the already investigated tail-to-tail luminescence [60].

## Chapter 6

# Hydrogenated Amorphous Silicon Based *pin* Devices

The requirements to hold up with the *reciprocity relation* ( $RR$ ) between the external quantum efficiency and the electroluminescence are mainly fulfilled in  $\text{Cu(In,Ga)Se}_2$  (see Chapter 4), however, partly broken in  $\mu\text{c-Si:H}$  due to broad valence and conduction band-tail densities of states, which characteristic energy is higher than the thermal energy (see Chapter 5). Small influence on the  $RR$  between the external quantum efficiency ( $Q_e$ ) and the electroluminescence spectra ( $\varphi_{\text{EL}}$ ) is observed from mid-gap defect states in  $\mu\text{c-Si:H}$ .

This chapter investigates the external quantum efficiency and luminescence in hydrogenated amorphous silicon ( $a\text{-Si:H}$ ) thin-film based *pin* devices as presented in Section 3.1.1 with measurements (see Section 6.1), and discusses the results with the help of full one dimensional numerical device simulations in Section 6.2. As far as the electronic inter-band states in  $a\text{-Si:H}$  are similar to hydrogenated microcrystalline silicon ( $\mu\text{c-Si:H}$ ), it compares the results to  $\mu\text{c-Si:H}$ .

The structure is quite the same as shown in Chapter 5 for  $\mu\text{c-Si:H}$ . At the beginning of this chapter, the photo- (PL) and electroluminescence (EL) (see Section 6.1.1), and the  $RR$  to  $Q_e$  (Section 6.1.2) measurements are presented. In contrast to  $\text{Cu(In,Ga)Se}_2$  or  $\mu\text{c-Si:H}$ , the luminescence spectra from  $a\text{-Si:H}$  yield two peaks, predominantly around room temperature. The high photon energy peak is associated to the already presented tail-to-tail luminescence [58, 73, 119–123, 125, 203, 204], whereas the low photon energy peak, which is experimentally found to be approximately 0.2 eV below the tail-to-tail peak, is ascribed to band-to-defect transitions [60, 127, 128, 205]. For this reason, the evaluation of the PL, EL, and even the  $Q_e$  in  $a\text{-Si:H}$  has to consider both transitions. It is observed that the  $RR$  between the  $\varphi_{\text{EL}}$  and the  $Q_e$  is strongly influenced by this additional band-to-defect luminescence.

Due to this additional band-to-defect luminescence, two different radiative ideality factors can be determined by fitting a common diode law to the luminescence/voltage characteristics from either tail-to-tail and band-to-defect transitions (see Section 6.1.3).

The measurements are extensively discussed with the help of well fitted full one dimensional numerical device simulations using *ASA* in connection with *LUME*. Though, the discussion focusses on the results from the band-to-defect luminescence. And the simulations can show that the  $RR$  between  $Q_e$  and  $\varphi_{\text{EL}}$  is preserved under very low injection conditions, which are not accessible within measurements due to insufficient detector sensitivity.



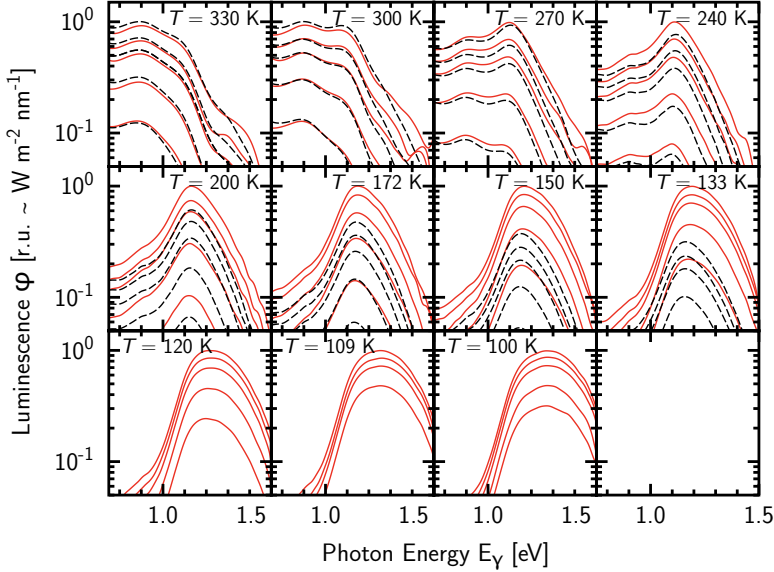


**Figure 6.1:** Measured spectra of photo- (PL) and electroluminescence (EL) from *a*-Si:H *pin* device. The EL is plotted as black dashed lines, and the PL as red solid lines. All spectra are normalized to the highest signal at each temperature. Spectra are measured at the temperatures  $T = 330, 300, 270, 240, 200, 172, 150, 133, 120, 109$ , and  $100$  K. The PL is excited with photon fluxes  $\phi = 3.2 \times 10^{22}, 2.2 \times 10^{22}, 1.5 \times 10^{22}, 7.3 \times 10^{21}$ , and  $3.1 \times 10^{21} \text{ m}^{-2} \text{ s}^{-1}$  at the wavelength  $\lambda = 532 \text{ nm}$ . This yields current densities  $J = J_d = -J_{sc} = 402, 274, 185, 91.5$ , and  $39.0 \text{ mA cm}^{-2}$  at temperature  $T = 300 \text{ K}$ . The EL spectra below  $T = 133 \text{ K}$  are not accessible for the reason of technical limitations.

## 6.1 Experimental Results

As already mentioned in the introduction, the experiments within *a*-Si:H focus on the influence from mid-gap defect states with respect to the *RR* between the external quantum efficiency and the electroluminescence. The Figure 6.1 shows the measured spectra from PL ( $\varphi_{\text{PL}}$ ), which are plotted as red solid lines, and from EL ( $\varphi_{\text{EL}}$ ), which are plotted as black dashed lines. The temperature is varied from above room temperature  $T = 330 \text{ K}$  to  $T = 100 \text{ K}$ . The charge carrier injection is altered within one order of magnitude. The photon fluxes under PL conditions are  $\phi = 3.2 \times 10^{22}, 2.2 \times 10^{22}, 1.5 \times 10^{22}, 7.3 \times 10^{21}$ , and  $3.1 \times 10^{21} \text{ m}^{-2} \text{ s}^{-1}$  at the excitation wavelength  $\lambda = 532 \text{ nm}$ . The  $\varphi_{\text{EL}}$  are measured with injection current densities ( $J_d$ ) equivalent to the short circuit current densities ( $J_{sc}$ ) under PL conditions, *i.e.*  $J_d = -J_{sc}$ . Due to technical limitations and a high series resistance of the device in the dark at low temperatures, the EL is restricted to temperatures above  $T = 133 \text{ K}$ . To meet  $J_d = -J_{sc}$  at very low temperatures, junction voltages  $V > 8 \text{ V}$  are required.

At the highest temperature the  $\varphi_{\text{EL}}$  and  $\varphi_{\text{PL}}$  coincide within the measurement errors. At lower

temperatures  $T \leq 270$  K the  $\varphi_{\text{EL}} < \varphi_{\text{PL}}$ , and at a given luminescence intensity the spectral shapes of  $\varphi_{\text{EL}}$  and  $\varphi_{\text{PL}}$  are slightly different to each other.

The photon peak energies around  $\hat{E}_\gamma = 1.08$  eV continuously shift to higher photon energies with decreasing temperature. Whereas this shift is weak in the temperature range  $T = 270\text{--}200$ , it gets stronger below  $T = 150$  K. This peak shifts  $\Delta\hat{E}_\gamma \approx 0.20$  eV within a change of temperature  $\Delta T = 230$  K at highest injection. Similar peak shifts are known from tail-to-tail luminescence in  $\mu\text{c-Si:H}$  (see Chapter 5). In fact, tail-to-tail luminescence yields this high photon energy peak [58, 73, 119–123, 125, 203, 204].

However, at  $\hat{E}_\gamma = 0.90$  eV, the spectra show an additional peak, which is dominant at high temperatures and/or low injection. This peak is often cited as transition from occupied band to mid-gap defect states [127, 128, 205]. Street *et al.* attributed these defect states to neutral dangling bonds [60]. It could be that the PL and EL spectra are affected by unintentional doping/contamination. It is supposed that even slight boron  $p$ -type doping, which yields a dopant concentration of  $N_d > 3$  ppm, introduces additional mid-gap defects to  $a\text{-Si:H}$ , which yields luminescence at  $\hat{E}_\gamma \approx 0.9$  eV. A higher phosphorus  $n$ -type doping level ( $N_d > 10$  ppm) is required to quench the tail-to-tail luminescence. However, the peak luminescence from band-to-defect transitions in phosphorus  $n$ -type doped  $a\text{-Si:H}$  is found to be  $\hat{E}_\gamma = 0.81$  eV [60].

With increasing injection, *i.e.* increasing quasi-Fermi level separation, the tail-to-tail luminescence increases faster than the band-to-defect transition. For this reason of higher quasi-Fermi level separation at lower temperatures, the band-to-defect peak luminescence intensity decreases relative to the tail-to-tail luminescence. The mid-gap defect states are almost half-full even at moderate quasi-Fermi level separation, whereas the occupation of the band-tail density of states drastically changes with temperature, since the quasi-Fermi levels lie within the band-tail states.

To investigate the influence of any absorber layer contamination to the luminescence spectra, the Figure 6.2 shows  $a\text{-Si:H}$  *pin* devices, where the thick, nominally intrinsic absorber layer is intentionally contaminated with dopant gases during *PECVD* deposition. The spectra are measured at  $T = 300$  K and the injection current density is  $J_d = 402$  mA cm<sup>-2</sup>. The concentrations ( $N_d$ ) of the dopants are determined from *secondary ion mass spectroscopy (SIMS)*. Woerdenweber *et al.* and Merdzhanova *et al.* previously presented these different types of absorber layer contamination: boron  $p$ -doped ( $N_d = 8 \times 10^{17}$  cm<sup>-3</sup>) [206], phosphorus  $n$ -doped ( $N_d$  unknown) [207], nitrogen  $n$ -doped ( $N_d = 4 \times 10^{19}$  cm<sup>-3</sup>) [208], and oxygen  $n$ -doped ( $N_d = 1 \times 10^{19}$  cm<sup>-3</sup>) [208–210]. For comparison, the nominally undoped  $a\text{-Si:H}$  *pin* device as investigated here, is also plotted in Figure 6.2 as black solid line.

All spectra from the doped devices show less EL intensity in the high photon energy range compared to the nominally undoped device. The highly nitrogen  $n$ -doped device shows a clear peak at  $\hat{E}_\gamma^{\text{bd}} = 0.88$  eV and another peak in the shoulder at  $\hat{E}_\gamma^{\text{tt}} = 1.18$  eV from a quenched tail-to-tail transition can be suspected. Since the  $\hat{E}_\gamma^{\text{bd}}$  and  $\hat{E}_\gamma^{\text{tt}}$  are slightly higher than typical  $a\text{-Si:H}$  devices from the same deposition, the mobility gap seems to be increased due to the nitrogen doping. However, the difference between the peak photon energies  $\Delta\hat{E}_\gamma = \hat{E}_\gamma^{\text{tt}} - \hat{E}_\gamma^{\text{bd}} \approx 0.3$  eV is typical for  $n$ -doped  $a\text{-Si:H}$ , which is observed for phosphorus  $n$ -doping by Street *et al.* [60]. The situation is different for the oxygen and the phosphorus  $n$ -doped devices compared to the nitrogen  $n$ -doping. In the high energy range, it is very hard to distinguish between these and the boron  $p$ -doped device. All these devices may show a quenched tail-to-tail transition approxi-

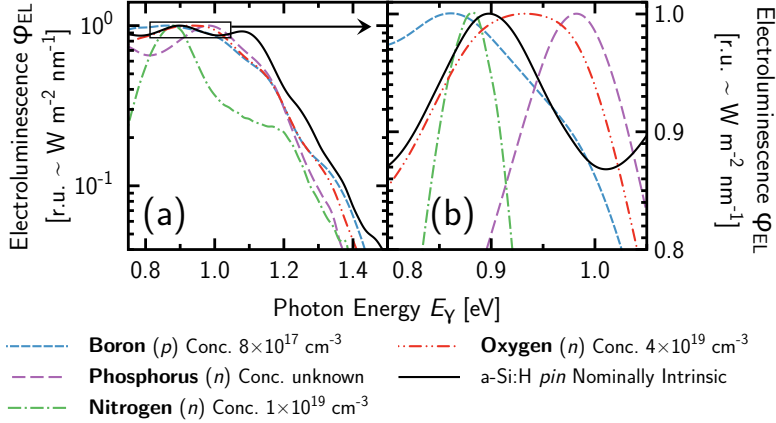


**Figure 6.2:** Measured electroluminescence spectra of different *a*-Si:H *pin* devices with intentionally contaminated intrinsic layer. Contamination gases are boron (plotted as blue dashed line, *p*-doping, dopant concentration  $N_d = 8 \times 10^{17} \text{ cm}^{-3}$ ), phosphorus (purple dashed line, *n*-doping, dopant concentration is unknown), nitrogen (green dot-dashed line, *n*-doping, dopant concentration  $N_d = 1 \times 10^{19} \text{ cm}^{-3}$ ), and oxygen (red double dot-dashed line, *n*-doping, dopant concentration  $N_d = 4 \times 10^{19} \text{ cm}^{-3}$ ). For comparison, the in-depth investigated standard *a*-Si:H *pin* device is also plotted as black solid line. All spectra are normalized to its highest signal. Spectra are measured at temperature  $T = 300 \text{ K}$  and high injection  $J_d = 402 \text{ mA cm}^{-2}$ . (a) General plot and (b) magnification of the electroluminescence peaks.

ately at  $\hat{E}_\gamma^{\text{tt}} = 1.14 \text{ eV}$ , however, the low photon energy peak is suspicious. The phosphorus *n*-doped device shows a rather sharp peak at  $\hat{E}_\gamma^{\text{bd}} = 0.98 \text{ eV}$ , whereas the oxygen *n*-doped device in contrast shows a very broad peak at  $\hat{E}_\gamma^{\text{bd}} \approx 0.93 \text{ eV}$  (see Figure 6.2(b)). And from the boron *p*-doped device a peak at  $\hat{E}_\gamma^{\text{bd}} = 0.87 \text{ eV}$  can be observed. However, at  $E_\gamma = 0.98 \text{ eV}$  the EL spectrum from this *p*-doped device shows a kink, which may arise from an additional dopant.

However, boron and oxygen are possible candidates for an increased band-to-defect luminescence from a nominally intrinsic absorber layer. On the one hand, silicon has a very high chemical affinity to oxygen. And on the other hand, the absorber layer of this investigated *pin* device is grown on top of a boron doped *p*-layer. Therefore, a diffusion of boron atoms to the nominally intrinsic absorber layer is feasible. Additionally, the *n*-doped devices in Figure 6.2 tend to show a narrow band-to-defect lineshape or at least a steep edge in case of oxygen, in contrast to the *p*-doped devices, which is also reported by Street *et al.* [60]. The rather broad lineshape of the investigated *a*-Si:H *pin* device here, may indicate the induction of additional mid-gap defect states due to a slight boron doping.

Furthermore, Street *et al.* found the same difference between the peak photon energies  $\Delta \hat{E}_\gamma = \hat{E}_\gamma^{\text{tt}} - \hat{E}_\gamma^{\text{bd}} \approx 0.20 \text{ eV}$  [60] as the here investigated *a*-Si:H *pin* device. However, the  $\Delta \hat{E}_\gamma$  is no clear indicator for the doping, since the tail-to-tail luminescence from *a*-Si:H shows a strong blue shift. Qiu and Pankove for instance reported  $\Delta \hat{E}_\gamma = \hat{E}_\gamma^{\text{tt}} - \hat{E}_\gamma^{\text{bd}} = 0.45 \text{ eV}$  with  $\hat{E}_\gamma^{\text{bd}} = 0.75 \text{ eV}$

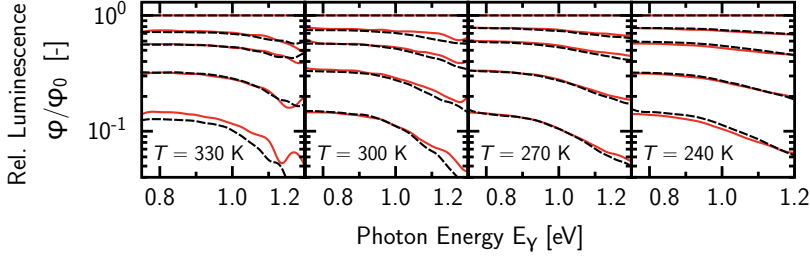


**Figure 6.3:** Measured spectra ( $\varphi$ ) from electro- (black solid lines) and photoluminescence (red dashed lines) of  $a$ -Si:H  $pin$  device as shown in Figure 6.1 related to the most intense spectrum ( $\varphi_0$ ) each.

and  $\hat{E}_\gamma^{tt} = 1.20$  eV from heavily  $p$ -doped  $a$ -Si:H [205]. Therefore, the difference between both peak photon energies from boron doped  $a$ -Si:H can be expected within  $\Delta\hat{E}_\gamma = 0.20 - 0.45$  eV, which may indicate that the investigated  $a$ -Si:H  $pin$  device is only slightly boron doped, since we found  $\Delta\hat{E}_\gamma \approx 0.20$  eV.

In summary, high quasi-Fermi level separation in an  $a$ -Si:H  $pin$  device yields PL and EL spectra predominantly from tail-to-tail transitions. This is the case either at low temperatures or under high injection around room temperature. In the contrary case of low injection around room temperature with little quasi-Fermi level separation, transitions from band to neutral mid-gap defect states dominate the PL or EL. These mid-gap defect states are maybe induced by an unintentional diffusion of boron atoms from the  $p$ -doped to the nominally intrinsic absorber layer.

### 6.1.1 Temperature and Voltage Dependent Luminescence Spectra

And again, the  $RR$  requires unchanged spectral shape from EL under different bias conditions. For this reason, Figure 6.3 shows the  $\varphi_{PL}$  and  $\varphi_{EL}$  from Figure 6.1 related to the most intense spectrum ( $\varphi_0$ ) each, *i.e.*  $\varphi_{PL}/\varphi_{PL,0}$  plotted as red dashed, and  $\varphi_{EL}/\varphi_{EL,0}$  plotted as black solid lines at high temperatures  $T = 330, 300, 270$ , and  $240$  K, where the band-to-defect luminescence is present. The  $\varphi_{PL}$  is plotted in Figure 6.3 for comparison with  $\varphi_{EL}$ , since the radiative ideality factor is deduced from PL and the linear superposition of  $\varphi_{PL}$  and  $\varphi_{EL}$  is required by the  $RR$ .

The spectra at different temperatures show almost the same behavior. In the low photon energy range  $E_\gamma < 0.9$  eV, predominantly at low injection, where the band-to-defect luminescence is present, the spectra show less blue shift than in the high photon energy range  $E_\gamma > 0.9$  eV, where the tail-to-tail luminescence is present. These different blue shifts between band-to-defect and tail-to-tail luminescence yield a very distinctive kink at  $E_\gamma \approx 0.9$  eV and low injection.

Blue shifts are known from band-tail states involved luminescence as already presented within Cu(In,Ga)Se<sub>2</sub> (see Chapter 4) and  $\mu c$ -Si:H (see Chapter 5). The blue shift from tail-to-tail transitions increases with increasing characteristic energy of the band-tail densities of states. The characteristic energies of the band-tail densities of states in  $a$ -Si:H are expected to be higher

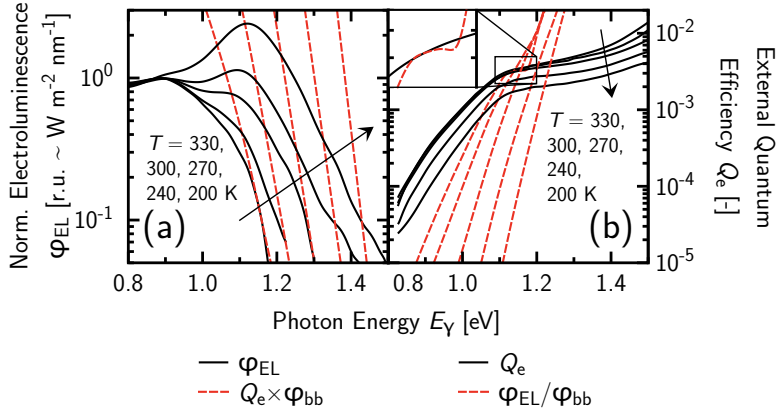


**Figure 6.4:** Reciprocity relation between measured electroluminescence (EL) spectra ( $\varphi_{\text{EL}}$ ) and external quantum efficiency ( $Q_e$ ) of *a*-Si:H *pin* device. Temperature varies in the range  $T = 330, 300, 270, 240$ , and  $200$  K (arrows). The injection current density under EL conditions is  $J_d = 39.0 \text{ mA cm}^{-2}$ . (a) Normalized  $\varphi_{\text{EL}}$  is plotted as black solid lines, and  $\varphi'_{\text{EL}} \propto Q_e \times \varphi_{\text{bb}}$  as red dashed lines, where  $\varphi_{\text{bb}}$  is the hemispheric black-body radiation. (b) The  $Q_e$  is plotted as black solid lines, and  $Q'_e \propto \varphi_{\text{EL}}/\varphi_{\text{bb}}$  as red dashed lines. The magnification box shows little overlap between  $Q_e$  and  $Q'_e$  at  $T = 330$  K.

than in  $\text{Cu(In,Ga)Se}_2$  or  $\mu\text{c-Si:H}$ . Therefore, the here observed blue shift in *a*-Si:H is stronger than in  $\text{Cu(In,Ga)Se}_2$  or  $\mu\text{c-Si:H}$ . The characteristic energies of the valence  $E_{v0} \approx 45 \text{ meV}$  [85, 169, 170, 174] and conduction  $E_{c0} \approx 27 \text{ meV}$  [174] band-tail densities of states, where  $E_{v0} > E_{c0}$  is regularly found.

The band-to-defect luminescence is present in the photon energy region  $E_\gamma < 0.9 \text{ eV}$ . The mid-gap defect states are almost saturated even at moderate quasi-Fermi level separation, and therefore almost no blue shift can be observed at this rather high injection.

### 6.1.2 Reciprocity Relation

The *RR* between the  $\varphi_{\text{EL}}$  and the  $Q_e$  shows strong disagreement from measurements, since mid-gap defect states strongly influence the  $Q_e$ . The Figure 6.4(a) shows the  $\varphi_{\text{EL}}$ , which are normalized to the low photon energy band-to-defect peak, which is plotted as black solid lines in the high temperature range  $T = 330 - 200$  K. The  $\varphi_{\text{EL}}$  are measured at lowest feasible injection, *i.e.* current density  $J_d = 39.0 \text{ mA cm}^{-2}$ . The  $\varphi'_{\text{EL}} \propto Q_e \times \varphi_{\text{bb}}$ , where  $\varphi_{\text{bb}}$  is the hemispheric black body radiation, are plotted as red dashed lines. The Figure 6.4(b) shows the opposite process, *i.e.*  $Q_e$  plotted as black solid lines, and the  $Q'_e \propto \varphi_{\text{EL}}/\varphi_{\text{bb}}$  from electroluminescence. Only a small overlap between  $\varphi_{\text{EL}}$  and  $\varphi'_{\text{EL}}$  at the highest temperature can be observed in Figure 6.4(a) at the high energy edge of  $\varphi_{\text{EL}}$ . Even the slopes of  $\varphi_{\text{EL}}$  and  $\varphi'_{\text{EL}}$  do not fit in any case of lower temperatures  $T \leq 300$  K. In Figure 6.4(b), the primarily measured  $Q_e$  is shallower than the deduced  $Q'_e$ . The  $Q_e$  decreases with decreasing temperature due to lowered charge carrier transport.

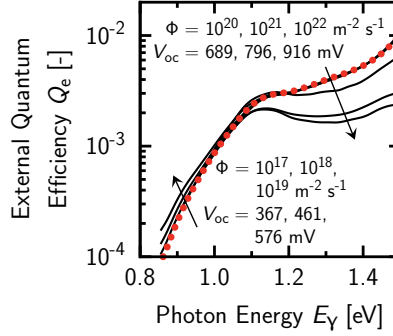


**Figure 6.5:** External quantum efficiency ( $Q_e$ ) of  $a$ -Si:H  $pin$  device at temperature  $T = 300$  K measured with bias light (black solid lines). The reference without bias light is plotted as red dotted line. Photon flux of bias light at a wavelength of  $\lambda = 671$  nm is  $\phi = 10^{17} - 10^{22} \text{ m}^{-2} \text{ s}^{-1}$  (compare arrows). This yields the open circuit voltages  $V_{oc} = 367, 461, 576, 689, 796, \text{ and } 916$  mV.

However, the inset in Figure 6.4(b) shows a small overlap between  $Q_e$  and  $Q'_e$ . The  $Q_e$  shows dominant defect absorption (compare Figure 2.11), whereas the  $Q'_e$  shows a contribution from band-tail states. This indicates that there is a Stokes-shift in  $a$ -Si:H [123]. The  $\hat{E}_\gamma$  from tail-to-tail transitions is lower than the primarily difference between the occupied band-tail densities of states due to interaction with the lattice, which absorbs the Stokes-shift energy ( $\Delta E_\gamma^{\text{Stokes}}$ ) in this case. Street *et al.* estimated the  $\Delta E_\gamma^{\text{Stokes}} \leq 0.40$  eV, so that the relaxation energy is about 0.20 eV [124], however, the Stokes-shift depends on the deposition conditions, *i.e.* the substrate temperature or the power of the PECVD plasma for instance [121]. Even influences from the excitation energy to the  $\Delta E_\gamma^{\text{Stokes}}$  are reported [122, 125] (however, this may be related to the excitation dependent blue shift, which is observed from band-tail states). Therefore, various Stokes-shift energies in  $a$ -Si:H and similar materials are cited. Shah *et al.* observed  $\Delta E_\gamma^{\text{Stokes}} = 0.29$  eV in  $a$ -Si:H [122]. And Park *et al.* found  $\Delta E_\gamma^{\text{Stokes}} = 0.30$  eV in  $a$ -Si quantum dots [126].

The opposite point of view to a Stokes-shift is that the electrons ( $E_{tn}$ ) and holes ( $E_{tp}$ ), respectively, thermalize from the conduction ( $E_c$ ) and valence ( $E_v$ ) band mobility edges into the band-tails without significant relaxation effects. Therefore, the  $\hat{E}_\gamma = E_c - E_v - E_{tn} - E_{tp}$  [211]. From the comparison between  $Q_e$  and  $Q'_e$  in Figure 6.4(b) a Stokes-shift  $\Delta E_\gamma^{\text{Stokes}} \approx 0.20 - 0.30$  eV can be estimated. However, a Stokes-shifted tail-to-tail luminescence is one aspect for the insufficient  $RR$  between  $Q_e$  and  $Q'_e$ . Another aspect is the difference between the almost equilibrium conditions at low injection for the  $Q_e$  measurements and the non-equilibrium conditions in case of high injection for  $\varphi_{EL}$ .

To reduce the difference between the non-equilibrium conditions at  $\varphi_{EL}$  and the equilibrium conditions at  $Q_e$ , the  $Q_e$  is measured with bias light (see Figure 6.5). Note that the contacts are still short circuited. This bias light may reduce the mid-gap defect contribution to the  $Q_e$ , since the mid-gap defect occupation should saturate with increasing injection, and therefore

the  $\varphi'_{\text{EL}} \propto Q_e \times \varphi_{\text{bb}}$  could be compatible with the  $\varphi_{\text{EL}}$ . The Figure 6.5 shows the reference without bias light at  $T = 300$  K, which is plotted as red dotted line. The  $Q_e$  under different bias conditions from photon fluxes  $\phi = 10^{17} - 10^{22} \text{ m}^{-2} \text{ s}^{-1}$  at the wavelength  $\lambda = 671 \text{ nm}$  ( $E_{\text{ph}} = 1.85 \text{ eV}$ ), which is approximately equivalent to the mobility gap, are plotted as black solid lines.

The  $Q_e$  in the low photon energy region with low photon flux ( $\phi = 10^{17} - 10^{19} \text{ m}^{-2} \text{ s}^{-1}$ ) increases with increasing injection, whereas the  $Q_e$  in the high energy range  $E_\gamma > 1.10 \text{ eV}$  is not affected. This low bias light slightly improves the collection efficiency of deep trapped charge carriers, since the low energy edge of  $Q_e$  originates from the interaction between band-tail and mid-gap defect states.

However, the  $Q_e$  in the high energy range under high bias conditions ( $\phi = 10^{20} - 10^{22} \text{ m}^{-2} \text{ s}^{-1}$ ), where the absorption from the interaction between band and mid-gap defect states is present, is reduced by the factor of 2.5. Thus the disagreement between  $Q_e$  and  $Q'_e$  is not only due to a Stokes-shifted tail-to-tail luminescence, also the difference between equilibrium and non-equilibrium hampers the *RR*. However, the bias light does not close the gap in the *RR* between  $Q_e$  and  $\varphi_{\text{EL}}$ , as long as a Stokes-shift is present.

In summary, it is hard to prove the *RR* between  $\varphi_{\text{EL}}$  and  $Q_e$  within experiments, since the  $\varphi_{\text{EL}}$  from tail-to-tail transitions is influenced by a Stokes-shift and the bias conditions between  $\varphi_{\text{EL}}$  and  $Q_e$  strongly diverge. However, this incompatibility is discussed later on within numerical simulations.

### 6.1.3 Radiative Ideality Factor

The radiative ideality factor ( $n_r$ ) can indicate the states, which are involved in the luminescence process. The  $n_r$  is determined by fitting a common diode law to the luminescence intensity ( $\phi$ ) versus the bias voltage ( $V$ ) under EL, or the open circuit voltage ( $V_{\text{oc}}$ ) for various excitation intensities under PL conditions. These measured  $\phi_{\text{PL}}/V_{\text{oc}}$  characteristics from PL are plotted as red solid lines in Figure 6.6(a) from band-to-defect and in (c) from tail-to-tail luminescence in a wide temperature range  $T = 330 - 100 \text{ K}$ . To test if blue shifted tail-to-tail luminescence in combination with an unequal spectral sensitivity of the used setup influences the evidence of the  $\phi_{\text{PL}}/V_{\text{oc}}$  characteristics, the numerically integrated spectra from Figure 6.1 ( $\phi'_{\text{PL}} [\text{m}^{-2} \text{ s}^{-1}] = \int \varphi_{\text{PL}} [\text{W m}^{-2} \text{ nm}^{-1}] E_\gamma^{-3} d E_\gamma$ ) are plotted as red open circles together with the integrally measured PL (red solid lines). Since the band-to-defect and the tail-to-tail luminescence are similar in intensity around room temperature, the  $\phi_{\text{PL}}$  and  $\phi_{\text{EL}}$  are measured with an adapted setup. The low photon energies  $E_\gamma < 1.1 \text{ eV}$ , where the band-to-defect luminescence is present, are measured with the liquid nitrogen cooled germanium detector and additionally a 1.1 mm thick crystalline silicon wafer as edge filter. The high photon energies  $E_\gamma > 1.1 \text{ eV}$ , where the tail-to-tail luminescence is present are measured with an uncooled silicon detector, which has a circular active area of 2 mm diameter. Note that the comparison between Figure 6.6(a) and (c) shows a more reliable signal from the germanium than from the silicon detector. The slopes of the  $\phi_{\text{PL}}/V_{\text{oc}}$  characteristics are plotted as black dotted lines at the highest temperature  $T = 330 \text{ K}$ . The band-to-defect luminescence shows a shallower  $\phi_{\text{PL}}/V_{\text{oc}}$  characteristic than the tail-to-tail luminescence in a wide temperature range. Since the  $n_r$  from tail-to-tail lu-

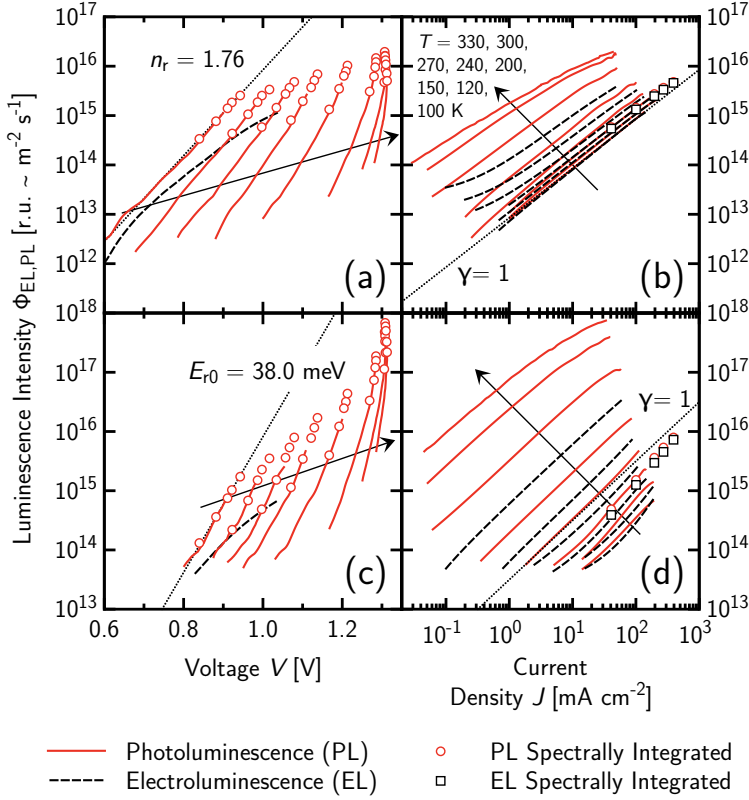


**Figure 6.6:** Integrally measured photo- (PL) and electroluminescence (EL) of *a*-Si:H *pin* device at temperatures  $T = 330, 300, 270, 240, 200, 150, 120$ , and  $100$  K (arrows). The EL is plotted as black dashed lines, and the PL as red solid lines. Integrated signals from EL spectra are plotted as black open squares, and from PL as red open circles. The PL is excited at the wavelength  $\lambda = 532$  nm. The PL as a function of the open circuit voltage at (a) photon energies  $E_\gamma < 1.1$  eV (band-to-defect luminescence) and (c)  $E_\gamma > 1.1$  eV (tail-to-tail luminescence). The PL/voltage characteristics, which follow a common diode law with ideality factor (a)  $n_r = 1.76$  and (c) times thermal energy  $n_r kT = E_{r0} = 38.0$  meV are plotted as black dotted lines for highest temperature  $T = 330$  K. The PL and EL at (b)  $E_\gamma < 1.1$  eV (band-to-defect luminescence) and (d)  $E_\gamma > 1.1$  eV (tail-to-tail luminescence) as a function of injection current density  $J = J_d = -J_{sc}$ , where  $J_{sc}$  is the short circuit current density under illumination for PL. The luminescence intensity, which scales linear with  $J$  is plotted as black dotted lines.



minescence is allocated to the characteristic energies of the valence ( $E_{v0}$ ) and conduction ( $E_{c0}$ ) band-tail densities of states, a mixed characteristic energy ( $E_{r0} = n_r kT$ ) can be determined. The derived  $E_{r0}$  indicates the theoretical, mixed characteristic energy ( $E_0$ ). As already mentioned (see Eq. (2.27)), the tail-to-tail luminescence writes as

$$\phi \propto \exp\left(\frac{qV}{2E_{c0}}\right) \exp\left(\frac{qV}{2E_{v0}}\right) \quad (6.1)$$

if the quasi-Fermi level separation  $\Delta E_f = V$ . From the denominators of the exponential functions follows

$$E_0 = \frac{2E_{c0}E_{v0}}{E_{c0} + E_{v0}} = n_r kT. \quad (6.2)$$

The derived  $E_{r0} = 38.0 \text{ meV}$  seems to be consistent with already reported results from *a*-Si:H and similar materials. If the  $E_{v0}$  is assumed to be approximately 45 meV [85, 169, 170], it follows the  $E_{c0} \approx 34 \text{ meV}$  from Eq. (6.2), which is in the region of the  $\mu\text{c}$ -Si:H conduction band-tails, which is determined in Chapter 5.

In comparison, the  $n_r$  from band-to-defect luminescence hides the information of the width of the dangling bond distribution ( $\sigma_{db}$ ). However, even at moderate quasi-Fermi level separation, the mid-gap defect states are far from the quasi-Fermi levels and the  $\sigma_{db}$  is not accessible. In fact, at moderate quasi-Fermi level separation, the charge carrier occupation function at the mid-gap defect states is almost constant, and for this reason, the  $n_r$  from band-to-defect luminescence is also expected to be constant, which is discussed in detail later on.

Furthermore, both  $\phi_{PL}/V_{oc}$  characteristics in Figure 6.6(a) and (c) show an increasing upward bending at lower temperatures and/or with increasing injection due to band-bending, which is already observed from  $\mu\text{c}$ -Si:H.

Whereas the band-to-defect luminescence changes one order of magnitude at highest injection in the given temperature range, the tail-to-tail luminescence changes almost three orders of magnitude. However, an increasing influence to the band-to-defect  $\phi_{PL}/V_{oc}$  characteristics from the tail-to-tail luminescence at lower temperatures is feasible, since the tail-to-tail luminescence intensity increases faster than the band-to-defect luminescence (see Figure 6.1), and the silicon edge filter does not eliminate the tail-to-tail luminescence at  $E_\gamma < 1.1 \text{ eV}$ .

As can be seen from Figure 6.6(a) and (c) the bias contact voltage ( $V$ ) under EL conditions (plotted as black dashed line) is hardly influenced by series resistance effects. Therefore, the Figure 6.6(b) and (d) compare the  $\phi_{PL}$  and  $\phi_{EL}$  as a function of injection current  $J_d = -J_{sc}$ , where  $J_{sc}$  is the short circuit current under PL conditions. The  $\phi_{EL}$  is plotted as black dashed lines, and the  $\phi'_{EL}$  from numerically integrated spectra is plotted as black open squares. Additionally, black dotted lines with a slope of unity are plotted as a guide to the eye. And again, the fast increase of the tail-to-tail luminescence with decreasing temperature is noticeable compared to the band-to-defect luminescence. Generally, the lower the temperature, the higher the PL and EL intensity, which originates from a higher quasi-Fermi level separation. The  $J_{sc}$  continuously decreases with decreasing temperature due to lower charge carrier collection efficiency. Whereas the  $\phi_{EL}/J_d$  and  $\phi_{PL}/J_{sc}$  characteristics from band-to-defect luminescence coincide at highest temperatures  $T = 330 - 270 \text{ K}$ , the PL and EL from tail-to-tail transitions deviate. In general the

EL is less intense than the PL at the same injection levels. Such a deviation from band-to-defect luminescence occurs at lower temperatures  $T = 240 - 150$  K, where charge carrier transport plays an important role.

Furthermore, the band-to-defect luminescence shows distinctive linear behavior ( $\gamma = 1$ ), which is also reported by Street *et al.* [60]. At lower temperatures, the measurements are affected by dominant tail-to-tail luminescence, and therefore show a shift from linear to sub-linear behavior as known from tail-to-tail luminescence in  $\mu\text{c-Si:H}$  in Chapter 5. The tail-to-tail luminescence in Figure 6.6(d) shows the same continuous shift, however, in the whole given temperature range.

In conclusion, the luminescence intensities from band-to-defect and tail-to-tail transitions can be separated from each other around room temperature. Dominant tail-to-tail luminescence at lower temperatures influences the evaluation of band-to-defect luminescence.

The  $\phi_{\text{PL}}/V_{\text{oc}}$  characteristics from tail-to-tail luminescence show a  $n_{\text{r}} = 1.34$  at  $T = 330$  K, which is equivalent to  $E_{\text{r0}} = 38.0$  meV. This indicates the characteristic energy of the conduction band-tail density of states  $E_{\text{c0}} = 34$  meV if the slope of the valence band-tail is assumed to be  $E_{\text{v0}} = 45$  meV according to [85, 169, 170, 174]. The  $n_{\text{r}} = 1.76$  from band-to-defect luminescence shows a shallower  $\phi_{\text{PL}}/V_{\text{oc}}$  characteristic.

In contrast to the tail-to-tail luminescence, which is already known from  $\mu\text{c-Si:H}$ , the band-to-defect luminescence intensity shows temperature independent linear behavior in the temperature range  $T = 330 - 172$  K from  $\phi_{\text{PL}}/J_{\text{sc}}$  and  $\phi_{\text{EL}}/J_{\text{d}}$  characteristics.

## 6.2 Discussion

This section models the investigated  $a\text{-Si:H}$  *pin* device with the full one dimensional numerical device simulator *ASA* in connection with *LUME* for luminescence and external quantum efficiency calculations around room temperature  $T = 330 - 270$  K, where the band-to-defect luminescence is present. Subsequently, the measurements are discussed with the help of the well modeled device with respect to the *reciprocity relation* (*RR*). Furthermore, the simulations show results from luminescence and external quantum efficiency calculations, which are beyond the limits of the measurements. These simulations give a deeper understanding predominantly for the *RR* between luminescence and external quantum efficiency from mid-gap defect states. The luminescence from these states is only accessible at high temperatures, which therefore requires high injection within the measurements, far from the thermal equilibrium.

### 6.2.1 Device Modeling and Characterization

The modeling of the investigated  $a\text{-Si:H}$  *pin* device follows the same procedure as shown in Chapter 5. The parameter set used here bases on the References [72, 154] as presented in detail in Section 3.2.1. The contact series resistance ( $R_{\text{s}}$ ), which is limited by the ohmic offset ( $R_{\text{s}}^{\text{e}}$ ), and the mobility gap ( $E_{\mu}$ ) is investigated separately. The remaining parameters are calibrated with common current/voltage ( $J/V$ ) characteristics of the device in the dark and under illumination. The already shown PL and EL spectra, and the external quantum efficiency measurements complete this calibration.

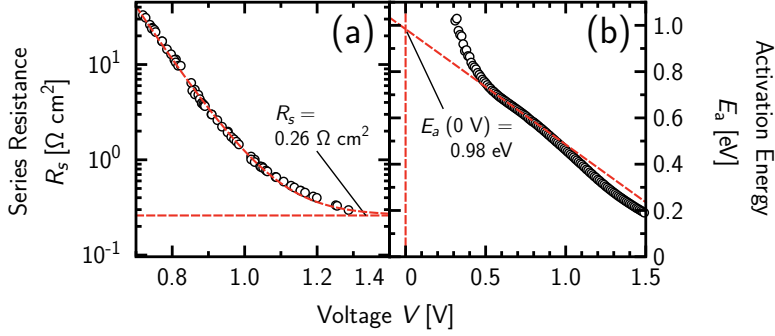


**Figure 6.7:** (a) Series resistance ( $R_s$ ) and (b) activation energy ( $E_a$ ) measured from *a*-Si:H *pin* device. Measurements are plotted as black open circles. (a) Ohmic contact series resistance  $R_s^e = 0.26 \Omega \text{ cm}^2$  at temperature  $T = 330 \text{ K}$  is determined by fitting an offset value to the exponential behavior (see Eq. (3.8)). This fit is plotted as red dashed lines. (b) Measured activation energy ( $E_a$ ) is determined from dark current/voltage characteristics at temperatures  $T = 290, 298, 309$ , and  $323 \text{ K}$ . An extrapolated linear fit shows  $E_a = 0.98 \text{ eV}$  at zero volt. This fit is plotted as red dashed line.

### Contacts

The Figure 6.7(a) shows the  $R_s$  of the device in the dark, determined from the difference between a dark  $J/V$  characteristic and the  $J_{sc}/V_{oc}$  characteristic under different bias illumination at  $T = 330 \text{ K}$  as already presented in Section 3.2.1. The measurement is plotted as black open circles. The red dashed line shows a fit of Eq. (3.8). The resistance decreases with increasing quasi-Fermi level separation and saturates due to an ohmic offset, namely  $R_s^e$ . This offset is not very distinctive, however, the  $R_s^e = 0.26 \Omega \text{ cm}^2$  can be estimated by fitting the bending at  $V > 1.0 \text{ V}$ .

### Mobility Gap

The mobility gap ( $E_\mu$ ) is determined by activation energy ( $E_a$ ) measurements of the device in the dark (see Figure 6.7(b)). The  $E_a$  is determined from  $J/V$  characteristics at  $T = 290, 298, 309$ , and  $323 \text{ K}$ , which yields the medium  $E_\mu$  at  $T = 305 \text{ K}$ . The  $E_a$  at  $V \approx 300 - 500 \text{ mV}$  rapidly decreases to higher voltages. The recombination in this low voltage region is dominated by mid-gap defect states. Influences by a shunt would yield a  $E_a \approx 0 \text{ eV}$ , which is not observed here.

Above  $V \approx 500 \text{ mV}$  at  $V = 574 - 720 \text{ mV}$  the medium slope of  $E_a$  is  $-1/2$ , which therefore corresponds to the  $E_\mu$  according to Pieters *et al.* [61]. A linear extrapolation of the  $E_a$  from this voltage region to  $V = 0 \text{ V}$  together with Eq. (3.10) yields the  $E_\mu = 2E_a(0 \text{ V}) - 6kT = 1.80 \text{ eV}$ . Willemen, and Zhu *et al.* found a similar  $E_\mu = 1.75 \text{ eV}$  [62, 68]. However, previously reported  $E_\mu$  from *a*-Si:H vary in the range  $\approx 1.7 - 2.1 \text{ eV}$  within uncertainties of a few tenths of an eV [153, 212–215].

Above  $V \approx 750 \text{ mV}$  the  $E_a$  strongly decreases with increasing bias voltage due to limited charge

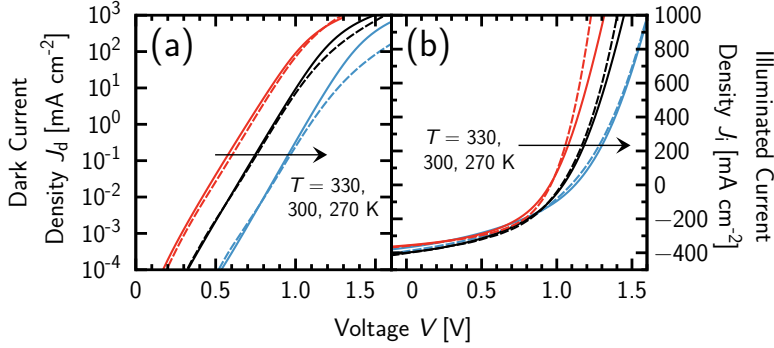


**Figure 6.8:** Temperature dependent current/voltage characteristics of *a*-Si:H pin device (a) in the dark and (b) under illumination. Temperatures are  $T = 330, 300$ , and  $270$  K (arrows). Measurements are plotted as dashed lines, and simulations are plotted as solid lines. (b) Charge carrier generation is excited with a photon flux  $\phi = 3.2 \times 10^{22} \text{ m}^{-2} \text{ s}^{-1}$  at the wavelength  $\lambda = 532 \text{ nm}$ .

carrier transport and may converge to  $E_a = 0 \text{ eV}$  due to the influence of an ohmic contact series resistance.

A detailed description of the parameter fitting to  $J/V$  characteristics is given in the following through Figure 6.8. The Figure 6.8(a) shows a semilogarithmic  $J/V$  characteristic of the *a*-Si:H pin device in the dark at  $T = 330, 300$ , and  $270$  K. The corresponding linear  $J/V$  characteristics of the device under illumination with a photon flux  $\phi = 3.2 \times 10^{22} \text{ m}^{-2} \text{ s}^{-1}$  at the wavelength  $\lambda = 532 \text{ nm}$  are shown in Figure 6.8(b). The simulated  $J/V$  characteristics, which are plotted as solid lines, are fitted to the measurements, which are plotted as dashed lines. Whereas the fitting shows good results up to  $V \approx 1.0 \text{ V}$ , the simulations and the measurements deviate in the higher voltage region, where the  $J/V$  characteristics saturate. The  $E_\mu$  is characterized beforehand, however, this and the effective densities of band states ( $N_c = 2.5 \times 10^{20} \text{ m}^{-3}$  and  $N_v = 3.0 \times 10^{20} \text{ m}^{-3}$ ) are adjusted by the current density in the higher voltage range, right below the saturation of the dark  $J/V$  characteristics. Whereas Zhu *et al.* reported  $N_v = 4.0 \times 10^{20} \text{ cm}^{-3}$  [68], Sellmer found a smaller  $N_v = 0.5 \times 10^{19} \text{ cm}^{-3}$  with thermoelectric power and Hall effect measurements in *p*-doped *a*-Si:H samples [155], which are very similar to the here investigated *a*-Si:H material. The reason for this discrepancy (between simulations and measurements) is unknown so far.

By fitting the  $J/V$  characteristics, the mobility gap is adjusted to  $E_\mu = 1.87 \text{ eV}$ , which is  $0.07 \text{ eV}$  higher than determined through activation energy measurements around  $T = 305 \text{ K}$ . According to Cody *et al.*, who measured the temperature dependence of the optical band gap from optical absorption spectroscopy [70], and Liang *et al.*, who measured electroabsorption [71, 72], the change of the temperature dependent mobility gap (see Eq. (2.5)) is assumed to be  $\alpha_\mu = 4.7 \times 10^{-4} \text{ eV K}^{-1}$ . Tsang *et al.* found a similar value  $\alpha_\mu = 4.3 \times 10^{-4} \text{ eV K}^{-1}$  in *a*-Si:H [73].

The charge carrier band mobilities for electrons ( $\mu_n$ ) and holes ( $\mu_p$ ) can be adjusted by fit-

ting the current saturation in the high voltage region of the dark  $J/V$  characteristics altogether with  $R_s^e$ , which is characterized beforehand. In the illuminated  $J/V$  characteristics the  $\mu_n$  and  $\mu_p$  influence the fill factor ( $FF$ ), *i.e.* the curvature at the point of maximum power, around  $V = 900 - 1100$  mV. However, this  $FF$  is also strongly influenced by the mid-gap defect states, *i.e.* the concentration of dangling bond states ( $N_{db}$ ), and its capture cross-sections can be modeled with the curvature of the illuminated  $J/V$  characteristics. The same holds for the dark  $J/V$  characteristics. Whereas steep  $J/V$  characteristics in the low voltage region are observed from the  $\mu c$ -Si:H *pin* device (see Figure 5.6), this *a*-Si:H *pin* device shows predominant recombination through mid-gap defects, which is the main reason for the poor fill factor  $FF = 44.1\%$  at  $T = 300$  K for instance. The device is treated under high injection and long exposure times of several hours at a given temperature, before the temperature is changed within the experiment. This originates a high mid-gap defect concentration, which slightly increases with prolonged treatment due to the Staebler-Wronski-Effect (SWE) [216, 217]. Although this SWE is also observed in  $\mu c$ -Si:H, the defect creation in *a*-Si:H is expected to be more efficient [218]. The dangling bond concentration is fitted to  $N_{db} = 5.1, 6.8, \text{ and } 8.9 \times 10^{16} \text{ cm}^{-3}$  at decreasing temperatures  $T = 330, 300, \text{ and } 270$  K.

However, the reason for the deviation between the measurements and the simulations in the high voltage region, where the current in the dark  $J/V$  characteristics saturates, is not clearly known. Whereas the deviation increases with decreasing temperature in the dark  $J/V$  characteristics, the opposite case holds for the device under illumination. Although, no distinctive influence can be observed from the activation energy (see Figure 6.7(b)), this may originate from a contact barrier at the *p*-contact between the zinc-oxide and the *p*-doped layer. Illumination reduces the influence of this feasible barrier, and higher temperature reduces its effective height.

Beside the  $J/V$  characteristics, the device is additionally modeled with PL and EL spectra at the same temperatures. Under PL conditions, the illumination is the same as for the corresponding  $J/V$  characteristics. The Figure 6.9(a) shows the PL spectra normalized to the lower photon energy peak around  $\hat{E}_\gamma = 0.89$  eV. The same applies to the EL spectra in Figure 6.9(b). The measurements are plotted as colored dashed lines, and the fitted simulations as colored solid lines. The simulated spectra from single transitions, *i.e.* band-to-defect and tail-to-tail, are exemplarily plotted as light red solid lines at  $T = 330$  K each.

The luminescence from tail-to-tail transitions increases with decreasing temperature compared to the band-to-defect luminescence as already mentioned. The EL simulations seem to fit better to the measurements than the PL. However, the simulated PL shows a more distinctive tail-to-tail peak compared to the EL, which can be also observed from the peak luminescence ratios in the measurements in Figure 6.1. In the measurements below  $T = 240$  K (see Figure 6.1) the low energy shoulder (band-to-defect transitions) from  $\varphi_{EL}$  is slightly more intense than from  $\varphi_{PL}$  compared to the tail-to-tail luminescence peak each. This relatively higher band-to-defect contribution to the  $\varphi_{EL}$  may yield from the defect-rich doped layers, since the recombination profile of the device in the dark, *i.e.* under EL conditions is slightly broader than of the illuminated device for PL.

Since the high photon energy peak around  $\hat{E}_\gamma = 1.10$  eV originates from tail-to-tail luminescence, the  $E_{c0}$  and  $E_{v0}$ , and the band-tail capture cross-sections can be fitted in this high photon energy region. The width and the position of the spectra are influenced by the  $E_{c0}$  and  $E_{v0}$ , re-

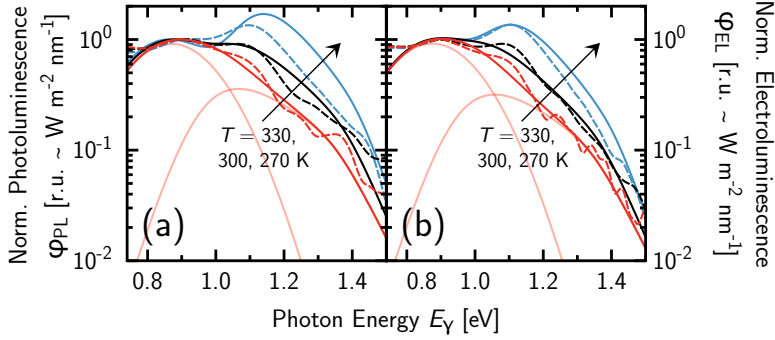


**Figure 6.9:** Temperature dependent (a) photo- (PL) and (b) electroluminescence (EL) spectra of *a*-Si:H *pin* device. Temperatures are  $T = 330, 300$ , and  $270$  K (arrows). Measurements are plotted as dashed lines, and composed simulations are plotted as solid lines. All spectra are normalized to unity at the low energy peak around  $E_\gamma = 0.89$  eV. The simulated spectra from single transitions are exemplarily plotted as light red solid lines at  $T = 330$  K each. (a) Charge carrier generation is excited with photon flux  $\phi = 3.2 \times 10^{22} \text{ m}^{-2} \text{ s}^{-1}$  at the wavelength  $\lambda = 532$  nm. (b) Injection current density  $J_d = -J_{sc} = 401 \text{ mA cm}^{-2}$  for EL, where  $J_{sc}$  is the short circuit current density of the device under illumination, *e.g.* PL conditions.

spectively. Additionally, the width is influenced by the ratio of the capture cross-sections of the band-tail states  $\sigma_r = \sigma_n/\sigma_p$ . And the position can be shifted with  $E_\gamma^{\text{Stokes}}$ . However, the characterization of  $E_{c0}$  and  $E_{v0}$  by fitting the spectra is ambiguous, since  $\sigma_r$  and  $E_\gamma^{\text{Stokes}}$  are not well known. Following the radiative ideality factor, which yields  $E_{r0} = 38.0$  meV, and the valence band-tail slope to be assumed  $E_{v0} = 45$  meV, the  $E_{c0} = 34$  meV is obtained. Furthermore, the ratio of the capture cross-sections of the band-tail states is assumed to be  $\sigma_r = 10$  [61, 62]. And a Stokes-shift  $E_\gamma^{\text{Stokes}} = 0.115$  eV fits to the measurement, although the comparison between  $Q_e$  and  $\varphi_{\text{EL}}$  in Figure 6.4(b) may yield  $E_\gamma^{\text{Stokes}} > 0.20$  eV.

In fact, the luminescence, which originates from the interaction between the extended band states and the mid-gap defect states, implies two different kinds of transitions, since dangling bonds are of amphoteric nature. The transition from either neutral mid-gap defects to valence band states, or from conduction band states to neutral mid-gap defects is dominant for band-to-defect luminescence. Simulations show that the interaction between charged mid-gap defects and band states is less intense with a photon peak energy  $\hat{E}_\gamma \approx 1.07$  eV. Beside the mobility gap, the spectral position of the band-to-defect luminescence depends on the position of the mid-gap defect state distributions ( $E_{\text{db}}$ ), the correlation energy between both kinds of amphoteric states ( $U$ ), and the width of each distribution ( $\sigma_{\text{db}}$ ). It is not much known about  $E_{\text{db}}$ . For this reason, the mid-gap defect states are assumed to be symmetrically distributed in the center of the mobility gap, *i.e.*  $E_{\text{db}} = 0.00$  eV. According to Lee *et al.* [168], and Willems [62], the correlation energy is assumed to be  $U = 0.20 - 0.30$  eV. This fitting here yields  $U = 0.20$  eV. The distribution width is fitted to  $\sigma_{\text{db}} = 120$  meV.

Note that the peak intensities may indicate the ratio between the density of states and mid-gap

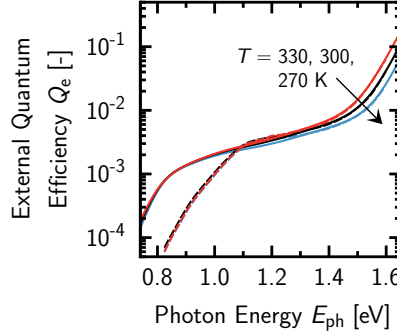


**Figure 6.10:** Measured external quantum efficiency ( $Q_e$ ) of *a*-Si:H *pin* device compared to simulations. Temperature varies in the range  $T = 330, 300$ , and  $270$  K (arrow). Measurements are plotted as colored dashed lines and simulations as colored solid lines.

defect concentration, *i.e.* on the one hand the  $N_{db}$ ,  $N_c$ , and  $N_v$  for band-to-defect luminescence, and on the other hand the  $N_{cvt}$  and  $N_{vbt}$  for tail-to-tail luminescence.

Furthermore, the simulation fitting parameters can be checked with the comparison between the measurements and the simulations of the  $Q_e$  in Figure 6.10. The measurements at  $T = 330, 300$ , and  $270$  K are plotted as colored dashed lines, and the corresponding simulations are plotted as colored solid lines. The  $Q_e$  continuously increases with increasing photon energy ( $E_\gamma$ ). In the lower photon energy range  $E_\gamma = 0.75 - 1.10$  eV, the  $Q_e$  is very similar at different temperatures. Beyond this photon energy range, the different  $Q_e$  deviate from each other. Since the  $Q_e$  in this photon energy range  $E_\gamma > 1.10$  eV originates from tail-to-tail and band-to-tail absorption (compare Figure 2.11), the  $Q_e$  gives additional indicators for well modeled conduction and valence band-tail states, *i.e.*  $E_{c0}$  and  $E_{v0}$ , and its density of states at the band edges ( $N_{c0}$  and  $N_{v0}$ ).

The broad plateau at  $E_\gamma \approx 0.90 - 1.40$  eV originates from the interaction between band and mid-gap defect states (compare Figure 2.11).

However, at low photon energies the measurements deviate from the simulations. This deviation could indicate to a much larger correlation energy  $U > 0.20$  eV, since this low photon energy edge originates from the interaction between band-tail and mid-gap defect states. And in addition to that, note that the  $Q_e$  needs two processes, namely the charge carrier generation due to *light absorption* and the charge carrier transport to the contacts. Therefore, it is more feasible that the low photon energy deviation yields from the poor charge carrier transport at the localized states, which is not included in the simulations of the  $Q_e$ .

Finally, after model calibration, the simulated  $\phi_{PL}/V_{oc}$  and  $\phi_{EL}/V$  characteristics (see Figure 6.11(a) and (c)), which yield the  $n_r$ , fit to the measurements as well as the  $\phi_{PL}/J_{sc}$  and  $\phi_{EL}/J_d$  characteristics (see Figure 6.11(b) and (d)). The Figure 6.11(a) and (b) correspond to luminescence photon energies  $E_\gamma < 1.10$  eV, where the band-to-defect luminescence is present.

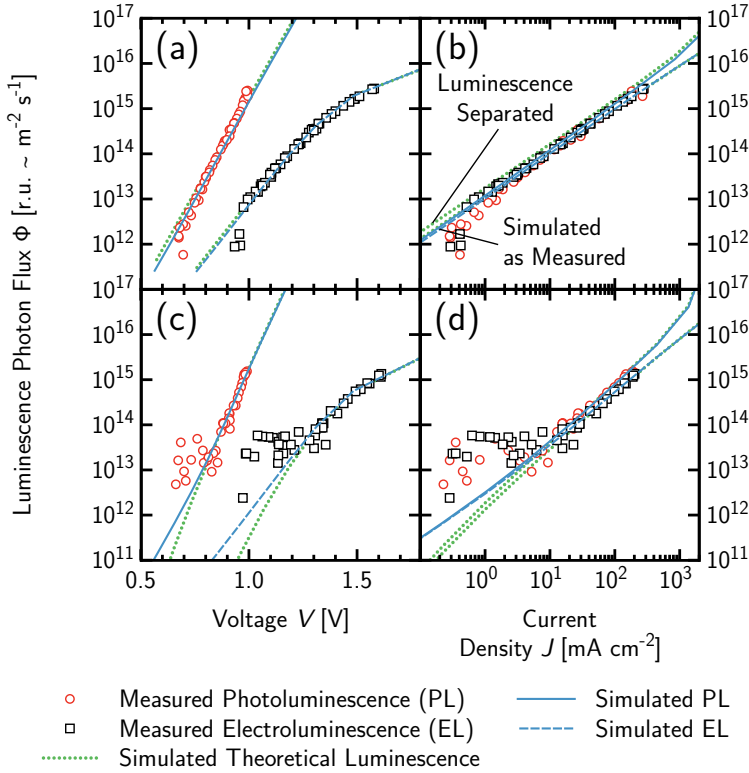


**Figure 6.11:** Comparison between measurements and simulations of integrated luminescence of *a*-Si:H *pin* device at temperature  $T = 300$  K. Measured photoluminescence (PL) is plotted as red open circles, and electroluminescence (EL) as black open squares. Charge carrier generation is excited with photon fluxes  $\phi = 2.3 \times 10^{20} - 3.2 \times 10^{22} \text{ m}^{-2} \text{ s}^{-1}$  at the wavelength  $\lambda = 532$  nm. Luminescence/voltage and luminescence/current characteristics from PL and EL in the photon energy range (a)+(b)  $E_\gamma < 1.10$  eV (band-to-defect transitions) and (c)+(d)  $E_\gamma > 1.10$  eV (tail-to-tail transitions). The injection current density is  $J = J_d = -J_{sc}$  under EL conditions, where  $J_{sc}$  is the short circuit current density of the device under illumination for PL.

Simulated PL with respect to the spectral sensitivity of the detector setup is plotted as blue solid lines, and EL as blue dashed lines. The green dotted lines show simulated PL and EL from (a)+(b) band-to-defect and (c)+(d) tail-to-tail recombination without accounting for the detector setup.



The Figure 6.11(c) and (d) show the results from tail-to-tail luminescence in the high photon energy range  $E_\gamma > 1.10$  eV. The PL measurements at medium temperature  $T = 300$  K are plotted as red open circles, and the EL is plotted as black open squares. Since the PL and EL is measured with a germanium and a silicon detector setup, the simulations also account for both setups. The PL and EL simulations, which include the detector setup, are plotted as blue solid and dashed lines, respectively. However, the luminescence from band-to-defect and tail-to-tail transitions superimpose. Since this superposition affects the measurements of integrated luminescence, the single spectra from band-to-defect and tail-to-tail luminescence simulations, which do not account for the detector setup, are plotted as green dotted lines.

Generally, the simulations fit well to the measurements. Even the saturation of the  $\phi_{EL}/V$  characteristics in the high injection region seems to be handled well. The influence due to the detector setup is rather small in the low photon energy region (see Figure 6.11(a) and (b)), since the slow increasing band-to-defect luminescence is dominant at  $T = 300$  K. However, the detector influence increases with decreasing injection, since the contribution from tail-to-tail transitions shifts into the low photon energy region, where the band-to-defect luminescence is present. Nevertheless, the detector influence in the high photon energy region is rather high (see Figure 6.11(c) and (d)), predominantly at low injection, where the fast decreasing tail-to-tail luminescence is negligible and the band-to-defect luminescence is dominant.

Both measured  $\phi_{PL}/V_{oc}$  characteristics in Figure 6.11(a) and (c) are steeper than the simulations. Whereas the measurements of the tail-to-tail luminescence intensity, which yield  $E_{r0} = 32.0$  meV, only cover a small range of about two orders of magnitude, the simulations ( $E_{r0} = 35.0$  meV) fit within the error. The difference between simulations and measurements of the band-to-defect luminescence in contrast, is significant. Whereas the measurements yield  $n_r = 1.69$ , the simulations show  $n_r = 1.95$ . The reason is an uncalibrated spectral sensitivity of the measurement setup in connection with the silicon edge filter, which has a broad spectral overlap with the tail-to-tail luminescence.

The measurements and simulations of the  $\phi/J$  characteristics in Figure 6.11(b) and (d) fit as well as the  $\phi/V$  characteristics. The  $\phi/J$  characteristics yield the exponent  $\gamma$  and the prefactor  $\phi_0$  by fitting  $\phi = \phi_0 J^\gamma$ . Whereas the  $\gamma = 1.0 - 1.1$  in the low photon energy region shows rather linear behavior (see Figure 6.11(b)), the  $\gamma = 1.3$  in the high photon energy region is super-linear (see Figure 6.11(d)). Super-linear  $\phi/J$  characteristics are already known from tail-to-tail luminescence in  $\mu c$ -Si:H *pin* devices (see Chapter 5). And Street *et al.* also reported the same super-linear behavior from tail-to-tail [60, 219] and a linear behavior from band-to-defect luminescence in *a*-Si:H *pin* devices around room temperature [60].

Overall, the modeling of the device shows good results yielding a parameter set, which is comparable to the results from Willemen [62], and Liang *et al.* [72, 154]. The whole parameter set is summarized in Table 6.1. However, the ratio between the peak intensities from band-to-defect and tail-to-tail luminescence are not handled very well. And the evaluation of the luminescence intensity from band-to-defect is strongly affected by the measurement setup.

**Table 6.1:** Simulation parameters of modeled *a*-Si:H *pin* device.

	<i>p</i> -Layer	<i>i</i> -Layer	<i>n</i> -Layer	Unit
STRUCTURE				
<i>d</i>	20	330	20	nm
TRANSPORT, DOPING, AND EXTENDED STATES				
$E_\mu$	1.87	1.87	1.87	eV
$\varepsilon_r$	11.9	11.9	11.9	—
$\chi$	3.97	4.00	3.97	eV
$\alpha_\mu$	0.47	0.47	0.47	meV K <sup>-1</sup>
$N_v$	$3.0 \times 10^{20}$	$3.0 \times 10^{20}$	$3.0 \times 10^{20}$	cm <sup>-3</sup>
$N_c$	$2.5 \times 10^{20}$	$2.5 \times 10^{20}$	$2.5 \times 10^{20}$	cm <sup>-3</sup>
$\mu_n$	14	14	14	cm <sup>2</sup> V <sup>-1</sup> s <sup>-1</sup>
$\mu_p$	5	5	5	cm <sup>2</sup> V <sup>-1</sup> s <sup>-1</sup>
$E_a$	0.35	0.00	0.25	eV
VALENCE BAND-TAIL STATES				
$E_{v,0}$	45	45	45	meV
$N_{v,0}$	$7.0 \times 10^{20}$	$7.0 \times 10^{20}$	$7.0 \times 10^{20}$	eV <sup>-1</sup> cm <sup>-3</sup>
$\sigma_p^0$	$1.0 \times 10^{-17}$	$1.0 \times 10^{-17}$	$1.0 \times 10^{-17}$	cm <sup>2</sup>
$\sigma_n^+$	$1.0 \times 10^{-16}$	$1.0 \times 10^{-16}$	$1.0 \times 10^{-16}$	cm <sup>2</sup>
CONDUCTION BAND-TAIL STATES				
$E_{c,0}$	34	34	34	meV
$N_{c,0}$	$7.0 \times 10^{20}$	$7.0 \times 10^{20}$	$7.0 \times 10^{20}$	eV <sup>-1</sup> cm <sup>-3</sup>
$\sigma_n^0$	$1.0 \times 10^{-17}$	$1.0 \times 10^{-17}$	$1.0 \times 10^{-17}$	cm <sup>2</sup>
$\sigma_p^-$	$1.0 \times 10^{-16}$	$1.0 \times 10^{-16}$	$1.0 \times 10^{-16}$	cm <sup>2</sup>
DANGLING BOND STATES				
$N_{db}$	$\geq 5.1 \times 10^{16}$	$\geq 5.1 \times 10^{16}$	$\geq 5.1 \times 10^{16}$	cm <sup>-3</sup>
$\sigma_{db}$	0.12	0.12	0.12	eV
$E_{db}$	0.00	0.00	0.00	eV
$U$	0.20	0.20	0.20	eV
$\sigma_p^0$	$4.0 \times 10^{-15}$	$4.0 \times 10^{-15}$	$4.0 \times 10^{-15}$	cm <sup>2</sup>
$\sigma_n^-$	$4.0 \times 10^{-15}$	$4.0 \times 10^{-15}$	$4.0 \times 10^{-15}$	cm <sup>2</sup>
$\sigma_p^-$	$4.0 \times 10^{-14}$	$4.0 \times 10^{-14}$	$4.0 \times 10^{-14}$	cm <sup>2</sup>
$\sigma_n^+$	$4.0 \times 10^{-14}$	$4.0 \times 10^{-14}$	$4.0 \times 10^{-14}$	cm <sup>2</sup>
ELECTRICAL CONTACT				
$R_s^{\text{ext}}$	0.26			$\Omega \text{ cm}^2$

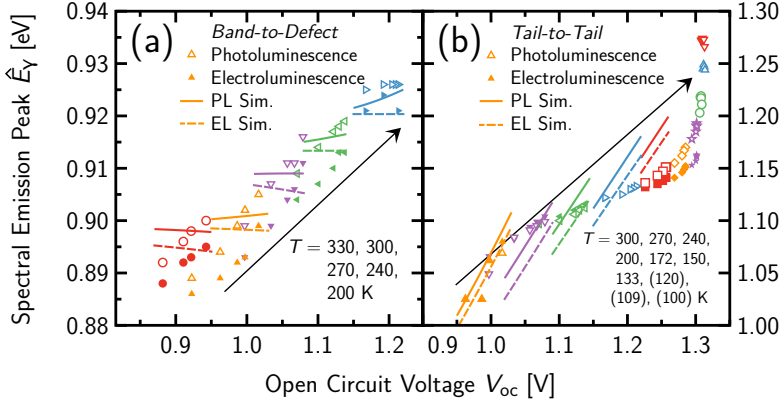


**Figure 6.12:** Temperature dependent spectral emission peak energy ( $\hat{E}_\gamma$ ) as a function of open circuit voltage ( $V_{oc}$ ) derived from measured electro- (EL) and photoluminescence (PL) spectra of *a*-Si:H *pin* device as shown in Figure 6.1. The PL is plotted as colored open symbols, and the EL as colored closed symbols. The PL is excited with photon fluxes  $\phi = 3.2 \times 10^{22}$ ,  $2.2 \times 10^{22}$ ,  $1.5 \times 10^{22}$ ,  $7.3 \times 10^{21}$ , and  $3.1 \times 10^{21} \text{ m}^{-2} \text{ s}^{-1}$  at the wavelength  $\lambda = 532 \text{ nm}$ . This yields short circuit current densities  $J_{sc} = 402, 274, 185, 91.5$ , and  $39.0 \text{ mA cm}^{-2}$  at temperature  $T = 300 \text{ K}$ . The  $V_{oc}$  at PL conditions is also allocated to the EL with corresponding injection current density ( $J = J_d = -J_{sc}$ ). (a) Low photon energy peaks from band-to-defect luminescence determined at temperatures  $T = 330, 300, 270, 240$ , and  $200 \text{ K}$  (arrow). (b) High photon energy peaks from tail-to-tail luminescence determined at temperatures  $T = 300, 270, 240, 200, 172, 150, 133, 120, 109$ , and  $100 \text{ K}$  (arrow). The  $\hat{E}_\gamma$  from EL are limited to  $T > 133 \text{ K}$  and the simulations are limited to  $T > 172 \text{ K}$  for technical reasons.

### 6.2.2 Change of Luminescence Spectra

The PL and EL spectra from tail-to-tail luminescence show an already mentioned blue shift, whereas the spectra from band-to-defect luminescence show almost no shift. The Figure 6.12 shows the photon peak energies ( $\hat{E}_\gamma$ ) from PL, which is plotted as colored open symbols, and from EL, which is plotted as colored closed symbols. The  $\hat{E}_\gamma$  from PL and EL are both allocated to the  $V_{oc}$  under illumination, *i.e.* PL conditions, since the bias voltage under EL conditions is strongly influenced by series resistance. The excitation photon fluxes are  $\phi = 3.2 \times 10^{22}$ ,  $2.2 \times 10^{22}$ ,  $1.5 \times 10^{22}$ ,  $7.3 \times 10^{21}$ , and  $3.1 \times 10^{21} \text{ m}^{-2} \text{ s}^{-1}$  at the wavelength  $\lambda = 532 \text{ nm}$ . The results from band-to-defect luminescence are plotted in Figure 6.12(a). The measurements are determined in the temperature range  $T = 330 - 200 \text{ K}$ . Below this temperature, the  $\hat{E}_\gamma$  cannot be determined, since the luminescence from tail-to-tail transitions dominates the spectra. The simulations are determined from single spectra. Generally, the  $\hat{E}_\gamma$  increases  $\Delta \hat{E}_\gamma \approx 26 \text{ meV}$  within a change of temperature  $\Delta T = 130 \text{ K}$ . The  $\hat{E}_\gamma$  of the PL is approximately  $5 \text{ meV}$  higher than of the EL. Due to more abrupt charge carrier occupation probabilities at lower temperatures, the  $V_{oc}$  increases  $\Delta V_{oc} \approx 272 \text{ mV}$  at constant charge carrier injection. At a given temperature, the measured  $\hat{E}_\gamma$  increases with increasing charge carrier injection. At  $T = 300 \text{ K}$  the  $\Delta \hat{E}_\gamma / \Delta V_{oc} = 175 \text{ meV V}^{-1}$  and  $\Delta \hat{E}_\gamma / \Delta J_{sc} \approx 16 \text{ meV dec}^{-1}$  for instance. The simula-

tions in contrast, show almost constant  $\hat{E}_\gamma$  at a given temperature. The charge carrier occupation probability of the mid-gap defect states is almost constant, even at moderate quasi-Fermi level separation (compare Figure 2.6). And the position of the maximum band state occupation at the band edges does not change with injection. For this reason, the increase of  $\hat{E}_\gamma$  with increasing injection in the measurements may indicate band gap fluctuations. However, these fluctuations are neglected within the simulations. Since the  $\hat{E}_\gamma$  indicates the mobility gap, the temperature dependence  $\Delta\hat{E}_\gamma/\Delta T = 26.2 \text{ meV}/130 \text{ K} = 2.02 \times 10^{-4} \text{ eV K}^{-1}$  can be associated with the temperature dependence of the mobility gap ( $\alpha_\mu$ ). From the  $\Delta\hat{E}_\gamma/\Delta T$  follows  $\alpha_\mu = 2 \times \Delta\hat{E}_\gamma/\Delta T = 4.03 \times 10^{-4} \text{ eV K}^{-1}$ . However, the determination of  $\alpha_\mu$  via PL or EL seems to be hampered, since the  $\alpha_\mu$  is set to a slightly higher value of  $4.7 \times 10^{-4} \text{ eV K}^{-1}$  within the simulations.

The results from tail-to-tail luminescence are plotted in Figure 6.12(b). The  $\hat{E}_\gamma$  from PL measurements is determined in the temperature range  $T = 300 - 100 \text{ K}$ . Due to technical limitations, the  $\hat{E}_\gamma$  from EL is limited to  $T > 133 \text{ K}$ . Also the  $\hat{E}_\gamma$  from tail-to-tail transitions increases with decreasing temperature. In the higher temperature range  $T = 300 - 200 \text{ K}$  the  $\hat{E}_\gamma$  from PL and EL coincide ( $\Delta\hat{E}_\gamma < 1 \text{ meV}$ ). Below  $T = 200 \text{ K}$  the difference between the  $\hat{E}_\gamma$  from PL and EL increases with decreasing temperature due to charge carrier transport limitations under EL conditions. The recombination region under EL conditions is broad and the quasi-Fermi level separation is less compared to the PL conditions. The simulations show qualitatively the same behavior. However, the difference between the  $\hat{E}_\gamma$  from PL and EL is bigger ( $\Delta\hat{E}_\gamma < 4 \text{ meV}$ ). And the overall curvature in the simulations is not that distinctive compared to the measurements. Whereas the measurements show a minimal  $\Delta\hat{E}_\gamma/\Delta V_{oc} = 237 \text{ meV V}^{-1}$  at  $T = 200 \text{ K}$ , the  $\Delta\hat{E}_\gamma/\Delta V_{oc}$  within the simulations slightly decreases with decreasing temperature.

However, compared to the results from the  $\mu\text{c-Si:H}$  *pin* device in Chapter 5 (compare Figure 5.10), this  $\hat{E}_\gamma/V_{oc}$  characteristic in Figure 6.12(b) does not show a local minimal kink. The broad temperature dependent band-tail densities of states yield an increasing  $\hat{E}_\gamma$  with increasing  $V_{oc}$ . The  $\hat{E}_\gamma = V_{oc} + E_x$ , where  $E_x$  depends on the temperature and the characteristic energies of the band-tail densities of states (compare Figure 2.10). On the one hand, a kink in the  $\hat{E}_\gamma/V_{oc}$  characteristic is suppressed, since the decrease of the temperature dependent characteristic energies of the band-tail densities of states dominates the decrease of the temperature. And on the other hand, at  $T = 300 \text{ K}$  the characteristic energies of the band-tail densities of states are broad ( $E_{c0} = 34 \text{ meV}$  and  $E_{v0} = 45 \text{ meV}$ ). Both features yield the  $\Delta E_x/\Delta T < -\Delta V_{oc}/\Delta T$  in Figure 6.13 at the temperatures  $T = 300 - 172 \text{ K}$ , which is the opposite case in  $\text{Cu(In,Ga)Se}_2$  (compare Figure 4.9) or  $\mu\text{c-Si:H}$  (compare Figure 5.10 and Figure 5.11). In  $\text{Cu(In,Ga)Se}_2$  and  $\mu\text{c-Si:H}$  the temperature independent band-tail densities of states are steeper than in *a-Si:H*. Note that the maximal  $E'_x = qV_{oc} - \hat{E}_\gamma = 0.115 \text{ eV} > 0.0 \text{ eV}$  in Figure 6.13 at  $T = 150 \text{ K}$ , which remarkably fits to the Stokes-shift found by modeling the PL and EL spectra. Additionally, from simulations a kink in the  $\hat{E}_\gamma/V_{oc}$  characteristics around room temperature and above is observed if the broad band-tail states are temperature independent (with  $E_{c0} = 34 \text{ meV}$  and  $E_{v0} = 45 \text{ meV}$ ). However, it is hard to conclude if the measured  $\hat{E}_\gamma/V_{oc}$  characteristic from tail-to-tail luminescence in Figure 6.12(b) indicates the temperature dependence of the characteristic energies of the band-tail densities of states, since the measurements do not show a distinctive increase of  $\hat{E}_\gamma$  with decreasing temperature. And note that the temperature

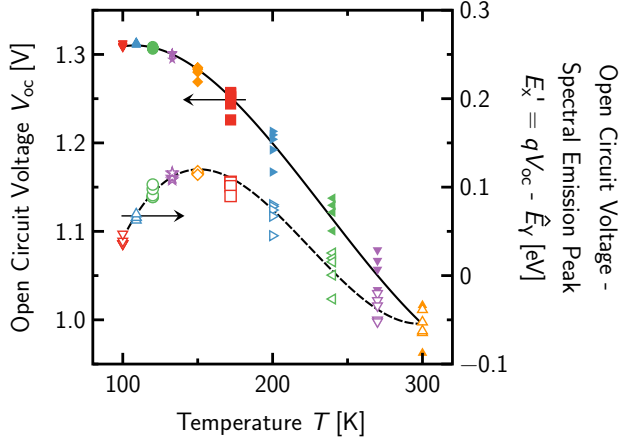


**Figure 6.13:** Temperature dependent difference between spectral emission peak energy ( $\hat{E}_\gamma$ ) and open circuit voltage ( $V_{oc}$ ), which is derived from measured photoluminescence (PL) spectra of the *a*-Si:H *pin* device as shown in Figure 6.1 (compare Figure 6.12). The  $V_{oc}$  is plotted as colored closed, and the  $E'_x = qV_{oc} - \hat{E}_\gamma$  is plotted as colored open symbols.

dependence of the mobility gap only slightly influences the  $\hat{E}_\gamma/V_{oc}$  characteristics.

### 6.2.3 Radiative Ideality Factor

The results of the temperature dependent radiative ideality factor ( $n_r$ ) from the measurements (see Figure 6.6), and the fitted simulations (see Figure 6.11) are summarized in Figure 6.14. The results are also separated by the origin of the luminescence. The PL and EL in the low photon energy range ( $E_\gamma < 1.10$  eV), which originate from band-to-defect transitions, are plotted as red open circles (PL) and black open squares (EL), respectively. And the luminescence, which originates from tail-to-tail transitions at high photon energies ( $E_\gamma > 1.10$  eV), is plotted as red closed circles (PL) and black closed squares (EL), respectively. The simulations of PL are plotted as blue solid lines, and of EL as blue dashed lines. Green dotted lines show the unaffected results from single spectra, since both kinds of spectra (band-to-defect and tail-to-tail) can be separated within simulations.

The measurements include the temperature range  $T = 330 - 100$  K, whereas the simulations are only stable within  $T = 330 - 172$  K. The values are derived at the injection current densities  $J = 10 - 100$  mA cm<sup>-2</sup> at room temperature. The increasing upward bending in the  $\phi_{PL}/V_{oc}$  characteristics under high injection conditions in connection with the increasing signal-to-noise ratio at low injection with decreasing temperature requires a continuous shift of the fitting range to  $J = 1 - 10$  mA cm<sup>-2</sup> at lowest temperature  $T = 100$  K.

The Figure 6.14(a) shows the radiative ideality factor from band-to-defect ( $n_r^{bd}$ ) and tail-to-tail ( $n_r^{tt}$ ) transitions, derived under PL conditions. The measured  $n_r^{bd}$  decreases almost continuously

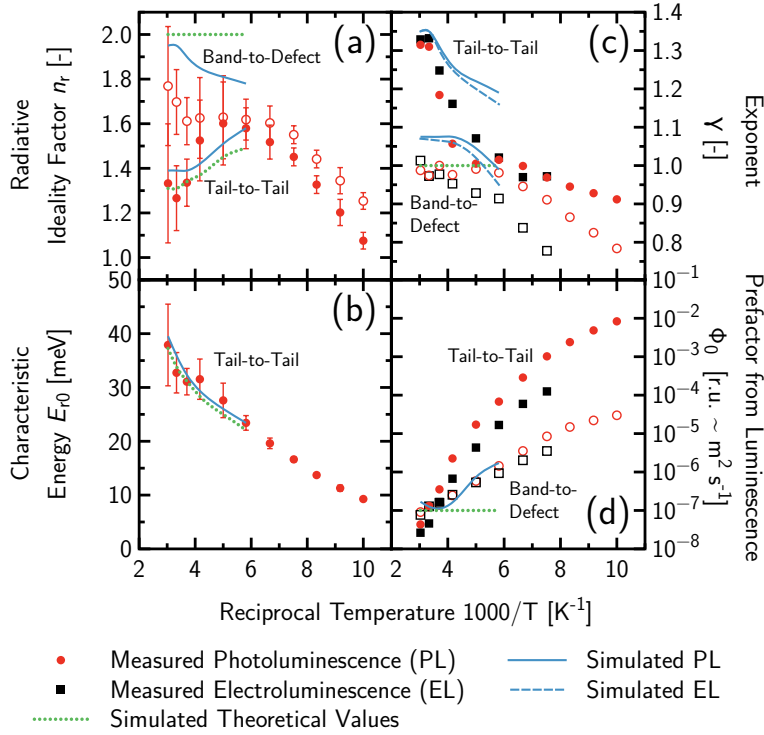


**Figure 6.14:** Temperature dependent evaluation of integrally measured electro- (EL) and photoluminescence (PL) of the *a*-Si:H pin device as shown in Figure 6.6. Temperatures are  $T = 330, 300, 270, 240, 200, 172, 150, 133, 120, 109$ , and  $100$  K. Luminescence at high photon energies  $E_\gamma > 1.1$  eV from tail-to-tail transitions is plotted as closed symbols. Luminescence at low photon energies  $E_\gamma < 1.1$  eV from band-to-defect transitions is plotted as open symbols. The PL is plotted as red circles, and the EL as black squares. The PL simulations accounting for the detector setup are plotted as blue solid lines, and the EL simulations are plotted as blue dashed lines. The corresponding simulated theoretical values, which do not account for the detector setup, are plotted as green dotted lines. At temperature  $T = 300$  K the values are derived in the injection current density range  $J = 10 - 100 \text{ mA cm}^{-2}$ . Due to the upward bending in the PL/voltage characteristics under high injection conditions, and due to the increasing signal-to-noise ratio with decreasing temperature at low injection, this region continuously shifts to one decade less injection at  $T = 100$  K. (a) The radiative ideality factor ( $n_r$ ) derived from Figure 6.6(a) and (c) by fitting a common diode law to the PL/voltage characteristics. (b) The characteristic energy ( $E_{r0} = n_r kT$ ) from tail-to-tail transitions derived from  $n_r$  in Figure 6.14(a), where  $kT$  is the thermal energy. (c)+(d) The fitting of an exponential behavior to the luminescence  $\phi = \phi_0 J^\gamma$  to the  $\phi_{\text{PL}}/J_{\text{sc}}$  and  $\phi_{\text{EL}}/J_d$  characteristics in Figure 6.6(b) and (d) yields the exponent  $\gamma$  and the prefactor  $\phi_0$  as a function of the temperature, where  $J_{\text{sc}}$  and  $J_d = -J_{\text{sc}}$  is the injection current density for PL and EL, respectively.

with decreasing temperature, whereas the  $n_r^{tt}$  increases down to  $T = 200$  K. Both radiative ideality factors are quite similar below  $T = 200$  K. In fact, below  $T = 200$  K both  $n_r^{bd}$  and  $n_r^{tt}$  correspond to the tail-to-tail transitions, since the band-to-defect transitions yield negligible low luminescence intensity at these temperatures. The comparison with the simulations shows that the deduction of  $n_r^{bd}$  is strongly influenced by the measurement setup, which integrates the luminescence from photon energies  $E_\gamma < 1.10$  eV, although the photon peak energy from tail-to-tail luminescence is  $\hat{E}_\gamma = 1.01 - 1.13$  eV. The simulations show an unaffected and constant  $n_r^{bd} = 2.0$  from band-to-defect transitions. The charge carrier occupation of the mid-gap defect states is almost constant and not influenced by either a change of the illumination photon flux or the temperature if the quasi-Fermi levels are sufficiently separated. For this reason, the luminescence intensity writes with the Eq. (2.31) as

$$\phi \propto \bar{n} \exp\left(\frac{qV}{2kT}\right) \quad (6.3)$$

if the quasi-Fermi level separation  $\Delta E_f = V$ , and where  $\bar{n}$  is the constant charge carrier concentration in the mid-gap defect states. From the denominator of the exponential function directly follows

$$n_r^{bd} = 2 \quad (6.4)$$

for band-to-defect transitions.

The increasing  $n_r^{tt}$  is already known from tail-to-tail transitions in  $\mu c$ -Si:H (see Chapter 5). The Figure 6.14(b) shows the  $E_{r0} = n_r^{tt} kT$ , which corresponds to the characteristic energy of the band-tail densities of states (compare Eq. (6.2)). The  $E_{r0}$  decreases with decreasing temperature. And the simulations fit the measurements within the error. An unequal quasi-Fermi level separation ( $\Delta E_f$ ) through the device, where the device contact voltage does not correspond to the  $\Delta E_f$  in the recombination region is one aspect for the decreasing  $E_{r0}$ . This is also discussed for  $\mu c$ -Si:H, where the characteristic energies of the band-tail densities of states are assumed to be temperature independent. Therefore, the continuously decreasing  $E_{r0}$  as another aspect indicates the temperature dependence of the band-tail slopes in  $a$ -Si:H. However, a freeze-in temperature according to Smith and Wagner [220], and Crandall [221], where the  $E_{c0}$  and  $E_{v0}$  get temperature independent, is not clearly indicated, since the electrical field affects the decrease of  $E_{r0}$ .

The luminescence from either band-to-defect or tail-to-tail transitions can also be distinguished by the linearity ( $\gamma$ ) between the luminescence ( $\phi$ ) and injection current density ( $J$ ), *i.e.*  $\phi = \phi_0 J^\gamma$ . The  $\gamma$  from PL and EL of tail-to-tail transitions in Figure 6.14(c) shows super-linear behavior around room temperature, and continuously decreases with decreasing temperature to sub-linear behavior, which is already known from  $\mu c$ -Si:H. The PL and the EL are quite similar, which indicates their superposition in Eq. (2.3). The same is observed from the corresponding simulations, which however, decrease more slowly than the experiments. As long as the  $\gamma$  in the measurements is derived from composed spectra, and the band-to-defect luminescence is dominant at the higher temperatures, the measurements seem to be strongly influenced by the setup, as already mentioned before. However, the measured  $\gamma$  of band-to-defect transitions therefore shows pretty good results, which are similar to the simulations. In fact, the measured PL shows

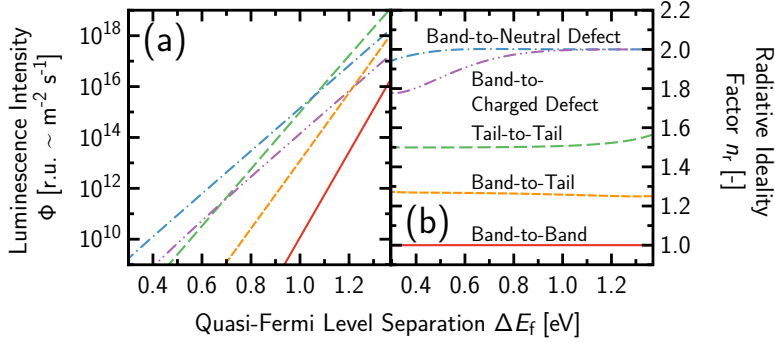


**Figure 6.15:** Evaluation of quasi-Fermi level separation ( $\Delta E_f$ ) in dependency of luminescence intensity ( $\phi$ ) of *a*-Si:H *pin* device by *local recombination model*. (a) The  $\phi$  from different luminescent transitions, *i.e.* band-to-band (red solid line), band-to-tail (orange dashed line), tail-to-tail (green dashed line), band-to-charged defects (purple two dot-dashed line), and band-to-neutral defects (blue dot-dashed line). (b) The corresponding radiative ideality factors  $n_r$  are derived from (a).

linear behavior in a wide temperature range  $T = 330 - 200$  K, which is also observed by Street *et al.* [60]. The corresponding EL is limited to  $T = 330 - 240$  K. Below these temperatures, the measurements are affected by the dominant tail-to-tail luminescence, and additionally, the EL may be influenced by transport phenomena. Nevertheless, both kinds of transitions show characteristic  $\gamma$  around room temperature, which can help to distinguish between luminescence from either band-to-defect or tail-to-tail transitions.

The luminescence intensity, which is derived from the prefactor  $\phi_0$  in  $\phi = \phi_0 J^\gamma$  shows a strong increase of the PL from tail-to-tail transitions within almost six orders of magnitude with decreasing temperature (see Figure 6.14(d)). The corresponding EL shows slightly less increase. The measured PL and EL from band-to-defect transitions show a similar increase with decreasing temperature within three orders of magnitude. However, the comparison with the simulations again shows the influence of the measurement setup. In fact, the band-to-defect luminescence from simulations does not increase with decreasing temperature.

The Figure 6.15(a) summarizes the results from  $\phi/V$  characteristics at  $T = 300$  K and the derived  $n_r$  (see Figure 6.15(b)) from different luminescent transitions, which are discussed within this thesis.

The  $\phi/V$  characteristics in Figure 6.15(a) result from the *local recombination model*, which neglects transport phenomena and/or contact series resistance. The different  $\phi$  depend on the absolute densities of involved states. Therefore, the ratio between the different luminescent transitions may vary between different devices. However, the  $\phi/V$  characteristics in Figure 6.15(a) are representative for *a*-Si:H as long as the modeling parameters of this *a*-Si:H *pin* device here are common. The quasi-Fermi level separation ( $\Delta E_f$ ) at the upper end is restricted to the radiative limit  $qV_{\text{oc,rad}} = (1 - T/T_s)E_\mu + kT \ln(T_s/T) - kT \ln Q_{\text{LED}} = 1.37$  eV with  $E_\mu = 1.87$  eV, the temperature of the sun  $T_s = 5500$  K, the device temperature  $T = 300$  K, and



a radiative efficiency  $Q_{\text{LED}} = 10^{-8}$  [21, 222].

In Figure 6.15(a) it can be seen that the luminescence (either PL or EL) in a broad region of quasi-Fermi level separation  $\Delta E_f = 300 - 1075$  meV is dominated by band-to-neutral mid-gap defect transitions (plotted as blue dot-dashed line). The band-to-charged mid-gap defect transitions (plotted as purple dot-dashed line) are similar, however, approximately one order of magnitude less intense. At  $\Delta E_f > 1075$  meV the faster increasing tail-to-tail luminescence intensity (plotted as green dashed line) dominates the  $\phi/V$  characteristics. Although, the  $\phi/V$  characteristics from band-to-tail (plotted as orange dashed line) or band-to-band (plotted as red solid line) transitions are even steeper than the  $\phi/V$  characteristics from band-to-defect or tail-to-tail transitions, the band-to-band and band-to-tail transitions are not relevant in *a*-Si:H, since these transitions are only dominant at very high quasi-Fermi level separation close to the band edges, which is forbidden due to the radiative limit.

The  $n_r = 1$  as required by the *reciprocity relation* can be observed from band-to-band transitions in Figure 6.15(b). The more localized inter-band defect states are involved in the luminescence process, the higher the  $n_r$ . The  $n_r = 2E_0/(kT + E_0)$  (see Eq. (4.4)) from band-to-tail transitions, as observed in Cu(In,Ga)Se<sub>2</sub> in Chapter 4 depends on the temperature and the characteristic energy of the band-tail densities of states ( $E_0$ ). The luminescence from tail-to-tail transitions can be written as  $n_r = E_0/kT$  if the characteristic energies of the conduction ( $E_{c0}$ ) and the valence ( $E_{v0}$ ) band-tail densities of states are symmetric, *i.e.*  $E_0 = E_{c0} = E_{v0}$ . In the more general case  $E_{c0} \neq E_{v0}$  like in *a*-Si:H, the  $E_0$  rewrites as  $E_0 = 2E_{c0}E_{v0}/(E_{c0} + E_{v0})$ . This holds in the case of moderate and high quasi-Fermi level separation.

The radiative ideality factor from band-to-defect transitions is  $n_r = 2$  if the  $\Delta E_f$  is moderate, *i.e.* the charge carrier occupation at the mid-gap defect states is approximately constant. The luminescence from band-to-charged mid-gap defect transitions is more sensitive to the  $\Delta E_f$  than the luminescence from band-to-neutral mid-gap defect transitions, predominantly at  $\Delta E_f < 950$  meV. Whereas the occupation probability function of neutral defects ( $F^0$ ) is symmetric between the quasi-Fermi levels, the occupation probabilities of charged defects ( $F^+$  and  $F^-$ ) are two-step Fermi-Dirac functions. This yields the constant plateau of  $F^0$  to be broader than of  $F^+$  or  $F^-$ , and therefore a constant  $n_r = 2$  to lower  $\Delta E_f$  (compare Figure 2.6).

## 6.2.4 Reciprocity Relation

The *RR* between the electroluminescence spectra ( $\varphi_{\text{EL}}$ ) and the external quantum efficiency ( $Q_e$ ) in *a*-Si:H is hampered due to high quasi-Fermi level separation ( $\Delta E_f$ ) and Stokes-shifted tail-to-tail luminescence within experiments. High  $\Delta E_f$  drives the device far off the thermal equilibrium conditions. The influence of the  $\Delta E_f$  to the *RR* between the  $Q_e$  and the  $\varphi_{\text{EL}}$  illustrates Figure 6.16 at  $T = 300$  K. For this reason, single EL spectra from band-to-neutral mid-gap defect and from band-to-charged mid-gap defect transitions are simulated. Tail-to-defect transitions at even lower photon energies are neglected, since these transitions are only dominant at very low injection, and not accessible within experiments for this reason. Thus, only the interaction between band and mid-gap defect states is considered in the simulated  $Q_e$  and  $\varphi_{\text{EL}}$ , which are plotted as black solid lines each. The  $\varphi_{\text{EL}}$  are composed of single EL spectra from band-to-charged mid-gap defect transitions, which are plotted as purple shaded areas, and from dominant band-to-neutral mid-gap defect transitions, which are plotted as green dotted lines.

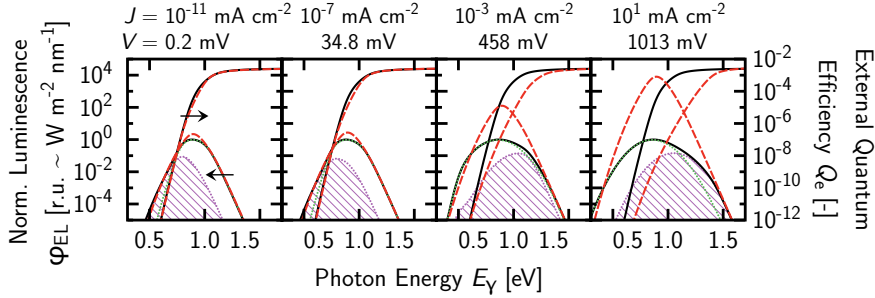


**Figure 6.16:** Influence of injection current density ( $J$ ) on reciprocity relation between electroluminescence ( $\varphi_{\text{EL}}$ ) and external quantum efficiency ( $Q_e$ ) of  $a\text{-Si:H}$  pin device at temperature  $T = 300$  K and injection current densities  $J = 10^{-11}$ ,  $10^{-7}$ ,  $10^{-3}$ , and  $10^1$   $\text{mA cm}^{-2}$ . The width of the Gaussian-distributed mid-gap defect states is  $\sigma_{\text{db}} = 0.12$  eV. And its correlation energy is  $U = 0.20$  eV. Black solid lines show full one dimensional numerical device simulations of  $\varphi_{\text{EL}}$  and  $Q_e$ . The red dashed lines show the correspondence each, i.e.  $\varphi'_{\text{EL}} \propto Q_e \times \varphi_{\text{bb}}$  and  $Q'_e \propto \varphi_{\text{EL}} / \varphi_{\text{bb}}$ , where  $\varphi_{\text{bb}}$  is the hemispheric black body radiation. The green dotted lines show the single  $\varphi_{\text{EL}}$  from transitions between band and neutral mid-gap defect states. And the purple shaded areas show the single  $\varphi_{\text{EL}}$  from transitions between band and charged mid-gap defect states.

The red dashed lines show the  $Q'_e \propto \varphi_{\text{EL}} / \varphi_{\text{bb}}$  and  $\varphi'_{\text{EL}} \propto Q_e \times \varphi_{\text{bb}}$  each, where  $\varphi_{\text{bb}}$  is the hemispheric black body radiation.

The injection current density is altered within  $J = 10^{-11}$ ,  $10^{-7}$ ,  $10^{-3}$ , and  $10^1$   $\text{mA cm}^{-2}$ , which yields  $V = 0.2$ ,  $34.8$ ,  $458$ , and  $1013$  mV. The  $\Delta E_f$  is very similar, since the injection current is moderate. The parameters of the Gaussian-distributed mid-gap defect states are taken from the modeling of the device, i.e.  $N_{\text{db}} = 6.8 \times 10^{16} \text{ cm}^{-3}$ ,  $\sigma_{\text{db}} = 0.12$  eV, and  $U = 0.20$  eV.

The main part of the neutral mid-gap defect occupation function ( $F^0$ ) is in between the quasi-Fermi levels, and broadens with increasing  $\Delta E_f$ . In contrast, the main part of the two-step Fermi-Dirac distributions of charged mid-gap defects (either  $F^+$  or  $F^-$ ) shifts to the band edges with increasing  $\Delta E_f$ . Therefore, the peak photon energy ( $\hat{E}_\gamma$ ) of the band-to-neutral mid-gap defect transitions is constant and the spectrum is broadened under different bias conditions, whereas the  $\hat{E}_\gamma$  of the band-to-charged mid-gap defect transitions shifts to higher photon energies with increasing  $\Delta E_f$ . As already stated before, since the intensity of the band-to-neutral mid-gap defect transitions dominates the band-to-charged mid-gap defect transitions, the  $\varphi_{\text{EL}}$  from band-to-charged mid-gap defect transitions is hardly to detect within experiments.

If the  $\Delta E_f$  is increased, the RR between  $Q_e$  and  $\varphi_{\text{EL}}$  is insufficient due to the broadening of  $F^0$ . Since the high photon energy range of  $\varphi_{\text{EL}}$  and  $\varphi'_{\text{EL}}$  is determined by the temperature, the overlap of  $\varphi_{\text{EL}}$  and  $\varphi'_{\text{EL}}$  is adjusted in the high photon energy range above  $\hat{E}_\gamma$ . The same holds for the overlap of  $Q_e$  and  $Q'_e$ , which is also adjusted in the high photon energy range, where  $Q_e$  saturates.

The case of  $J = 10 \text{ mA cm}^{-2}$  in Figure 6.16 is similar to the measurements in Figure 6.4. A small overlap of  $\varphi_{\text{EL}}$  and  $\varphi'_{\text{EL}}$  in the high photon energy range can be observed from the simulations and measurements. In both cases, the  $\varphi'_{\text{EL}}$  increases faster than the  $\varphi_{\text{EL}}$  with decreasing

photon energy, which originates from the different  $\Delta E_f$  under  $Q_e$  and  $\varphi_{EL}$  conditions. Since transitions from band-tail states affect the measurements, the comparison between measured and simulated  $Q_e$  is even harder. The band-tail states in the measurements yield  $Q'_e$  not to saturate in the high photon energy range (see Figure 6.4). Only a small kink, which may indicate the saturation of the measured  $Q'_e$ , can be observed.

Note, from simulations can be observed that the  $\varphi_{EL}$  from band-to-neutral mid-gap defect transitions broadens with increasing correlation energy  $U$ . And the width of the mid-gap defect distribution ( $\sigma_{db}$ ) also affects the width of  $\varphi_{EL}$ , however, the *RR* between  $Q_e$  and  $\varphi_{EL}$  holds the more, the sharper the mid-gap defect distributions, *i.e.* the smaller  $\sigma_{db}$ .

In summary, the luminescence and the external quantum efficiency from *a*-Si:H tie in with the results from  $\mu$ c-Si:H in Chapter 5 with respect to the *reciprocity relation*. Additional to the already known luminescence from tail-to-tail transitions, band-to-defect transitions affect the luminescence in *a*-Si:H. The observed luminescence spectra and the radiative ideality factor can be properly explained with the help of full numerical device simulations. Furthermore, an analytical approach can explain the radiative ideality factor. And even an insufficient *reciprocity relation* between the luminescence from band-to-defect transitions and the external quantum efficiency, which involves mid-gap defect states, can be explained with simulations.

## Chapter 7

# Conclusions and Outlook

The *reciprocity relation* by Donolato [20] and Rau [21, 22] connects *light absorption* and *radiative recombination*. This connection holds if the luminescence spectra show constant unshifted curvature under different bias conditions, the luminescence/voltage characteristic yields a radiative ideality factor of one, and if the voltage-driven EL spectra and the illumination-driven PL spectra under short circuit conditions superimpose linearly. Following these requirements of the *reciprocity relation*, this thesis investigates Cu(In,Ga)Se<sub>2</sub> *np* heterojunction, hydrogenated microcrystalline ( $\mu$ c-Si:H) *pin*, and amorphous (*a*-Si:H) *pin* devices with experiments and simulations. The requirements of the *reciprocity relation* are mainly fulfilled in semiconductors, which are free of defect states. However, additional inter-band states, which arise from defects, affect the relation between *light absorption* and *radiative recombination*.

The main part of the *radiative recombination*, *i.e.* luminescence, in Cu(In,Ga)Se<sub>2</sub> *np* heterojunction devices around room temperature as investigated in this thesis, is found to originate from band-to-tail transitions. Defect states at the CdS/Cu(In,Ga)Se<sub>2</sub> interface and in the Cu(In,Ga)Se<sub>2</sub> bulk can be reduced by accelerated light soaking. Most of the treatment lasts permanently. The band-tail densities of states, which yield a characteristic energy  $E_0 = 17.5$  meV by fitting simulations to the luminescence spectra are quite steep. The additional broadening of the luminescence spectra is found to originate from band gap fluctuations, which are assumed to be Gaussian-like with a distribution width of  $\sigma_{E_\mu} = 38$  meV.

The luminescence spectra and the external quantum efficiency, which corresponds to the *light absorption*, as required by the *reciprocity relation* are compatible within experiments. The *local recombination model* shows that the external quantum efficiency and the luminescence spectra are not compatible if the band-tail densities of states become broad, *i.e.*  $E_0 > kT$ .

Steep band-tail densities of states even prohibit the luminescence spectra to shift under different bias conditions. Therefore, the *reciprocity relation* between the electroluminescence and the external quantum efficiency is almost not affected even at high charge carrier injection.

However, the radiative ideality factor ( $n_r$ ), which is deduced from luminescence/voltage characteristics, deviates from the postulated temperature and injection independent  $n_r = 1$ , which holds for band-to-band transitions. The influence of the band-tail states yields  $n_r = 2E_0/(kT + E_0)$  if  $E_0 > kT$ .

The situation is different in  $\mu\text{c-Si:H}$  *pin* devices. The main part of the luminescence originates from tail-to-tail transitions, since the band-tail densities of states are found to be broader than in  $\text{Cu(In,Ga)Se}_2$ . From the comparison between the measurements and well fitted full one dimensional numerical device simulations, the characteristic energy of the band-tail densities of states is calculated to be  $E_0 = 31.0$  meV.

The *reciprocity relation* between the luminescence and the external quantum efficiency is only valid in a small spectral range, since the characteristic energy of the band-tail densities of states is higher than the thermal energy. The *reciprocity relation* only holds in the high photon energy range above the spectral emission peak. Simulations show that this *reciprocity relation* is affected even at moderate injection levels ( $J \approx 10^{-1} \text{ mA cm}^{-2}$ ). However, in case of very low injection ( $J \approx 10^{-5} \text{ mA cm}^{-2}$ ) close to the thermal equilibrium, the *reciprocity relation* holds. Additional mid-gap defect states, which do not contribute to the luminescence, however, contribute to the external quantum efficiency in the low photon energy range. This fact, in addition, affects the validity of the *reciprocity relation* in  $\mu\text{c-Si:H}$ .

As a consequence of the the broad band-tail densities of states, the luminescence spectra show a distinctive blue shift with increasing injection level.

The radiative ideality factor from tail-to-tail transitions at room temperature indicates the characteristic energy of the symmetric and temperature independent band-tail density of states, which can be approximated as  $n_r = E_0/kT$ . The simulations show that the characteristic energy of the band-tail densities of states can be deduced from luminescence/voltage characteristics within small errors.

The luminescence around room temperature in  $a\text{-Si:H}$  *pin* devices yields luminescence from band-to-defect transitions, in addition to tail-to-tail transitions. However, the characteristic energies of the band-tail densities of states are found to be even broader than in  $\mu\text{c-Si:H}$ . The characteristic energy of the valence band-tail is assumed to be  $E_{v0} = 45$  meV, which then yields the conduction band-tail  $E_{c0} = 34$  meV by fitting full one dimensional device simulations.

The broad band-tails, a high mid-gap defect state concentration, and Stokes-shifted luminescence from tail-to-tail luminescence in  $a\text{-Si:H}$  completely hamper the *reciprocity relation* between the luminescence and the external quantum efficiency. Fitting our model to the experimental data indicates that in the presence of mid-gap defects, the *reciprocity relation* is only valid at extreme low injection conditions ( $J < 10^{-7} \text{ mA cm}^{-2}$ ), where the device is almost in thermal equilibrium.

Regarding the broad band-tail density of states in  $a\text{-Si:H}$ , the spectral shift of the tail-to-tail luminescence is similar to  $\mu\text{c-Si:H}$ . The temperature dependent spectral shift of the band-to-defect luminescence indicates the temperature dependent increase of the mobility gap, since the quasi-Fermi levels at moderate and high injection ( $J \approx 10 - 100 \text{ mA cm}^{-2}$ ) are far from the bands and the mid-gap defect states. Additionally, this yields the band-to-defect luminescence also to indicate the mobility gap if the position of the mid-gap defect states is known.

The deduction of the radiative ideality factor from band-to-defect luminescence/voltage characteristics needs an adapted measurement setup. A not well adapted setup and a luminescence intensity almost equal to the tail-to-tail luminescence hinders the right deduction of the radiative ideality factor from band-to-defect luminescence. However, fitting our model to the experimental data indicates a constant radiative ideality factor  $n_r = 2$  at moderate and high injection.

The parallel validation of photo- and electroluminescence in all three materials shows that the photo- and electroluminescence superimpose fairly well around room temperature and at low injection levels, *i.e.* with small quasi-Fermi level separation.

In summary, the requirements of the *reciprocity relation* hold the more, the less defect states, either band-tails or mid-gap defects are in the gap. Hence, the *reciprocity relation* between the external quantum efficiency and the luminescence is affected by the density of defect states, *i.e.* it only holds if the device is close to the thermal equilibrium. In dependence of the density of defect states, the injection level has to be lowered by several orders of magnitude to achieve a sufficient *reciprocity relation*. However, even in the case of medium mid-gap defect state concentration, the compatibility is not accessible within experiments.

The temperature dependent radiative ideality factor correlates fairly well to the dominant luminescent transition. With the luminescence/voltage characteristic calibrated, the local quasi-Fermi level separation can be deduced from whole modules by electro- or photoluminescence imaging, even in low mobility materials. Therefore, the results from this thesis help to analyze luminescence imaging, where the solar cells are not limited to the devices, which are investigated here.

Furthermore, the investigation methods, which are used within this thesis can be expanded to new solar cell concepts, like organic materials for instance.

And for the optical simulations, the self-absorption of luminescence light is neglected in this thesis so far. The influence of self-absorption to luminescence spectra could be improved in a future work.



# Bibliography

- [1] International Energy Agency, “Key World Energy Statistics 2012,” tech. rep., International Energy Agency, Paris, France, 2012.
- [2] Intergovernmental Panel on Climate Change, “Climate Change 2007: Mitigation of Climate Change,” tech. rep., Intergovernmental Panel on Climate Change, 2007.
- [3] Intergovernmental Panel on Climate Change, “Climate change 2007: The Physical Science Basis: Contribution of Working Group I to the Fourth Assessment Report of the Intergovernmental Panel on Climate Change,” tech. rep., Intergovernmental Panel on Climate Change, 2007.
- [4] P. Würfel, *Physics of Solar Cells: From Principles to New Concepts*. Wiley-VCH, 2005.
- [5] C. Breyer, A. Gerlach, D. Schäfer, and J. Schmid, “Fuel-Parity : New Very Large and Sustainable Market Segments for PV Systems,” in *IEEE EnergyCon 2010*, (Manama/Bahrain), pp. 18–22, 2010.
- [6] D. M. Chapin, C. S. Fuller, and G. L. Pearson, “A New Silicon p-n Junction Photocell for Converting Solar Radiation into Electrical Power,” *Journal of Applied Physics*, vol. 25, no. 5, pp. 676–677, 1954.
- [7] N. S. Lewis, “Toward Cost-Effective Solar Energy Use,” *Science*, vol. 315, pp. 798–801, Feb. 2007.
- [8] R. F. Service, “Can the Upstarts Top Silicon?,” *Science*, vol. 319, no. 5864, pp. 718–720, 2008.
- [9] C. W. Tang, “Two-layer organic photovoltaic cell,” *Applied Physics Letters*, vol. 48, no. 2, pp. 183–185, 1986.
- [10] G. Yu, J. Gao, J. C. Hummelen, F. Wudl, and A. J. Heeger, “Polymer Photovoltaic Cells: Enhanced Efficiencies via a Network of Internal Donor-Acceptor Heterojunctions,” *Science, New Series*, vol. 270, no. 5243, pp. 1789–1791, 1995.
- [11] C. J. Brabec, N. S. Sariciftci, and J. C. Hummelen, “Plastic Solar Cells,” *Advanced Functional Materials*, vol. 11, pp. 15–26, Feb. 2001.
- [12] H. Hoppe and N. S. Sariciftci, “Organic solar cells: An overview,” *Journal of Materials Research*, vol. 19, pp. 1924–1945, Mar. 2004.



- [13] P. W. M. Blom, V. D. Mihailetschi, L. J. A. Koster, and D. E. Markov, "Device Physics of Polymer:Fullerene Bulk Heterojunction Solar Cells," *Advanced Materials*, vol. 19, pp. 1551–1566, June 2007.
- [14] J. Y. Kim, K. Lee, N. E. Coates, D. Moses, T.-Q. Nguyen, M. Dante, and A. J. Heeger, "Efficient Tandem Polymer Solar Cells Fabricated by All-Solution Processing," *Science*, vol. 317, pp. 222–225, July 2007.
- [15] W. U. Huynh, J. J. Dittmer, and A. P. Alivisatos, "Hybrid Nanorod-Polymer Solar Cells," *Science*, vol. 295, pp. 2425–2427, Mar. 2002.
- [16] R. Schaller and V. Klimov, "High Efficiency Carrier Multiplication in PbSe Nanocrystals: Implications for Solar Energy Conversion," *Physical Review Letters*, vol. 92, pp. 186601–1–4, May 2004.
- [17] I. Gur, N. A. Fromer, M. L. Geier, and A. P. Alivisatos, "Air-Stable All-Inorganic Nanocrystal Solar Cells Processed from Solution," *Science*, vol. 310, pp. 462–465, Oct. 2005.
- [18] W. J. E. Beek, M. M. Wienk, M. Kemerink, X. Yang, and R. a. J. Janssen, "Hybrid Zinc Oxide Conjugated Polymer Bulk Heterojunction Solar Cells," *The Journal of Physical Chemistry B*, vol. 109, pp. 9505–9516, May 2005.
- [19] U. Bach, D. Lupo, P. Comte, J. E. Moser, F. Weissoertel, J. Salbeck, H. Spreitzer, and M. Graetzel, "Solid-state dye-sensitized mesoporous TiO<sub>2</sub> solar cells with high photon-to-electron conversion efficiencies," *Nature*, vol. 395, no. 6702, pp. 583–585, 1998.
- [20] C. Donolato, "A reciprocity theorem for charge collection," *Applied Physics Letters*, vol. 46, no. 3, pp. 270–271, 1985.
- [21] U. Rau, "Reciprocity relation between quantum efficiency and electroluminescent emission of solar cells," *Physical Review B*, vol. 76, no. 8, pp. 085303–1–8, 2007.
- [22] U. Rau, "Superposition and Reciprocity in the Electroluminescence and Photoluminescence of Solar Cells," *IEEE Journal of Photovoltaics*, vol. 2, no. 2, pp. 169–172, 2012.
- [23] J. Mattheis, U. Rau, and J. H. Werner, "Light absorption and emission in semiconductors with band gap fluctuations - A study on Cu(In,Ga)Se<sub>2</sub> thin films," *Journal of Applied Physics*, vol. 101, no. 11, pp. 113519–1–11, 2007.
- [24] D. Han, K. Wang, and L. Yang, "Recombination and metastability in amorphous silicon pin solar cells made with and without hydrogen dilution studied by electroluminescence," *Journal of Applied Physics*, vol. 80, no. 4, pp. 2475–2482, 1996.
- [25] D. Przado, M. Igalson, R. Bacewicz, and M. Edoff, "The Influence of Metastabilities on the Luminescence in the Cu(In,Ga)Se<sub>2</sub> Solar Cells," *Acta Physica Polonica A*, vol. 112, no. 2, pp. 183–189, 2007.
- [26] F. Dreckschmidt, H. Fiedler, D. Kreßner - Kiel, and H. J. Möller, "Sub-Bandgap Electroluminescence at Room Temperature of Extended Defects in Multicrystalline Silicon," in *23rd European Photovoltaic Solar Energy Conference*, (Valencia), pp. 407–410, 2008.

- 
- [27] O. Breitenstein, J. Bauer, M. Kittler, T. Arguirov, and W. Seifert, "EBIC and Luminescence Studies of Defects in Solar Cells," *Scanning*, vol. 30, no. 4, pp. 331–338, 2008.
- [28] U. Hoyer, M. Wagner, T. Swonke, J. Bachmann, R. Auer, A. Osvet, and C. J. Brabec, "Electroluminescence imaging of organic photovoltaic modules," *Applied Physics Letters*, vol. 97, no. 23, pp. 233303–1–3, 2010.
- [29] P. Würfel, S. Finkbeiner, and E. Daub, "Generalized Planck's radiation law for luminescence via indirect transitions," *Applied Physics A: Materials Science & Processing*, vol. 60, no. 1, pp. 67–70, 1995.
- [30] R. Brüggemann, "Kirchhoff's generalised law applied to amorphous silicon/crystalline silicon heterostructures," *Philosophical Magazine*, vol. 89, pp. 2519–2529, Oct. 2009.
- [31] M. Zazoui and J. C. Bourgoin, "Space degradation of multijunction solar cells: An electroluminescence study," *Applied Physics Letters*, vol. 80, no. 23, pp. 4455–4457, 2002.
- [32] S. Makham, M. Zazoui, and J. C. Bourgoin, "Analysis of Multijunction solar cells: Electroluminescence study," *MJ Condensed Matter*, vol. 5, no. 2, pp. 181–185, 2004.
- [33] O. Breitenstein, J. Bauer, T. Trupke, and R. A. Bardos, "On the detection of shunts in silicon solar cells by photo- and electroluminescence imaging," *Progress in Photovoltaics: Research and Applications*, vol. 16, no. 4, pp. 325–330, 2008.
- [34] M. Kasemann, D. Grote, B. Walter, W. Kwapil, T. Trupke, Y. Augarten, R. A. Bardos, E. Pink, M. D. Abbott, and W. Warta, "Luminescence imaging for the detection of shunts on silicon solar cells," *Progress in Photovoltaics: Research and Applications*, vol. 16, no. 4, pp. 297–305, 2008.
- [35] D. Hinken, K. Ramspeck, K. Bothe, B. Fischer, and R. Brendel, "Series resistance imaging of solar cells by voltage dependent electroluminescence," *Applied Physics Letters*, vol. 91, no. 18, pp. 182104–1–3, 2007.
- [36] K. Ramspeck, K. Bothe, D. Hinken, B. Fischer, J. Schmidt, and R. Brendel, "Recombination current and series resistance imaging of solar cells by combined luminescence and lock-in thermography," *Applied Physics Letters*, vol. 90, no. 15, pp. 153502–1–3, 2007.
- [37] A. Helbig, T. Kirchartz, R. Schaeffler, J. H. Werner, and U. Rau, "Quantitative electroluminescence analysis of resistive losses in Cu(In, Ga)Se<sub>2</sub> thin-film modules," *Solar Energy Materials & Solar Cells*, vol. 94, no. 6, pp. 979–984, 2010.
- [38] T. Fuyuki, H. Kondo, T. Yamazaki, Y. Takahashi, and Y. Uraoka, "Photographic surveying of minority carrier diffusion length in polycrystalline silicon solar cells by electroluminescence," *Applied Physics Letters*, vol. 86, no. 26, pp. 262103–262108, 2005.
- [39] P. Würfel, T. Trupke, T. Puzzer, E. Schaffer, W. Warta, and S. W. Glunz, "Diffusion lengths of silicon solar cells from luminescence images," *Journal of Applied Physics*, vol. 101, no. 12, p. 123110, 2007.

- [40] T. Kirchartz, A. Helbig, and U. Rau, "Note on the interpretation of electroluminescence images using their spectral information," *Solar Energy Materials & Solar Cells*, vol. 92, no. 12, pp. 1621–1627, 2008.
- [41] D. Hinken, K. Bothe, K. Ramspeck, S. Herlufsen, and R. Brendel, "Determination of the effective diffusion length of silicon solar cells from photoluminescence," *Journal of Applied Physics*, vol. 105, no. 10, pp. 104516–1–6, 2009.
- [42] C. G. Zimmermann, "Performance Mapping of Multijunction Solar Cells Based on Electroluminescence," *IEEE Electron Device Letters*, vol. 30, no. 8, pp. 825–827, 2009.
- [43] T. Trupke, J. Nyhus, and J. Haunschild, "Luminescence imaging for inline characterisation in silicon photovoltaics," *Physica Status Solidi (RRL) - Rapid Research Letters*, vol. 5, pp. 131–137, Apr. 2011.
- [44] T. Kirchartz and U. Rau, "Electroluminescence analysis of high efficiency Cu(In,Ga)Se<sub>2</sub> solar cells," *Journal of Applied Physics*, vol. 102, no. 10, pp. 104510–1–8, 2007.
- [45] B. E. Pieters, T. Kirchartz, T. Merdzhanova, and R. Carius, "Modeling of photoluminescence spectra and quasi-Fermi level splitting in  $\mu\text{-Si:H}$  solar cells," *Solar Energy Materials & Solar Cells*, vol. 94, no. 11, pp. 1851–1854, 2010.
- [46] S. Wagner, J. L. Shay, P. Migliorato, and H. M. Kasper, "CuInSe<sub>2</sub>/CdS heterojunction photovoltaic detectors," *Applied Physics Letters*, vol. 25, no. 8, pp. 434–435, 1974.
- [47] L. L. Kazmerski and Y. J. Juang, "Vacuum-deposited CuInTe<sub>2</sub> thin films: Growth, structural, and electrical properties," *Journal of Vacuum Science and Technology*, vol. 14, pp. 769–776, May 1977.
- [48] P. Torres, H. Keppner, J. Meier, U. Kroll, N. Beck, and A. Shah, "Fast Deposition of c-Si:H by Restrictive Dilution and Enhanced HF-Power," *Physica Status Solidi (A) - Rapid Research Notes*, vol. 163, no. 2, pp. R9–R10, 1997.
- [49] O. Vetterl, F. Finger, R. Carius, P. Hapke, L. Houben, O. Kluth, A. Lambertz, A. Mück, B. Rech, and H. Wagner, "Intrinsic microcrystalline silicon: A new material for photovoltaics," *Solar Energy Materials & Solar Cells*, vol. 62, no. 1-2, pp. 97–108, 2000.
- [50] B. Rech, T. Roschek, T. Repmann, J. Müller, R. Schmitz, and W. Appenzeller, "Microcrystalline silicon for large area thin film solar cells," *Thin Solid Films*, vol. 427, no. 1-2, pp. 157–165, 2003.
- [51] S. Klein, T. Repmann, and T. Brammer, "Microcrystalline Silicon Films and Solar Cells Deposited by PECVD and HWCVD," *Solar Energy*, vol. 77, no. 6, pp. 893–908, 2004.
- [52] D. E. Carlson and C. R. Wronski, "Amorphous silicon solar cell," *Applied Physics Letters*, vol. 28, no. 11, pp. 671–673, 1976.
- [53] S. R. Kodigala, *Cu(In<sub>1-x</sub>Ga<sub>x</sub>)Se<sub>2</sub> Based Thin-Film Solar Cells*. Burlington, USA: Academic Press by Elsevier, 2010.

- 
- [54] T. Shioda, S. Chichibu, T. Irie, H. Nakanishi, and T. Kariya, "Influence of nonstoichiometry on the Urbachs tails of absorption spectra for CuInSe<sub>2</sub> single crystals," *Journal of Applied Physics*, vol. 80, no. 2, pp. 1106–1111, 1996.
  - [55] S. Wasim, C. Rincón, G. Marín, P. Bocaranda, E. Hernández, I. Bonalde, and E. Medina, "Effect of structural disorder on the Urbach energy in Cu ternaries," *Physical Review B*, vol. 64, pp. 195101–1–8, Oct. 2001.
  - [56] T. Kirchartz, U. Rau, M. Kurth, J. Mattheis, and J. H. Werner, "Comparative study of electroluminescence from Cu(In,Ga)Se<sub>2</sub> and Si solar cells," *Thin Solid Films*, vol. 515, no. 15, pp. 6238–6242, 2007.
  - [57] E. Daub and P. Würfel, "Ultralow Values of the Absorption Coefficient of Si Obtained from Luminescence," *Physical Review Letters*, vol. 74, no. 6, pp. 1020–1023, 1995.
  - [58] R. A. Street, "Luminescence and recombination in hydrogenated amorphous silicon," *Advances in Physics*, vol. 30, no. 5, pp. 593–676, 1981.
  - [59] T. Merdzhanova, R. Carius, S. Klein, F. Finger, and D. Dimova-Malinovsk, "A comparison of model calculations and experimental results on the photoluminescence energy and open circuit voltage of  $\mu\text{c-Si:H}$  solar cells," *Journal of Optoelectronics and Advanced Materials*, vol. 7, no. 1, pp. 485–489, 2005.
  - [60] R. A. Street, D. K. Biegelsen, and R. L. Weisfield, "Recombination in a-Si: H: Transitions through defect states," *Physical Review B (Condensed Matter)*, vol. 30, no. 1, pp. 5861–5870, 1984.
  - [61] B. E. Pieters, H. Stiebig, M. Zeman, and R. A. C. M. M. van Swaaij, "Determination of the mobility gap of intrinsic  $\mu\text{c-Si:H}$  in p-i-n solar cells," *Journal of Applied Physics*, vol. 105, no. 4, pp. 044502–1–10, 2009.
  - [62] J. A. Willemsen, *Modelling of Amorphous Silicon Single- and Multi-Junction Solar Cells*. PhD thesis, Technische Universiteit Delft, Delft, 1998.
  - [63] B. E. Pieters, *Characterization of thin-film Silicon materials and solar cells through numerical modeling*. PhD thesis, Technische Universiteit Delft, Delft, 2008.
  - [64] J. E. Jaffe and A. Zunger, "Theory of the band-gap anomaly in ABC<sub>2</sub> chalcopyrite semiconductors," *Physical Review B*, vol. 29, no. 4, pp. 1882–1906, 1984.
  - [65] S.-H. Han, A. M. Hermann, F. S. Hasoon, H. a. Al-Thani, and D. H. Levi, "Effect of Cu deficiency on the optical properties and electronic structure of CuInSe<sub>2</sub> and CuIn<sub>0.8</sub>Ga<sub>0.2</sub>Se<sub>2</sub> determined by spectroscopic ellipsometry," *Applied Physics Letters*, vol. 85, no. 4, pp. 576–578, 2004.
  - [66] J. M. Marshall, "Carrier diffusion in amorphous semiconductors," *Reports on Progress in Physics*, vol. 46, no. 10, p. 1145, 1983.

- [67] N. F. Mott, "The mobility edge since 1967," *Journal of Physics C: Solid State Physics*, vol. 20, no. 21, pp. 3075–3102, 1987.
- [68] K. Zhu, J. Yang, W. Wang, E. A. Schiff, J. Liang, and S. Guha, "Bandtail Limits to Solar Conversion Efficiencies in Amorphous Silicon Solar Cells," in *Material Research Society Symposium Proceedings*, pp. 297–302, 2003.
- [69] Y. P. Varshni, "Temperature dependence of the energy gap in semiconductors," *Physica*, vol. 34, no. 1, pp. 149–154, 1967.
- [70] G. D. Cody, T. Tiedje, B. Abeles, B. Brooks, and Y. Goldstein, "Disorder and the optical-absorption edge of hydrogenated amorphous silicon," *Physical Review Letters*, vol. 47, no. 20, pp. 1480–1483, 1981.
- [71] J. Liang, E. Schiff, S. Guha, B. Yan, and J. Yang, "Temperature-Dependent Open-Circuit Voltage Measurements and Light-Soaking in Hydrogenated Amorphous Silicon Solar Cells," in *Material Research Society Symposium Proceedings*, vol. 862, pp. 1–6, 2005.
- [72] J. Liang, E. A. Schiff, S. Guha, B. Yan, and J. Yang, "Hole-mobility limit of amorphous silicon solar cells," *Applied Physics Letters*, vol. 88, no. 6, pp. 063512–1–3, 2006.
- [73] C. Tsang and R. Street, "Recombination in plasma-deposited amorphous Si:H. Luminescence decay," *Physical Review B*, vol. 19, no. 6, pp. 3027–3040, 1979.
- [74] S. M. Sze and K. K. Ng, *Physics of Semiconductor Devices*, vol. 3. Wiley-Interscience, 2006.
- [75] P. G. Le Comber and W. E. Spear, "Electronic Transport in amorphous Silicon films," *Physical Review Letters*, vol. 25, no. 8, pp. 509–511, 1970.
- [76] R. Crandall, "Band-Tail Absorption in Hydrogenated Amorphous Silicon," *Physical Review Letters*, vol. 44, no. 19, p. 1980, 1980.
- [77] T. Tiedje, J. M. Cebulka, D. L. Morel, and B. Abeles, "Evidence for exponential band tails in amorphous silicon hydride," *Physical Review Letters*, vol. 46, no. 21, pp. 1425–1428, 1981.
- [78] E. O. Kane, "Thomas-Fermi Approach to Impure Semiconductor band Structure," *Physical Review*, vol. 131, no. 1, pp. 79–88, 1963.
- [79] T. N. Morgan, "Broadening of Impurity Bands in Heavily Doped Semiconductors," *Physical Review*, vol. 139, no. 1A, pp. 343–348, 1965.
- [80] A. P. Levanyuk and V. V. Osipov, "Theory of Luminescence of Heavily Doped Semiconductors," *Soviet Physics Semiconductors-USSR*, vol. 7, no. 6, pp. 721–726, 1973.
- [81] A. P. Levanyuk and V. V. Osipov, "Theory of Luminescence of Heavily Doped Compensated Nondegenerate Semiconductors," *Soviet Physics Semiconductors-USSR*, vol. 7, no. 6, pp. 727–733, 1973.

- 
- [82] S. Siebentritt, N. Papathanasiou, and M. Lux-Steiner, "Potential fluctuations in compensated chalcopyrites," *Physica B: Condensed Matter*, vol. 376-377, pp. 831–833, Apr. 2006.
- [83] M. Stutzmann, "A comment on thermal defect creation in hydrogenated amorphous silicon," *Philosophical Magazine Letters*, vol. 66, no. 3, pp. 147–150, 1992.
- [84] S. Aljishi, J. D. Cohen, S. Jin, and L. Ley, "Band Tails in Hydrogenated Amorphous Silicon and Silicon-Germanium Alloys," *Physical Review Letters*, vol. 64, no. 23, pp. 2811–2814, 1990.
- [85] E. A. Schiff, "Drift-mobility measurements and mobility edges in disordered silicon," *Journal of Physics: Condensed Matter*, vol. 16, pp. S5265–S5275, Nov. 2004.
- [86] R. N. Hall, "Electron-hole recombination in germanium," *Physical Review*, vol. 87, no. 2, p. 387, 1952.
- [87] W. Shockley and W. T. Read Jr, "Statistics of the recombinations of holes and electrons," *Physical Review*, vol. 87, no. 5, pp. 835–842, 1952.
- [88] J. G. Simmons and G. W. Taylor, "Nonequilibrium steady-state statistics and associated effects for insulators and semiconductors containing an arbitrary distribution of traps," *Physical Review B*, vol. 4, no. 2, pp. 502–511, 1971.
- [89] G. W. Taylor and J. G. Simmons, "Basic equations for statistics, recombination processes, and photoconductivity in amorphous insulators and semiconductors," *Journal of Non-Crystalline Solids*, vol. 8-10, pp. 940–946, 1972.
- [90] J. C. Anderson, "Noise spectroscopy in amorphous silicon films," *Philosophical Magazine B*, vol. 48, no. 1, pp. 31–45, 1983.
- [91] M. Stutzmann, "Weak bond-dangling bond conversion in amorphous silicon," *Philosophical Magazine B*, vol. 56, no. 1, pp. 63–70, 1987.
- [92] W. E. Spear and P. G. Le Comber, "Substitutional Doping of Amorphous Silicon," *Solid State Communications*, vol. 17, no. 9, pp. 1193–1196, 1975.
- [93] W. E. Spear and P. G. Le Comber, "Electronic properties of substitutionally doped amorphous Si and Ge," *Philosophical Magazine*, vol. 33, no. 6, pp. 935–949, 1976.
- [94] K. Winer, "Defect formation in a-Si:H," *Physical Review B*, vol. 41, no. 17, pp. 12150–12161, 1990.
- [95] M. J. Powell and S. C. Deane, "Improved defect-pool model for charged defects in amorphous silicon," *Physical Review B*, vol. 48, no. 15, pp. 10815–10827, 1993.
- [96] M. J. Powell and S. C. Deane, "Defect-pool model and the hydrogen density of states in hydrogenated amorphous silicon," *Physical Review B*, vol. 53, no. 15, pp. 10121–10132, 1996.

- [97] G. Schumm, "Chemical equilibrium description of stable and metastable defect structures in a-Si:H," *Physical Review B*, vol. 49, no. 4, pp. 2427–2442, 1994.
- [98] J. Kakalios, R. A. Street, and W. B. Jackson, "Stretched-exponential relaxation arising from dispersive diffusion of hydrogen in amorphous silicon," *Physical Review Letters*, vol. 59, no. 9, pp. 1037–1040, 1987.
- [99] R. A. Street, "Hydrogen chemical potential and structure of a-Si:H," *Physical Review B*, vol. 43, no. 3, pp. 2454–2457, 1991.
- [100] Y. Bar-Yam and J. Joannopoulos, "Theories of defects in amorphous semiconductors," *Journal of Non-Crystalline Solids*, vol. 97-98, no. Part 1, pp. 467–474, 1987.
- [101] C. T. Sah and W. Shockley, "Electron-hole recombination statistics in semiconductors through flaws with many charge conditions," *Physical Review*, vol. 109, no. 4, pp. 1103–1115, 1958.
- [102] W. Shockley and J. T. Last, "Statistics of the Charge Distribution for a Localized Flaw in a Semiconductor," *Physical Review*, vol. 107, no. 2, pp. 392–396, 1957.
- [103] H. Okamoto and Y. Hamakawa, "Electronic behaviors of the gap states in amorphous semiconductors," *Solid State Communications*, vol. 24, no. 1, pp. 23–27, 1977.
- [104] P. Wurfel, "The chemical potential of radiation," *Journal of Physics C: Solid State Physics*, vol. 15, no. 18, pp. 3967–3985, 1982.
- [105] T. Kirchartz and U. Rau, "Detailed balance and reciprocity in solar cells," *Physica Status Solidi (A)*, vol. 205, no. 12, pp. 2737–2751, 2008.
- [106] T. Kirchartz, *Generalized detailed balance theory of solar cells*. PhD thesis, Rheinisch-Westfälische Technische Hochschule Aachen, Aachen, Germany, 2009.
- [107] T. Kirchartz, A. Helbig, W. Reetz, M. Reuter, J. H. Werner, and U. Rau, "Reciprocity between electroluminescence and quantum efficiency used for the characterization of silicon solar cells," *Progress in Photovoltaics: Research and Applications*, vol. 17, no. 6, pp. 394–402, 2009.
- [108] T. Kirchartz, U. Rau, M. Hermle, A. W. Bett, A. Helbig, and J. H. Werner, "Internal voltages in GaInPGaInAsGe multijunction solar cells determined by electroluminescence measurements," *Applied Physics Letters*, vol. 92, no. 12, pp. 123502–1–3, 2008.
- [109] E. Daub and P. Wurfel, "Ultra-low values of the absorption coefficient for bandband transitions in moderately doped Si obtained from luminescence," *Journal of Applied Physics*, vol. 80, no. 9, pp. 5325–5330, 1996.
- [110] A. Jasenek and U. Rau, "Defect generation in Cu(In,Ga)Se<sub>2</sub> heterojunction solar cells by high-energy electron and proton irradiation," *Journal of Applied Physics*, vol. 90, no. 2, pp. 650–658, 2001.

- 
- [111] T. Nakashiba and M. Konagai, "Fabrication of  $\text{Cu(InGa)Se}_2$  thin-film solar cells grown with ionized Ga source," in *2008 Conference on Optoelectronic and Microelectronic Materials and Devices*, pp. 281–284, Ieee, July 2008.
  - [112] T.-H. Cheng, W. W. Hsu, C. Huang, J.-a. Lu, J. Y. Chen, and C. W. Liu, "Photoluminescence Characterization and Passivation of CIGS Absorber," *ECS Transactions*, vol. 33, no. 17, pp. 191–197, 2011.
  - [113] I. Dirnstorfer, M. Wagner, D. M. Hofman, M. D. Lampert, F. Karg, and B. K. Meyer, "Characterization of  $\text{CuIn(Ga)Se}_2$  Thin Films," *Physica Status Solidi (A)*, vol. 168, no. 1, pp. 163–176, 1998.
  - [114] A. Bauknecht, S. Siebentritt, J. Albert, and M. C. Lux-Steiner, "Radiative recombination via intrinsic defects in  $\text{Cu}_x\text{Ga}_y\text{Se}_2$ ," *Journal of Applied Physics*, vol. 89, no. 8, pp. 4391–4400, 2001.
  - [115] U. Rau and J. H. Werner, "Radiative efficiency limits of solar cells with lateral band-gap fluctuations," *Applied Physics Letters*, vol. 84, no. 19, pp. 3735–3737, 2004.
  - [116] J. H. Werner, J. Mattheis, and U. Rau, "Efficiency limitations of polycrystalline thin film solar cells: case of  $\text{Cu(In,Ga)Se}_2$ ," *Thin Solid Films*, vol. 480–481, pp. 399–409, June 2005.
  - [117] R. Carius, T. Merdzhanova, S. Klein, and F. Finger, "Band tail states in microcrystalline silicon solar cells probed by photoluminescence and open circuit voltage," *Journal of Optoelectronics and advanced materials*, vol. 7, no. 1, pp. 121–128, 2005.
  - [118] T. C. M. Müller, B. E. Pieters, T. Kirchartz, R. Carius, and U. Rau, "Modelling of photo- and electroluminescence of hydrogenated microcrystalline silicon solar cells," *Physica Status Solidi (C)*, vol. 9, pp. 1963–1967, Sept. 2012.
  - [119] N. F. Mott, E. A. Davis, and R. A. Street, "States in the gap and recombination in amorphous semiconductors," *Philosophical Magazine*, vol. 32, no. 5, pp. 961–996, 1975.
  - [120] R. A. Street, "Luminescence in amorphous semiconductors," *Advances in Physics*, vol. 25, no. 4, pp. 397–453, 1976.
  - [121] R. A. Street, J. C. Knights, and D. K. Biegelsen, "Luminescence studies of plasma-deposited hydrogenated silicon," *Physical Review B*, vol. 18, no. 4, pp. 1880–1891, 1978.
  - [122] J. Shah, A. Pinczuk, F. B. Alexander, and B. G. Bagley, "Excitation wavelength dependence of luminescence spectra of a-Si:H," *Solid State Communications*, vol. 42, no. 10, pp. 717–720, 1982.
  - [123] R. A. Street, *Hydrogenated amorphous silicon*. Cambridge ; New York : Cambridge University Press, 1991.
  - [124] R. A. Street, "Phonon interactions in the luminescence of amorphous silicon," *Philosophical Magazine B*, vol. 37, no. 1, pp. 35–42, 1978.



- [125] P. K. Bhat, T. M. Searle, I. G. Austin, R. A. Gibson, and J. Allison, "Low Energy Excitation of Photoluminescence in a-Si:H: Temperature and Intensity Effects," *Solid State Communications*, vol. 45, no. 6, pp. 1–5, 1983.
- [126] N.-M. Park, C.-J. Choi, T.-Y. Seong, and S.-J. Park, "Quantum Confinement in Amorphous Silicon Quantum Dots Embedded in Silicon Nitride," *Physical Review Letters*, vol. 86, pp. 1355–1357, Feb. 2001.
- [127] R. A. Street, "Recombination in a-Si:H: Defect luminescence," *Physical Review B*, vol. 21, no. 12, pp. 5775–5784, 1980.
- [128] R. A. Street, D. K. Biegelsen, and J. C. Knights, "The luminescence of doped and compensated amorphous silicon," *Journal of Luminescence*, vol. 24/25, pp. 51–54, 1981.
- [129] M. Vaněček, J. Kočka, J. Stuchlik, Z. Kozisek, O. Stika, and A. Triska, "Density of the Gap States in Undoped and Doped Glow Discharge a-Si:H," *Solar Energy Materials*, vol. 8, no. 4, pp. 411–423, 1983.
- [130] M. Vaněček, A. Abraham, O. Stika, J. Stuchlik, and J. Kočka, "Gap States Density in a-Si: H Deduced from Subgap Optical Absorption Measurement on Schottky Solar Cells," *Physica Status Solidi (A)*, vol. 83, no. 2, pp. 617–623, 1984.
- [131] P. Jensen, "Deconvolution of CPM Absorption Spectra: A New Technique," *Solid State Communications*, vol. 76, no. 11, pp. 1301–1303, 1990.
- [132] H. G. Grimmeiss and L.-a. Ledebro, "Spectral distribution of photoionization cross sections by photoconductivity measurements," *Journal of Applied Physics*, vol. 46, no. 5, pp. 2155–2162, 1975.
- [133] K. Pierz, B. Hilgenberg, H. Mell, and G. Weiser, "Gap-state distribution in n-type and p-type a-Si:H from optical absorption," *Journal of Non-Crystalline Solids*, vol. 97-98, no. 1, pp. 63–66, 1987.
- [134] K. Pierz, W. Fuhs, and H. Mell, "On the mechanism of doping and defect formation in a-Si: H," *Philosophical Magazine B*, vol. 63, no. 1, pp. 123–141, 1991.
- [135] A. O. Kodolbas and O. Öktü, "Comparison of the methods used to calculate the density of states from measured subbandgap absorption in a-Si:H and related alloys," *Optical Materials*, vol. 20, no. 2, pp. 147–151, 2002.
- [136] Y. Bouizem, A. Belfedal, J. D. Sib, and L. Chahed, "Density of states in hydrogenated amorphous germanium seen via optical absorption spectra," *Solid State Communications*, vol. 126, pp. 675–680, June 2003.
- [137] G. Voorwinden, R. Kniese, and M. Powalla, "In-line Cu(In,Ga)Se<sub>2</sub> co-evaporation processes with graded band gaps on large substrates," *Thin Solid Films*, vol. 431-432, pp. 538–542, May 2003.

- 
- [138] Z. Jehl, M. Bouttemy, D. Lincot, J. F. Guillemoles, I. Gerard, A. Etcheberry, G. Voorwinden, M. Powalla, and N. Naghavi, "Insights on the influence of surface roughness on photovoltaic properties of state of the art copper indium gallium diselenide thin films solar cells," *Journal of Applied Physics*, vol. 111, no. 11, pp. 114509–1–7, 2012.
  - [139] R. Caballero, V. Izquierdo-Roca, X. Fontané, C. Kaufmann, J. Álvarez García, A. Eicke, L. Calvo-Barrio, A. Pérez-Rodríguez, H. Sock, and J. Morante, "Cu deficiency in multi-stage co-evaporated Cu(In,Ga)Se<sub>2</sub> for solar cells applications: Microstructure and Ga in-depth alloying," *Acta Materialia*, vol. 58, pp. 3468–3476, May 2010.
  - [140] Y. Mai, S. Klein, R. Carius, J. Wolff, A. Lambert, F. Finger, and X. Geng, "Microcrystalline silicon solar cells deposited at high rates," *Journal of Applied Physics*, vol. 97, no. 11, pp. 114913–1–12, 2005.
  - [141] M. Berginski, J. Hupkes, M. Schulte, G. Schope, H. Stiebig, B. Rech, and M. Wuttig, "The effect of front ZnO:Al surface texture and optical transparency on efficient light trapping in silicon thin-film solar cells," *Journal of Applied Physics*, vol. 101, no. 7, pp. 074903–1–11, 2007.
  - [142] National Renewable Energy Laboratory, "Reference Solar Spectral Irradiance: Air Mass 1.5," 2012.
  - [143] B. Rech and H. Wagner, "Potential of amorphous silicon for solar cells," *Applied Physics A: Materials Science & Processing*, vol. 69, pp. 155–167, Aug. 1999.
  - [144] B. E. Pieters, J. Krč, and M. Zeman, "Advanced Numerical Simulation Tool For Solar Cells - ASA5," in *Photovoltaic Energy Conversion, Conference Record of the 2006 IEEE 4th World Conference*, vol. 2, pp. 1513–1516, Piscataway, NJ: Institute of Electrical and Electronics Engineers, Inc. (IEEE), 2006.
  - [145] G. Tao, *Optical Modeling and Characterization of Hydrogenated Amorphous Silicon Solar Cells*. PhD thesis, Delft University of Technology, 1994.
  - [146] G. Tao, M. Zeman, and J. W. Metselaar, "Accurate generation rate profiles in a-Si:H solar cells with textured TCO substrates," *Solar Energy Materials & Solar Cells*, vol. 34, no. 1-4, pp. 359–366, 1994.
  - [147] J. M. Bennett and H. E. Bennett, "Non-Normal-Incidence Reflection and Transmission Polarizers," in *Handbook of Optics*, ch. Polarizers, p. 1100, McGraw-Hill Professional, 1995.
  - [148] R. E. I. Schropp and M. Zeman, *Amorphous and Microcrystalline Solar Cells: Modeling, Materials, and Device Technology*. Kluwer Academic Publishers, 1998.
  - [149] M. Zeman, R. A. C. M. M. van Swaaij, J. W. Metselaar, and R. E. I. Schropp, "Optical modeling of a-Si:H solar cells with rough interfaces: Effect of back contact and interface roughness," *Journal of Applied Physics*, vol. 88, no. 11, pp. 6436–6443, 2000.

- [150] H. E. Bennett and J. O. Porteus, "Relation Between Surface Roughness and Specular Reflectance at Normal Incidence," *Journal of the Optical Society of America*, vol. 51, no. 2, pp. 123–129, 1961.
- [151] M. Wolf and H. Rauschenbach, "Series resistance effects on solar cell measurements," *Advanced Energy Conversion*, vol. 3, no. 2, pp. 455–479, 1963.
- [152] T. C. M. Müller, B. E. Pieters, T. Kirchartz, and U. Rau, "Analysis of the series resistance in pin-type thin-film silicon solar cells Analysis of the series resistance in pin-type thin-film silicon solar cells," *Journal of Applied Physics*, vol. 113, no. 13, pp. 134503–1–6, 2013.
- [153] I.-S. Chen and C. R. Wronski, "Internal photoemission on a-Si:H Schottky barrier structures revisited," *Journal of Non-Crystalline Solids*, vol. 190, no. 1-2, pp. 58–66, 1995.
- [154] E. A. Schiff, "Parameter Values for Modeling Photocarrier Processes in Hydrogenated Amorphous Silicon," 2006.
- [155] C. W. H. Sellmer, *Untersuchung der Ladungsträgerkonzentration und -beweglichkeit in mikrokristallinen Siliziumlegierungen mit Hall-Effekt und Thermokraft*. PhD thesis, RWTH Aachen University, 2011.
- [156] M. H. Cohen, "Theory of amorphous semiconductors," *Physics Today*, vol. 24, no. 5, p. 26, 1971.
- [157] T. P. Eggarter, "Semiclassical Theory of Electron Transport Properties in a Disordered Material," *Physical Review B*, vol. 5, no. 6, pp. 2496–2509, 1972.
- [158] S. Kirkpatrick, "Percolation and Conduction," *Reviews of Modern Physics*, vol. 45, no. 4, pp. 574–588, 1973.
- [159] K. Shimakawa, "Percolation-controlled electronic properties in microcrystalline silicon: effective medium approach," *Journal of Non-Crystalline Solids*, vol. 266-269, no. Part 1, pp. 223–226, 2000.
- [160] S. B. Concari, R. H. Buitrago, M. T. Gutiérrez, and J. J. Gandía, "Electric transport mechanism in intrinsic and p-doped microcrystalline silicon thin films," *Journal of Applied Physics*, vol. 94, no. 4, pp. 2417–2422, 2003.
- [161] A. Fejfar, T. Mates, O. Čertk, B. Rezek, J. Stuchlk, I. Pelant, and J. Kočka, "Model of electronic transport in microcrystalline silicon and its use for prediction of device performance," *Journal of Non-Crystalline Solids*, vol. 338-340, pp. 303–309, 2004.
- [162] F. Liu, M. Zhu, and Q. Wang, "Anisotropic electronic transport in microcrystalline silicon thin films," *Physics Letters A*, vol. 331, no. 6, pp. 432–436, 2004.
- [163] H. Matsuura, T. Okuno, H. Okushi, and K. Tanaka, "Electrical properties of n-amorphous p-crystalline silicon heterojunctions," *Journal of Applied Physics*, vol. 55, no. 4, pp. 1012–1019, 1984.

- 
- [164] M. Schmidt, L. Korte, A. Laades, R. Stangl, C. Schubert, H. Angermann, E. Conrad, and K. Maydell, "Physical aspects of a-Si:H/c-Si hetero-junction solar cells," *Thin Solid Films*, vol. 515, no. 19, pp. 7475–7480, 2007.
- [165] K. Y. Chan, D. Knipp, A. Gordijn, and H. Stiebig, "Influence of crystalline volume fraction on the performance of high mobility microcrystalline silicon thin-film transistors," *Journal of Non-Crystalline Solids*, vol. 354, no. 19–25, pp. 2505–2508, 2008.
- [166] P. Kanschä, H. Mell, K. Lips, and W. Fuhs, "Defect and Tail States in Microcrystalline Silicon investigated by pulsed ESR," *Material Research Society Symposium Proceedings*, vol. 609, no. A27.3, pp. 1–6, 2000.
- [167] T. Dylla, F. Finger, and E. A. Schiff, "Hole drift-mobility measurements in microcrystalline silicon," *Applied Physics Letters*, vol. 87, no. 3, pp. 032103–1–3, 2005.
- [168] J.-K. Lee and E. Schiff, "Modulated electron-spin-resonance measurements and defect correlation energies in amorphous silicon," *Physical Review Letters*, vol. 68, no. 19, pp. 2972–2975, 1992.
- [169] Q. Gu, Q. Wang, E. A. Schiff, and C. T. Malone, "Hole drift mobility measurements in amorphous silicon-carbon alloys," *Journal of Applied Physics*, vol. 76, no. 4, pp. 2310–2315, 1994.
- [170] S. Dinca, G. Ganguly, Z. Lu, E. A. Schiff, V. Vlahos, C. R. Wronski, and Q. Yuan, "Hole Drift-Mobility Measurements in Contemporary Amorphous Silicon," in *Materials Research Society Symposium Proceeding*, vol. 762, pp. 1–6, 2003.
- [171] J. M. Hvam and M. H. Brodsky, "Dispersive Transport and Recombination Lifetime in Phosphorous-Doped Hydrogenated Amorphous Silicon," *Physical Review Letters*, vol. 46, no. 5, pp. 371–374, 1981.
- [172] J. M. Marshall, R. A. Street, and M. J. Thompson, "Electron drift mobility in amorphous Si:H," *Philosophical Magazine B*, vol. 54, no. 1, pp. 51–60, 1986.
- [173] Q. Wang, H. Antoniadis, E. A. Schiff, and S. Guha, "Electron-drift-mobility measurements and exponential conduction-band tails in hydrogenated amorphous silicon-germanium alloys," *Physical Review B*, vol. 47, no. 15, pp. 9435–9448, 1993.
- [174] K. Winer and L. Ley, "Surface states and the exponential valence-band tail in a-Si:H," *Physical Review B*, vol. 36, no. 11, pp. 6072–6078, 1987.
- [175] T. Dylla, *Electron Spin Resonance and Transient Photocurrent Measurements on Microcrystalline Silicon*. PhD thesis, Freie Universität Berlin, Berlin, 2004.
- [176] S. Reynolds, V. Smirnov, C. Main, F. Finger, and R. Carius, "Interpretation of Transient Photocurrents in Coplanar and Sandwich PIN Microcrystalline Silicon Structures," in *Material Research Society Symposium Proceedings*, vol. 808, pp. 127–132, 2004.

- [177] R. A. Street, J. Zesch, and M. J. Thompson, "Effects of doping on transport and deep trapping in hydrogenated amorphous silicon," *Applied Physics Letters*, vol. 43, no. 7, pp. 672–674, 1983.
- [178] H. Antoniadis and E. Schiff, "Transient photocharge measurements and electron emission from deep levels in undoped a-Si:H," *Physical Review B*, vol. 46, no. 15, pp. 9435–9448, 1992.
- [179] G. Juska, J. Kočka, M. Viliunas, and K. Arlauskas, "Subnanosecond bimolecular non-radiative recombination in a-Si:H," *Journal of Non-Crystalline Solids*, vol. 164-166, no. 1, pp. 579–582, 1993.
- [180] E. A. Schiff, "Diffusion-controlled bimolecular recombination of electrons and holes in a-Si:H," *Journal of Non-Crystalline Solids*, vol. 190, no. 1-2, pp. 1–8, 1995.
- [181] T. Brammer, *Die optoelektronischen Eigenschaften von mikrokristallinen Silizium-Solarzellen*. PhD thesis, Heinrich-Heine Universität Düsseldorf, 2001.
- [182] B. E. Pieters, S. Schicho, and H. Stiebig, "Characterization of Mobility Gap in  $\mu\text{c-Si:H}$  Pin Devices," *Amorphous and polycrystalline thin-film silicon science and technology*, vol. 1066, pp. 93–98, 2008.
- [183] T. C. M. Müller, *Temperatur- und Generationsratenabhängigkeit von  $\mu\text{c-Si:H}$ -Solarzellen: Experiment und Simulation elektrischer Eigenschaften*. PhD thesis, Rheinisch-Westfälische Technische Hochschule Aachen, Aachen, Germany, 2010.
- [184] J. Lee, *Metastability of copper indium gallium diselenide polycrystalline thin film solar cell devices*. PhD thesis, University of Oregon, 2008.
- [185] M. N. Ruberto and A. Rothwarf, "Time-dependent open-circuit voltage in  $\text{CuInSe}_2/\text{CdS}$  solar cells: Theory and experiment," *Journal of Applied Physics*, vol. 61, no. 9, pp. 4662–4669, 1987.
- [186] R. Sasala and J. Sites, "Time Dependent Voltage In  $\text{CuInSe}_2$  And  $\text{CdTe}$  Solar Cells," in *Photovoltaic Specialists Conference, 1993, Conference Record of the Twenty Third IEEE*, no. 1, pp. 543–548, 1993.
- [187] M. Igalsen and H. W. Schock, "The metastable changes of the trap spectra of  $\text{CuInSe}_2$ -based photovoltaic devices," *Journal of Applied Physics*, vol. 80, no. 10, pp. 5765–5769, 1996.
- [188] U. Rau and H. W. Schock, "Electronic properties of  $\text{Cu(In,Ga)Se}_2$  heterojunction solar cells-recent achievements, current understanding, and future challenges," *Applied Physics A: Materials Science & Processing*, vol. 69, pp. 131–147, Aug. 1999.
- [189] A. E. Delahoy, A. Ruppert, and M. Contreras, "Charging and discharging of defect states in CIGS/ $\text{ZnO}$  junctions," *Thin Solid Films*, vol. 361-362, pp. 140–144, Feb. 2000.

- 
- [190] J. Heath, J. Cohen, and W. Shafarman, "Distinguishing metastable changes in bulk CIGS defect densities from interface effects," *Thin Solid Films*, vol. 431-432, pp. 426-430, May 2003.
  - [191] J. T. Heath, "Bulk and metastable defects in  $\text{CuIn}_{1-x}\text{Ga}_x\text{Se}_2$  thin films using drive-level capacitance profiling," *Journal of Applied Physics*, vol. 95, no. 3, pp. 1000-1010, 2004.
  - [192] J. Serhan, Z. Djebbour, W. Favre, A. Migan-Dubois, A. Darga, D. Mencaraglia, N. Naghavi, G. Renou, J.-F. Guillemoles, and D. Lincot, "Investigation of the metastability behavior of CIGS based solar cells with  $\text{ZnMgOZn}(\text{S}, \text{O}, \text{OH})$  window-buffer layers," *Thin Solid Films*, vol. 519, pp. 7606-7610, Aug. 2011.
  - [193] A. Rothwarf, J. Phillips, and N. C. Wyeth, "Junction Field and Recombination Phenomena in The  $\text{CdS}/\text{Cu}_2\text{S}$  Solar Cell: Theory and Experiment," in *Conference Record of the 13th IEEE Photovoltaic Specialists Conference 1978*, pp. 399-405, 1978.
  - [194] B. J. Shklovskii and A. L. Efros, *Electronic Properties of Doped Semiconductors*. Berlin: Springer-Verlag KG, 1984.
  - [195] T. Löher, W. Jaegermann, and C. Pettenkofer, "Formation and electronic properties of the  $\text{CdS}/\text{CuInSe}_2$  (011) heterointerface studied by synchrotroninduced photoemission," *Journal of Applied Physics*, vol. 77, no. 2, pp. 731-738, 1995.
  - [196] M. Kohyama and R. Yamamoto, "Theoretical study of grain boundaries in Si: Effects of structural disorder on the local electronic structure and the origin of band tails," *Physical Review B*, vol. 50, no. 12, pp. 8502-8522, 1994.
  - [197] R. Schäffler and H. W. Schock, "Composition dependent optical properties of polycrystalline  $\text{CuInSe}_2$  thin films," *Diffusion and Defect Data Part B (Solid State Phenomena)*, vol. 51-52, pp. 347-352, 1996.
  - [198] U. Rau, "Tunneling-enhanced recombination in  $\text{Cu}(\text{In}, \text{Ga})\text{Se}_2$  heterojunction solar cells," *Applied Physics Letters*, vol. 74, no. 1, pp. 111-113, 1999.
  - [199] A. Rose, "Space-Charge-Limited Currents in Solids," *Physical Review*, vol. 97, no. 6, pp. 1538-1544, 1955.
  - [200] P. N. Murgatroyd, "Theory of space-charge-limited current enhanced by Frenkel effect," *Journal of Physics D: Applied Physics*, vol. 3, no. 5-6, pp. 151-156, 1970.
  - [201] A. A. Anatoly, S. Luryi, M. R. Pinto, and N. Schryer, "Space-Charge-Limited Current in a Film," *IEEE Transactions on Electron Devices*, vol. 36, no. 6, pp. 1162-1170, 1989.
  - [202] T. Tiedje, C. R. Wronski, B. Abeles, and M. Cebulka, "Electron transport in hydrogenated amorphous silicon: Drift mobility and junction capacitance," *Solar Cells*, vol. 2, no. 3, pp. 301-318, 1980.
  - [203] T. S. Nashashibi, I. G. Austin, and T. M. Seakle, "Photoluminescence in pure and doped amorphous silicon," *Philosophical Magazine*, vol. 35, no. 3, pp. 831-835, 1977.

- [204] K. M. Hong, J. Noolandi, and R. A. Street, "Theory of radiative recombination by diffusion and tunneling in amorphous Si:H," *Physical Review B*, vol. 23, no. 6, pp. 2967–2976, 1981.
- [205] C. Qiu and J. I. Pankove, "Light-induced change in defect-band photoluminescence of doped hydrogenated amorphous silicon," *Physical Review B*, vol. 41, no. 18, pp. 12744–12749, 1990.
- [206] T. Merdzhanova, J. Woerdenweber, T. Zimmermann, U. Zastrow, A. J. Flikweert, H. Stiebig, W. Beyer, and A. Gordijn, "Single-chamber processes for a-Si:H solar cell deposition," *Solar Energy Materials & Solar Cells*, vol. 98, pp. 146–153, 2012.
- [207] J. Woerdenweber, T. Merdzhanova, T. Zimmermann, A. Flikweert, H. Stiebig, W. Beyer, and A. Gordijn, "Cross-contamination in single-chamber processes for thin-film silicon solar cells," *Journal of Non-Crystalline Solids*, vol. 358, pp. 2183–2186, Sept. 2012.
- [208] J. Woerdenweber, T. Merdzhanova, R. Schmitz, A. Mück, U. Zastrow, L. Niessen, A. Gordijn, R. Carius, W. Beyer, H. Stiebig, and U. Rau, "Influence of base pressure and atmospheric contaminants on a-Si:H solar cell properties," *Journal of Applied Physics*, vol. 104, no. 9, pp. 94507–1–6, 2008.
- [209] J. Woerdenweber, T. Merdzhanova, H. Stiebig, W. Beyer, and A. Gordijn, "Critical oxygen concentration in hydrogenated amorphous silicon solar cells dependent on the contamination source," *Applied Physics Letters*, vol. 96, no. 10, pp. 103505–1–3, 2010.
- [210] J. Woerdenweber, T. Merdzhanova, A. Gordijn, H. Stiebig, and W. Beyer, "Incorporation and critical concentration of oxygen in a-Si:H solar cells," *Solar Energy Materials & Solar Cells*, vol. 95, no. 10, pp. 2811–2815, 2011.
- [211] T. M. Searle and W. A. Jackson, "Static versus electron-phonon disorder in amorphous Si:H and its alloys," *Philosophical Magazine Part B*, vol. 60, no. 2, pp. 237–255, 1989.
- [212] D. V. Lang, J. D. Cohen, and J. P. Harbison, "Measurements of the density of gap states in hydrogenated amorphous silicon by space charge spectroscopy," *Physical Review B*, vol. 25, no. 8, pp. 5285–5320, 1982.
- [213] J. Jang and C. Lee, "Temperature dependent field effect conductance in a-Si:H," *Journal of Non-Crystalline Solids*, vol. 59-60, no. 1, pp. 281–284, 1983.
- [214] H. Haruki, H. Sakai, M. Kamiyama, and Y. Uchida, "Effect of Boron Doping And Its Profile On Characteristics of p-i-n a-Si:H Solar Cells," *Solar Energy Materials*, vol. 8, no. 4, pp. 441–455, 1983.
- [215] M. Vaněček, J. Stuchlik, J. Kočka, and A. Triska, "Determination of the mobility gap in amorphous silicon from a low temperature photoconductivity measurement," *Journal of Non-Crystalline Solids*, vol. 77-78, no. 1, pp. 299–302, 1985.
- [216] D. L. Staebler and C. R. Wronski, "Reversible conductivity changes in discharge-produced amorphous Si," *Applied Physics Letters*, vol. 31, no. 4, pp. 292–294, 1977.

- 
- [217] D. L. Staebler and C. R. Wronski, "Optically induced conductivity changes in discharge-produced hydrogenated amorphous silicon," *Journal of Applied Physics*, vol. 51, no. 6, pp. 3262–3268, 1980.
  - [218] A. K. O. Odziej, "Staebler-Wronski effect in amorphous silicon and its alloys," *Opto-Electronics Review*, vol. 12, no. 1, pp. 21–32, 2004.
  - [219] R. Street, "Recombination in a-Si:H: Auger effect and nongeminate recombination," *Physical Review B*, vol. 23, no. 2, pp. 861–868, 1981.
  - [220] Z. E. Smith and S. Wagner, "Band tails, entropy, and equilibrium defects in hydrogenated amorphous silicon," *Physical Review Letters*, vol. 59, no. 6, pp. 688–691, 1987.
  - [221] R. S. Crandall, "Defect relaxation in amorphous silicon: Stretched exponentials, the Meyer-Neldel rule, and the Staebler-Wronski effect," *Physical Review B*, vol. 43, no. 5, pp. 4057–4070, 1991.
  - [222] T. Markvart, "Solar cell as a heat engine: energy-entropy analysis of photovoltaic conversion," *Physica Status Solidi (a)*, vol. 205, pp. 2752–2756, Dec. 2008.





# List of Symbols

$\alpha$	Absorption	$\text{m}^{-1}$
$\alpha_\mu$	Temperature coefficient of the mobility gap	$\text{eV K}^{-1}$
$\beta_\mu$	Offset temperature of the temperature dependent mobility gap	K
$\chi$	Electron affinity	V
$\Delta \hat{E}_\gamma$	Change of peak photon energy	eV
$\Delta E_{\text{ft}}$	Quasi-Fermi level separation of trapped charge	eV
$\Delta E_{\text{f}}$	Quasi-Fermi level separation	eV
$\Delta V_{\text{oc}}$	Change of open circuit junction contact voltage	V
$\delta_{\text{rms}}$	Root-mean-square roughness	—
$\eta$	Photovoltaic efficiency	%
$\gamma$	Exponent from luminescence/current characteristics	—
$\hat{E}_\gamma$	Peak photon energy	eV
$\hbar$	Planck's constant	eV s
$\kappa$	Imaginary part of the refraction index	—
$\lambda$	Wavelength of light	m
$\mu_{\text{n}}$	Free electron mobility	$\text{m}^2 \text{V}^{-1} \text{s}^{-1}$
$\mu_{\text{p}}$	Free hole mobility	$\text{m}^2 \text{V}^{-1} \text{s}^{-1}$
$\Omega$	Phonon angular frequency	$2\pi \text{s}^{-1}$
$\phi$	Excitation photon flux	$\text{m}^{-2} \text{s}^{-1}$
$\phi$	Luminescence photon flux	$\text{m}^{-2} \text{s}^{-1}$
$\phi_{\text{EL}}$	Electroluminescence photon flux	$\text{m}^{-2} \text{s}^{-1}$
$\phi'_{\text{EL}}$	Electroluminescence photon flux from spectral distribution	$\text{m}^{-2} \text{s}^{-1}$
$\phi_{\text{PL}}$	Photoluminescence photon flux	$\text{m}^{-2} \text{s}^{-1}$
$\phi'_{\text{PL}}$	Photoluminescence photon flux from spectral distribution	$\text{m}^{-2} \text{s}^{-1}$
$\Psi$	Vacuum potential	V
$\rho$	Space charge density	$\text{C m}^{-3}$
$\rho_{\text{s},0}^{\text{i}}$	Specific resistance	$\Omega \text{m}$
$\sigma_{\text{db}}$	Standard deviation of Gaussian mid-gap defect distribution	eV
$\sigma_{\text{n}}$	Electron capture cross-section	$\text{m}^2$
$\sigma_{\text{n}}^+$	Electron capture cross-section of positively charged states	$\text{m}^2$
$\sigma_{\text{n}}^0$	Electron capture cross-section of neutral states	$\text{m}^2$
$\sigma_{\text{p}}$	Hole capture cross-section	$\text{m}^2$
$\sigma_{\text{p}}^-$	Hole capture cross-section of negatively charged states	$\text{m}^2$
$\sigma_{\text{p}}^0$	Hole capture cross-section of neutral states	$\text{m}^2$

$\sigma_r$	Relative capture cross section	—
$\tau$	Charge carrier life time	s
$\theta^{\text{in}}$	Angle of incident light	rad
$\theta^{\text{out}}$	Angle of outbound light	rad
$\theta_i$	Angle of incident light	rad
$\varepsilon_0$	Dielectric constant of vacuum	$\text{F m}^{-1}$
$\varepsilon_r$	Relative dielectric constant	—
$\varphi$	Spectral luminescence distribution	$\text{W m}^{-2} \text{nm}^{-1}$
$\varphi_{\text{bb}}$	Hemispherical black-body radiation	$\text{W m}^{-2} \text{nm}^{-1}$
$\varphi_{\text{EL}}$	Spectral electroluminescence distribution	$\text{W m}^{-2} \text{nm}^{-1}$
$\varphi'_{\text{EL}}$	Spectral electroluminescence distribution derived from $Q_e$	$\text{W m}^{-2} \text{nm}^{-1}$
$\varphi_{\text{PL}}$	Spectral photoluminescence distribution	$\text{W m}^{-2} \text{nm}^{-1}$
$\varphi_{\text{PL}}^{\text{sc}}$	Spectral photoluminescence distribution under short circuit conditions	$\text{W m}^{-2} \text{nm}^{-1}$
$A$	Optical absorptance	—
$ADF$	Angular distribution function of scattered light	—
$d$	Thickness of the absorber layer	m
$d_\alpha$	Absorption length	cm
$E$	Electrical field	$\text{V m}^{-1}$
$E_0$	Symmetric characteristic energy of the conduction and valence band tail	eV
$E_\gamma$	Photon energy	eV
$E_\mu$	Mobility gap	eV
$E_a$	Activation energy	eV
$E_{c0}$	Characteristic energy of the conduction band tail	eV
$E_c$	Conduction band mobility edge	eV
$E_{\text{db}}$	Center between Gaussian mid-gap defect distributions	eV
$E_{\text{db}}^{+/0}$	Center of the Gaussian mid-gap defect distribution of $+/0$ transition levels	eV
$E_{\text{db}}^{0/-}$	Center of the Gaussian mid-gap defect distribution of $0/-$ transition levels	eV
$E_{\text{fnt}}$	Quasi-Fermi level for trapped electrons	eV
$E_{\text{fnt}}$	Quasi-Fermi level for trapped holes	eV
$E_{\text{fnt}}^{\text{cbt}}$	Quasi-Fermi level for trapped electrons in the conduction band tail states	eV
$E_{\text{fnt}}^{\text{vbt}}$	Quasi-Fermi level for trapped electrons in the valence band tail states	eV
$E_{\text{fn}}$	Quasi-Fermi level for electrons	eV
$E_{\text{fp}}$	Quasi-Fermi level for holes	eV
$E_{\text{f}}$	Fermi-level	eV
$e_n$	Electron emission coefficient	$\text{s}^{-1}$
$e_n$	Hole emission coefficient	$\text{s}^{-1}$
$E_{r0}$	Characteristic energy derived from $n_r$	eV
$E_{v0}$	Characteristic energy of the valence band tail	eV
$E_v$	Valence band mobility edge	eV
$E_x$	Energy difference between $\hat{E}_\gamma$ and $\Delta E_{\text{ft}}$	eV
$f$	Frequency	$\text{s}^{-1}$
$F^+$	Occupation function for positively charged mid-gap defect states	—
$F^-$	Occupation function for negatively charged mid-gap defect states	—
$F^0$	Occupation function for neutral mid-gap defect states	—

$f_c$	Charge carrier collection efficiency	—
$F_{eq}^+$	Equilibrium occupation function for positively charged mid-gap defect states	—
$F_{eq}^-$	Equilibrium occupation function for negatively charged mid-gap defect states	—
$F_{eq}^0$	Equilibrium occupation function for neutral mid-gap defect states	—
$f_{FD}$	Fermi-Dirac distribution	—
$f_n$	Electron occupation probability	—
$f_p$	Hole occupation probability	—
$f_R^{in}$	Dependence of scattering on incident angle for reflectance	—
$f_R^{out}$	Angular distribution of the scattered reflected light	—
$f_T^{in}$	Dependence of scattering on incident angle for transmittance	—
$f_T^{out}$	Angular distribution of the scattered transmitted light	—
$FF$	Photovoltaic fill factor	—
$G$	Charge carrier generation rate	$m^{-3} s^{-1}$
$H$	Optical opacity	—
$H_R$	Haze for optical reflection	—
$H_T$	Haze for optical transmission	—
$J$	Charge carrier current density	$A m^{-2}$
$J_d$	Charge carrier current density in the dark	$A m^{-2}$
$J_i$	Charge carrier current density under illumination	$A m^{-2}$
$J_n$	Electron current density	$A m^{-2}$
$J_p$	Hole current density	$A m^{-2}$
$J_{sc}$	Short circuit charge carrier current density	$A m^{-2}$
$k$	Boltzmann's constant	$eV K^{-1}$
$k$	Inverse lattice coordinate	$C m^{-1}$
$n$	Electron concentration	$m^{-3}$
$n'$	Real part of the refraction index	—
$N_{c0}$	Density of conduction band tail states at band edge	$eV^{-1} m^{-3}$
$N_{cbt}$	Density of conduction band tail states	$eV^{-1} m^{-3}$
$n_{cbt}$	Trapped electron concentration density	$eV^{-1} m^{-3}$
$N_{cb}$	Conduction band density of states	$m^{-3}$
$n_{cb}$	Band electron concentration density	$eV^{-1} m^{-3}$
$N_c$	Conduction band effective density of states	$m^{-3}$
$N_{db}$	Total mid-gap defect concentration	$m^{-3}$
$N_{db}^{+/0}$	Distribution of energy levels arising from the $E^{+/0}$ transition level	$m^{-3}$
$N_{db}^{0/-}$	Distribution of energy levels arising from the $E^{0/-}$ transition level	$m^{-3}$
$n_r$	Radiative ideality factor	—
$N_{v0}$	Density of valence band tail states at band edge	$eV^{-1} m^{-3}$
$N_{vbt}$	Density of valence band tail states	$eV^{-1} m^{-3}$
$n_{vbt}$	Trapped hole concentration density	$eV^{-1} m^{-3}$
$N_{vb}$	Valence band density of states	$m^{-3}$
$N_v$	Valence band effective density of states	$m^{-3}$
$n_i$	Complex optical refraction index	—
$p$	Hole concentration	$m^{-3}$
$p_{vb}$	Band hole concentration density	$eV^{-1} m^{-3}$

$q$	Elementary charge	C
$Q_e$	External quantum efficiency	—
$Q'_e$	External quantum efficiency derived from $\varphi_{EL}$	—
$R$	Charge carrier recombination rate	$\text{m}^{-3} \text{s}^{-1}$
$R$	Optical reflectance	—
$R_{\text{sct}}$	Reflectance of scattered light	—
$R_s$	Series resistance	$\Omega \text{m}^2$
$R_s^e$	External ohmic contact series resistance	$\Omega \text{m}^2$
$r_i$	Electron/hole capture/emission rate	$\text{m}^{-3} \text{s}^{-1}$
$S_{\text{Ge}}$	Germanium detector sensitivity	$\text{W}^{-1} \text{m}^2 \text{nm}$
$T$	Temperature	K
$T$	Transmittance	—
$t$	Time	s
$T_0$	Reference temperature	K
$T_{\text{sct}}$	Transmittance of scattered light	—
$U$	Correlation energy of Gaussian mid-gap defect distributions	eV
$V$	Junction contact voltage	V
$V_d$	Junction contact voltage in the dark	V
$V_{\text{oc}}$	Open circuit junction contact voltage	V
$v_{\text{th}}$	Thermal velocity	$\text{m s}^{-1}$
$z$	Position through the device	m

# List of Publications

## First Author

T. C. M. Müller, E. Moulin, and U. Aeberhard, "Improvement of hydrogenated microcrystalline ( $\mu\text{c-Si:H}$ ) single junction solar cells with upconverter at rear side.," *Energy Procedia*, vol. 10, pp. 76–82, Januar 2011

T. C. M. Müller, B. E. Pieters, T. Kirchartz, R. Carius, and U. Rau, "Modelling of photo- and electroluminescence of hydrogenated microcrystalline silicon solar cells," *Physica Status Solidi (C)*, vol. 9, no. 10-11, pp. 1963–1967, September 2012

T. C. M. Müller, B. E. Pieters, T. Kirchartz, and U. Rau, "Analysis of the series resistance in *pin*-type thin-film silicon solar cells," *Journal of Applied Physics*, vol. 113, no. 13, pp. 134503–1–6, April 2013

T. C. M. Müller, T. M. H. Tran, B. E. Pieters, A. Gerber, R. Carius, und U. Rau, "Effect of light soaking on the electro- and photoluminescence of  $\text{Cu(In,Ga)Se}_2$  solar cells," *Applied Physics Letters*, vol. 103, no. 18, p. 183504–1–5, August 2013

T. C. M. Müller, B. E. Pieters, T. Kirchartz, R. Carius, und U. Rau, "Effect of localized states on the reciprocity between quantum efficiency and electroluminescence in  $\text{Cu(In,Ga)Se}_2$  and Si thin-film solar cells," *Solar Energy Materials & Solar Cells*, vol. 129, pp. 95 – 103, May 2014

## Coauthor

E. Moulin, P. Luo, B. E. Pieters, J. Sukmanowski, J. Kirchhoff, W. Reetz, T. C. M. Müller, R. Carius, F. X. Royer, and H. Stiebig, "Photoresponse enhancement in the near infrared wavelength range of ultrathin amorphous silicon photosensitive devices by integration of silver nanoparticles," *Applied Physics Letters*, vol. 95, no. 3, pp. 033505-1–3, July 2009

U. Rau, T. C. M. Müller, T. M. H. Tran, B. E. Pieters, and A. Gerber, "Electroluminescence of Cu(In,Ga)Se<sub>2</sub> solar cells and modules," *Materials Research Society Symposium Proceedings*, vol. 1538, pp. 133 – 144, March 2013

T. M. H. Tran, B. E. Pieters, M. Schneemann, T. C. M. Müller, A. Gerber, T. Kirchartz, and U. Rau, "Local junction voltages and radiative ideality factors of a-Si:H solar modules determined by electroluminescence imaging technique," *Materials Research Society Symposium Proceedings*, vol. 1536, pp. 105 – 111, March 2013

T. M. H. Tran, B. E. Pieters, M. Schneemann, T. C. M. Müller, A. Gerber, T. Kirchartz, und U. Rau, "Quantitative evaluation method for electroluminescence images of a-Si:H thin-film solar modules," *Physica Status Solidi – Rapid Research Letters*, vol. 7, no. 9, pp. 627 – 630, August 2013

A. Kampker, C. Deutschens, P. Müller, and T. C. M. Müller, "Reduzierung der Gesamtbetriebskosten durch den Einsatz von Elektrofahrzeugen," *Automobiltechnische Zeitschrift*, vol. 117, no. 3, pp. 48 – 51, March 2015

E. Moulin, T. C. M. Müller, M. Warzecha, A. Hoffman, U. W. Paetzold, U. Aeberhard, und R. Carius, "Highly transparent front electrodes with metal fingers for p-i-n thin-film silicon solar cells," *EPJ Photovoltaics*, vol. 6, pp. 60501–1–6, March 2015

# Curriculum Vitae

Thomas Christian Mathias Müller born June 23<sup>rd</sup>, 1984 in Aachen, Germany

## Education

8 / 1990	–	6 / 1994	Gemeinschaftsgrundschule Alsdorf-Ofden
8 / 1994	–	6 / 2003	Gymnasium der Stadt Alsdorf
6 / 2003			Abitur
7 / 2003	–	10 / 2003	Training as emergency medical assistant for civilian service
10 / 2004	–	2 / 2010	Studies of physics at the RWTH Aachen University
9 / 2006			Vordiplom
10 / 2006	–	9 / 2013	Studies of economic sciences at the RWTH Aachen University
10 / 2006	–	9 / 2008	Hauptstudium physics, main subject: experimental solid state physics
1 / 2009	–	1 / 2010	Diploma thesis physics at the Institute of Photovoltaic Title: "Temperatur- und Generationsratenabhängigkeit von $\mu\text{c-Si:H}$ -Solarzellen: Experiment und Simulation elektrischer Eigenschaften"
2 / 2010			Diploma in physics
4 / 2013	–	6 / 2013	Diploma thesis economic sciences at the Institute for International Economics Title: "Reduktion der Gesamtbetriebskosten von Fahrzeugflotten durch die Nutzung von Elektrofahrzeugen"
9 / 2013			Master in Business Administration

## Experience

7 / 2003	–	4 / 2004	Emergency medical assistant for civilian service at Deutsches Rotes Kreuz Aachen Stadt e.V.
11 / 2007	–	1 / 2008	Student assistant at RWTH Aachen university medical center
11 / 2008	–	11 / 2009	Diploma student at the IEK-5 – Photovoltaics at the Forschungszentrum Jülich
3 / 2010	–	2 / 2013	PhD student at the IEK-5 – Photovoltaics
10 / 2013	–	now	PostDoc at the IEK-5 – Photovoltaics





# Acknowledgements

During my time in Jülich many people helped and supported me and made me enjoy the whole time of my PhD thesis. Therefore, I would like to especially thank

my supervisor Prof. Dr. Uwe Rau for the opportunity to do this research and write this PhD thesis, for his criticism and ideas, which inspire my work, and for being able to learn from him most of what I know about Cu(In,Ga)Se<sub>2</sub> solar cells,

my group leader Prof. Dr. Reinhard Carius, who gave me the great opportunity to realize the experiments, which consumed a huge amount of liquid nitrogen fully automated, for his helpful advices to structure my work during the PhD thesis, and for sharing his experience in the field of spectroscopy and optics in general,

Dr. Bart Pieters, who taught me the physics of semiconductor devices and its modeling, for the discussions with him, which motivated me during the PhD thesis, and for being able to learn from him about writing papers,

Dr. Thomas Kirchartz, who gave me almost instantaneous advice and answers via eMail, whenever I suffered a lack of knowledge or ideas,

my project leader of the *nanospec* project Dr. Urs Aeberhard, who gave me the opportunity to work for this project and join the travels to the project meetings, for the general discussions beyond the physics of semiconductors, and his interest in my work,

Dr. Etienne Moulin, for his experimental work in the *nanospec* project, which supported my work for simulations tremendously well,

Josef Klomfaß, who taught me more about electrical circuits and experimental setups, for his technical advice,

Markus Hülsbeck, and Oliver Thimm for many other technical advices,

Thi Minh Hang Tran for supporting me with the Cu(In,Ga)Se<sub>2</sub> modules, and Joachim Kirchhoff for supporting me with the  $\mu$ c-Si:H, and *a*-Si:H devices, which I used for the experimental work in this PhD thesis,

Markus Ermes for supporting me with optical *nk*-characteristics for the simulations,

Dr. Tsvetelina Merdzhanova, and Dr. Jan Wördenweber for providing me with specially defect-rich *a*-Si:H devices,

Maurice Nuys for being a friend and colleague from the beginning of our studies of physics until our PhD thesis,

and last but not least all colleagues in Jülich.



Band / Volume 258

**Failure Analysis of Thin Film Solar Modules using Lock-in Thermography**

M. Siegloch (2015), XIII, 131 pp

ISBN: 978-3-95806-047-0

Band / Volume 259

**Relation between growth rate, material quality, and device grade condition for intrinsic microcrystalline silicon:**

From layer investigation to the application to thin-film tandem solar cells

S. Michard (2015), vi, 184 pp

ISBN: 978-3-95806-048-7

Band / Volume 260

**Quantitative analysis of spatially resolved electroluminescence of Cu(In,Ga)Se<sub>2</sub> and a-Si:H thin-film solar cells and modules**

T. Tran (2015), iii, 161 pp

ISBN: 978-3-95806-050-0

Band / Volume 261

**Influence of the surface composition and morphology on the reflectivity of diagnostic mirrors in a fusion reactor**

M. Matveeva (2015), 158 pp

ISBN: 978-3-95806-051-7

Band / Volume 262

**Very High Cycle Fatigue Behavior of Riblet Structured High Strength Aluminum Alloy Thin Sheets**

S. Stille (2015), XII, 123 pp

ISBN: 978-3-95806-054-8

Band / Volume 263

**The role of soil heterogeneity on field scale evapotranspiration: 3D integrative modelling and upscaling of root water uptake**

K. Huber (2015), xii, 128 pp

ISBN: 978-3-95806-057-9

Band / Volume 264

**Strontium-Diffusion in Cer-Gadolinium-Oxide als Degradationsmechanismus der Festoxid-Brennstoffzelle**

T. Mandt (2015), iii, 160 pp

ISBN: 978-3-95806-058-6

Band / Volume 265

**Cluster analysis of European surface ozone observations for evaluation of MACC reanalysis data**

O. Lyapina (2015), 187 pp

ISBN: 978-3-95806-060-9

Band / Volume 266

**Real-time quantification of oxygen isotope exchange between carbon dioxide and leaf/soil water in terrestrial ecosystems with laser-based spectroscopy**

L. Gangi (2015), XX, 156 pp

ISBN: 978-3-95806-061-6

Band / Volume 267

**Secondary Uranium Phases of Spent Nuclear Fuel – CoXnite, USiO<sub>4</sub>, and Studtite, UO<sub>4</sub>H<sub>2</sub>O – Synthesis, Characterization, and Investigations Regarding Phase Stability**

S. Labs (2015), 153, xlii pp

ISBN: 978-3-95806-063-0

Band / Volume 268

**Chemische, verfahrenstechnische und ökonomische Bewertung von Kohlendioxid als Rohstoff in der chemischen Industrie**

A. Otto (2015), viii, 272 pp

ISBN: 978-3-95806-064-7

Band / Volume 269

In Vorbereitung

Band / Volume 270

**Investigation of light propagation in thin-film silicon solar cells by dual-probe scanning near-field optical microscopy**

S. Lehnen (2015), 120 pp

ISBN: 978-3-95806-066-1

Band / Volume 271

**Characterization of soil water content variability at the catchment scale using sensor network and stochastic modelling**

W. Qu (2015), XVI, 123 pp

ISBN: 978-3-95806-067-8

Band / Volume 272

**Light Absorption and Radiative Recombination in Thin-Film Solar Cells**

T. C. M. Müller (2015), ii, 146 pp

ISBN: 978-3-95806-068-5

Weitere **Schriften des Verlags im Forschungszentrum Jülich** unter  
<http://www.zbw1.fz-juelich.de/verlagextern1/index.asp>



**Energie & Umwelt /**  
**Energy & Environment**  
**Band / Volume 272**  
**ISBN 978-3-95806-068-5**

